Dpto. de Física de la Materia Condensada
Facultad de Ciencias
Universidad Autónoma de Madrid

Synthesis and characterization of ZnO thin films and ZnO:Co system

Tesis para optar al grado de Doctor en Ciencias Físicas
presentada por

Cristiana Sonia Steplecaru

Dirigida por los doctores:

Mª Soledad Martín González y José L. Costa Krämer

Instituto de Microelectrónica de Madrid IMM-CNM (CSIC)

Junio de 2012

Instituto de Microelectrónica de Madrid
(Centro Nacional de Microelectrónica)

To my family

and all the special people in my life

ACKNOWLEDGMENTS

There are several people I would like to thank for different reasons.

First and foremost, my appreciation goes to my supervisors Dr. Marisol Martín González and Dr. Jose Luis Costa-Krämer for supervising the work and being a source of inspiration at each stage of this PhD research work. Their confidence in me has always been a motivating factor to keep me striving to reach my goals. I would like to express my gratitude to Dr. Jose Luis Costa-Krämer for his mentoring, support and for the opportunities he gave me throughout this study. I benefited from his wide experience in many fields. I am thankful to him for supervising this thesis and for constant discussions. Dr. Marisol Martín González has been a mentor during these years. Her patience and guidance have been precious. The completion of this thesis has been possible due to her intellectual support. I hope that her example would continue to inspire me in the future.

I would also like to thank my advisor at the University Autonoma of Madrid, Prof. Juan José Sáenz as core part of my graduate studies, for the guidance and support.

I would like to extend my thanks to Jose Francisco Fernández, Miguel Angel García, Juanjo, Adrian (the team from Instituto de Ceramica y Vidrio de Madrid) for the collaboration and invaluable discussions about magnetism; to Dr. Raquel Gonzalez for her important collaboration: the experimental guidance and help analyzing the data, and to Frans Munnik. I would also like to acknowledge the contributions of Anna Crespi, Mar García Hernandez and Pablo Fernández Sáez.

There are many people to thank in the IMM group. I am grateful to Prof. Fernando Briones for all the fruitful scientific discussions and to Dr. Benito Alen for discussions on photoluminescence.

To Dr. Mónica Luna, Dr. Javi Martinez, and Dr. Iván Fernández I am thankful for their suggestions and comfort that have helped me to grow professionally. I would also like to thank Dr. Fernando García for assistance.

I was really pleased about the companionship of my lab mates, especially Dani (Alegria), Raquel Alvaro, Patricia, Diego and Cristina, who provided a better working atmosphere inside the lab. I would like to thank them for their unconditional help and kindness. It was a pleasure working with you.

Special thanks to Kike for his help and assistance, and countless others who have made this journey enjoyable: PG, Merce, Maria, Marco, Elias, Marcos, Juan, Maki, Chon, Rui, Ram…

I also want to mention all the people from Administration and services especially: Mercedes, Margarita, Toña, Manuel, Judit, José Pulpón and Antonio Lerma. I wish to thank all of them for their cooperation during my research period, for administrative assistance and technical help.

And last, but not least, I express my sincere appreciation to my *family and friends*, who have helped to shape me into the person I am today. To *my friends: Elvi, Moni, Ana, Jose and Mariana* for being there at all moments and above all for their friendship. To *Rober*: for his encouragement and moral support, for his love and care. To *my parents and my brother*: although thousands of miles separate us, they have been always there for me.

It was their love, which kept me going, and words would fail to express feeling of indebtedness to them. I, therefore, offer my sincere silence words of acknowledgement to them.

INDEX OF CONTENTS

Capítulo 1

Introducción y objetivos 1

1.1. Introducción a la spintrónica 1

1.2. Semiconductores ferromagnéticos 4

1.3. Semiconductores Magnéticos Diluidos para spintrónica 5

1.4. Objetivos y planteamiento 9

Referencias 11

Chapter 1

Introduction and objectives 17

1.1. Introduction to Spintronics 17

1.2 Ferromagnetic Semiconductors 19

1.3. Diluted Magnetic Semiconductors for Spintronics 21

1.4. Research problems statement, objectives, and approach 24

References 26

Chapter 2

Experimental techniques 31

2.1. Thin film growth 32

2.1.1. Pulsed Laser Deposition (PLD) 32

2.1.2. Irradiation 44

2.1.3. Ion implantation 46

2.2. Thin film characterization 51

2.2.1. Profilometer 51

2.2.2. X-Ray Diffraction 53
2.2.3. Rutherford Backscattering Spectrometry 57
2.2.4. Proton Induced X-ray Emission 62
2.2.5. Atomic Force Microscopy 66
2.2.6. Photoluminescence 68
2.2.7. HALL 71
2.2.8. SQUID 80
References 82

Chapter 3

ZnO Thin films 87

3.1. Optimization of polycrystalline ZnO thin films 90
3.1.1. Substrate 92
3.1.2. Oxygen chamber pressure 94
3.1.3. Growth temperature 99
3.1.4. Oxygen plasma assisted deposition 102
3.2. Epitaxial ZnO thin films on sapphire substrate 106
3.2.1. Structural characterization 107
3.2.1.1. Profilometer 107
3.2.1.2. X-ray diffraction 108
3.2.1.3. Rutherford backscattering spectrometry 114
3.2.1.4. Particle induced x-ray emission 120
3.2.2. Morphology characterization: AFM 121
3.2.3. Electrical properties: Hall effect measurements 123
3.2.4. Magnetic properties of *p*- and *n*-type ZnO 129
References 135

Chapter 4

Some clues about the *p*-type behavior in un-doped ZnO 139

4.1. Twinning effect in ZnO 141

4.1.1. Influence of growth Temperature 142

4.1.2. Influence of substrate cleaning 145

4.2. Generating defects in ZnO by irradiation 152

4.2.1. Irradiation process 153

4.2.2. Structural characterization 154

4.2.3. Electrical properties-HALL measurements 160

4.3. Study of the *p*-type behavior by photoluminescence 165

4.4. Study of the aging mechanism 170

References 175

Chapter 5

ZnO with cobalt oxides (Zn-O-Co): Different approaches 179

5.1. ZnO/Co_3O_4 co-growth 179

5.2. ZnO/Co_3O_4 multilayers 183

5.2.1. Co_3O_4 thin films 185

5.2.1.1. Co_3O_4 targets 185

5.2.1.2. Polycrystalline Co_3O_4 thin films 187

5.2.1.3. Epitaxial Co_3O_4 thin films 190

5.2.2. Multilayers 199

5.2.2.1. Structural characterization 199

5.2.2.2. Electrical properties (HALL measurements) 202

5.2.2.3. Magnetic properties (SQUID) 204
5.3. ZnO implanted with Co 207
5.3.1. Structural characterization 210
5.3.2. Electrical properties 217
5.3.3. Optical properties 221
5.3.4. Magnetic properties 223
References 228

Conclusions 231

Conclusiones 233

Acronyms 235
Symbols 239

1

INTRODUCCIÓN Y OBJETIVOS

Capítulo 1

Introducción y objetivos

1.1. Introducción a la espintrónica

Los dispositivos electrónicos tradicionales basan su funcionamiento en el transporte de los electrones, utilizando para ello su carga eléctrica. Hoy en día, los científicos están tratando de explotar el espín de los electrones en lugar de su carga, con el fin de crear una nueva generación de dispositivos "espintrónicos". Esta nueva tecnología dará lugar a dispositivos más pequeños, más versátiles y más robustos que los que actualmente constituyen los chips de silicio. En la literatura, existen diferentes términos como magnetoelectrónica, electrónica de espín y espintrónica, para describir la misma temática: el uso controlado del espín del electrón (no sólo su carga eléctrica) en los circuitos integrados.

Ventajas

Bien sea agregando el grado de libertad del espín a dispositivos electrónicos convencionales basados en la carga, o utilizando el espín por sí solo, la espintrónica presenta numerosas ventajas en comparación con los dispositivos semiconductores convencionales. La principal ventaja es la no volatilidad, que aumenta la velocidad de procesamiento de datos, disminuye el consumo de energía eléctrica y aumenta la densidad de integración [1].Otra ventaja fundamental del

espín comparado con la carga es que el espín puede ser manipulado fácilmente aplicando un campo magnético. Otra ventaja del espín es que, a diferencia de los estados de carga que son fácilmente destruidos por la dispersión o colisión con defectos/impurezas, el espín tiene un tiempo de relajación más largo [2].

Aplicaciones

La densidad de almacenamiento de información de las unidades de disco duro está aumentando exponencialmente, en parte porque los dispositivos espintrónicos como son los sensores de Magnetoresistencia Gigante (GMR) y la Resistencia Túnel Magnética (TMR) han aumentado la sensibilidad de la cabeza de lectura.

En las MRAM o memorias magnéticas de acceso aleatorio, del inglés Magnetic Random Access Memory, se utiliza un patrón de elementos de almacenamiento magnético llamado Uniones Túnel Magnéticas (MTJ). Las MRAM son sistemas de almacenamiento no volátil (a diferencia de las DRAM, o Memorias Dinámica de Acceso Aleatorio, que se basan en la carga y que se utilizan hoy en día en los ordenadores), por lo que la información se mantiene incluso cuando se apaga el ordenador. Motorola ha desarrollado una primera generación de MRAM de 256 kb basada en una sola unión de túnel magnético y un solo transistor [3]. Desde entonces Everspin, una spin-off de Motorola, ha desarrollado una versión de 4 Mbit [4]. Actualmente hay dos técnicas MRAM en desarrollo: Conmutación Térmica Asistida (TAS) [5] que está siendo desarrollado por Crocus Technology, y la Transferencia del par de torsión del espín (STT) en la que están trabajando Crocus, Hynix, IBM, etc [6]. Otro diseño en desarrollo es el llamado memoria "pista de carrera" (conocida en inglés como Racetrack memory).

Entre esta nueva clase de dispositivos se pueden destacar: las válvulas de espín, los transistores de espín (que funcionan con bajo

consumo y por lo tanto son adecuados para aplicaciones móviles), los emisores ópticos con información codificada a través de luz polarizada, las memorias semiconductoras no volátiles, y los dispositivos magnéticos/electrónicos/fotónicos integrados. Un esquema de tecnologías complementarias y aplicaciones para dispositivos basados en el espín se muestra en la Fig.1.1.

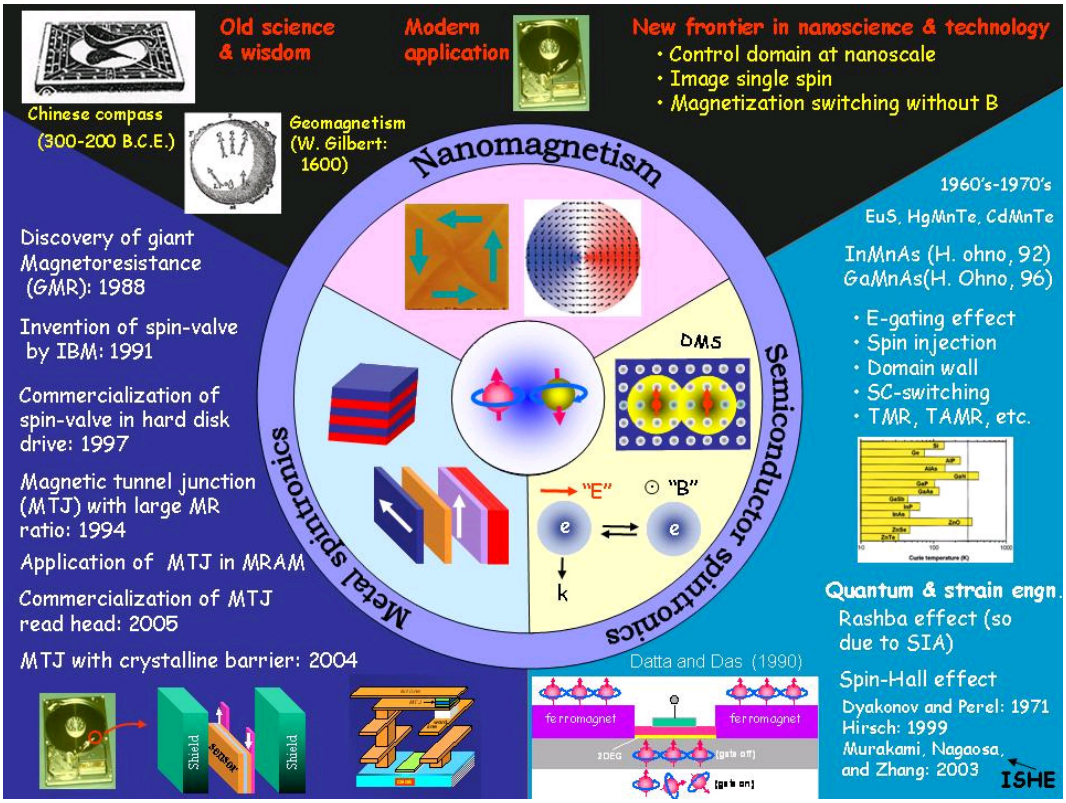

Fig.1.1. Evolución de los dispositivos espintrónicos (Extraído del Ref. [7])

La tecnología espintrónica recién desarrollada requiere materiales que permitan el control de la carga así como los grados de libertad del espín de los portadores de carga.

1.2. Semiconductores ferromagnéticos

La búsqueda de materiales adecuados para desarrollar dispositivos espintrónicos comenzó en los años sesenta. Para alcanzar este objetivo es esencial resolver los problemas relacionados con la generación estable de suficientes portadores polarizados en espín y de su transporte, de forma fiable, dentro de los dispositivos. Esto impone dos requisitos al sistema: en primer lugar debe tener un elemento ferromagnético que admita un almacenamiento adecuado de los electrones polarizados en espín, y en segundo lugar, el sistema debe tener una porción de semiconductor a través del cual se puede realizar la operación convencional del dispositivo. A primera vista, una interfaz metal ferromagnético/ semiconductor podría servir. Sin embargo, el desajuste de conductividad entre el metal ferromagnético y el semiconductor provoca la dispersión en la interfase, y solo algunos de los átomos magnéticos son difundidos a la parte semiconductora. Cuando los electrones polarizados en espín pasan a través de la interfaz, experimentan una dispersión entre dos canales de espín diferente y los electrones pierden la polarización de su espín en poco tiempo. Por lo tanto el grado de polarización de espín debe ser muy bajo, como se muestra en la Fig.1.2.

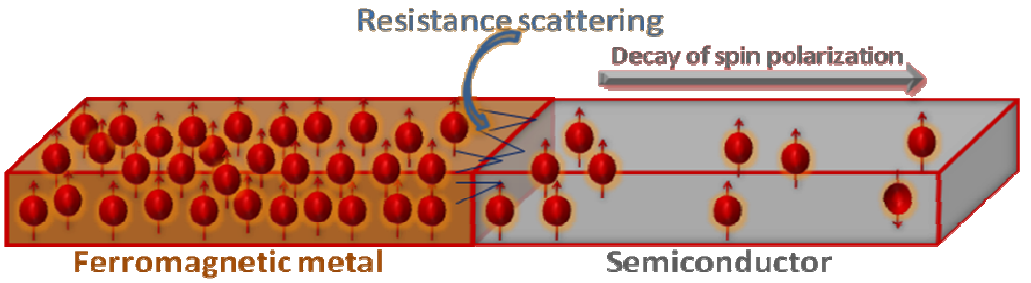

Fig.1.2. Esquema de la heteroestructura metal ferromagnético y semiconductor mostrando el problema de la dispersión en la interfase y la rápida caída de la polarización de espín lejos de la interfase

Con el fin de lograr un nivel alto de polarización de los espines utilizando una fuente de metal ferromagnética hay dos posibilidades: o bien la conductividad de los dos materiales es parecida, o el grado de polarización del espín en el metal debe ser de un 100%. Ninguna de estas soluciones es fácilmente alcanzable en dispositivos semiconductor/metal [8].

1.3. Semiconductores Magnéticos Diluidos para espintrónica

El uso de Semiconductores Magnéticos Diluidos (DMS) como inyectores de espín puede eliminar el problema de la diferencia de conductividad en la interfaz. Los DMSs son semiconductores en los cuales una fracción de sus cationes se sustituye por iones magnéticos o tierras raras [9]. Sin embargo, los semiconductores magnéticos tienen Temperaturas de Curie (T_C) que están por debajo de la temperatura ambiente (RT), haciéndolos inadecuados para aplicaciones en dispositivos.

En los últimos años se han hecho importantes esfuerzos para el crecimiento de materiales semiconductores que exhiban ferromagnetismo (FM) por encima de la RT [10-12]. En el año 2000, Dietl *et al.* estimaron las temperaturas Curie de varios sistemas semiconductores y óxidos [13]. Sus cálculos predijeron la existencia de ferromagnetismo por encima de la RT en semiconductores tipo *p* cuando se dopan con metales de transición tipo manganeso (véase Fig.1.3).

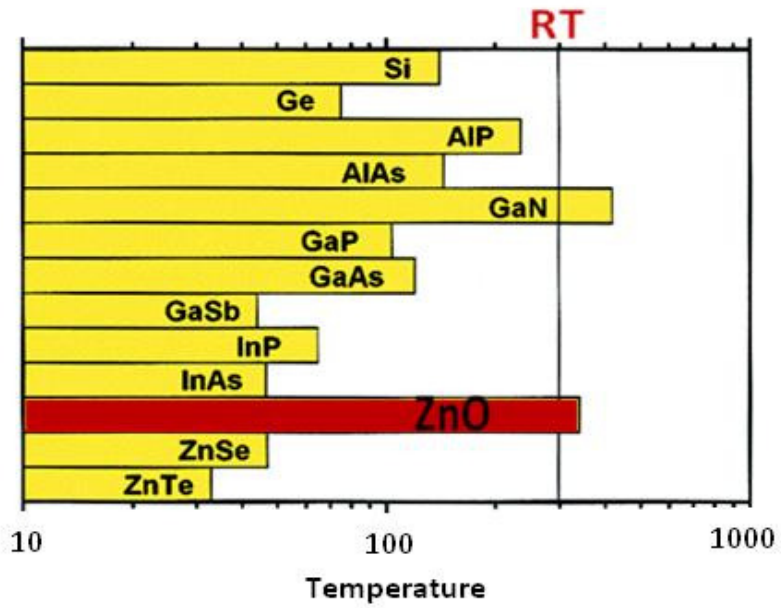

Fig.1.3. Valores Tc calculadas para diversos semiconductores de tipo *p*. La línea vertical corresponde a la temperatura ambiente (Del Ref. [13], © 2000. Reimpreso con el permiso de AAAS)

Por lo que se observa en la Fig.1.3 existen dos semiconductores que teóricamente presentan ferromagnetismo por encima de temperatura ambiente cuando se dopan con Mn: ZnO y GaN. Entre estos dos semiconductores, tal vez el más interesante para estudiar sea el ZnO puesto que presenta una energía de ligadura excitónica de 60 meV que es más del doble que la del GaN (28 meV). [14-16]. Sin embargo, la dificultad más importante que obstaculiza el uso de ZnO para dispositivos semiconductores es la falta de un método fiable y reproducible para conseguir su dopaje tipo *p* [17,18]. Aunque el ZnO tipo *n* puede ser producido de forma fiable, el tipo *p* es mucho más difícil de lograr. Esta es la razón por la que la búsqueda de técnicas para producir ZnO tipo *p* constituye una gran parte de la investigación en ZnO en la actualidad.

Tres años después del trabajo de Dietl, Sharma *et al.* [19] comunicaron la existencia de FM a RT en el sistema Mn:ZnO tanto en blancos fabricados mezclando cantidades apropiadas de ZnO y MnO_2, como en películas delgadas crecidas mediante ablación láser.

Desde entonces, ha habido varios trabajos experimentales que describen la aparición de FM por encima de 300 K en sistemas como Mn:ZnO [20], Co:ZnO [21], Co:TiO_2 [22,23], GaMnN [24], GaMnP [25].

Aunque el sistema ZnO con óxidos de Mn exhibe FM a RT, aun persisten amplias dudas sobre su origen [26]. Hoy en día, existen tres enfoques diferentes en la literatura para explicar el origen del magnetismo en el sistema Zn-O-Mn. a) El primero, relacionado con el hecho de que el metal de transición, como por ejemplo el Mn, entra en la red de ZnO [27,28] de forma substitucional. Por tanto los electrones de conducción están polarizados en espín y se trata de semiconductores magnéticos diluidos. b) Un segundo enfoque, en el que se explica que el magnetismo es debido no sólo a la presencia de iones magnéticos, sino también a la presencia de defectos de oxígeno en la red del ZnO [29-31]. Y, c) un tercero, en el que nuevos descubrimientos apuntan hacia una dirección diferente: que estos materiales no son DMS y que el magnetismo es debido a fases secundarias [32] o a un mecanismo de doble canje en la intercara en el frente de difusión de cationes del Zn dentro de las partículas de MnO_2. Esto está publicado para el caso del ZnO:MnO_2 [33-35].

Para el sistema Zn-O-Co la situación es aún más compleja debido a que la segregación ´de pequeños "clusters" metálicos de Co puede inducir FM a temperatura ambiente [36-39]. Su origen y su mecanismo tampoco están bien establecidos. En un trabajo anterior se ha sugerido que este FM está mediado por portadores en una banda de impurezas desdoblada en espín procedente de orbitales donores extendidos [40].

Otra explicación podría ser que el FM observado proviene del FM débil de CoO [41]. Es bien conocido que el CoO es antiferromagnético, con una temperatura Néel de 290K, cerca de RT. El FM se ha observado también en muestras masivas o "bulk" de Zn-O-Co obtenidas por diferentes técnicas. En el caso de muestras obtenidas por métodos de combustión el FM proviene del Co metálico debido a la reducción atmosférica del proceso [42]. Por otro lado, las medidas efectuadas sobre las muestras preparadas por *Lawes et al.* confirman

la sustitución de los iones magnéticos en el semiconductor, pero no se ha encontrado FM en este sistema hasta una temperatura de 2K [43]. Tampoco presentaron FM las muestras preparadas por técnicas hidrotermicas o reacciones de estado sólido estándar [44,45]. Esto fue atribuido a la carencia de portadores libres y al acoplamiento antiferromagnético de los iones de cobalto cercanos, según trabajos teóricos [46,47].

Posteriormente nuevos resultados mostraron que el origen del FM está en la intercara [48,49]. Recientemente se ha demostrado que una reacción electroquímica espontánea en la intercara entre nanopartículas de óxido de ZnO/Co_3O_4, TiO_2/Co_3O_4, Al_2O_3/Co_3O_4, SiO_2/Co_3O_4 podría ser el origen de la aparición de nuevas propiedades como el ferrimagnetismo [50]. Este comportamiento ferrimagnético es similar al de ferritas con estructura de espinela. El mecanismo por el cual aparece la fase magnética ordenada está relacionado con una reducción superficial del Co_3O_4 a CoO durante la mezcla. Este magnetismo existe no sólo en semiconductores como ZnO o TiO_2 (anteriormente descritos en la literatura), sino también en otros óxidos aislantes como SiO_2 o Al_2O_3. La eficacia de la reacción en la intercara es proporcional aproximadamente a la diferencia de basicidad entre las superficies de los óxidos.

Debido a la complejidad de los sistemas DMS basados en ZnO resulta difícil todavía encontrar una teoría universal para explicar todos los fenómenos anteriormente descritos observados. Se podría afirmar que el estado de los sistemas de ZnO "dopados con TM" todavía está en su infancia, y es demasiado pronto para dar una descripción definitiva de los mecanismos que rigen las observaciones experimentales. Un mejor conocimiento de los mecanismos mencionados proporcionará sin duda la información necesaria para el diseño de dispositivos espintrónicos.

1.4. Objetivos y planteamiento

La revisión realizada en la sección anterior describe el presente estado del arte en DMS basados en ZnO para aplicaciones de espintrónica. Muchos grupos han investigado la síntesis y las propiedades magnéticas del ZnO tipo *n* usando varios métodos de crecimiento. Después de un estudio exhaustivo de la literatura, hemos identificado algunos de los problemas críticos de los DMS basados en ZnO, los cuales necesitan una investigación en más detalle para que estos materiales puedan usarse en la práctica:

- Quizás uno de los problemas más importantes es que, aunque el trabajo teórico de Dietl es para ZnO tipo *p*, la mayoría de los trabajos publicados en la literatura se han realizado con ZnO tipo *n*. La razón de esto es que no es fácil obtener ZnO tipo *p*. Este es uno de los principales obstáculos en el desarrollo de la microelectrónica basada en ZnO
- Hay muchas teorías para explicar el FM a RT en DMSs basados en ZnO, pero hay una gran falta de entendimiento del mecanismo que está detrás

Objetivos:

El objetivo de este trabajo de doctorado es esclarecer los problemas arriba mencionados. El trabajo se ha estructurado de la siguiente manera:

1. Preparar películas de ZnO de alta calidad con el comportamiento tipo *p* y tipo *n*.
2. Crecer películas de Co_3O_4 de alta calidad.
3. Investigar el sistema de ZnO:Co como un posible DMS, comparando ZnO tipo *p* y tipo *n* utilizando diferentes enfoques. En todos los casos el objetivo ha sido investigar

su estructura y correlacionarla con las propiedades de transporte, contribuyendo a identificar el origen de ferromagnetismo observado en este sistema.

Planteamiento:

El *Capítulo 1* introduce el tema de la tesis y describe los objetivos.

En el *Capítulo 2* se presentan las técnicas experimentales que han sido necesarias para desarrollar este trabajo, tanto en la deposición de películas como en su caracterización. Adicionalmente, se describen los procesos necesarios para la preparación de películas para su medida.

Los objetivos de este trabajo se han abordado de acuerdo con la siguiente descripción:

El *Capítulo 3* está dedicado a la optimización de las películas de ZnO para lograr películas epitaxiales ZnO tipo *p* y tipo *n*. La caracterización estructural, morfológica, eléctrica y magnética de películas tanto policristalinas como epitaxiales de ZnO crecidas por ablación laser (PLD) se muestra en este capítulo.

El *Capítulo 4* se centra en entender el comportamiento de las películas delgadas epitaxiales de ZnO tipo *p* sin dopaje extrínseco intencionado. Este capítulo trata de comprender el origen del comportamiento de tipo *p*. Para ello, se estudian los defectos del maclado, y los defectos intrínsecos producidos por irradiación de iones sobre las propiedades eléctricas de películas de ZnO. Además, se lleva a cabo un estudio por fotoluminescencia (PL) para determinar qué tipos de defectos contribuyen a la conducción tipo *p*. Por último se hace un estudio del mecanismo de envejecimiento o "aging" que sufre el ZnO tipo *p*.

El *Capítulo 5* está dedicado a estudiar el sistema Zn-O-Co como semiconductor magnético diluido. El estudio se realiza mediante tres enfoques diferentes. En el primer enfoque, se estudia la posibilidad de co-crecimiento utilizando blancos de ZnO/Co_3O_4. En el segundo, se investigan las multicapas ZnO/Co_3O_4. En esta sección, en primer lugar se realiza un estudio de las películas delgadas de Co_3O_4, incluyendo la optimización de las condiciones de crecimiento desde películas policristalinas a epitaxiales. Además, se realiza la caracterización estructural, eléctrica, óptica y magnética de las multicapas. En el tercer enfoque, se estudian películas delgadas de ZnO tipo *p* y *n* implantadas con Co, y se investigan sus propiedades estructurales, eléctricas, ópticas y magnéticas.

Referencias

[1] S.A. Wolf, D.D. Awschalom, R.A. Buhrman, J.M. Daughton, S. von Molnár, M.L. Roukes, A.Y. Chtchelkanova, D.M. Treger, Science 294 (2001) 1488

[2] S.D. Sarma, American Scientist 89 (2001) 516

[3]http://www.sigmaaldrich.com/materials-science/alternative-energy - materials/magnetic-materials/tutorial/spintronics.html

[4] http://www.everspin.com/technology.html

[5]http://www.crocus-technology.com/pdf/BH%20GSA%20 Article.pdf

[6]http://www.eetimes.com/news/latest/showArticle.jhtml?articleID=218000269

[7]http://urtechfriend-paperpresentations5.blogspot.com.es/p/spintronics.html

[8] B.T. Jonker, S.C. Erwin, A. Petrou, A.G. Petukhov, MRS Bulletin 28 (2003) 740

[9] H. Ohno, Science 281, 5379 (1998) 951

[10] S.J. Pearton, W.H. Hep, M. Ivill, D.P. Norton, T. Steiner, Semicond. Sci. Technol. R59-R74 (2004) 19

[11] S.J. Pearton, C.R. Abernathy, D.P. Norton, A.F. Hebard, Y.D. Park, L.A. Boatner, J.D. Budai, Mat. Sci. and Eng. R 40 (2003) 137

[12] J.M.D. Coey, S. Sanvito, J. Phys. D: Appl. Phys. 37 (2004) 988

[13] T. Dietl, H. Ohno, F. Matsukura, J. Cibert, D. Ferrand, Science 287 (2000) 1019

[14] S.W. Jung, S.J. An, G.C. Yi, C.U. Jung, S.I. Lee, S. Cho, Appl. Phys. Lett. 80 (2002) 4561

[15] A.B. Mahmoud, H.J. von Bardeleben, J.L. Cantin, A. Mauger, E. Chikoidze, Y. Dumont, Phys. Rev. B 74 (2006) 115203

[16] Z. Yang, W.P. Beyermann, M.B. Katz, O.K. Ezekoye, Z. Zuo, Y. Pu, J. Shi, X.Q. Pan, J.L. Liu, J. Appl. Phys. 105 (2009) 053708

[17] D.C. Look, B. Claflin , Phys. Status Solidi B, 241 no.3 (2004) 624-30

[18] D.C. Look, Semicond. Sci. Tech. 20 no.4 (2005) S55-61

[19] P. Sharma, A. Gupta, K.V. Rao, F.J. Ownes, R. Sharma, R. Ahuja, J.M.O. Guillen, B. Johansson, A.G. Gehring, Nature Mater. **2** (2003) 673

[20] N.A. Theodoropoulou, A.F. Hebard, D.P. Norton, J.D. Budai, L.A. Boatner, J.S. Lee, Z.G. Khim, Y.D. Park, M.E. Overberg, S.J. Pearton, R.G. Wilson, Solid State Electronics 47 (2003) 2231

[21] K. Rode, A. Anane, R. Mattana, J.P. Contour, O. Durand, R. LeBourgeois, J. Appl. Phys. 93 (2003) 7676

[22] J.Y. Kim, J.H. Park, B.G. Park, H.J. Noh, S.J. Oh, J.S. Yang, D.H. Kim, S.D. Bu, T.W. Noh, H.J. Lin, H.H. Hsieh, C.T. Chen, Phys. Rev. Lett. 90 (2003) 017401

[23] S.R. Shinde, S.B. Ogale, S. Das Sarma, J.R. Simpson, H.D. Drew, S.E. Lofland, C Lanci, J.P. Buban, N.D. Browning, V.N.

Kulkarni, J. Higgins, R.P. Sharma, R.L. Greene, T. Venkatesan, Phys. Rev. B 67 (2003) 115211

[24] S. Sonoda, S. Shimizu, T. Sasaki, Y. Yamamoto, and H. Hori, J. Cryst. Growth 237-239 (2002) 1358

[25] N. Theodoropoulou, A.F. Hebard, M.E. Overberg, C.R. Abernathy, S.J. Pearton, S.N.G. Chu, R.G. Wilson, Phys. Rev. Lett. 89 (2002) 107203

[26] J.M.D. Coey, Curr. Opin. Solid. State Mater. Sci. 10 (2006) 83

[27] P. Sharma, A. Gupta, K.V. Rao, F.J. Owens, R. Sharma, R. Ahuja, J.M. Osorio Guillen, B. Johansson, G.A. Gehring, Nature Mater. 2 (2003) 673

[28] C.B. Fitzgerald, M. Venkatesan, J.G. Lunney, L.S. Dorneles, J.M.D. Coey, Appl. Surf. Sci. 247 (2005) 493

[29] M. Venkatesan, C.B. Fitzgerald, J.M.D. Coey, Nature 430 (2004) 630

[30] K.R. Kittilstved, D.R. Gamelin, J. Am. Chem. Soc. 127 (2005) 5292

[31] J.M.D. Coey, M. Venkatesan, C.B. Fitzgerald, Nature Mater. 4 (2006) 173

[32] D. Kundaliya, S.B. Ogale, S.E. Lofland, S. Dhar, C.J. Metting, S.R. Shinde, Z. Ma, B. Varughese, K.V. Ramanujachari, L. Salamanca-Riba, T. Venkatesan, Nature Mater. 3 (2004) 709

[33] J.L. Costa-Kramer, F. Briones, J.F. Fernandez, A.C. Caballero, M. Villegas, M. Diaz, M.A. Garcia, A. Hernando, Nanotechnology Vol.16,2 (2005) 214

[34] M.A. García, M.L. Ruiz-Gonzalez, A. Quesada, J.L. Costa-Krämer, J.F. Fernández, S.J. Khatib, A. Wennberg, A.C. Caballero, M.S. Martin-Gonzalez, M. Villegas, F. Briones, J.M. Gonzalez-Calbet, A. Hernando, Phys. Rev. Lett. 94 (2005) 217206

[35] E. López-Ponce, A. Wennberg, M.S. Martín-González, J.L. Costa-Krämer, M.A. García, A. Quesada, A. Hernando, A.C. Caballero, M. Villegas, J.F. Fernández, Jap. J. Appl. Phys, 45, 10A (2006) 7667

[37] S.R. Shinde, S.B. Ogale, J.S. Higgins, H. Zheng, A.J. Millis, V.N. Kulkarni, R. Ramesh, R.L. Greene, T. Venkatesan, Phys. Rev. Lett. 92 (2004) 166601

[38] J.H. Park, G. Kim, H.M. Jang, S. Ryu, Y.M. Kim, Appl. Phys. Lett. 84 (2004) 1338

[38] E.C. Lee, K.J. Chang, Phys. Rev. B 69 (2004) 085205

[39] J. Hyun Kim, H. Kim, D. Kim, Y. Ihm, W.K. Choo, J. Eur. Ceram. Soc. 24 (2004) 1847

[40] C.B. Fitzgerald, M. Venkatesan, J.G. Lunney, L.S. Dorneles, J.M.D. Coey, Appl. Surf. Sci. 247 (2005) 493

[41] K. Ueda, H. Tabata, T. Hawai, Appl. Phys. Lett. 79 (2001) 988

[42] S. Deka, P.A. Joy, Solid State Commun. 134 (2005) 665

[43] G. Lawes, A.S. Risbud, A.P. Ramírez, R. Seshadri, Phys. Rev. B 71 (2005) 045201

[44] M. Bouloudenine, N. Viart, S. Colis, A. Dinia, Chem. Phys. Lett. 73 (2004) 397

[45] S.J. Han, B.Y. Lee, J.S. Ku, Y.B. Kim, Y.H. Jeong, J. Magn. Magn. Mater. 272–276 (2004) 2008

[46] E.C. Lee, K.J. Chang, Phys. Rev. B 69 (2004) 085205

[47] A.S. Risbud, N.A. Spaldin, Z.Q. Chen, S. Stemmer, R. Seshadri, Phys. Rev. B 68 (2003) 205202

[48] A. Quesada, M.A. García, M. Andrés, A. Hernando, J.F. Fernández, A.C. Caballero, M.S. Martín-González, F. Briones, J. App. Phys. 100 (2006) 113909

[49] M.S. Martín-González, J.F. Fernández, F. Rubio-Marcos, I. Lorite, J.L. Costa-Krämer, A. Quesada, M.A. Bañares, J.L.G. Fierro, J. App. Phys. 103 (2008) 083905

[50] M.S. Martin-González, M.A. García, I. Lorite, J.L. Costa-Krämer, F. Rubio-Marcos, N. Carmona, J.F. Fernández , J. Electroch. Soc. 157 (2010) E31

1

INTRODUCTION AND OBJECTIVES

Chapter 1

Introduction and objectives

1.1. Introduction to Spintronics

Traditional electronic devices use the transport of electrons based on their electrical charge. During recent years, the efforts of the scientists have been concentrated on creating an outstanding new generation of 'spintronic' devices, which will use the 'spin' of the electron not just its charge. This kind of devices will present a few advantages compared to the conventional ones: non-volatile, smaller, versatile and sturdier. There are different names for this field: Magnetoelectronics, Spin Electronics, and Spintronics, but they all mean the same: devices which use the electrons' spins beside their electrical charge.

Advantages

The main advantage of using the spin degree of freedom, alone or together with the charge of the electron is non-volatility. This property will result in an increase of the data processing speed and a decrease of the electric power consumption [1]. Another very important advantage is that spin can be controlled externally by applying a magnetic field. An additional feature of the spin compared to the charge is that is not so quickly destroyed by scattering or collisions [2].

Applications

Controlling the electron spin is a big step in the evolution of electronic systems and communications technologies.

The storage density of hard-drives is increasing exponentially, due to the fact that spintronics-enabled devices like Giant Magneto Resistance (GMR) and Tunnel Magneto Resistance (TMR) sensors have increased the sensitivity of the read head.

MRAM, or Magnetic Random Access Memory, is nonvolatile, which means that information is stored including when power is turned off (it uses a lattice of magnetic storage elements called Magnetic Tunnel Junctions (MTJ's)). This non-volatility is one of the most important features compared to charge-based memory used in the computers, like Dynamic Random Access Memory (DRAM). The first generation MRAM of 256 kb has been developed by Motorola using just one MTJ and one transistor [3] Later on a 4 Mbit generation has been developed by Everspin [4]. Nowadays another 2nd generation MRAM techniques are in progress: Thermal Assisted Switching (TAS)[5] developed by Crocus Technology, and Spin Torque Transfer (STT) which is investigated by several companies like Crocus, Hynix, IBM, etc [6]. There is also another project still at research stage for what is called Racetrack memory.

Among the next-generation spintronic devices we can enumerate: spin valves, spin transistors (suitable for mobile applications), spin Light-Emitting Diodes (LEDs), fast non-volatile memory, ultra-fast optical switches and integrated magnetic/electronic/photonic devices. A scheme of complementary technologies and applications for spin-based devices is shown in Fig.1.1.

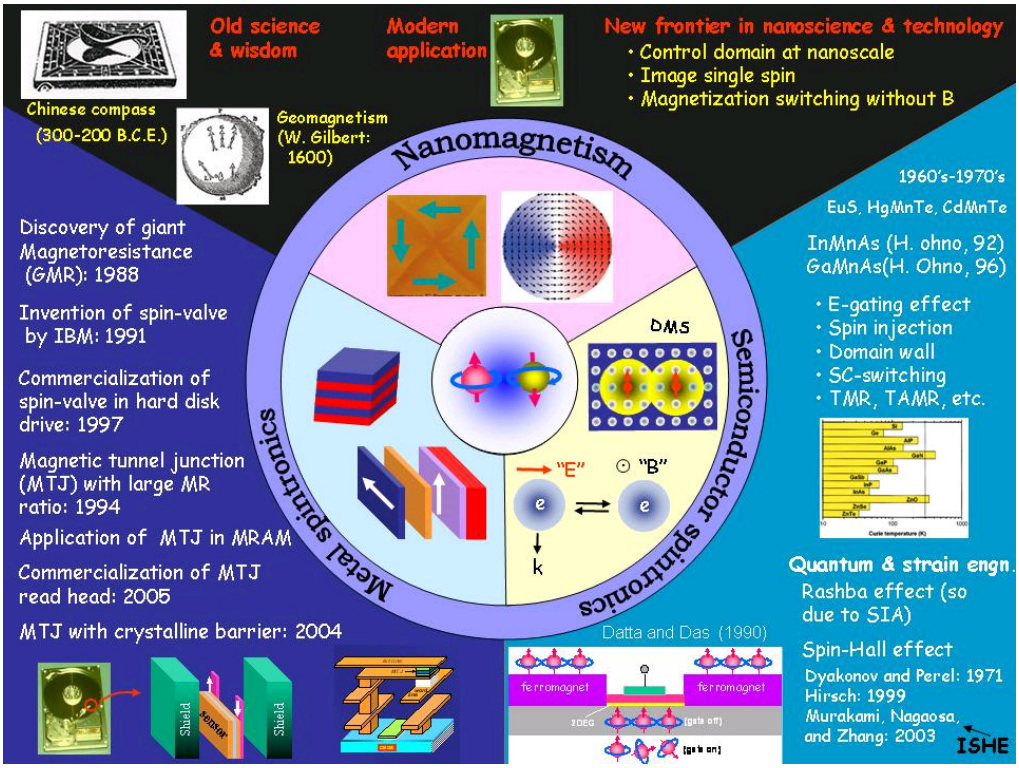

Fig.1.1. Evolution of spintronics devices (Extracted from Ref. [7])

In order to develop spintronics devices, materials able to control the charge and the spin degrees of freedom at the same time are required.

1.2 Ferromagnetic Semiconductors

It was in the sixties, when the search for suitable materials started. For this purpose it is necessary to find a source which would generate an adequate amount of spin polarized carriers, and a way to transport them within the devices. In other words the system has to fulfil two requirements: to have a ferromagnetic element which will support a sufficient storage of the spins polarized electrons, and to have a semiconducting portion through which conventional device process can be carried out. Therefore it was suggested that the ferromagnetic

metal and semiconductor hetero-structure may be a good candidate. However, due to the conductivity mismatch between the ferromagnetic metal and the semiconductor heterostructure a resistance scattering is observed at the interface, and only part of the magnetic atoms passes through the metal/semiconductor interface into the semiconductor portion. When passing through the interface, they will lose their spin-polarization in short time due to the scattering between two different spin channels, which will result in a decrease of the amount of spin polarization as shown in Fig.1.2.

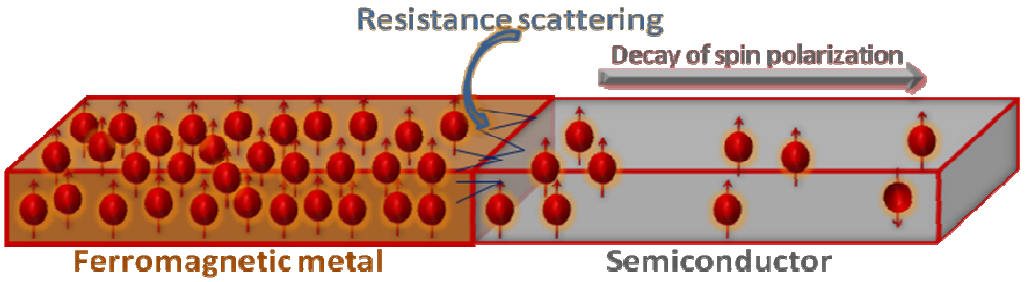

Fig.1.2. Drawing of the ferromagnetic metal and semiconductor hetero-structure illustrating the resistance scattering at the interface and the decay of spin polarization away from the interface

It was then concluded that metal-semiconductor devices are not a very good option for spintronics, because with a ferromagnetic metal source high spin polarization cannot be achieved. For a high spin polarization the two materials should have similar conductivity, or the degree of spin polarization in the metal must be close to 100%, but none of these solutions is likely to obtain in practice [8].

1.3. Diluted Magnetic Semiconductors for Spintronics

The issue of conductivity matching at the interface can be solved using Diluted Magnetic Semiconductor (DMS) as spin injector. The DMSs are semiconducting materials which have a small part of the host cations substituted by magnetic ions or rare earths [9]. However, magnetic semiconductors have Curie Temperatures (T_C) that are below Room Temperature (RT), making them unsuitable for normal device applications.

Over the last years, there have been significant efforts of growing semiconducting materials that present ferromagnetism (FM) above RT [10,11,12]. In the year 2000 Dietl *et al.* made calculations to estimate the Curie temperatures of different semiconductor systems and oxides [13]. According to their model ferromagnetism above RT can be achieved in p-type semiconductors when they are doped with transition metal ions like manganese (see Fig.1.3).

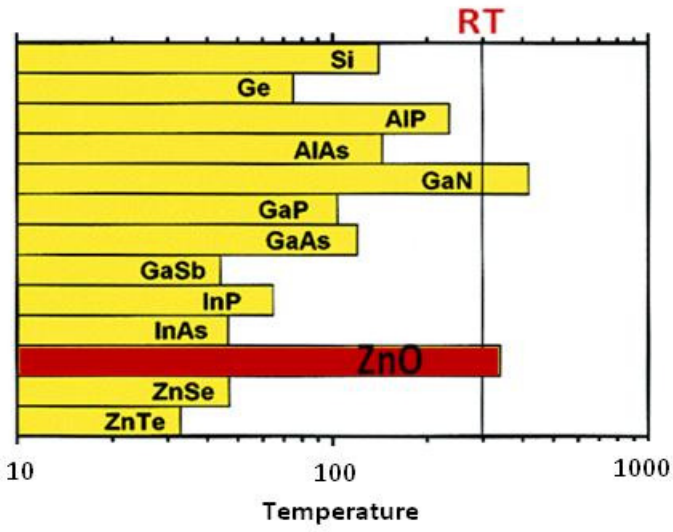

Fig.1.3. Calculated T_c values for various *p*-type semiconductors. Vertical line corresponds to room temperature (From Ref. [13], © 2000. Reprinted with permission from AAAS)

As it can be observed in Fig.1.3 there are two semiconductors which theoretically will present FM-RT when they are doped with Mn: ZnO and GaN. Among these two, zinc oxide seems to be a more interesting subject to study. The main reason for this was its wide band gap of 3.36 eV at room temperature and a high exciton binding energy of 60 meV (twice larger than that of GaN), which make this material a good option for optoelectronic devices in the ultraviolet spectral region [14-16]. Nevertheless, there is still need of a reliable method to achieve *p*-type material, being this the major issue which impedes the use of ZnO for semiconductor devices [17,18]. While *n*-type ZnO can be easily produced and reproducible, achieving *p*-type ZnO material is still a challenge, and constitutes a large portion of research in ZnO.

Three years after Dietl work, Sharma *et al.* [19] reported FM at RT in ZnO:Mn system (in pellets made of ZnO and MnO_2, as well as in thin films grown by Pulsed Laser Deposition (PLD)).

Since then, the appearance of FM above RT has been reported experimentally for different systems like Mn:ZnO [20], Co:ZnO [21], Co:TiO_2 [22,23], GaMnN [24], GaMnP [25].

Even though RT FM for ZnO with Mn oxides has been reported by different groups, its origin is still not elucidated [26]. Nowadays, one can find in literature three different approaches or scenarios of the origin of this magnetism. a) The first approach refers to the doping of the ZnO lattice with Transition Metals (TM) ions, and as a result the conduction electrons will become spin-polarized making these materials magnetic semiconductors [27,28]. b) The second approach discusses the existence of ZnO oxygen defects beside the presence of magnetic ions [29-31]. c) The third approach refers to the latest discoveries, suggesting that actually ZnO:Mn system is not a DMS. In this case, the observed magnetism could raise due to secondary phases [32] or due to a double-exchange mechanism at the interface as Zn cations diffuse into the MnO_2 particles [33-35].

For the Zn-O-Co system, the situation is still more complex as segregation of small metallic Co clusters can induce a RT FM response [36-39]. Its origin and mechanism are not well established either. In a previous work it has been suggested that this FM is mediated by carriers in a spin-split impurity band derived from extended donor orbitals [40]. Another explanation could be that the weak FM of CoO account for the observed FM [41]. CoO is well known to be antiferromagnetic, with a Néel temperature of 290K. The observed FM has been also reported in Zn-O-Co bulk samples obtained by various methods. In the case of samples obtained by combustion method, it seems that the FM comes from the metallic cobalt [42]. On the other hand, the measurements performed on bulk samples prepared by *Lawes et al.* confirm the replacement of the magnetic ions into the semiconductor, but could not find any magnetic ordering in this system down to 2K [43]. When the hydrothermal technique or standard solid-state reactions were employed, the samples did not exhibit FM [44,45]. In this case it has been ascribed to the lack of free carriers and the antiferromagnetic coupling of nearest cobalt ions, as suggested by theoretical works [46,47].

Later on, new results showed that the origin of the FM is at the interface [48,49]. More recently, it has been presented that a spontaneous solid-state electrochemical reaction at oxide nanoparticles interfaces between ZnO/Co_3O_4, TiO_2/Co_3O_4, Al_2O_3/Co_3O_4, SiO_2/Co_3O_4 could originate the appearance of ferrimagnetic behavior [50]. This behavior is comparable to the one of ferrites with spinel structure. The mechanism responsible has been associated to a surface reduction of Co_3O_4 to CoO during mixing. The novelty of this study is that this magnetism appears also in oxides with insulating properties (SiO_2 or Al_2O_3) not only in semiconductors (ZnO or TiO_2). The interface reaction has been correlated with the surface basicity of the oxides.

Nevertheless, the ZnO based DMS is a very complex system, and a theory that could explain all the observed phenomena has not been formulated. One could say that the state of TM-doped ZnO systems

demand more research, in order to achieve a better understanding of the mechanisms responsible for the reported magnetization behavior.

1.4. Research problems statement, objectives, and approach

A large number of groups have explored the synthesis and magnetic properties of *n*-type ZnO using a variety of growth methods. After a thorough literature survey on ZnO based DMS materials, we have identified some of the critical issues, which need further investigation in order to be able to apply these materials into devices:

- Maybe one of the most important issues is that, although the theoretical work of Dietl is for *p*-type ZnO, most of the works reported in the literature have been done with *n*-type ZnO. The reason for this is because is not easy to be obtained ZnO in *p*-type form. This is one of the main bottlenecks in the development of ZnO microelectronics.

- There are many theories to explain RT-FM in ZnO based DMS, but there is a strong lack of understanding of the mechanism behind.

Objectives:

The objectives of this PhD work are to shine some light on the issues mentioned above. For that reason the objectives can be broadly subdivided into the following:

1. To prepare high quality ZnO films with *p*- and *n*-type conduction if possible.
2. To synthesize and characterize high quality Co_3O_4 films.
3. To investigate the ZnO:Co system as a possible ZnO based DMS (comparing *p*- and *n*-type ZnO) by using different approaches. The prime focus is to correlate their structure with the transport properties, and to contribute to identify the origin of observed ferromagnetism in ZnO based DMS materials.

Thesis structure:

Chapter 1 introduces the subject and describes the objectives.

In *Chapter 2*, the experimental techniques for deposition and characterization that have been used in this PhD work are presented. Additional processes necessary for the preparation of films for measurements are also described.

The *different objectives* of this work have been tackled according with the following description:

Chapter 3 is dedicated to the optimization of the epitaxial growth of ZnO films *p* and *n*-type. The structural, morphological, electrical and

magnetic characterizations are carried out in polycrystalline and epitaxial ZnO films grown by PLD.

Chapter 4 is centered on understanding the *p*-type behavior in intentionally un-doped ZnO thin films. This chapter tries to understand the origin of *p*-type behavior. The effects of twining and of the intrinsic defects produced by ion irradiation on the electrical properties of ZnO films are studied. In addition, a photoluminescence (PL) study of the possible defects responsible for *p*-type behavior is carried out. And finally, a study of the aging mechanism of *p*-type ZnO is performed.

Chapter 5 is devoted to the Zn-O-Co system as a diluted magnetic semiconductor. The study is made by 3 different approaches. In the first approach the co-growth from ZnO/Co_3O_4 targets is taken into consideration. In the second approach, the multilayers ZnO/Co_3O_4 are investigated. In this section, first a study of the Co_3O_4 thin films is made, including the optimization of the growth condition from polycrystalline to epitaxial Co_3O_4 thin films. Furthermore, the structural characterization, electrical, optical and magnetic properties of the multilayers are studied. In the third approach *p*- and *n*-type ZnO thin films are implanted with Co, and their structure and, electrical, optical and magnetic properties are investigated.

References

[1] S.A. Wolf, D.D. Awschalom, R.A. Buhrman, J.M. Daughton, S. von Molnár, M.L. Roukes, A.Y. Chtchelkanova, D.M. Treger, Science 294 (2001) 1488

[2] S.D. Sarma, American Scientist 89 (2001) 516

[3]http://www.sigmaaldrich.com/materials-science/alternative-energy - materials/magnetic-materials/tutorial/spintronics.html

[4] http://www.everspin.com/technology.html

[5]http://www.crocus-technology.com/pdf/BH%20GSA%20 Article.pdf

[6]http://www.eetimes.com/news/latest/showArticle.jhtml?articleID=218000269

[7]http://urtechfriend-paperpresentations5.blogspot.com.es/p/ spintronics.html

[8] B.T. Jonker, S.C. Erwin, A. Petrou, A.G. Petukhov, MRS Bulletin 28 (2003) 740

[9] H. Ohno, Science 281, 5379 (1998) 951

[10] S.J. Pearton, W.H. Hep, M. Ivill, D.P. Norton, T. Steiner, Semicond. Sci. Technol. R59-R74 (2004) 19

[11] S.J. Pearton, C.R. Abernathy, D.P. Norton, A.F. Hebard, Y.D. Park, L.A. Boatner, J.D. Budai, Mat. Sci. and Eng. R 40 (2003) 137

[12] J.M.D. Coey, S. Sanvito, J. Phys. D: Appl. Phys. 37 (2004) 988

[13] T. Dietl, H. Ohno, F. Matsukura, J. Cibert, D. Ferrand, Science 287 (2000) 1019

[14] S.W. Jung, S.J. An, G.C. Yi, C.U. Jung, S.I. Lee, S. Cho, Appl. Phys. Lett. 80 (2002) 4561

[15] A.B. Mahmoud, H.J. von Bardeleben, J.L. Cantin, A. Mauger, E. Chikoidze, Y. Dumont, Phys. Rev. B 74 (2006) 115203

[16] Z. Yang, W.P. Beyermann, M.B. Katz, O.K. Ezekoye, Z. Zuo, Y. Pu, J. Shi, X.Q. Pan, J.L. Liu, J. Appl. Phys. 105 (2009) 053708

[17] D.C. Look, B. Claflin , Phys. Status Solidi B, 241 no.3 (2004) 624-30

[18] D.C. Look, Semicond. Sci. Tech. 20 no.4 (2005) S55-61

[19] P. Sharma, A. Gupta, K.V. Rao, F.J. Ownes, R. Sharma, R. Ahuja, J.M.O. Guillen, B. Johansson, A.G. Gehring, Nature Mater. 2 (2003) 673

[20] N.A. Theodoropoulou, A.F. Hebard, D.P. Norton, J.D. Budai, L.A. Boatner, J.S. Lee, Z.G. Khim, Y.D. Park, M.E. Overberg, S.J. Pearton, R.G. Wilson, Solid State Electronics 47 (2003) 2231

[21] K. Rode, A. Anane, R. Mattana, J.P. Contour, O. Durand, R. LeBourgeois, J. Appl. Phys. 93 (2003) 7676

[22] J.Y. Kim, J.H. Park, B.G. Park, H.J. Noh, S.J. Oh, J.S. Yang, D.H. Kim, S.D. Bu, T.W. Noh, H.J. Lin, H.H. Hsieh, C.T. Chen, Phys. Rev. Lett. 90 (2003) 017401

[23] S.R. Shinde, S.B. Ogale, S. Das Sarma, J.R. Simpson, H.D. Drew, S.E. Lofland, C Lanci, J.P. Buban, N.D. Browning, V.N. Kulkarni, J. Higgins, R.P. Sharma, R.L. Greene, T. Venkatesan, Phys. Rev. B 67 (2003) 115211

[24] S. Sonoda, S. Shimizu, T. Sasaki, Y. Yamamoto, and H. Hori, J. Cryst. Growth 237-239 (2002) 1358

[25] N. Theodoropoulou, A.F. Hebard, M.E. Overberg, C.R. Abernathy, S.J. Pearton, S.N.G. Chu, R.G. Wilson, Phys. Rev. Lett. 89 (2002) 107203

[26] J.M.D. Coey, Curr. Opin. Solid. State Mater. Sci. 10 (2006) 83

[27] P. Sharma, A. Gupta, K.V. Rao, F.J. Owens, R. Sharma, R. Ahuja, J.M. Osorio Guillen, B. Johansson, G.A. Gehring, Nature Mater. 2 (2003) 673

[28] C.B. Fitzgerald, M. Venkatesan, J.G. Lunney, L.S. Dorneles, J.M.D. Coey, Appl. Surf. Sci. 247 (2005) 493

[29] M. Venkatesan, C.B. Fitzgerald, J.M.D. Coey, Nature 430 (2004) 630

[30] K.R. Kittilstved, D.R. Gamelin, J. Am. Chem. Soc. 127 (2005) 5292

[31] J.M.D. Coey, M. Venkatesan, C.B. Fitzgerald, Nature Mater. 4 (2006) 173

[32] D. Kundaliya, S.B. Ogale, S.E. Lofland, S. Dhar, C.J. Metting, S.R. Shinde, Z. Ma, B. Varughese, K.V. Ramanujachari, L. Salamanca-Riba, T. Venkatesan, Nature Mater. 3 (2004) 709

[33] J.L. Costa-Kramer, F. Briones, J.F. Fernandez, A.C. Caballero, M. Villegas, M. Diaz, M.A. Garcia, A. Hernando, Nanotechnology Vol.16,2 (2005) 214

[34] M.A. García, M.L. Ruiz-Gonzalez, A. Quesada, J.L. Costa-Krämer, J.F. Fernández, S.J. Khatib, A. Wennberg, A.C. Caballero, M.S. Martin-Gonzalez, M. Villegas, F. Briones, J.M. Gonzalez-Calbet, A. Hernando, Phys. Rev. Lett. 94 (2005) 217206

[35] E. López-Ponce, A. Wennberg, M.S. Martín-González, J.L. Costa-Krämer, M.A. García, A. Quesada, A. Hernando, A.C. Caballero, M. Villegas, J.F. Fernández, Jap. J. Appl. Phys, 45, 10A (2006) 7667

[37] S.R. Shinde, S.B. Ogale, J.S. Higgins, H. Zheng, A.J. Millis, V.N. Kulkarni, R. Ramesh, R.L. Greene, T. Venkatesan, Phys. Rev. Lett. 92 (2004) 166601

[38] J.H. Park, G. Kim, H.M. Jang, S. Ryu, Y.M. Kim, Appl. Phys. Lett. 84 (2004) 1338

[38] E.C. Lee, K.J. Chang, Phys. Rev. B 69 (2004) 085205

[39] J. Hyun Kim, H. Kim, D. Kim, Y. Ihm, W.K. Choo, J. Eur. Ceram. Soc. 24 (2004) 1847

[40] C.B. Fitzgerald, M. Venkatesan, J.G. Lunney, L.S. Dorneles, J.M.D. Coey, Appl. Surf. Sci. 247 (2005) 493

[41] K. Ueda, H. Tabata, T. Hawai, Appl. Phys. Lett. 79 (2001) 988

[42] S. Deka, P.A. Joy, Solid State Commun. 134 (2005) 665

[43] G. Lawes, A.S. Risbud, A.P. Ramírez, R. Seshadri, Phys. Rev. B 71 (2005) 045201

[44] M. Bouloudenine, N. Viart, S. Colis, A. Dinia, Chem. Phys. Lett. 73 (2004) 397

[45] S.J. Han, B.Y. Lee, J.S. Ku, Y.B. Kim, Y.H. Jeong, J. Magn. Magn. Mater. 272–276 (2004) 2008

[46] E.C. Lee, K.J. Chang, Phys. Rev. B 69 (2004) 085205

[47] A.S. Risbud, N.A. Spaldin, Z.Q. Chen, S. Stemmer, R. Seshadri, Phys. Rev. B 68 (2003) 205202

[48] A. Quesada, M.A. García, M. Andrés, A. Hernando, J.F. Fernández, A.C. Caballero, M.S. Martín-González, F. Briones, J. App. Phys. 100 (2006) 113909

[49] M.S. Martín-González, J.F. Fernández, F. Rubio-Marcos, I. Lorite, J.L. Costa-Krämer, A. Quesada, M.A. Bañares, J.L.G. Fierro, J. App. Phys. 103 (2008) 083905

[50] M.S. Martin-González, M.A. García, I. Lorite, J.L. Costa-Krämer, F. Rubio-Marcos, N. Carmona, J.F. Fernández , J. Electroch. Soc. 157 (2010) E31

2

EXPERIMENTAL TECHNIQUES

Chapter 2

Experimental techniques

This chapter describes the tools, techniques, and procedures used to conduct the research presented in this thesis. The first sections describe the systems used to deposit thin films, and the procedures used to prepare the targets and the substrates. The following sections cover the techniques used for the characterization of the deposited thin films. Typical properties of interest include film stoichiometry, crystal structure, texture, surface morphology, and "grain size". The methods used to characterize the structural and compositional properties of the thin films include profilometry, X-ray diffraction (XRD), Rutherford Backscattering Spectrometry (RBS), Proton Induced X-ray Emission (PIXE), and Atomic Force Microscopy (AFM). Photoluminescence measurements are performed in order to study the optical properties of the films. For the electrical properties of the films four point probe Hall measurements are used to determine the carrier concentration (n), Hall mobility (μ), and resistivity (ρ). Magnetic characterization of the films is carried out using a Superconducting Quantum Interference Device (SQUID).

2.1. Thin film growth

2.1.1. Pulsed Laser Deposition (PLD)

The thin films investigated in this work are grown by PLD. One of the most important advantages of PLD technique is the possibility to modify the film composition by adjusting the target and the gas pressure in the chamber.

Another important advantage of the PLD is that it requires small targets and that the stoichiometry of the grown films is the same as the target´s. Upon the pulsed laser irradiation, due to the high heating rate, all the elements of the target will be evaporated regardless of their evaporating point. This feature allows one to grow stoichiometric thin films by ablating multi-component targets and to obtain epitaxial growth at low temperature [1].

Another advantage is the ability of the PLD technique to deposit multi-layer films by successive ablation of different targets.

Besides all these advantages, the PLD technique also presents a few issues. The main issue is the deposition of particulates on the films. These micrometers particulates could influence the growth of the succeeding layers. Another issue encountered when growing films by PLD is the narrow angular distribution of the plume, thus not being suitable to produce large area uniform thin films, and therefore limiting its applications.

Historical development of PLD

In 1916 Albert Einstein posited the process of stimulated emission of radiation. However, it was not until 44 years later that it was used in a device, when Theodore H. Maiman constructed at Hughes Research Laboratories the first optical maser, using ruby as the lasing medium. A few years later, ruby laser was used by Breech and Cross to vaporize atoms from a solid surface [2], and later on Smith and Turner were able to deposit thin films using ruby laser [3]. This was the beginning of the advancement of the pulsed laser deposition technique.

At that time Molecular Beam Epitaxy (MBE) was more suitable for fabrication of thin films with good quality. PLD became a good alternative only after the improvement of laser technology [4,5]. For the first lasers the stability output and repetition rate of the laser were too lowly in order to be able to deposit thin films. Once lasers with higher repetition rate were available (Q-switches lasers, UV excimer laser) the target material could be efficiently ablated, and the PLD was effective for depositing thin films.

It became a famous technique for deposition of thin films in 1987, after it has been employed to grow high-temperature Tc superconducting films. Recently PLD has been also used to fabricate epitaxial thin films and multilayers, nanotubes [6], nanopowders [7], and quantum dots [8]. Also issues related to reproducibility [9] and the ability to produce large-area samples [10] are investigated, due to the fact that it might be very helpful in material processing [11].

Mechanisms of PLD

Although the PLD set-up is very simple, its principle is a complex phenomenon, where several processes can be distinguished. Firstly an interaction takes place between the pulsed laser radiation and the solid target. As a consequence a plasma plume with high energetic species is formed. Then the ablated materials are transferred on the substrate via the plasma plume, where finally the species nucleates and grow to form the film.

Fig.2.1 illustrates the top-view of the deposition chamber of a PLD system. The laser beam enters through a quartz window into the chamber, and is focused by a lens onto the target. Due to the short pulse duration and high energy densities, the target´s surface is heated immediately. As a consequence all its elements are removed from the target´s surface. The ablation rate depends on the fluency of the laser.

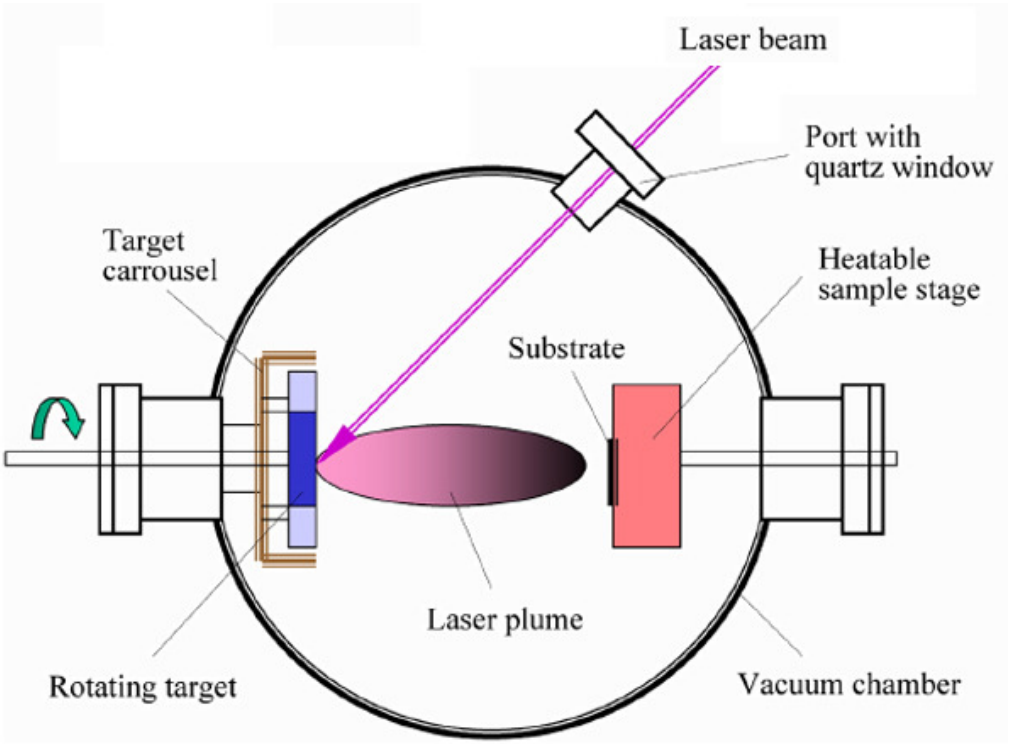

Fig.2.1. Schematic of the PLD system (With kind permission from Ref. [12])

The ablated materials (concentrated in form of a collimated beam) will move facing the substrate maintaining the stoichiometry of the target [13]. Fig.2.2 shows a live image of the plume during the deposition at Instituto Microelectronica Madrid (IMM). The bluish is the ZnO plume, and the reddish is the resistance which is heating the substrate.

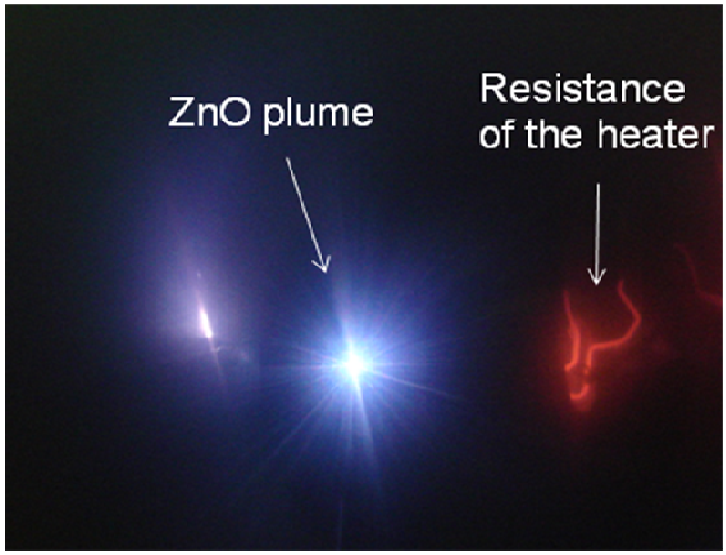

Fig.2.2. Live image of the plume during the PLD deposition experiment at the IMM

The high-energy materials ejected from the target will collide onto the substrate surface, and may cause some damage to the substrate. This step has a big impact on the quality of the thin film. Fig.2.3 draws a schematic of the interaction mechanism. The incident energetic materials sputter atoms from the surface, and therefore between this sputtered flux and the incident plasma flux a collision region is formed. This region is where the condensation of particles takes place. When the condensation rate is higher than the rate of particles coming from the sputtered flux, thermal equilibrium conditions are established and the film starts to grow on the substrate surface.

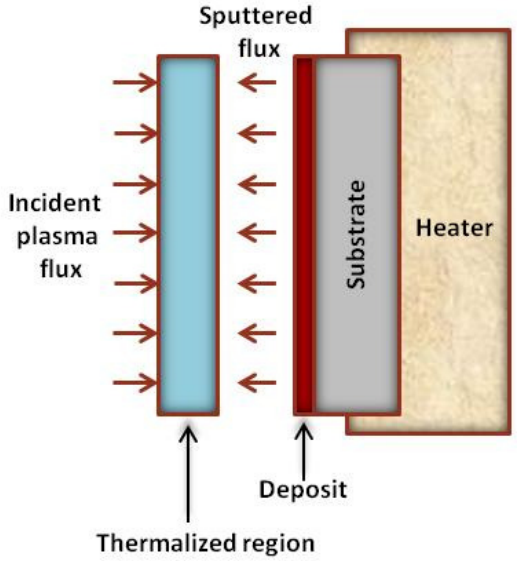

Fig.2.3. Schematic diagram of plasma-substrate interaction (Adapted from Ref.[14])

There are three different growth modes. The first one is the Volmer-Weber growth, where isolated islands are first formed on the surface. The second one is a layer-by-layer growth (also known as Frank - van der Merwe), where one monolayer is deposited at the time and this way very smooth epitaxial film is obtained. The third one is a mixed growth, where first a monolayer is formed, and only after that islands are grown.

The nucleation and growth of the films depends on various factors: substrate type, energy, density, degree of ionization, but the main parameters are the substrate temperature T and the supersaturation D_m. given by the equation

$$D_m = kT\ ln(R/R_e)$$

where k is the Boltzmann constant, R is the actual deposition rate, and Re is the equilibrium value at the temperature T. At high temperature crystals free of defects grow, while at low temperature the obtained structures are disordered or even amorphous.

However, PLD requires a relatively lower substrate temperature for crystalline film growth compared to other techniques. This can be explained by the fact that the deposition rate can be very high (~10 µm/s), because of the short laser pulsed duration and small temporal spread (~10 ns and <10 µs respectively). As the high-energetic ablated materials are rapidly deposited, the substrate surface temperature will increase, and therefore a layer by layer nucleation takes place resulting in a smooth thin film.

The number of macro-particles depends on the laser beam energy density and wavelength. A short wavelength laser (UV) will interact with the solid target and with the evaporated plasma, thus resulting on finer and hotter plasma. Hanabusa proposed the use of a mask near the substrate in order to reduce the spreading of the ablated materials [15]. In order to reduce the number of droplets, a second UV laser was used [16]. Another attempt was to use a mechanical velocity filter in the PLD. This filter will stop the macro-particles which are moving slowly, and will allow only the atomic and molecular particles which move faster [17]. Nevertheless, this setup was not practical due to the complexity of the installation of this filter and the contamination coming from the lubricating oil. Another approaches were the "off-axis" PLD [18,19] and the crossing fluxes laser deposition method [20], where a special geometrical arrangement avoids the particulate deposition.

The PLD set-up at IMM

In this thesis the deposition of the thin films was carried out in a lab-made PLD deposition chamber. The initial design of this system belongs to Prof. Fernando Briones. An ArF Excimer laser from Lambda Physics Lasertechnik, model LPX 205i MC, with the gas

mixture Fluoride, Helium, Argon and Neon was used. The laser was operating at 193 nm in order to ablate the target. Its energy was set at 200mJ per pulse, and pulse duration of 17 ns. The laser was operated at 22 kV and a repetition rate of 10 Hz. The laser beam entered into the vacuum chamber through a fuse silica window. It was focused into a spot size of 1mm diameter on the rotating target by a 200mm focal length convex lens. The distance between the target and the substrate was of 2.5cm, which is very close when compared with other PLD systems.

Chamber

The vacuum chamber used for the PLD, Fig.2.4, is completely lab-made and it was improved several times during this PhD work due to different shortcomings. The deposition chamber was first evacuated by a pump-system (turbo and rotary pumps) to a base pressure of $1x10^{-5}$ mbar, and then high purity oxygen was introduced through a mass flow controller and maintained at the desired pressure (~10^{-2}-10^{-1} mbar) during deposition.

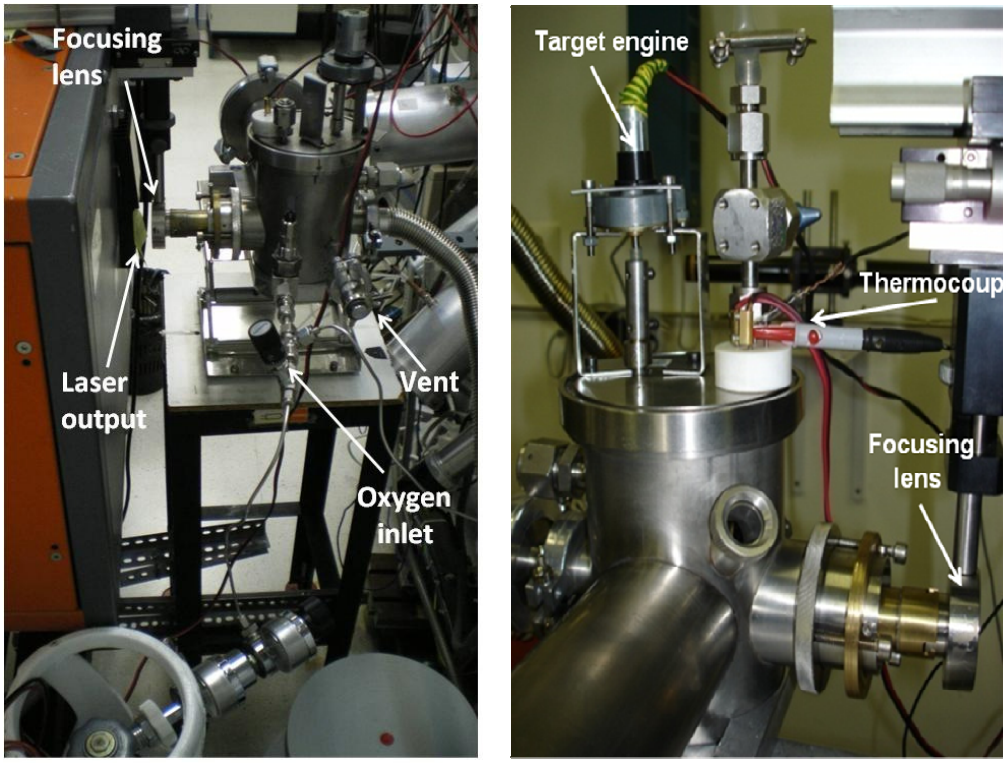

Fig.2.4. Images of the PLD chamber at IMM where the different elements engine, vent, lens, etc. can be observed.

It has an axis for the target attached to a DC engine with variable velocity, Fig.2.5. The target was then rotated at a proper speed in order to maintain an uniform ablation. The sample holder is at the same time a heater. Its temperature was maintained constant during the deposition adjusting the current intensity applied. The temperature was measured by a calibrated thermocouple (see Fig.2.5). The post growth immediate cooling down to room temperature of the thin films was performed maintaining the same oxygen pressure. A peculiarity of this system is the short working distance (between the laser output, focusing lens, target, and target-substrate).

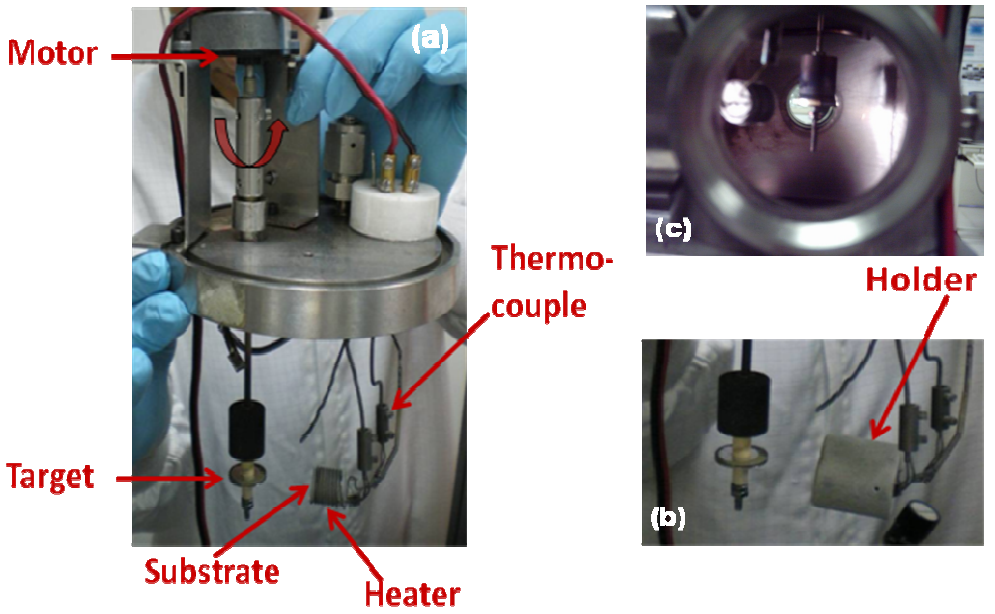

Fig.2.5. Images of the PLD chamber: (a-b) internal components (c) the laser entry to the target

The chamber was then attached to a level regulator, in order to be able to vary the height of the targets, Fig.2.6.

Fig.2.6. Level regulator attached to the chamber

While adjusting the plume unwanted deposition occurred on the chamber window for laser entry. This deposition will lower the intensity of the plume dramatically. In order to fix this issue, a cover cone was made and attached to the window. To further minimise this, the window was polished/cleaned before every deposition.

Targets Fabrication

Before starting the deposition of the films the targets had to be chosen. For that purpose, pellets have been prepared by conventional ceramic routes using high purity raw powders, in the laboratory of Prof. José Francisco Fernandez Lozano from the "Instituto de Cerámica y Vidrio de Madrid" ICV-CSIC. In order to eliminate any possible contamination, during the preparation of the targets, no metallic tools, containers or sieves were used [21]. For each study, different pellets have been prepared using the corresponding powders.

The fabrication procedure was as follows: high purity (>99.99% Aldrich) raw powders were first milled in water medium, after which were dried, sifted, and then treated at 400°C for 8 hours. Afterwards, the calcined powders were milled again and then dried, and the resulting sieved powders were pressed into pellets at 1000Kg/cm^2. Circular disks of 20mm in diameter and 2mm thick were obtained after this step, as shown in Fig.2.7 (a). The disks were then sintered (thermally treated) in different conditions. The error in the determination of the samples composition is ±0.5 of the total content.

After this procedure, pellets of different densities were obtained. The densities were calculated by the immersion Archimedes method using mercury as a liquid. The obtained ceramic pellets were then employed as targets for PLD.

For the deposition of ZnO thin films ZnO targets were used. During the deposition the target carousel is rotating continuously to avoid pitting. For the deposition of Co_3O_4 thin film a target system like the one shown in Fig.2.7 (b) was used. The yellowish one is the ZnO pellet, and the black one is the Co_3O_4 pellet. Firstly, for the deposition of a ZnO buffer layer the laser beam was focused onto the ZnO target. Then the height of the carousel target was adjusted so the laser beam was focused onto the Co_3O_4 target, and the Co_3O_4 thin film was grown. For the deposition of ZnO/Co_3O_4 multilayers, the first attempt was to use the same targets system as for Co_3O_4 thin films (Fig.2.7 (b)). But in this case, this setup was not very practical, because after the deposition of each layer, the height of the target carousel has to be modified continuously during the deposition, in order to switch to the other target, and therefore to deposit the next layer. In Fig.2.7 (c) an improvement on the setup of the targets on the target carousel is shown. This is termed the "portion-cake" target configuration. This time there is only one disk target rotating, which is formed by two halves of disks: 1 half of ZnO and the other half of Co_3O_4. This way there is no need to change the height of the target carousel: as the carousel is rotating different layers of ZnO and of Co_3O_4 are deposited, and so the multilayers are obtained. These novelty targets set-ups have been developed at IMM.

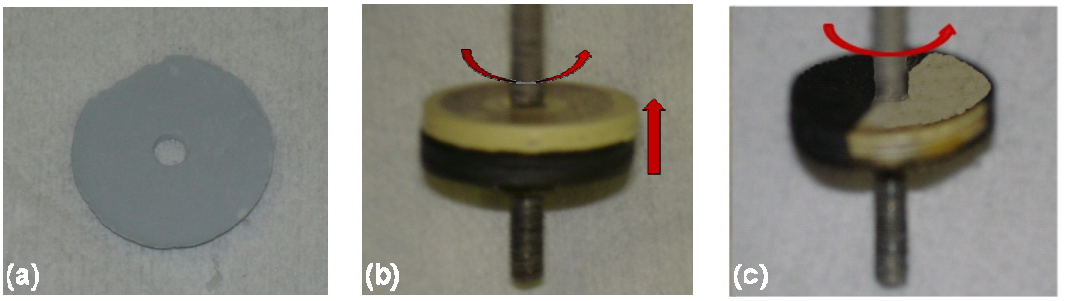

Fig.2.7. Different targets set-up. a) ZnO target, b) ZnO and Co_3O_4 targets for bilayer deposition, and c) rotating half ZnO and half Co_3O_4 target for multilayer deposition.

Substrates

Three different substrates were used, Pyrex, Silicon, and sapphire.

Pyrex: Was used because it has a similar thermal expansion coefficient as the film itself, so the risk of a cracked surface is minimised.

Silicon: It is an inexpensive substrate with a well known technology to do characterisations and measurements with. It also has matching parameters for the thermal expansion and is very easy to handle.

Sapphire: Due to the relatively low lattice mismatch is suitable for epitaxial growth of ZnO.

The substrates were cut into pieces with the dimension 8x8 mm. Prior to film growth, the sapphire substrates were cleaned by the standard chemical cleaning: First they were immersed in acetone for 10 minutes in ultrasound, in order to remove dust and surface contamination. The next step was sonication in isopropyl alcohol. Finally they were blown dried with high purity nitrogen gas. Again, during the cleaning/manipulation of the substrates no metal tweezers or tools were used, as a precaution to eliminate any possible contamination.

The substrate was then put into the holder/oven and fixed with a cover of boron nitride, to be sure that an even temperature was kept at the substrate surface. The chamber was then closed and pumped to a base vacuum pressure of ~10^{-5} mbar. When desirable base vacuum pressure and temperature was reached, high purity oxygen was introduced into the chamber. The chamber position with respect to the laser was then adjusted properly, to get the optimum angle of the plume. The setup was then ready for deposition.

2.1.2. Irradiation

In order to investigate the radiation hardness of ZnO semiconductor and the basic mechanism of radiation effects in semiconductor, ZnO thin films were irradiated with protons. These measurements were made in collaboration with Dra. Raquel Gonzalez Arrabal and Dr. Frans Munnik at the Facilities of the Forschungszentrum Dresden-Rossendorf, Germany. Fig.2.8 shows a scale model of the installations they have at this laboratory.

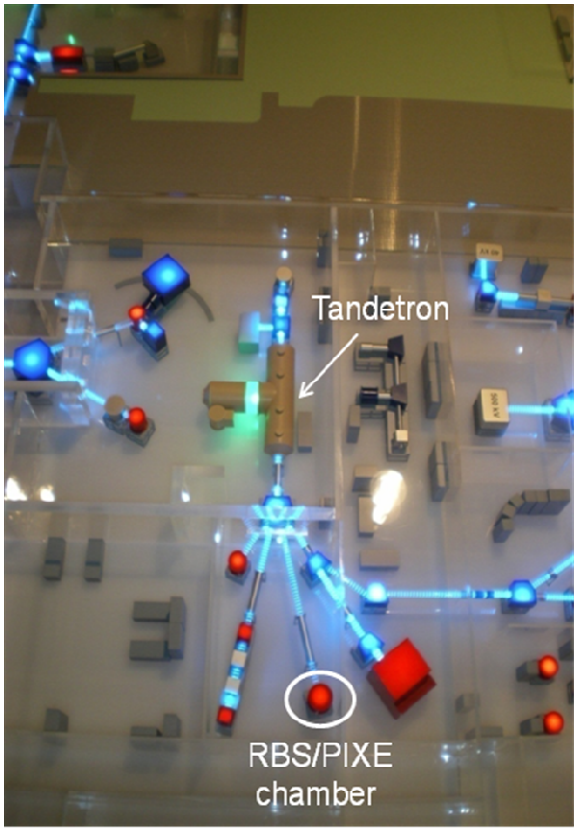

Fig.2.8. Scale model of the installations at the Forschungszentrum Dresden-Rossendor laboratory in Germany. Blue lines correspond to the different work lines coming from the tandetron, and the red points are the different work stations. The RBS/PIXE station where this work was done is highlight with a white circle.

For our films the line of H^+ beam at energy of 2 MeV was chosen (shown in Fig.2.9). The samples were loaded in a high vacuum chamber (pressure $< 10^{-6}$mbar). Fig.2.10 shows the vacuum chamber seen from different angles. The irradiation was performed at room temperature and out of channeling incidence. The irradiation fluencies were selected to be $1x10^{15}$, $1x10^{16}$ and $1x10^{17}$ ion/cm^2. The uncertainty in the fluency was less than ~10% in all cases and the beam current was maintained low in order to avoid excessive heating of the samples.

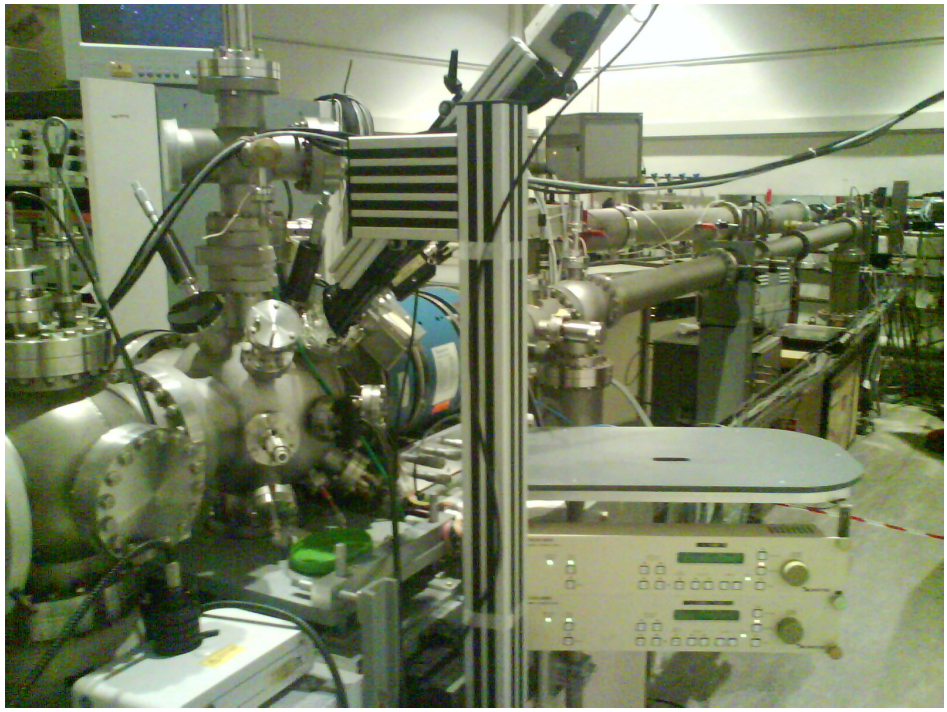

Fig.2.9. Line of H^+ beam at energy of 2 MeV at the Forschungszentrum Dresden-Rossendor laboratory

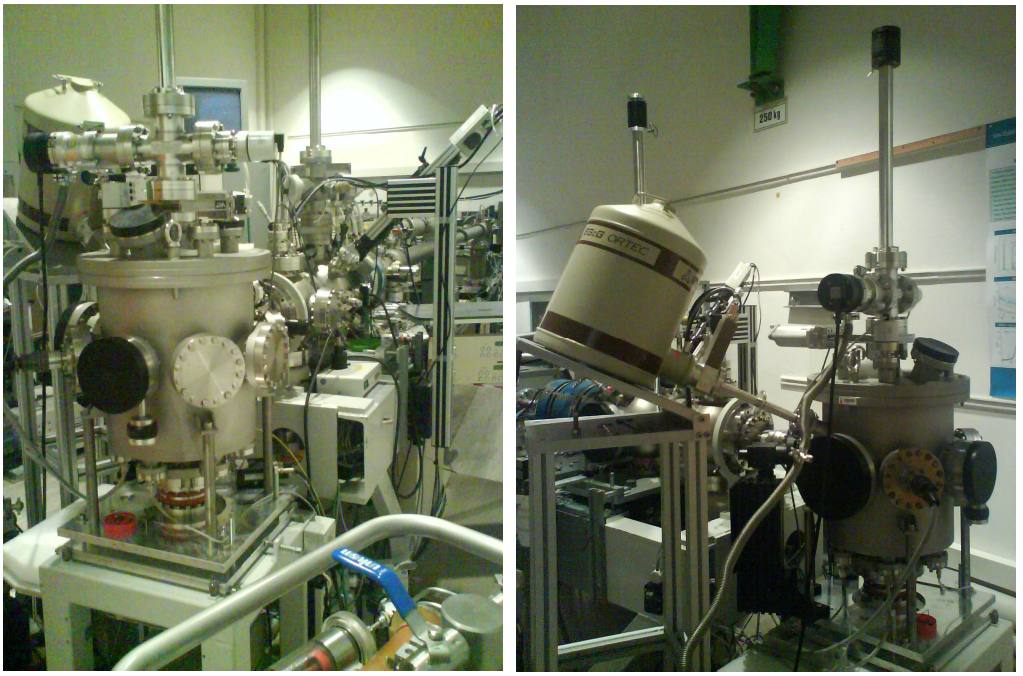

Fig.2.10. Vacuum chamber of the 2 MeV H^+ line seen from different angles

SRIM is a program which simulate the ion-atom collisions (where a moving atom is considered to be the "ion", and the target atoms to be "atoms"), and is used to calculate the Stopping and Range of Ions into Matter by means of statistical algorithms. According to SRIM calculations [22] at 2 MeV beam energy the electronic stopping power (S_e= $3.8\text{x}10^{-1}$ev/nm) is three orders of magnitude higher than the nuclear stopping power (S_n=$1.6\text{x}10^{-4}$ eV/nm). Thus, irradiation took place in an energy range clearly dominated by electronic processes.

2.1.3. Ion implantation

One of the most important features of semiconductors, which make them useful for electronic devices, is the possibility to change their conductivity by introducing a few percentages of dopant atoms in their host matrix.

After the semiconductor has been obtained, ion implantation can be performed. This way first a thin film of desired semiconductor is grown under optimal conditions (avoiding complications of doping during growth), and only after that, atoms of the desired dopant are introduced. This is very helpful when doping with transition metals, due to their predisposition to form clusters limiting thus the growth temperature.

When the dopant ions enter into the substrate material, their energy decreases due to the collision with the host atoms and change their direction (as drown in Fig.2.11). The total distance that the ion travels is called range (R) and its projection on the direction parallel to that of the incident ion beam is the projected range (R_p).

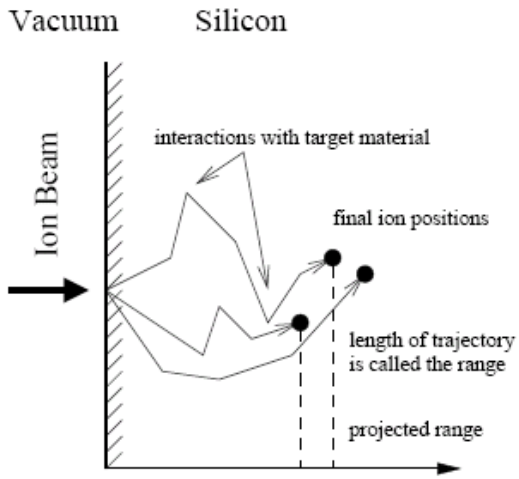

Fig.2.11. Range R and projected Range Rp (Extracted from Ref. [23])

Depending on their initial energy they will stop at some depth. Therefore, in order to place the dopant ions in a Gaussian shape into the thin ZnO layer, it is very important to know which initial energy is necessary. For that purpose simulations for implanting Co ions in ZnO layer are performed with the TRIM code and their energies are calculated [22]. The implant profile is defined by two important parameters: dose Φ (in $atoms/cm^2$) and energy E (in keV). The dose is given by the following formula:

$$\Phi = It/q_i A$$

I is the beam current, t implantation time, A beam area, and q_i is the charge per ion. Usually the beam current ranges from $1\mu A$ *to* $30mA$, the implantation dose from 10^{11} *to* $10^{16} atoms/cm^2$, and the energy from keV area to MeV range.

As the implanted ions penetrate into the substrate material, they will experience collisions with the nuclei and electron clouds of the semiconductor atoms. The electronic collisions do not damage the semiconductor crystal lattice, but the nuclear collisions do cause damage. However, this damage can be usually repaired by annealing. The loss of energy of the dopant ions inside the target is called stopping power. The *total stopping power* S is defined as the energy loss per unit path length of the ion:

$$S = (dE/dx)_{nuclear} + (dE/dx)_{electronic}$$

From Fig.2.12 it can be seen that nuclear stopping reigns at low ion velocities, while at higher velocities the electron loss dominates.

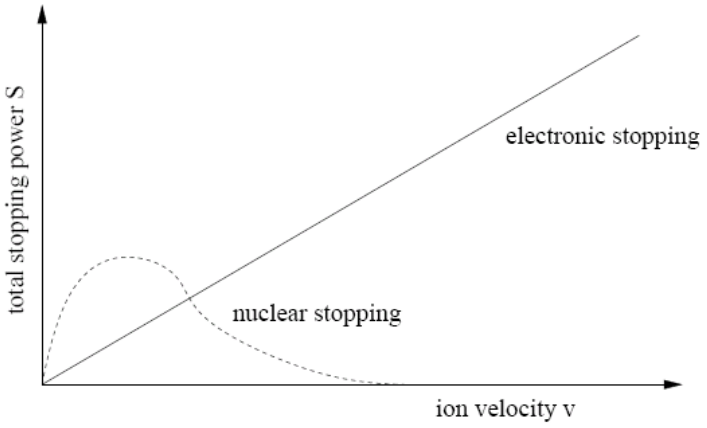

Fig.2.12. Ion stopping in the target material (Extracted from Ref. [23])

Some of the ZnO thin films have been implanted with Co ions. The implantation was performed at the laboratory "Centro de Asistencia a la Investigación (CAI) de Técnicas Físicas from Universidad Complutense de Madrid ", in collaboration with Dra. Raquel Gonzalez Arrabal and Dr. Pablo Fernández Sáez.

Fig.2.13 and Fig.2.14 show an ion implantation apparatus, exterior and interior respectively. The ZnO films were implanted with Co ions at fluences of $1x10^{16}$ions/cm^2 and at different energies depending on their thickness: energies of 120 KeV for the 130nm ZnO film and 140 KeV for the 150nm ZnO film. The projected ranges of the implanted Co ions are calculated to be 64 nm for the film implanted at 120 KeV and 70 nm for the one implanted at 140 KeV. All the implantations were carried out at room temperature and non-channeling incidence.

Fig.2.13. Ion implanting apparatus at the laboratory CAI de Técnicas Físicas from the Universidad Complutense de Madrid (exterior) (With kind permission from Ref. [24])

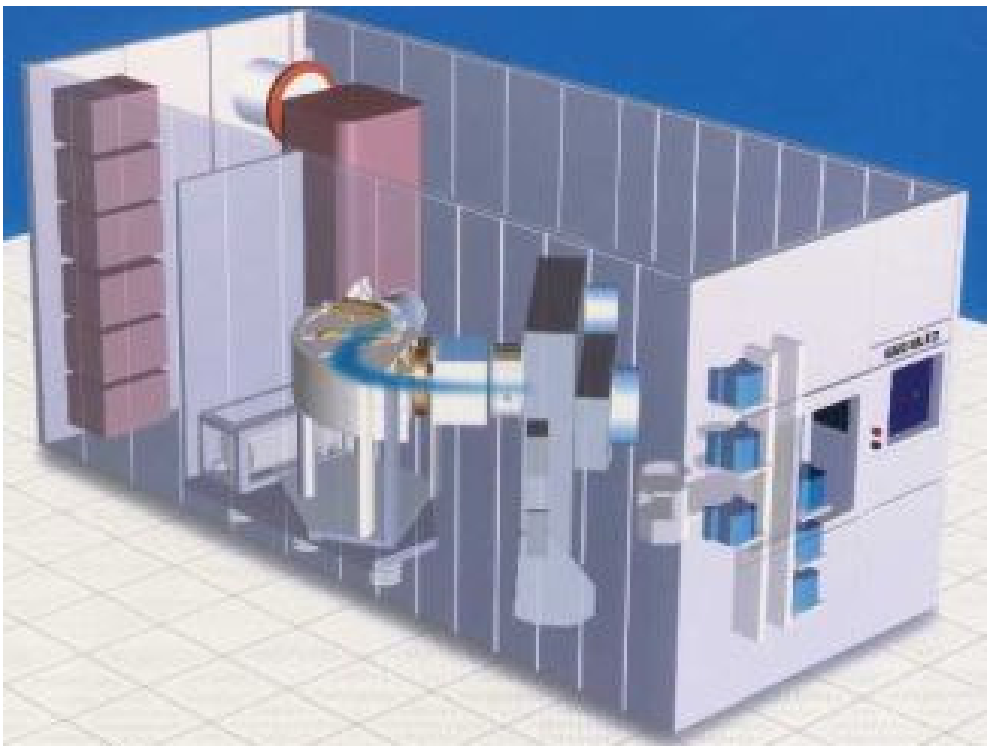

Fig.2.14. Inside view of ion implanting apparatus (Extracted from Ref. [25])

Rapid Thermal Annealing (RTA)

After the implantation some of the implanted ZnO films were rapidly annealed at the facilities of the same laboratory "CAI de Técnicas Físicas from the Universidad Complutense de Madrid". For that purpose a commercial RTA system model MPT-600 (shown in Fig.2.15) was used. The annealing was performed in Ar atmosphere for 30 seconds at temperatures of 400 and 750°C respectively. During annealing, the sample surface was covered with a ZnO/Al_2O_3 layer in order to prevent any possible evaporation or contamination.

Fig.2.15. Commercial RTA system (model MPT-600) used for heat treatments of the films at the laboratory CAI de Técnicas Físicas from the Universidad Complutense de Madrid (With kind permission from Ref. [24])

RTA is a procedure in which a wafer is heated up to high temperatures in a very short time (several seconds or less). Nevertheless, the cooling down of the wafer has to be made slowly in order to avoid a thermal shock and consequently its breakage. RTA is usually performed using high intensity lamp, hot chuck, or hot plate. This procedure has many applications, but it is used mainly to repair the damage caused by ion implantation.

2.2. Thin film characterization

2.2.1. Profilometer

In order to estimate the thickness of the films, their surface profile was measured using a profilometer. The first profilometer was a

phonograph-like device, where the measurement is performed as the surface is moved with regard to the contact tip of the profilometer. However, nowadays non-contact profilometers have been developed.

Contact profilometers

The diamond tip in contact with the sample is moved laterally along the sample with a certain contact force. As the tip encounters surface variations, it will move vertically. Usually a profilometer is able to measure vertical variations ranging from 10nm to 1mm.

Advantages of contact profilometers:

- ✓ It measures the surface itself, unlike the non-contact techniques where the measurements might be altered by surface contaminants.
- ✓ There is no modeling required.

Non-contact profilometers

The non-contact profilometer, also called optical profilometer, uses different techniques such as: laser triangulation, confocal microscopy and digital holography.

Advantages of optical profilometers:

- ✓ The measurements requires less time.
- ✓ The sample surface cannot be damaged.

To measure the thickness of our deposited thin films, both types of profilometers were used: a Sentech FTP advanced profilometer for transparent films (Fig.2.16), and a Dektak 150 profilometer for opaque films (Fig.2.17).

Fig.2.16. Sentech FTP advanced non-contact profilometer at IMM

Fig.2.17. Dektak 150 contact profilometer at IMM

2.2.2. X-Ray Diffraction (XRD)

XRD belongs to the non-destructive techniques, and provide information about structural properties. The XRD technique is generally used for characterization of crystalline materials including: unit cell lattice parameters, orientation, lattice mismatch between film and substrate. The main advantages of this technique are: is very

effective and fast finding the crystal structure of an unknown material; the sample preparation is minimal; and the data interpretation is relatively well-known.

A typical X-ray diffractometer setup is illustrated in Fig.2.18. The X-rays are produced in the X-ray tube. The sample holder is a 4 axis stage. The X-rays diffracted by the sample are detected by an electronic detector, which can rotate from 0 to 90°. The motion of the X-ray tube and the detector is controlled by a goniometer. The goniometer monitors the θ angle, and the detector registers the X-rays coming out from the sample (in units of counts/sec). All these information are sent to a computer.

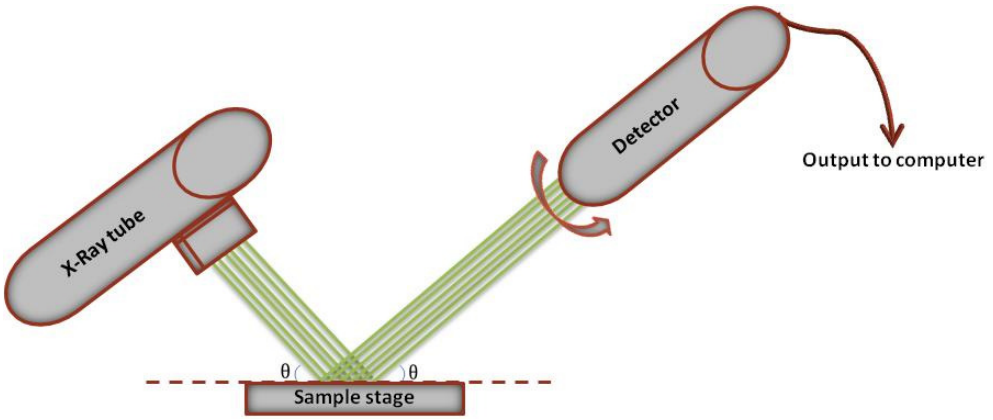

Fig.2.18. Experimental set-up of X-ray diffractometers. Main components: X-ray tube, sample holder, and X-ray detector (Adapted from Ref. [26])

This information is processed, and the X-ray intensity is plotted against the angle θ (sometimes reported as 2θ) obtaining thus an X-ray diffraction pattern.

Fig.2.19 shows an example of this kind of chart. The diffraction peaks can be correlated with atomic planes indicated by the Miller Index (*hkl*). For this purpose JCPDS Powder Diffraction Files are

used. JCPDS stands for Joint Committee on Powder Diffraction Standards, a group which has gathered these kinds of data for a very large number of crystalline substances.

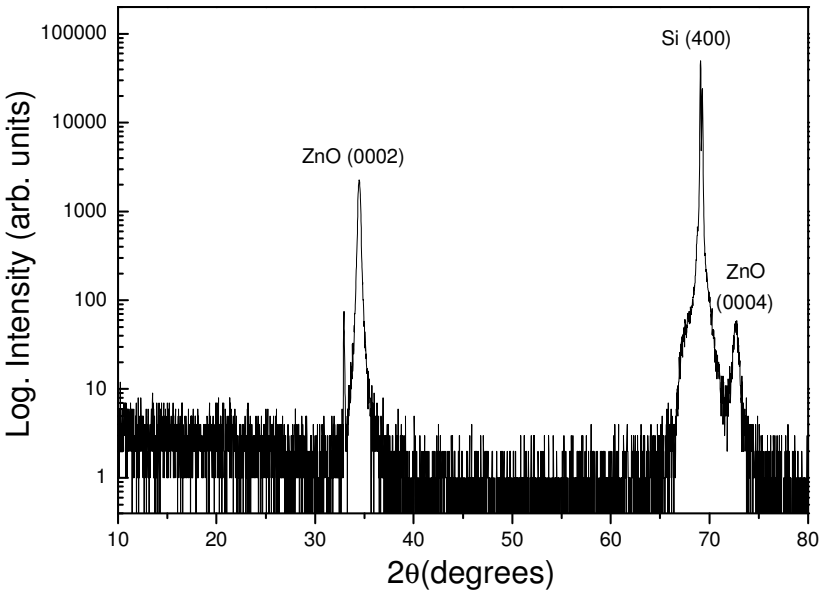

Fig.2.19. Typical X-ray diffraction pattern taken at IMM

For most of our films the measurements were carried out using a Philips X´Pert four-circle diffractometer, consisting in a Bragg Brentano system with CuK_{α} radiation (shown in Fig.2.20). The standard settings for the X-ray generator were 45 kV at 40 mA. A horizontal slit (1/4°) and a vertical divergence slit (1/4°) were inserted in the X-ray beam path, resulting in a spot size on the order of 3 mm^2. Double-sided tape was used to mount the sample on the sample holder. The film was positioned in the X-ray beam path by adjusting the X, Y and Z axes of the sample holder.

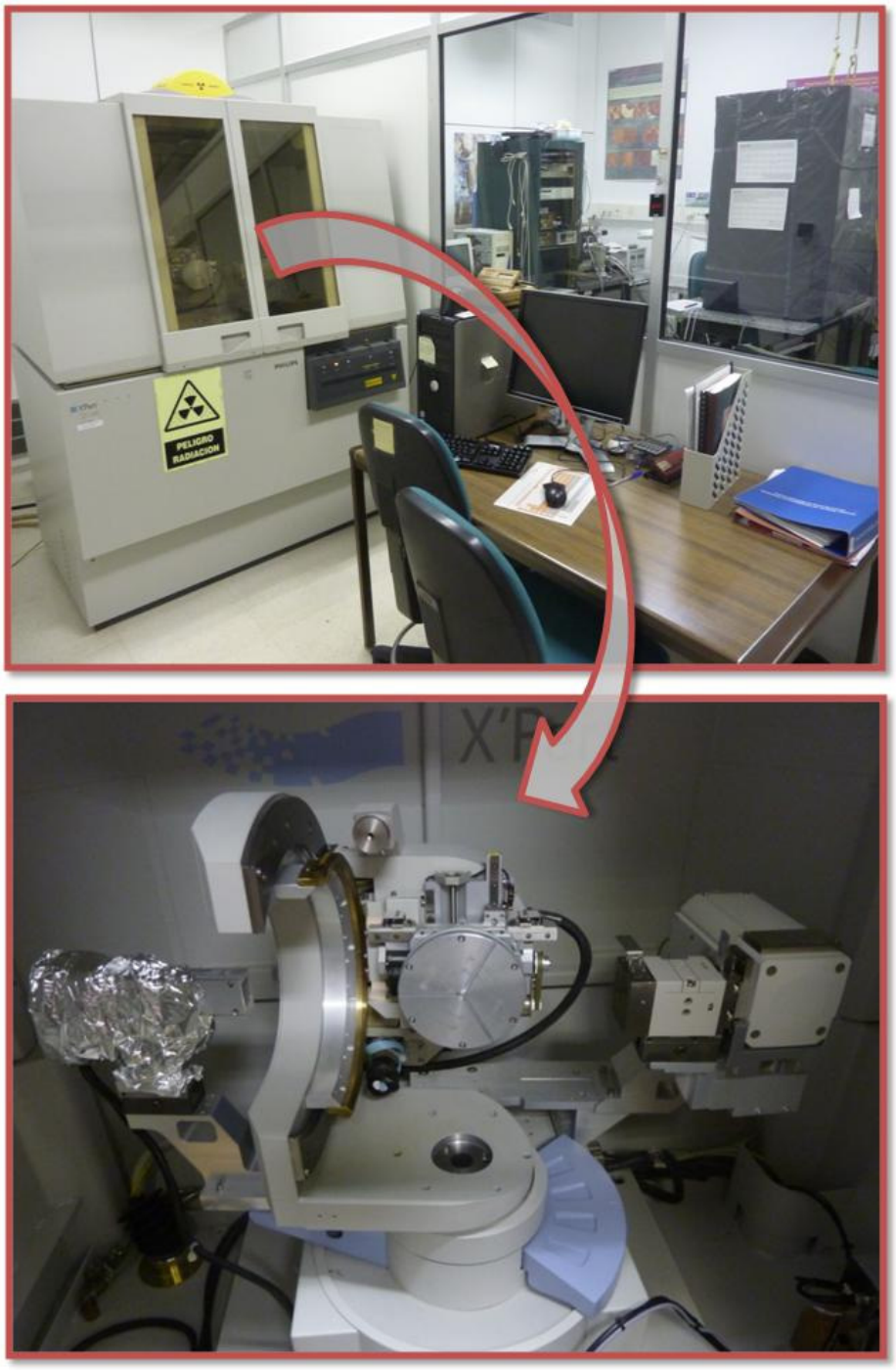

Fig.2.20. Philips X´Pert four-circle diffractometer at IMM laboratory (Bragg Brentano system with CuK_{α} radiation)

Three different types of scans were performed. 2Θ/ω measurements were carried out in order to study the out-of-plane orientation of the films. The structural quality of the films was defined by the Full-Width at Half-Maximum (FWHM) values of the rocking curves. A rocking curve (or ω-scan) plots the diffracted X-ray intensity as a function of ω, and is measured by moving the sample over a small angular range while fixing the detector to the 2Θ Bragg angle of the reflection. Before measuring the rocking curve a ψ-scan was done in order to optimize the tilt. Φ-scans were performed in order to see the in-plane alignment of the films relative to the sapphire substrates.

For some films the structural characterization was done ex-situ by μ-XRD in Debye-Scherrer geometry at "Laboratorio de difraccion de rayos X del Instituto de Ciencia de Materiales de Barcelona (ICMAB-CSIC)" in collaboration with Dra. Anna Crespi. In this case the diffractometer consisted in a General Area Detector Diffraction System (GADDS) bidimensional detector (Bruker-AXS, model D8 Advanced), a CuKα radiation source and a collimator of 0.3 mm.

2.2.3. Rutherford Backscattering Spectrometry (RBS)

Among the Ion Beam Analysis (IBA) techniques maybe one of the most important is the ion backscattering technique [27]. Usually this method is also called RBS. Its basic idea is that, the elastic scattering of energetic ions with the atoms of the sample to be studied is made via the repulsive Coulomb force of the positively charged atomic nuclei. Depending on the energy distribution of the backscattered ions one can find out the elemental composition (usually in a depth range of 1 μm).

The experimental setup is simple, as shown in Fig.2.21. Generally light ions as H, He or Li with low MeV energy are used as source. This beam is collimated and oriented toward the sample to be studied. As the ions enter into the matter, due to the collisions with electrons will lose their kinetic energy, until will stop in a depth of a few micrometers. The very few ions that come close to the atomic nuclei are scattered at large angles. The backscattered ions coming from the sample are analyzed by a spectrometer. The obtained spectra are then analyzed using specific software.

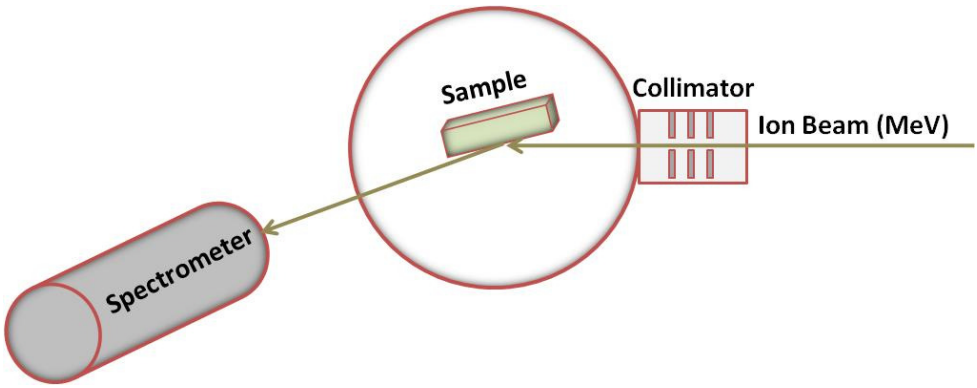

Fig.2.21. Typical experimental setup for RBS

By this method mostly all elements from Be to U can be identified. However, its resolution is determined by the combination of elements and the distribution of the layers. Generally using a 2 MeV ^{4}He beam backscattered at very large angle (almost 180°) is appropriate for most of the samples. The resolution limit of this technique is of the order of 1 %.

In Fig.2.22 the elastic collision between two particles is drawn. According to the conservation of kinetic energy and momentum applied on these two particles, the kinematic factor k is defined as the ratio of the energies after and before scattering.

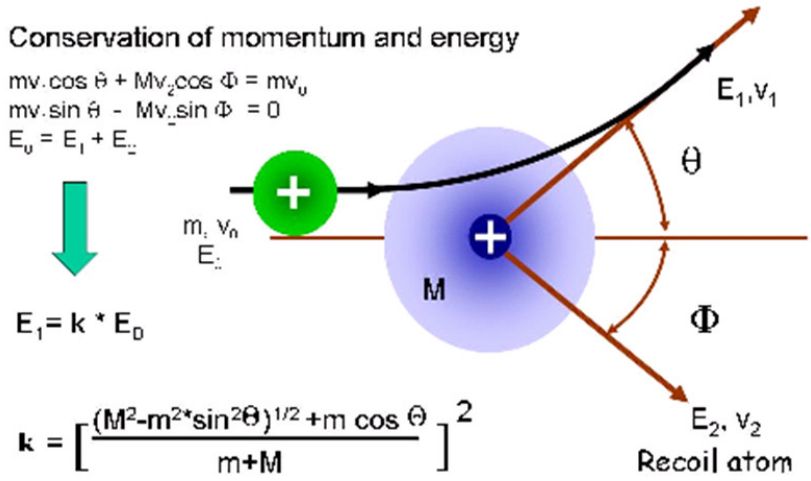

Fig.2.22. Elastic collision between two particles and the kinematic factor (k) (Extracted from Ref. [28])

This kinematic factor is used for the identification of a particular atomic mass in the target, as it is determined by the scattering angle (Θ) and the masses of ion (m) and target atom (M). It increases when the scattering atomic mass increases (see Fig.2.23), and decreases when the scattering angle increases (see Fig.2.24).

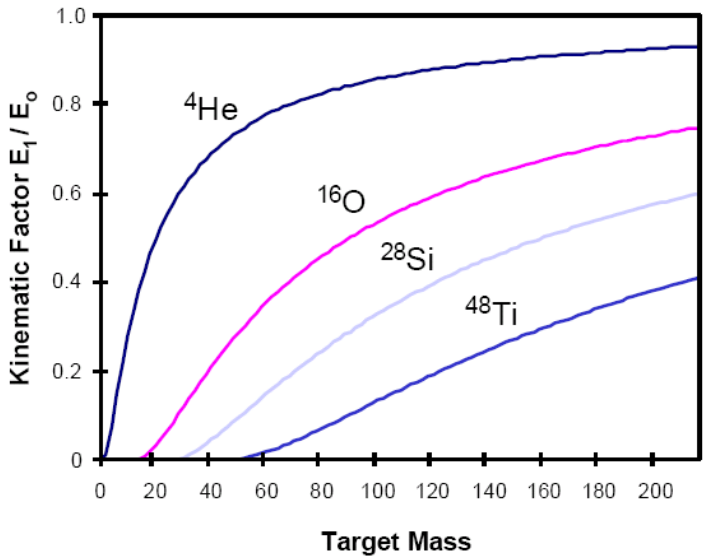

Fig.2.23. Kinematic factor as a function of target mass for a number of projectile types (Extracted from Ref. [28])

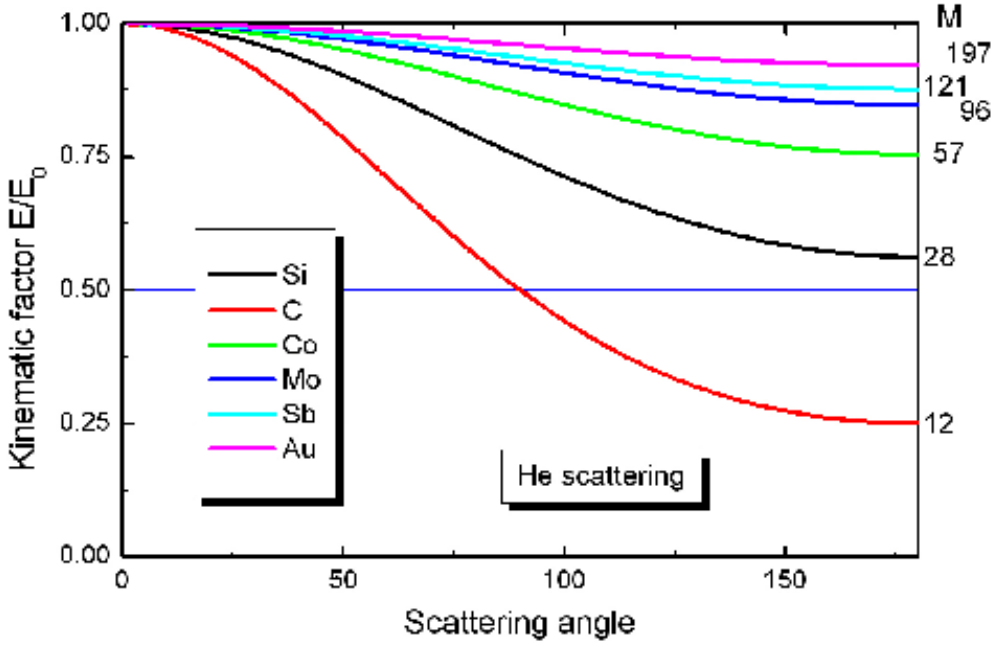

Fig.2.24. Kinematic factor as a function of scattering angle (Extracted from Ref. [28])

Fig.2.25 shows an example of RBS spectrum. The elemental area densities can be obtained from the spectrum, by dividing the peak sum to their corresponding cross sections. When the spectra are more complicated the evaluation is made by comparing the obtained spectra with theoretical spectrum simulations. For this purpose PC programs such as RUMP, SIMNRA and WiNDF are used.

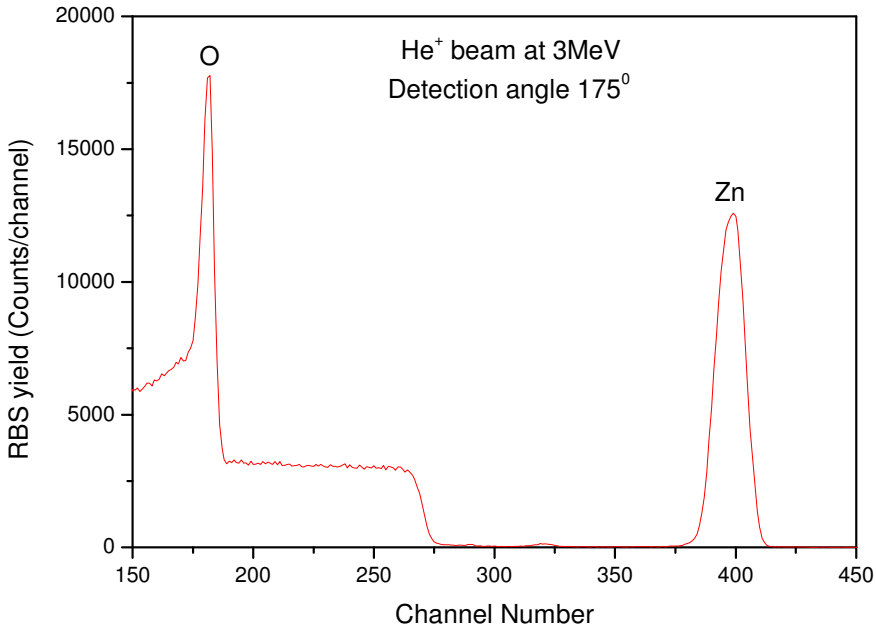

Fig.2.25. Typical RBS spectrum

In order to accurately determine the elemental area density for our ZnO films deposited on Al_2O_3 substrates, Non-RBS measurements were performed in random configuration with a He^+ beam at the oxygen resonance energy (3.0 MeV) [29]at the Forschungszentrum Rossendorf in Dresden (Germany). These measurements were made in collaboration with Dra. Raquel Gonzalez Arrabal and Dr. Frans Munnik. The narrow resonance (with a width of only KeV) enhances the effective oxygen cross section by a factor of 23 allowing to clearly distinguish the α particles backscattered from the O in the ZnO film from those backscattered from O within the Al_2O_3 substrates. The separation of the oxygen in the film (O_{film}) and oxygen in the substrate (O_{subs}) scan curve from the Non-RBS spectra has been done on the basis of stopping power (*S*) calculation. Non-RBS spectra were also measured in channeling configuration along the <0001> axis, to independently study the lattice order degree of both the O and Zn sublattices.

The backscattered α particles in Non-RBS were measured by a Si surface barrier detector placed at an angle of 175° with respect to the beam direction. The spot size was about 1.2 x1.2 mm^2. The analysis conditions (beam current and fluence) were calculated in order to avoid radiation-induced damage. The simulations were made using the commercial computer code SIMNRA [22].

2.2.4. Proton Induced X-ray Emission (PIXE)

Because of the similarity in mass numbers of Zn and Co, Non-RBS data did not allow to resolve the Zn and Co signals which can be done well by using PIXE.

The PIXE technique is very useful for the identification of heavy elements, as these elements present minor differences in RBS energies, but notable differences in PIXE spectra. Generally PIXE apparatus use H^+, although sometimes He^{++} is used. This method is very sensitive, being able to detect concentrations in ppm range. The fact that is a non-destructive technique makes it useful for various applications [30].

In Fig.2.26 a typical PIXE experimental setup and spectrum are shown. The proton beam coming from an accelerator enters into the analysis chamber. Polypropylene foils or cellulose acetate filters are used as support for the samples. The emitted X rays are first passing through an X-ray filter and then detected by a Si(Li) detector. By this method can be detected the elements heavier than C.

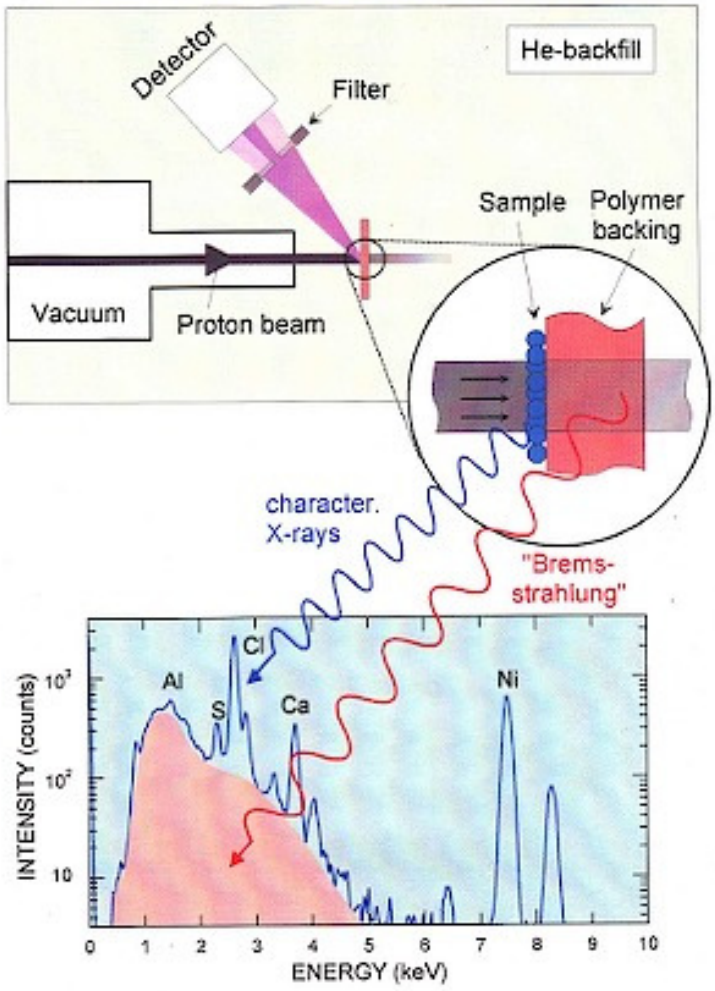

Fig.2.26. Schematic drawing of a typical experimental setup for PIXE analysis and a typical PIXE spectrum (Courtesy of HGMU, ISS Radiation Biophysics [31])

In Fig.2.27 the basic principle of the PIXE technique is drawn. The energetic incident protons stimulate the excitation of target atoms. In order to re-establish a stable energy, electronic transition takes place in these atoms. During the transition electromagnetic radiation (X-rays) is emitted.

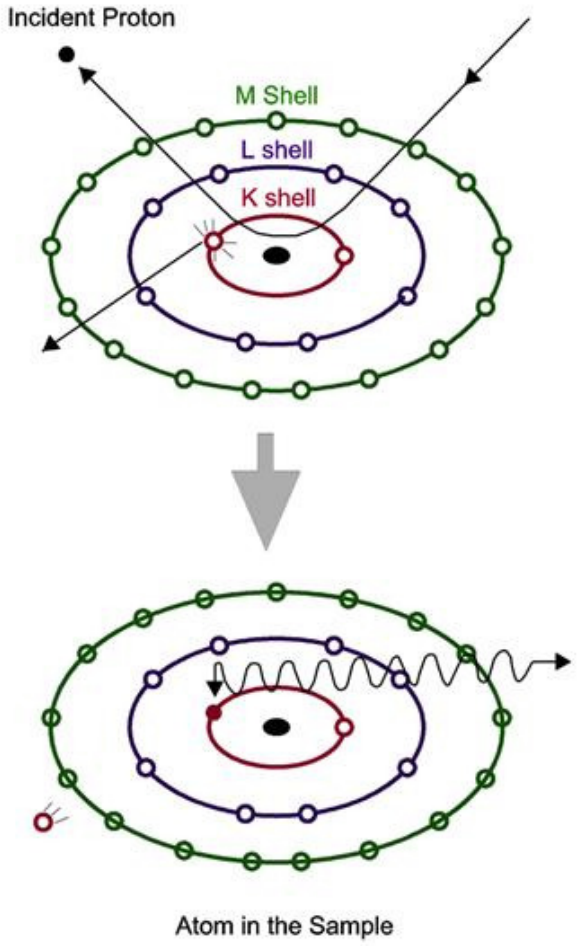

Fig.2.27. Basic principle of PIXE (Adapted from Ref. [32])

If the electron transition is made to the K, L, M,... shells, the corresponding K, L, M,... lines are emitted. Therefore, by identifying the X-rays emitted from the excited sample one can find out the elemental composition. For a sample containing a few elements the interpretation of PIXE spectrum is very easy. But sometimes the samples can be more complex, and consist of many elements. In this case as each element could originate one or more X-ray peaks, a large

number of peaks can be obtained. Also there is the probability that some of these peaks might overlap. Therefore, when the PIXE spectrum is so complicated analysis software is required.

For our implanted films, the PIXE technique was used for the determination of the Co lattice location within the ZnO host matrix. These measurements were made in collaboration with Dra. Raquel Gonzalez Arrabal and Dr. Frans Munnik at the Facilities of the Forschungszentrum Dresden-Rossendorf, Germany.

The position of the Co atoms in the ZnO host matrix has been determined by comparing the shape and position of the Co angular scan curve with that for Zn. The measurements of the emitted X-rays were performed with a Si(Li) detector placed at an angle of 135° with respect to the beam direction. The spot size was about 1.2 x1.2 mm^2. Like in the case of RBS measurements, the measurements conditions (beam current and fluence) were adjusted to avoid radiation-induced damage.

Additional PIXE measurements were carried out in channeling configuration along the <0001> axis using a He^{++} beam at an energy of 6 MeV. The implantation induced damage in the Zn and in the O sublattices for Co-implanted and Co-RTA films is characterized from the angular scan curves. The lattice disorder and the damage recovery after RTA is quantified by the minimum yield (χ_{min}) obtained from these angular scan curves. The minimum yield is defined as the ratio between the yield measured in channeling direction and the one measured in random configuration.

2.2.5. Atomic Force Microscopy (AFM)

The topography of the film surfaces was investigated by AFM measurements, in order to confirm the relation between the growth conditions and the surface morphology.

The AFM technique is a very powerful tool used for imaging and measuring with resolution within nanometers. The main advantage of this technique is that it can be used on various kinds of surfaces (glass, ceramics, composites, polymers, biological samples).

The basic idea of the AFM technique is very simple, as it is illustrated in Fig.2.28. The sample surface is scanned with a mechanical probe (a cantilever with a sharp tip). This cantilever is usually made of silicon or silicon nitride.

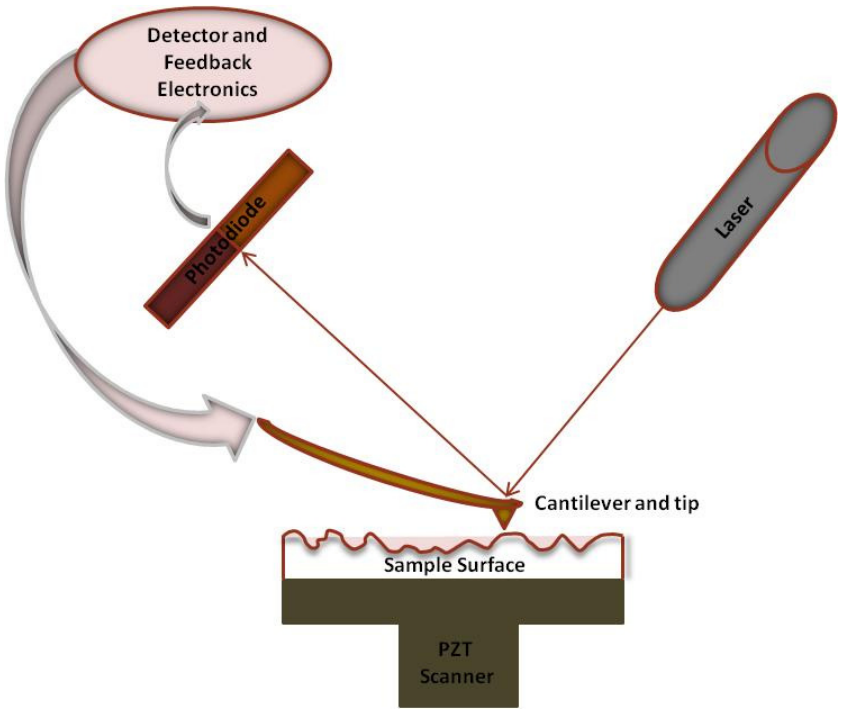

Fig.2.28. Block diagram of atomic force microscope (Adapted from Ref. [33])

As the tip gets near the sample surface, the forces between them will cause the deflection of the cantilever. Measuring this deflection, and knowing the stiffness of the cantilever, one can calculate the force. In order to measure the deflection of the lever an array of photodiodes is used. If the tip would be maintained at a constant height, it could smash into the surface. In order to avoid this collision a feedback mechanism is used. Therefore the distance between the tip and the sample is adjusted in order to maintain constant the force between them. For that purpose the sample holder is usually a 3 axis piezoelectric tube: the x and y directions are used to scan the sample, and the z direction to maintain the force constant.

There are three different operation modes for the AFM: static modes (or contact), dynamic modes (or non-contact) where the cantilever is vibrated and tapping mode.

For the topographic investigation of our films a commercial AFM (Nanotec Electronica, Spain) shown in Fig.2.29 was used. These measurements were made in collaboration with Mariana Köber. In order to avoid damage and scratching of the film surface the microscope was operated in tapping mode. The cantilevers used in this study were made of Si and have their backside coated with Al. All the measurements were performed in air at room temperature. The scanning area was 1.2μm X 1.2μm. Usually more images were taken from neighboring areas in order to assure that the images were characteristic of the local area. The vertical offsets induced by the experimental error were removed by performing a flattening using the control software [34].

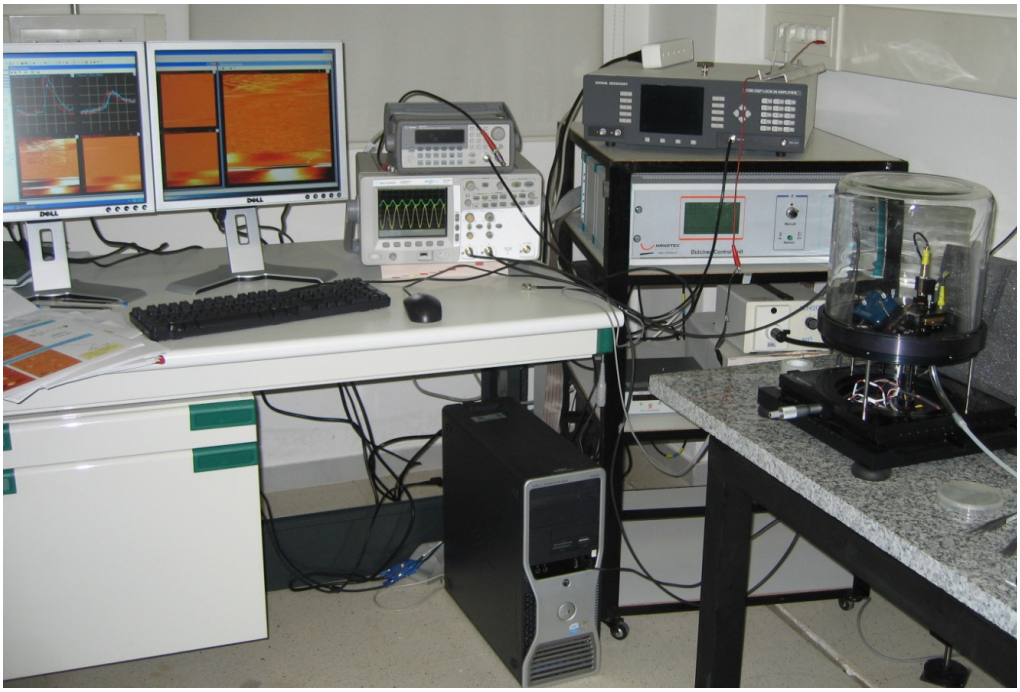

Fig.2.29. AFM (Nanotec Electronica, Spain) at IMM used for this PhD work

2.2.6. Photoluminescence (PL)

The optical properties of the films were characterized by PL spectroscopy. This is a very important technique used to investigate the electronic band structure, and therefore the defects within the sample. One of the most important features of this method is that is nondestructive as no contact is required.

In Fig.2.30 the experimental PL setup is shown. The main components are: an optical source (laser), an optical power meter (spectrometer) and a photodetector.

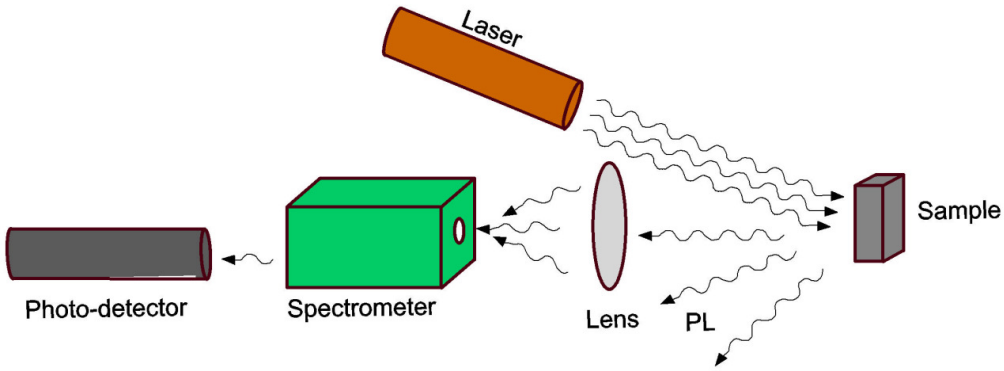

Fig.2.30. Typical experimental set-up for PL measurements (Adapted from Ref. [35])

The principle of the PL is very simple: as the light enters into the material, photons are absorbed having as consequence electronic excitations. As the excitations relax the electrons will return to the ground states, and the corresponding energy released can indicate a radiative process (when light is emitted) or a nonradiative process. When the process is radiative, the light that is emitted is known as PL. By analyzing this light one can find out information about the electronic band structure, donor and acceptor levels, defect types and impurities of the materials system. Because the PL emission depends on temperature, for high spectral resolution the measurements have to be performed at liquid helium temperatures. However, generally the measurements performed at room-temperature are sufficient.

In Fig.2.31 different recombination pathways are drawn (a-d). The one indicated in Fig.2.31 (a) is a radiative transition which takes place between states in the conduction and valence bands, with the corresponding energy difference being the band gap. This is the most common recombination pathway in semiconductors.

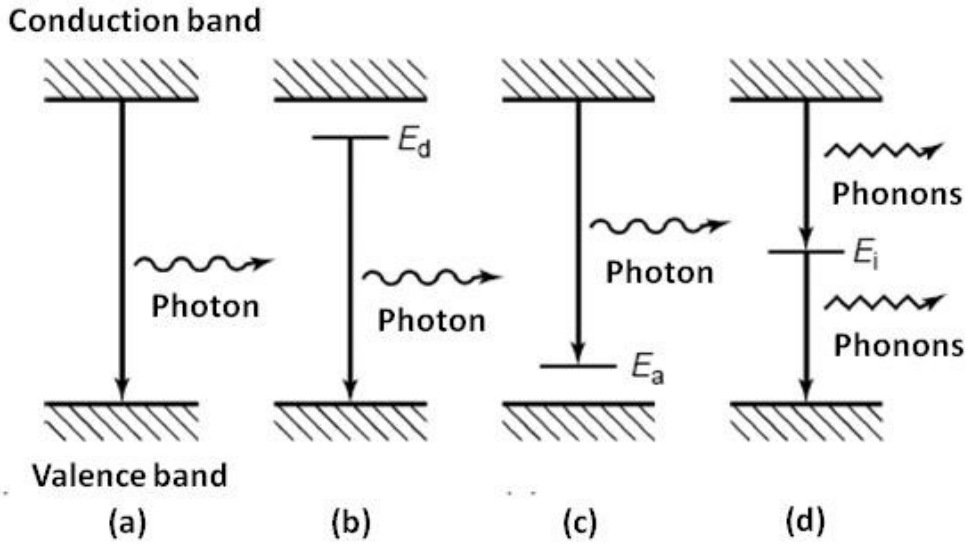

Fig.2.31. (a-c) Radiative recombination paths (a) band-to-band; (b) donor to valence band; (c) conduction band to acceptor. (d) Nonradiative recombination via an intermediate state (Reprinted with permission from Ref. [35] ©John Wiley & Sons Ltd, Chichester, 2000)

When the semiconductor has some defects and/or impurities, its band structure will endure a perturbation. This will be characterized by a discrete energy level placed between the conduction and the valence band. Usually this kind of levels is the one involved in radiative recombination (as shown in Fig.2.31 (b-c)). Depending on the nature of the defect/impurity, it will act as a donor or acceptor. The photoluminescence energy is useful to determine the defects, and its amount to quantify their concentration.

On the other hand, nonradiative recombination occurs, when the electrons use deep levels between the conduction and valence bands for a break, by emitting phonons (Fig.2.31 (d)).

In this work, the PL was excited by a frequency tripled Nd-Yag pulsed laser operated at 355 nm, pulse duration 15 ns and repetition rate 20 kHz (see Fig.2.32). The intensity of the laser was modulated by an optical modulator (177 Hz). The UV-Vis emitted light was collected by a 300mm monochromator with a 1200 g/mm grating, and then detected with a cooled-PMT connected to a lock-in amplifier. The spectra were recorded at room temperature. These measurements were made in collaboration with Daniel Alegre, Cristina Vicente and Dr. Benito Alen.

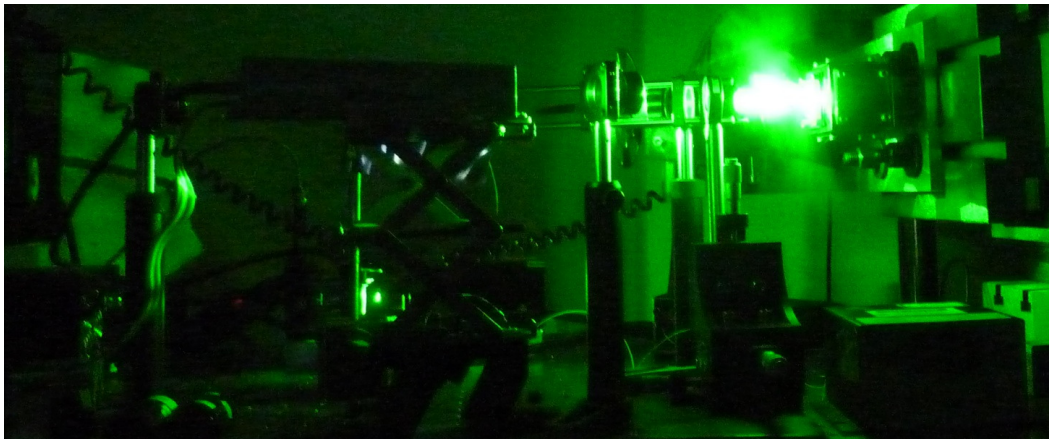

Fig.2.32. Laser operating for PL measurements at IMM

2.2.7. HALL

The electrical properties (resistivity, mobility and carrier density) of the films were determined by Hall effect measurements, using van der Pauw configuration.

The Hall effect is very useful for the characterization of semiconductor materials because it allows the determination of the type, concentration and mobility of the charge carriers when complemented with conductivity measurements. If performing just conductivity measurements one can only find out the product between the carrier concentration and mobility of the semiconducting material.

In Fig.2.33 a scheme of the Hall effect is illustrated. The force F which act on a charge q moving with a velocity $v=v_x i$ in a magnetic field $B=B_z k$ is given by Lorentz's law:

$$F= q(E + v \text{ x } B) \tag{2.1}$$

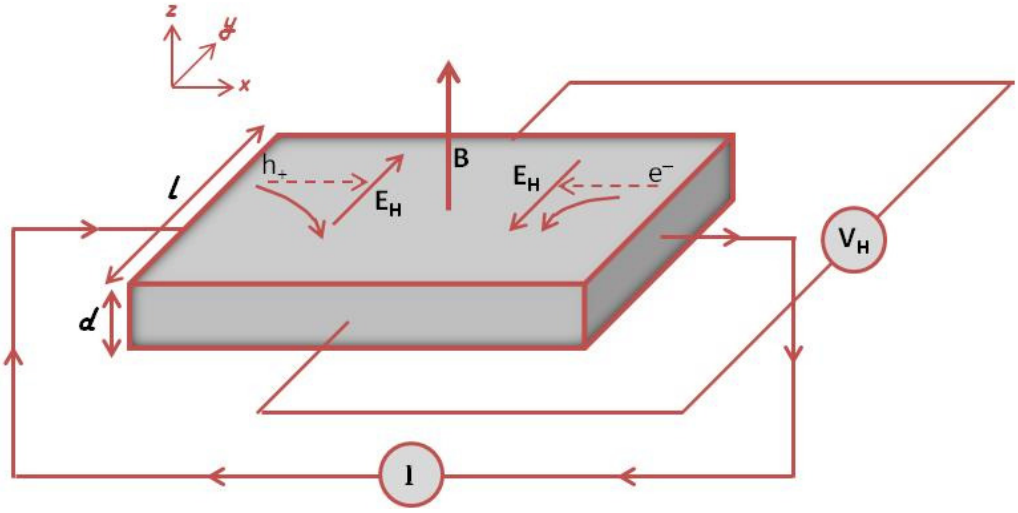

Fig.2.33. Schematic representation of the Hall effect

Besides measuring the carrier mobility and concentration, the Hall effect can be used to distinguish a p- from a n-type semiconductor. If the semiconductor is p-type, at $y=0$ a positive charge accumulation will be observed, and if is n-type a negative charge. At the same time at $y=l$ an excess of charge carriers with opposite sign will result (see Fig.2.33).

This excess of charge creates an electric field E_H along the y-axis direction, which is also called Hall field. This field creates a force which has the same magnitude as the magnetic force given by Lorentz's law and therefore:

$$qE_H = q\ v_x\ B_z \tag{2.2}$$

Consequently, along the y-axis direction a potential difference is created which is called the Hall voltage (V_H) and is given by

$$V_H = E_H l = v_x B_z l \tag{2.3}$$

If along the x direction a constant current flows (I_x), the Hall voltage may be given by:

$$V_H = I_x B_z / qnd = I_x B_z R_H / d \tag{2.4}$$

where n is the carrier concentration, d is the sample thickness, and $R_H = 1/(qn)$ is the Hall coefficient. For a p-type semiconductor the Hall voltage and the Hall coefficient are positive, and for a n-type semiconductor they are negative.

In order to determine the carrier concentration, type and mobility of a semiconducting material, measurements of the resistivity (ρ) can be performed using the van der Pauw method as illustrated in Fig.2.34.

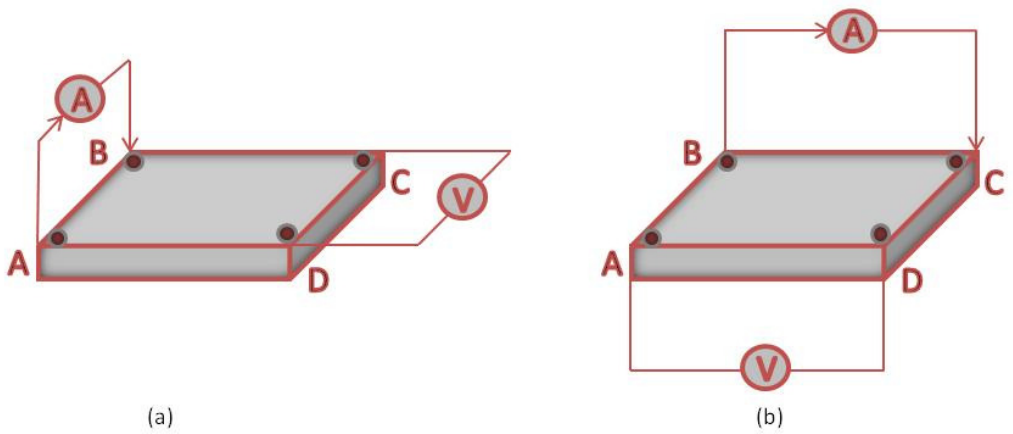

Fig.2.34. Van der Pauw configuration for measuring (a) V_{DC} and (b) V_{DA}

The van der Pauw configuration has some requirements: the sample has to be homogeneous; its thickness to be much smaller than the width and length; and four peripheric and very small Ohmic contacts are necessary. The resistivity ρ will be then given by

$$\rho = 1/\sigma = \pi d(R_{AB,DC}+R_{CB,DA})/2\ln 2 = \pi d[(V_D-V_C)/I_{AB}+(V_D-V_A)/I_{CB})]/2\ln 2 \qquad (2.5)$$

$R_{AB,DC}$ is the sheet resistance between the contacts A and B for a current flowing from A to B, and the potential difference is measured between the contacts D and C (see Fig.2.34). For these measurements the current is passed through contiguous contacts, and the voltage drop is measured across the opposite contacts. Eight voltage measurements are performed without applying any magnetic field.

For the determination of the carrier concentration n_H (or p_H) another eight measurements of voltages are performed, this time applying a magnetic field: four under a positive magnetic field ($B+$) and four under a negative magnetic field (B-). This combination of measurements is necessary in order to eliminate undesired voltages like Seebeck (V_S), Nernst (V_N), Righi-Leduc (V_R) and Ettingshausen (V_E) effects.

The carrier mobility (μ) can be determined from the values of V_H and R_H using the definitions of current density and conductivity σ

$$\mu = R_H \sigma \tag{2.6}$$

Fig.2.35 shows our Hall measurements experimental set-up developed at IMM. The Hall system was assembled from various components. A KEPCO bipolar operational Power Supply (model BOP20-5M) supplied current to a large field electromagnet, which was set to 2200 gauss field. The 224 model from Keithley was used as a current source, and a Keitley Nanovoltmeter model 181 was measuring the resulting voltages. A Lake Shore Cryotronics 805 with 2 sensors was used (one sensor for temperature reading and the other working as a heater). As switch/control unit network the model 3488A from Hewlett Packard was used. The angle between the sample surface normal and the magnetic field is 90 degrees. After the sample was mounted on the Hall measurement probe head, a metallic protective cover was placed on top in order to avoid condensation when performing low temperature measurements. The Hall measurements were carried out in the dark. All these instruments were controlled by a computer, which acquired and processed the data with a lab-view program developed by Dr. Fernando Garcia from IMM. The obtained data included carrier concentration, mobility, resistivity, carrier type, and error analysis.

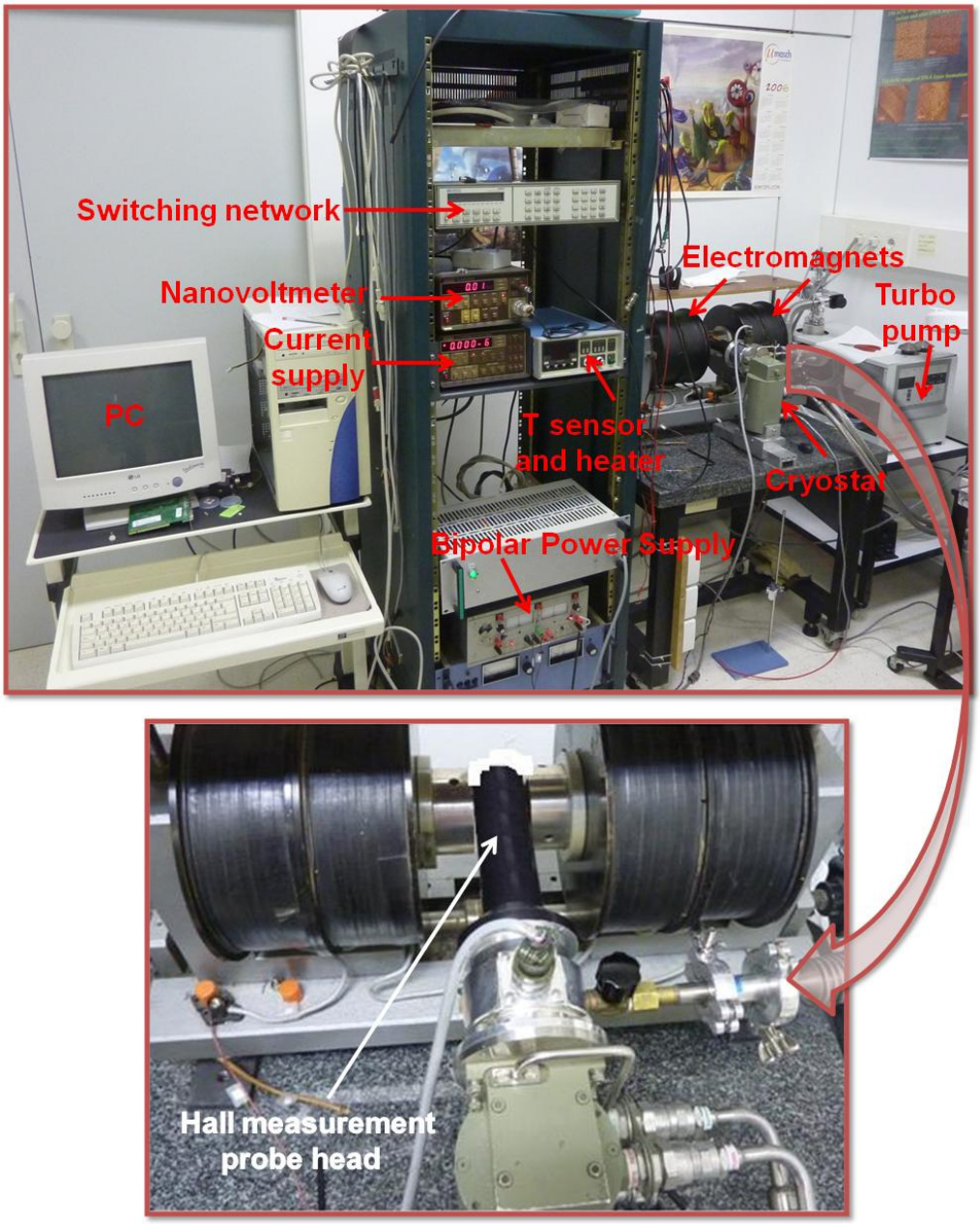

Fig.2.35. Hall measurements experimental set-up at IMM

E-beam deposition

The Electron Beam Evaporation (e-beam evaporation) belongs to the Physical Vapor Deposition (PVD) techniques. This technique is used for the deposition of metals. The basic idea of the PVD technique is very simple as it can be seen in Fig.2.36, where a typical set-up system for e-beam evaporation is shown. Inside a vacuum chamber an electron beam is oriented onto the chosen material causing its heating, and therefore the source material it will boil and evaporate on the desired substrate.

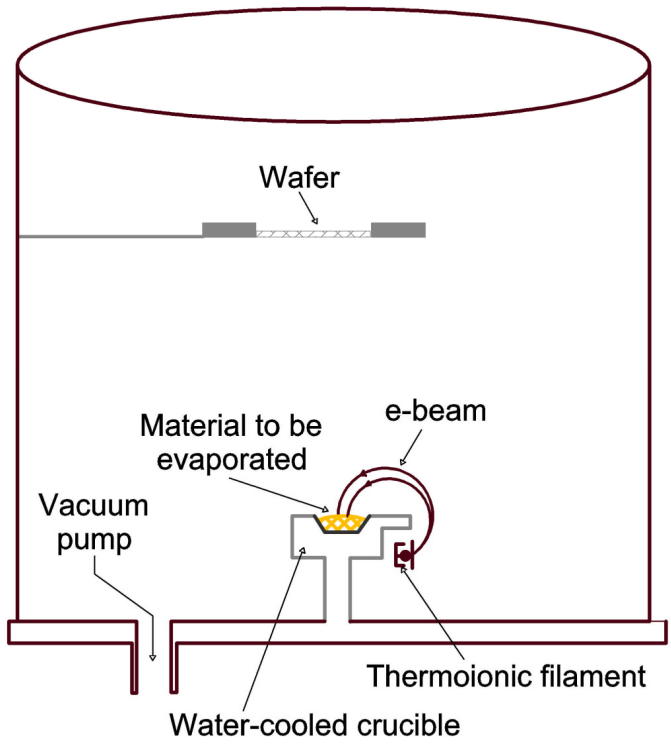

Fig.2.36. Typical system for e-beam evaporation of materials (Adapted from Ref. [36])

In order to improve the electronic device efficiency ohmic contacts with low specific resistance are mandatory [37]. Specific contact resistances of ≈ $3x10^{-4}$ Ωcm^2 were obtained for Pt-Ga contacts on ZnO epitaxial layers [38], $2x10^{-4}$ Ωcm^2 for Ti/Au on Al-doped epitaxial layers [39,40], 0.7 Ωcm^2 for non-alloyed In on laser-processed ZnO substrates [41], $2.5x10^{-5}$ Ωcm^2 for non-alloyed Al on epitaxial ZnO [42], $7.3x10^{-3}$ to $4.3x10^{-5}$ Ωcm^2 for Ti/Au on plasma exposed Al-doped epitaxial ZnO [43] and $9x10^{-7}$ Ωcm^2 for Ti/Al on epitaxial ZnO [44]. From all these works a general conclusion was made: that the specific contact resistance is lowered when annealing at 200°C. According to Pearton *et al.* [45] Ti/Al/Pt/Au contacts on ZnO layers deposited by pulsed laser deposition produce excellent Ohmic behavior with a minimum specific contact resistance of $8x10^{-7}$ Ωcm^2.

For the van der Pauw four-probe geometry, in this thesis metallic contacts have been deposited by e-beam evaporation on top of the films. Fig.2.37 shows the e-beam evaporation apparatus used (developed also at IMM). The contacts were patterned using a home-made shadow mask in intimate contact with the sample. The mask was fabricated by photolithography followed by chemical etching. The film was round shape with 8mm in diameter. The contacts were deposited on the edge of the circular film, and each metallic dot was approximately 0.5 mm in diameter. The sequence was Ti/Al/Pt/Au, each layer having a thickness of 150 Å. Afterwards they have been annealed at 200°C for 20 minutes [46].

Fig.2.37. e-beam evaporation apparatus at IMM

The film was then mounted for Hall measurements. The film with the corresponding substrate was pasted with epoxy on top of an 11x11mm alumina plate. 50 µm diameter golden wires were used to make the connection to 4 gold cover copper pads. These pads serve to mount the sample in the Hall measurement system. Fig.2.38 shows a sample of ZnO film (deposited on sapphire substrate) with Ti/Al/Pt/Au contacts, the golden wires, and the corresponding pads prepared for Hall measurements. Because the ZnO film on sapphire substrates are transparent and cannot be distinguished, the ZnO film had been marked by hand in this picture with a black circle. Before measuring the temperature dependence of the electrical properties, the ohmic character of the contacts was verified by measuring the characteristic linear I-V curve.

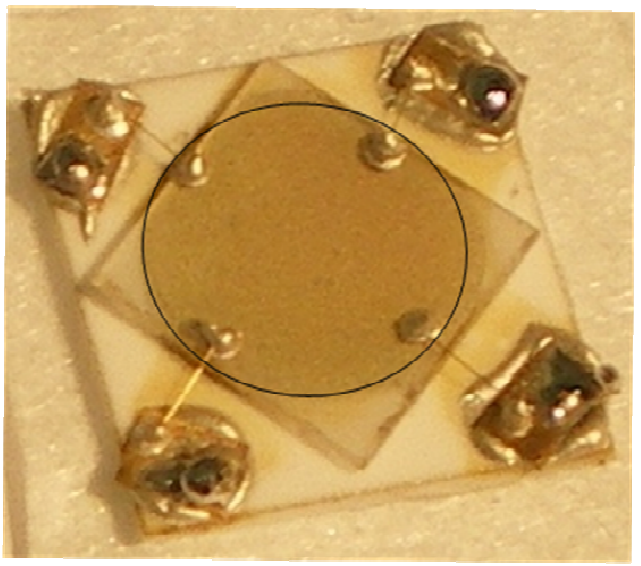

Fig.2.38. Sample of ZnO film with Ti/Al/Pt/Au contacts and the corresponding pads prepared for Hall measurements. The film edge has been underlined. The gray color corresponds to the silver epoxy.

2.2.8. SQUID

Magnetic characterization of the films was performed by Superconducting Quantum Interference Device measurements. The SQUID is the device that measures the magnetic fields with the best resolution (sensitivity of 10^{-8} emu).

In Fig.2.39 a typical experimental setup of the SQUID magnetometer is shown. The system consists of a He cryostat with a superconducting magnet, superconducting detection coil and a SQUID sensor connected to the detection coil (the SQUID detector). The temperature of the sample is adjusted by a He gas flow control system. The sample to be studied is exposed to the magnetic field and moved through the pick-up coil system. While passing through the coil arrangement step-by-step, a magnetized sample will induce a voltage

at each step. The induced voltage (which is proportional to the magnetic moment of the sample) is measured by the SQUID detector. A SQUID scan is the chart of this measured voltage as a function of the sample position. In order to evaluate the sample magnetization the scan data are fitted using special software.

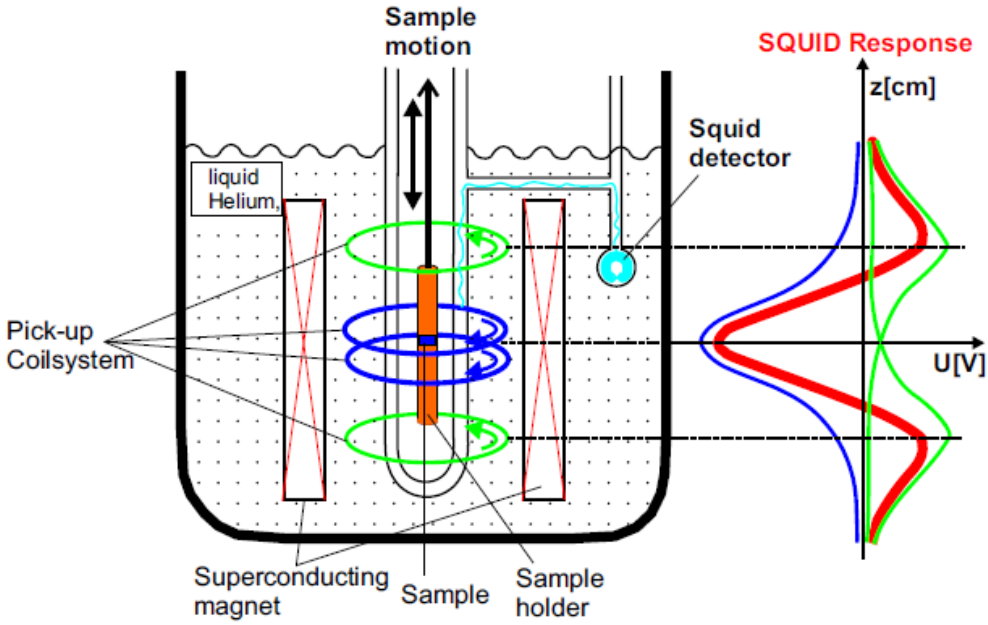

Fig.2.39. Typical experimental setup of a SQUID magnetometer (Reprinted with permission from Ref. [47])

This technique is very useful to obtain information about the magnetic properties of the samples from their hysteresis loop and from their initial magnetization curve. The parameters that one can obtain are the susceptibility, the coercive field, the remnant magnetization, and the saturation magnetization.

The magnetic characterization of our pellets was performed at the "Instituto de Magnetismo Aplicado Salvador Velayos UCM/Renfe, Las Rozas de Madrid" in collaboration with Dr. Miguel Angel García and Dr. Adrian Quesada [48]. The SQUID measurements of our films were

performed at the "Instituto de Ciencia de Materiales Madrid" ICMM-CSIC in collaboration with Dra. Mar García Hernandez. The measurements were made by cooling the sample to 5 K with no applied field for the zero-field-cooled (ZFC) protocol. The field dependence at constant temperature of 5K was measured. A magnetic field of 10000 Oe was then applied in order to enhance the magnetic signature of the sample and make the measurements less noisy. The temperature dependence of the magnetization at this constant field was then measured. The temperature was swept to 300K with measurements taken every 10 K. Upon reaching the temperature of 300 K, the field dependence of the magnetization was measured now at 300K. During the magnetic measurements the samples were handled with special care in order to avoid any possible source of spurious signals described in [21].

References

[1] D.B. Chrisey and G.K. Hubler, Pulsed Laser Deposition of Thin Film, John Wiley & Sons Inc., New York (1994)

[2] F. Breech and L. Cross, Appl. Spect. 16 (1962) 59

[3] H.M. Smith and A.F. Turner, Appl. Opt. 4 (1965) 147

[4] C.K.N. Patel, Phys. Rev. Lett. 12 (1964) 588

[5] J.E. Geusic, H.M. Marcos and L.G. Uitert, Appl. Phys. Lett. 4 (1964) 182

[6] Y. Zhang, H. Gu, and S. Iijima, Appl. Phys. Lett. 73 (1998) 3827

[7] D.B. Geohegan, A.A. Puretzky, and D.J. Rader, Appl. Phys. Lett. 74 (1999) 3788

[8] T.J. Goodwin, V. Leppert, S.H. Risbud, I.M. Kennedy, and H.W.H. Lee, Appl. Phys. Lett. 70 (1997) 3122

[9] J.T. Cheung, I.M. Gergis, J. James and R.E. DeWames, Appl. Phys. Lett. 60 (1992) 3180

[10] J.A Greer and H.J. Van Hook, Mater. Res. Soc. Symp. Proc. *191* (1990) 171

[11] S.M. Metev and V.P. Veiko, Laser Assisted Microtechnology, Springer, Berlin, Heidelberg (1994)

[12]http://groups.ist.utl.pt/rschwarz/rschwarzgroup_files/PLD_files/PLD.htm

[13] A. Namiki, T. Kawai, K. Ichige, Surf. Sci. 166 (1986) 129

[14] resources.edb.gov.hk/.../03PulsedLaserDeposition(English).doc

[15] M. Hanabusa, Mater. Res. Soc. Symp. *P*roc. 285 (1993) 447

[16] G. Koren, R.J Baseman, A. Gupta, M.I. Lutwyche and R.B. Laibowitz, Appl. Phys. Lett. 52 (1998) 1193

[17] T. Ventkatesan, X.D. Wu, A. Inam and J.B. Watchman, Appl. Phys. Lett. 52 (1998) 1193

[18] B. Holzapfel, B. Roas, L. Schultz, P. Bauer and G. Saemann-Ischenko, Appl. Phys. Lett. 61 (1992) 3178

[19] R.J. Cava, B. Batlogg, C.H. Chen, E.A. Rietman, S.M. Zahurak and D. Werder, Appl. Phys. Lett. B36 (1987) 5719

[20] T. Ventkatesan, X.D. Wu, A. Inam, and J.B. Watchman, Appl. Phys. Lett. 52 (1998) 1193

[21] M.A. Garcia, E. Fernandez Pinel, J. de la Venta, A. Quesada, V. Bouzas, J.F. Fernández, J.J. Romero, M.S. Martín González, and J.L. Costa-Krämer, J. Appl. Phys. 105 (2009) 013925

[22] J.F. Ziegler, M.D. Ziegler, and J.P. Biersack, SRIM-2006.02

[23]http://www.plasmaetch-gs68.de/tutorials/implant.pdf

[24] http://www.ucm.es/info/gpdym/medios.htm

[25] http://www.aps.org/units/dpb/upload/brochure.pdf

[26] http://www.tulane.edu/~sanelson/eens211/x-ray.htm

[27] W.K. Chu, J.W. Mayer and M.A. Nicolet, Backscattering Spectrometry, Academic Press, London (1978)

[28]http://www.scitopics.com/Rutherford_Backscattering_Spectrometry_RBS.html

[29] J.R. Tesmer, M. Nastasi, Handbook of Modern Ion Beam Materials Analysis, MRS (1995)

[30] I.V. Mitchell, and K.M. Barfoot, Nuclear Science Application, Harvard Academic Press, UK (1981) 99

[31]http://www.helmholtz-muenchen.de/iss/strahlenbiophysik/research/nanoanalytics/pixe-proton-induced-x-ray-emission-spectrometry/index.html

[32] http://www.ias.ac.in/currsci/jun252001/1542.pdf

[33] http://en.wikipedia.org/wiki/Atomic_force_microscopy

[34] I. Horcas, R. Fernandez, J.M. Gomez-Rodriguez, J. Colchero, J. Gomez-Herrero, and A.M. Baro, Review of Scientific Instruments 78 (2007) 013705

[35] Timothy H. Gfroerer, "Photoluminescence in Analysis of Surface and Interfaces", Encyclopedia of Analytical Chemistry, R.A. Meyers (Ed.), John Wiley & Sons Ltd, Chichester (2000) 9209

[36] http://www.memsnet.org/mems/processes/deposition.html

[37] A.A. Iliadis, R.D. Vispute, T. Venkatesan, K.A. Jones, Thin Solid Films 420-421–(2002) 478

[38] A. Inumpudi, A.A. Iliadis, S. Krishnamoorthy, S. Choopun, R.D. Vispute, T. Venkatesan, Solid State Electron 46 (2002) 1665

[39] H.K. Kim, S.H. Han, T.Y. Seong, W.K. Choi, Appl. Phys. Lett. 77 (2000) 1647

[40] H.K. Kim, S.H. Han, T.Y. Seong, W.K. Choi, J. Electrochem. Soc. 148 (2001) G114

[41] T. Akane, K. Sugioka, K. Midorikawa, J. Vac. Sci. Technol B 18 (2001) 1406

[42] J.E. Nause, III–V's Rev 12 (1999) 28

[43] H. Sheng, N.W. Emanetoglu, S. Muthukumar, S. Feng, Y. Lu, J Electron Mater 31 (2002) 811

[44] S.Y. Kim, H.W. Jang, J.K. Kim, C.M. Jeon, W.I. Park, G.C. Yi, *et al.* J Electron Mater 31 (2002) 868

[45] S.J. Pearton, D.P. Norton, K. Ip, Y.W. Heo, T. Steiner, Progress in Mat. Sci. 50 (2005) 293

[46] E. López-Ponce, J.L. Costa-Krämer, M.S. Martín-González, F. Briones, J.F. Fernández, A.C. Caballero, M. Villegas, and J. de Frutos, Phys. Stat. Sol. (a) 203, 6 (2006) 1383

[47]http://www.diss.fu-berlin.de/diss/servlets/MCRFileNodeServlet/FUDISS_derivate_000000000890/04_Kap4.pdf;jsessionid=BC73C3895520372B97065E9CBC2A7D1E?hosts

[48] A. Quesada, M.A. Garcia, M. Andrés, A. Hernando, J.F. Fernández, A.C. Caballero, M.S. Martín González, and F. Briones, J. Appl. Phys. 100 (2006) 113909

3

ZnO THIN FILMS

Chapter 3

ZnO Thin films

Although ZnO is considered an 'old' semiconductor, it is at the same time a new material. Old, because for a long time it has had applications in many industrial and scientific areas, being used like food additive, sun screening agent, piezoelectric transducers, optical waveguides, acousto-optic media, conductive gas sensors, transparent conductive electrodes, varistors. The microelectronically oriented scientific community lost interest in ZnO as a semiconductor, due to the fact that ZnO it cannot be doped both *n*- and *p*-type, and at the same time systems of reduced dimensionality based on semiconductors like GaAs/$Al_{1-y}Ga_yAs$ became more interesting to investigate. But in the mid-nineties a reawakening of ZnO research started, generating several workshops, conferences, and many papers. All these facts opened the prospect to obtain:

- a new material suitable for optoelectronics and blue/UV lasers,

- a transparent highly Conducting Oxide (TCO) as a less expensive alternative to Indium Tin Oxide (ITO), by doping with Al, Ga, In etc.,

- a radiation hard material for electronic devices required to operate in a “hard” environments, and

- a ferromagnetic material for spintronics when doped with transition metal ions.

For most of these applications is mandatory to achieve a stable and reproducible *p*-doping. However this issue is still a major and difficult

challenge. This is one of the goals addressed in this PhD work. The main objectives have been subdivided into the following tasks:

1. Optimization of growth conditions for deposition of ZnO thin films by PLD. After establishing the optimal growth conditions of polycrystalline ZnO thin films, the next step is their optimization in order to deposit reproducible *epitaxial* thin films. The obtained epitaxial thin films are characterized by different techniques.

2. To achieve intentionally undoped *p*-type ZnO thin films in a reproducible way. One of the main bottle-necks to use ZnO in devices is the difficulty to obtain reproducible undoped *p*-type ZnO films. Only a few reports can be found in the literature on nominally undoped *p*-type ZnO.

3. Another issue in epitaxial ZnO thin films is the presence of twinning, intergrown crystals that appear in a symmetrical form during growth (see Fig. 3.1). This symmetry is actually induced by the fact that the two crystals are sharing their lattice points. The appearance of twinning is something very repetitive in the literature for ZnO films and nanostructures, and regardless of the deposition techniques [1-6]. Therefore, a possible way of preventing the appearance of twinning for PLD grown ZnO films is investigated. It is also investigated if twinning has any relation with the observed *p*-type behavior of the ZnO films grown by PLD or any influence on the transport properties.

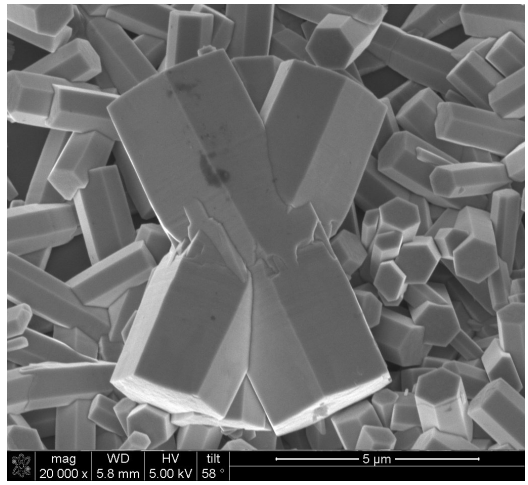

Fig.3.1. SEM image of ZnO nanorods with twinning defects (Reprinted with permission from Ref. [7])

4. The next objective is to determine if *p*-type conductivity can be associated with the presence of intrinsic defects. To assess this issue, epitaxial *n*-type ZnO films were irradiated in order to create vacancies and interstitials by radiation damage. These films were characterized by different techniques before and after the irradiation process. The influence of the irradiation on the electrical properties of the ZnO films is studied, as well as the effect of the different doses. It is also interesting to highlight that ZnO is a hard radiation resistant material. This property makes ZnO one of the best Wide Bandgap Semiconductor (WBS) suitable for space device operation. According to Khanna *et al.* [8] it is approximately 100 times more resistant than GaN to high-energy radiation.

3.1. Growth optimization of polycrystalline ZnO thin films

In general, polycrystalline ZnO films can be obtained by using a variety of deposition methods and they are well aligned along the *c*-axis direction, almost independently of substrate materials [9, 10]. In order to obtain high quality *n*-type ZnO thin films, many deposition techniques like sputtering, Chemical Vapor Deposition (CVD), MBE, and laser ablation have been employed [11-16]. PLD is an appropriate technique for growing oxide thin films due to its capability to control the oxygen gas pressure, obtaining thus a preferred *c*-axis orientation of the crystalline structure [5]. On the other hand, by PLD high crystal quality films can be grown at lower temperature compared to other methods. That is due to the fact that upon the ablation process the particles have a higher energy [17]. This advantage of the PLD technique is very important for the advancement of ZnO-based optoelectronics devices that require a low deposition temperature.

In this thesis the deposition of the ZnO films was carried out in our homemade PLD deposition chamber, which is described in the experimental techniques section.

The ZnO targets have been prepared by conventional ceramic method using high purity ZnO raw powders. The powders were milled and pressed into pellets, and afterwards sintered in different conditions. Following this procedure, pellets of different densities are obtained. The densities were calculated by the immersion Archimedes method using mercury as a liquid. The ceramic pellets used as targets for PLD have a round shape with 2cm radius and around 2mm thickness. The densities of the targets sintered at different temperatures are shown in Table 3.I.

Table 3.I. Densities of ZnO targets sintered at different temperatures

Sintering Temperature (°C)	Density (g/cm^3)
1000	5.33
1100	5.53
1200	5.52
1300	5.55

The pellets that exhibited the best density as targets for PLD were the ones made from 99.9% purity ZnO powder sintered at 1300°C for 8 hours, that had ~>98% of the theoretical density (5.66 g/cm^3). These pellets exhibited *n*-type behavior with a Hall mobility of ~ 20 $cm^2V^{-1}s^{-1}$ [18].

Fig.3.2 shows the 2Θ/ω X-Ray diffraction pattern of high density ZnO pellets sintered at 1300°C. The pellets were polycrystalline and all the diffraction maxima can be indexed according to the hexagonal wurtzite ZnO lattice (JCPDS 76-0704, a = 3.250 Å, c = 5.207 Å and spatial group P63mc) [19].

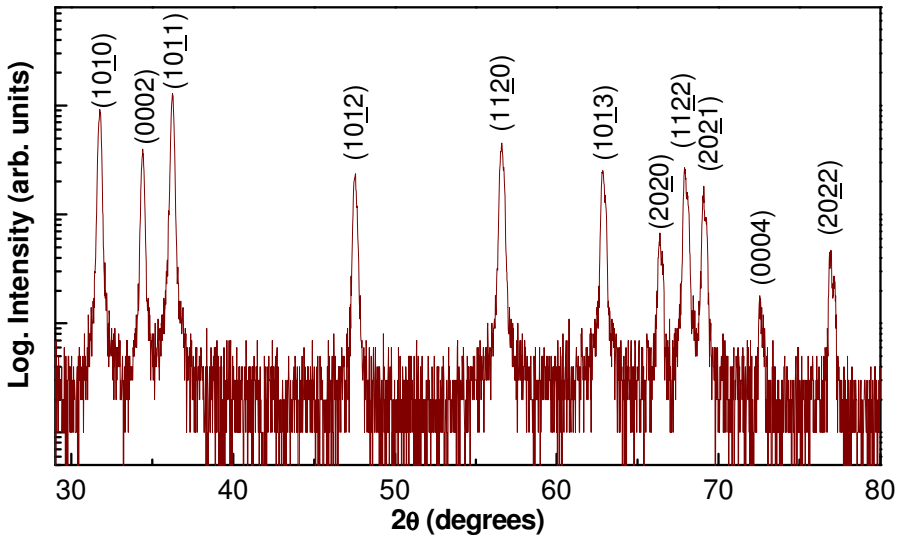

Fig.3.2. 2Θ/ω X-Ray diffraction pattern of high density ZnO pellets sintered at 1300°C

3.1.1. Substrate

The selection of the substrate is an important step since it influences the final quality of the films, especially their homogeneity. With substrates as quartz and glass it is very probable to obtain cracks in the films because of the different thermal expansion coefficients; while with Silicon or Pyrex this problem is almost eliminated [20].

The first set of films was studied as a function of the substrate type. ZnO thin films were deposited at a temperature of 400°C in $1.2x10^{-2}$ mbar oxygen, but on different substrates: silicon (Si) and Pyrex. The chosen growth temperature was 400°C since this temperature is critical for ZnO. At this temperature ZnO starts to lose oxygen and zinc atoms start to migrate, and various processes take place as observed in thermogravimetry experiments [21, 22]. So, if a good quality of films is obtained for this critical temperature, a good quality will be assured for higher temperatures.

In order to remove dust and surface contamination from the substrates, they were exposed to a standard cleaning procedure: sonication in acetone for 10 minutes, followed by isopropanol, and blown dried with high purity nitrogen gas.

Fig.3.3 shows XRD $2\Theta/\omega$ scans for the ZnO films grown on different substrates under the same oxygen pressure (Po_2=1.2 $x10^{-2}$ mbar) and at the same temperature of 400°C. All the diffraction maxima can be indexed either with the substrates or with the hexagonal wurtzite ZnO lattice (JCPDS 76-0704). For the film grown on Si two ZnO diffraction maxima corresponding to (0002) and (0004) were identified. For the film grown on Pyrex only the diffraction maxima corresponding to (0002) has been identified. So, it can be concluded that the ZnO films were oriented along the [0001] direction. Although, for the film deposited on Pyrex substrate, a much lower intensity is obtained in the (0002) diffraction maxima. The broadening of the (0002)

diffraction maxima and also the disappearance of the (0004) diffraction maxima are indicative of a poorer crystal texture of ZnO grown on Pyrex. *Therefore, Si is chosen as substrate to continue the study of ZnO polycrystalline films.*

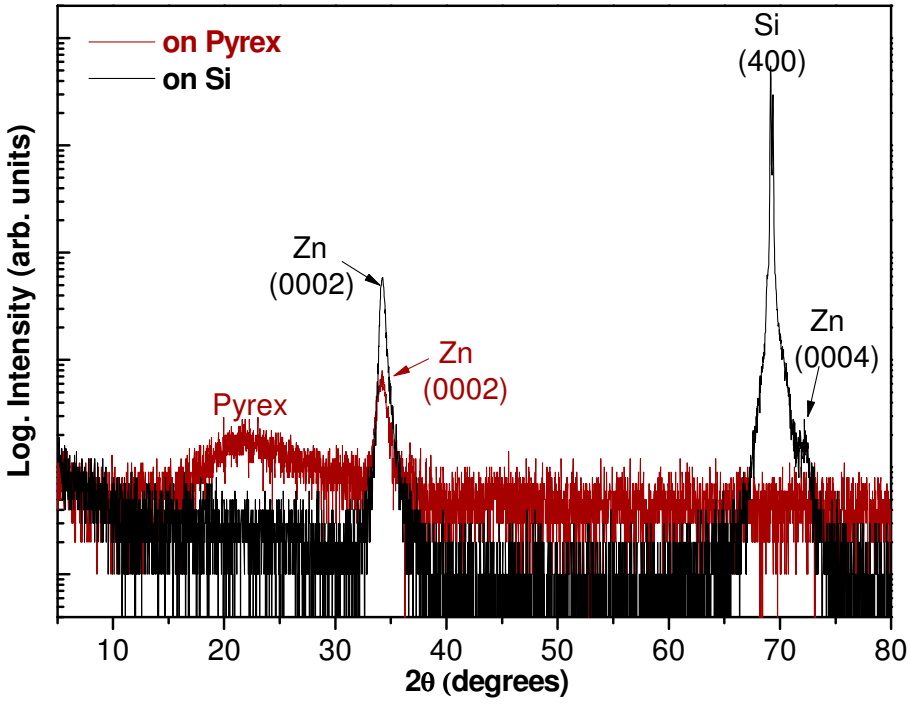

Fig.3.3. XRD 2Θ/ω scans of ZnO films grown under the same oxygen pressure (Po_2=1.2 x10^{-2} mbar) and the same temperature (400°C), but on different substrates

Fig.3.4 shows one PLD grown ZnO film (the dark circle) grown on a Si substrate. The ZnO polycrystalline films present different colors (due to light multiple interference) depending on the film thickness: orange at 180nm, pink at 196nm, blue at 220nm, green at 233nm, dark yellow at 260nm, and yellow at 269nm.

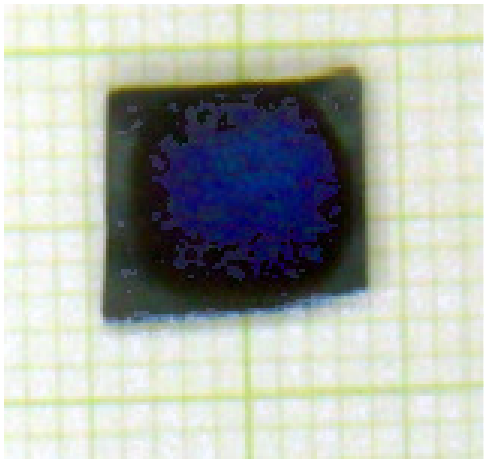

Fig.3.4. Polycrystalline ZnO thin film grown on Si substrate. The bluish circle corresponds to the ZnO film grown by PLD at 400°C.

3.1.2. Oxygen chamber pressure

To determine the optimal oxygen chamber pressure a set of films has been deposited at 400°C on Si substrate at different deposition pressures ranging from $1.2x10^{-2}$ mbar to $3x10^{-1}$ mbar. Their X-ray diffraction scans are shown in Fig.3.5. All the diffraction maxima are indexed with the substrates and with the ZnO lattice parameters. The film grown at $1.2x10^{-2}$ mbar presents two ZnO diffraction maxima corresponding to (0002) and (0004) planes, indicative of a preferential orientation of the ZnO film along [0001] direction as before. The film grown at $3x10^{-1}$ mbar presents only the diffraction maxima corresponding to (0002) ZnO plane. The lower intensity of these diffraction maxima suggested poorer crystalline texture quality.

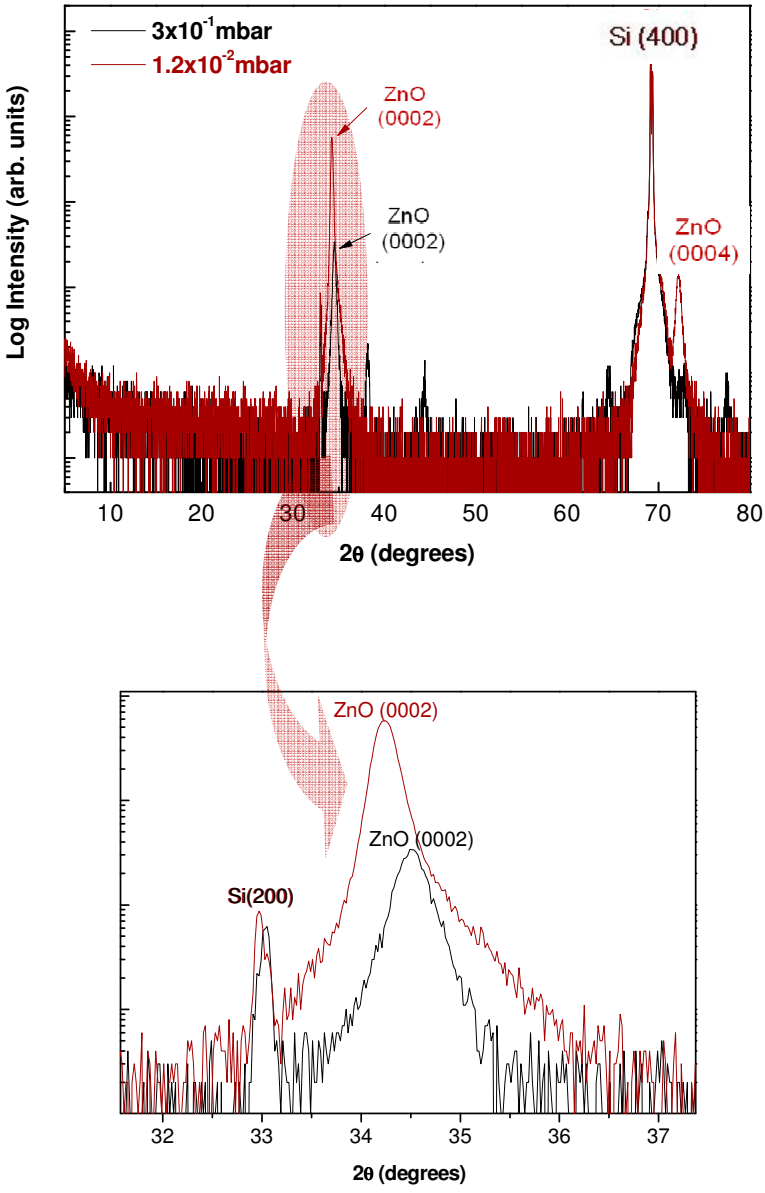

Fig.3.5. XRD 2Θ/ω scans of ZnO films grown at the same temperature (400°C), on the same substrate (Si), but at different oxygen pressures

This was also confirmed by ω-scans (rocking curves) of the diffraction peaks along the (0002) direction. Fig.3.6 shows the rocking-curves corresponding to the (0002)-ZnO reflection for the ZnO films grown at 400°C on Si substrate, but different oxygen pressure. The FWHM of the XRD rocking curve decreases from 8.2 to 2.3° when the deposition pressure decreases, revealing that the crystallite quality increases as the growth pressure decreases.

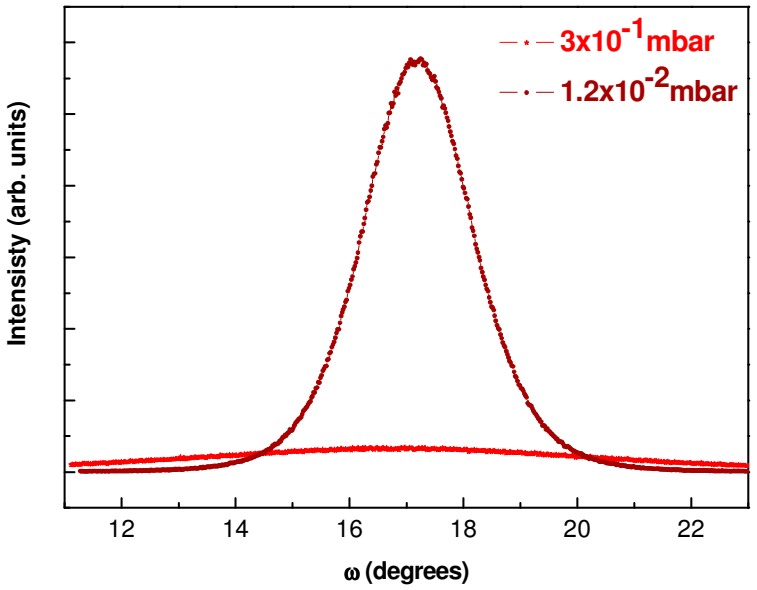

Fig.3.6. Rocking-curves corresponding to the (0002)-ZnO reflection for ZnO films grown at the same temperature (400°C), on the same substrate (Si), but at different oxygen pressures

Measurements of the electrical resistivity and carrier density were performed on these films. The ohmic character of the contacts was always verified previously. As an example of such a measurement Fig.3.7 shows the behavior of the current intensity versus voltage. The reversible lineal behavior confirms the ohmic character of the contacts.

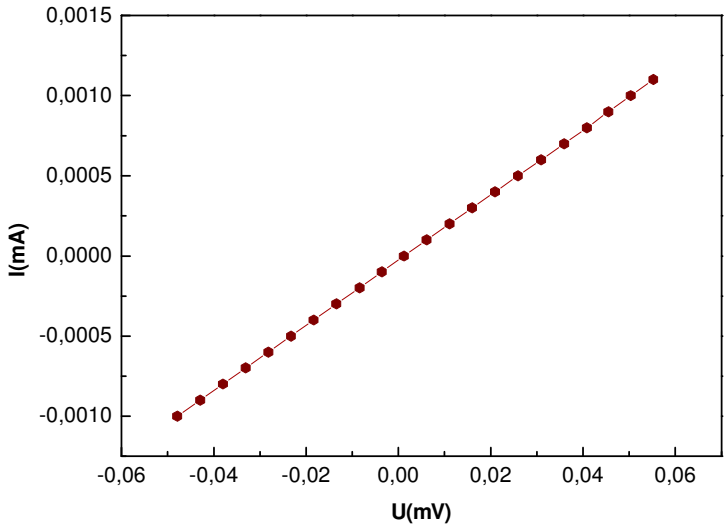

Fig.3.7. Measurements of current intensity versus voltage in order to check the Ohmic character of the contacts

All the films exhibited *n*-type conductivity. Fig.3.8 shows the electrical resistivity of the ZnO films grown at 400°C on Si substrate, but at different oxygen pressure, versus temperature. The values of the electrical resistivity and carrier density at RT are shown in Table 3.II. From these values it can be seen that the film grown at lower oxygen pressure presented lower resistivity and higher carrier density. Therefore, it can be concluded that the films grown at lower oxygen pressure have better crystalline quality and better electrical properties. *Accordingly, 1.2x10^{-2} mbar oxygen is chosen as the optimum film deposition pressure.*

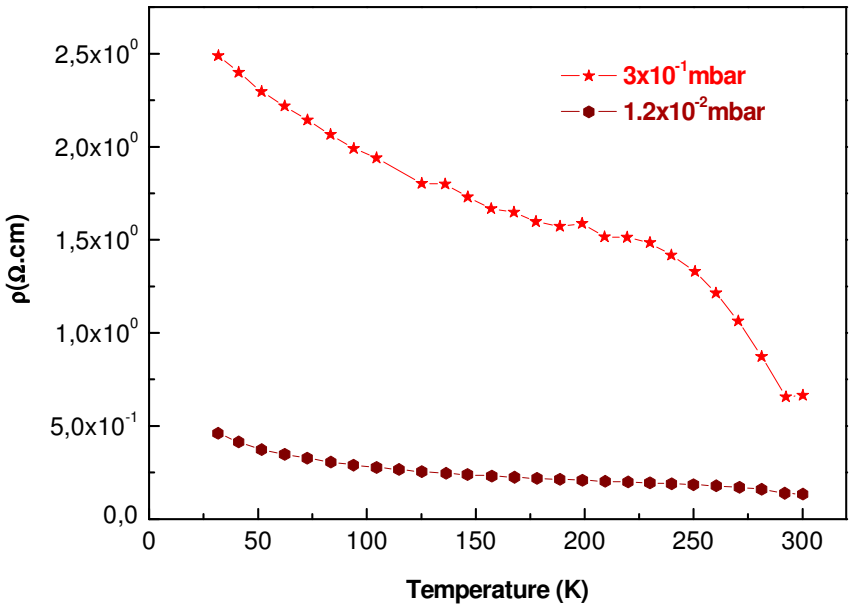

Fig.3.8. Electrical resistivity versus temperature for ZnO films grown at the same temperature (400°C), on the same substrate (Si), but at different oxygen pressures

Table 3.II. Values for the electrical resistivity and carrier density at RT for ZnO films grown at the same temperature (400°C), on the same type of substrate (Si), but at different oxygen pressures

Oxygen pressure (mbar)	Electrical resistvity (Ω.cm)	Carrier density (cm^{-3})
$1.2x10^{-2}$	$1.3x10^{-1}$	$0.7x10^{19}$ *n*-type conductivity
$3x10^{-1}$	$7x10^{-1}$	$1.5x10^{17}$ *n*-type conductivity

3.1.3. Growth temperature

To study the influence of growth temperature, ZnO thin films have been deposited on Si substrate in $1.2x10^{-2}$ mbar oxygen pressure, but at different temperatures (ranging from 400°C to 600°C).

Fig.3.9 shows XRD 2Θ/ω scans. All the diffraction maxima are indexed either with the substrates or with the ZnO lattice. Both films exhibit two ZnO diffraction maxima corresponding to (0002) and (0004) plane. These two diffraction maxima have higher intensity for the film grown at higher temperature (600°C) as expected. The higher intensity of these diffraction maxima suggested a better crystalline quality, as confirmed by ω-scans (rocking curves) of the diffraction peaks along the (0002) direction.

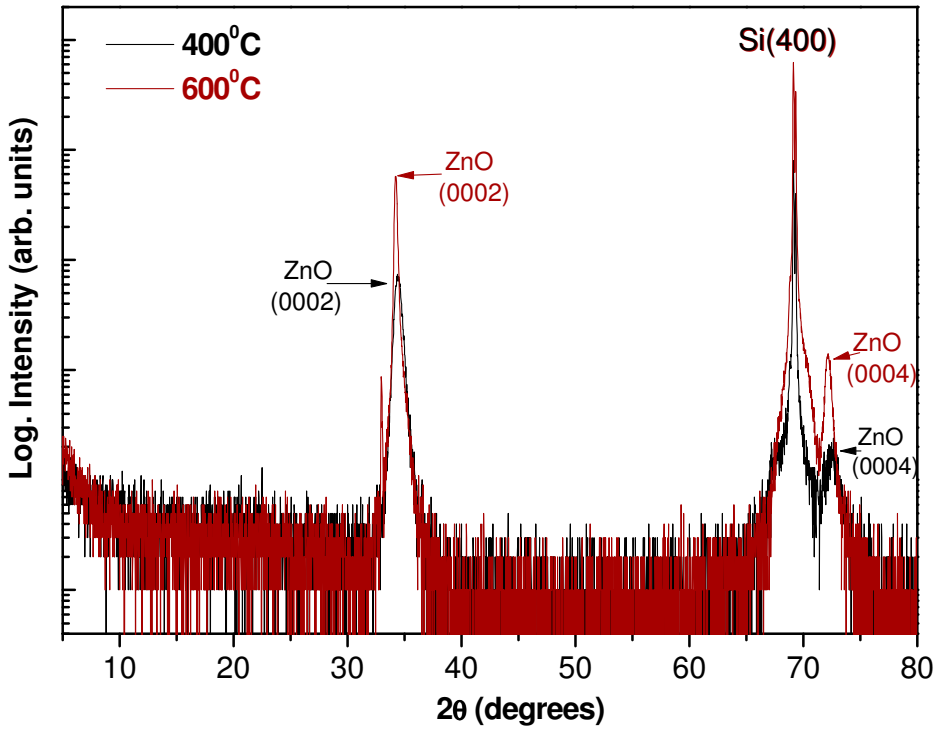

Fig.3.9. XRD 2Θ/ω scans for ZnO films grown on Si substrates, at the same $1.2x10^{-2}$ mbar oxygen pressure, but at different substrate temperatures

Fig.3.10 shows the rocking-curves corresponding to the (0002)-ZnO reflection for the ZnO films grown at $1.2x10^{-2}$ mbar oxygen pressure on Si substrate, but at different substrate temperatures. The FWHM of the XRD rocking curve decreases from 2.99 to 2.30° when the growth temperature increases revealing an increase of the crystalline quality.

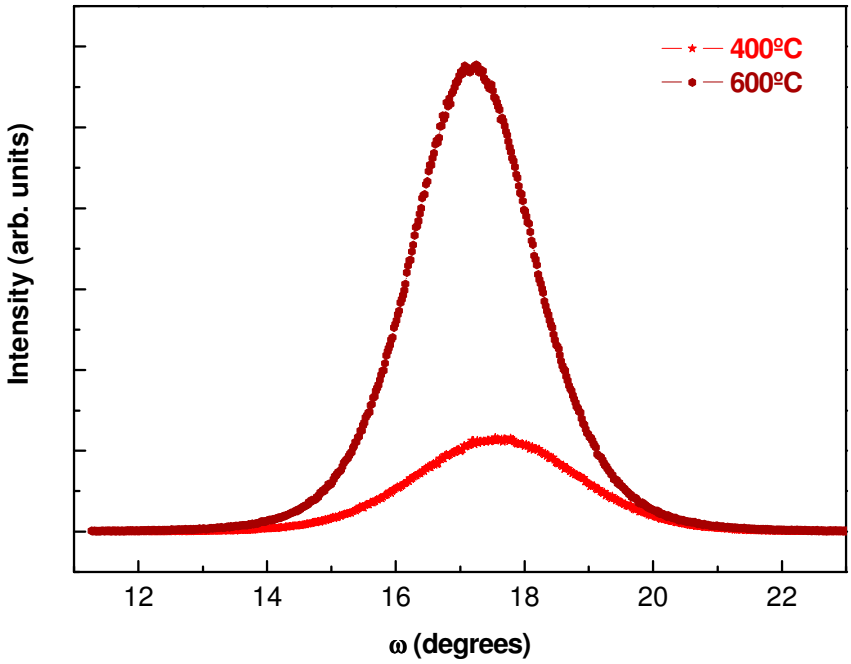

Fig.3.10. Rocking-curves corresponding to the (0002)-ZnO reflection for ZnO films grown at the same $1.2x10^{-2}$ mbar oxygen pressure on Si substrate, but at different temperatures

Measurements of the electrical properties were also performed on these films, revealing the *n*-type conductivity. Fig.3.11 shows the electrical resistivity versus temperature for ZnO films grown on Si substrate at $1.2x10^{-2}$ mbar, at 400 and 600°C. The values of the electrical resistivity and carrier density at RT are shown in Table 3.III. Comparing these values it can be concluded that the film grown at higher temperature has a much lower resistivity and a slightly higher carrier density. This is in agreement with the results obtained from XRD, confirming that the films grown at higher temperature exhibit better crystalline quality and electrical properties.

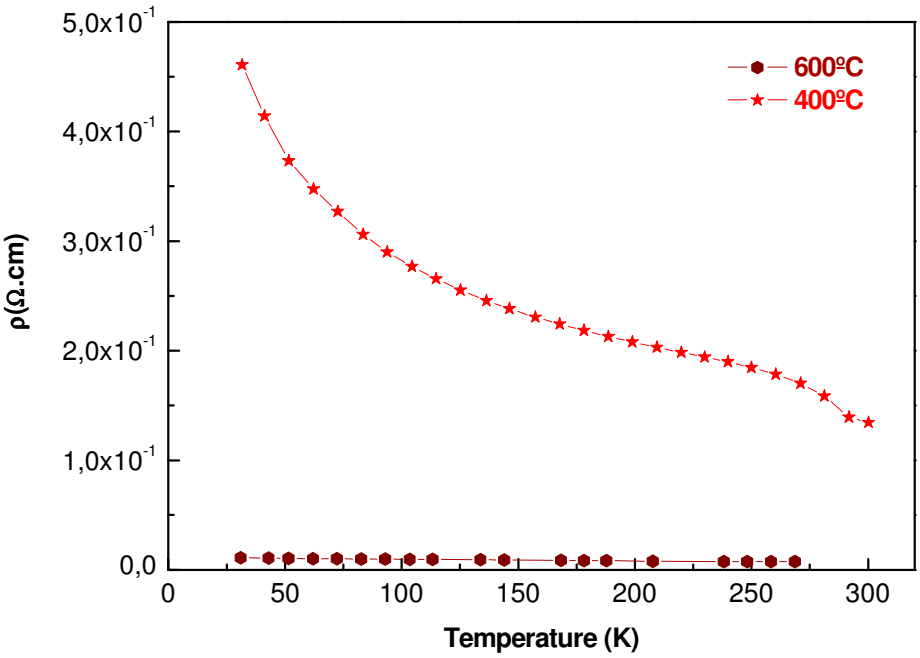

Fig.3.11. Electrical resistivity versus temperature for ZnO films grown on Si substrate at $1.2x10^{-2}$ mbar oxygen pressure

Table 3.III. Values of the electrical resistivity and carrier density at RT for ZnO films grown on Si substrates at $1.2x10^{-2}$ mbar oxygen pressure, at two different substrate temperatures

T_{growth} (°C)	Electrical resistvity (Ω.cm)	Carrier density (cm^{-3})
400	$1.3x10^{-1}$	$0.7x10^{19}$ *n*-type conductivity
600	$7x10^{-3}$	$1.1x10^{19}$ *n*-type conductivity

However, the measurements of the electrical properties revealed that all the films exhibited *n*-type conductivity. No doubt, the major obstacle of using ZnO material in electronic and optoelectronic devices is the difficulty to achieve *p*-type material. The physical properties of

ZnO films are determined by a few parameters, including their stoichiometry. Depending on the oxygen vacancy concentration the conductivity of ZnO thin films will change. At the same time the oxygen vacancies are one of the defects responsible for absorption in the visible region and for optical losses in waveguide design. Therefore, for ZnO thin films required for electrical and optical applications defects like oxygen vacancies should be avoided. There is the hypothesis that the oxygen plasma enhances the oxygen chemical potential, which will lower the formation energy of acceptor defects like Zn vacancies [21], and therefore will justify the *p*-type conductivity. Then, *could it be possible to change the conductivity type of the films by changing the reactivity of oxygen that is in the chamber during the deposition?*

To answer this question, new sets of films have been grown by PLD, with the difference that this time the deposition was assisted by *oxygen plasma*. This makes the oxygen to be more reactive, because instead of O_2 other species like O_2^+, O^-, etc. are present in the chamber.

3.1.4. Oxygen plasma assisted deposition

From the previous experiments it is concluded that the best conditions for the deposition of polycrystalline films are: Si substrates, temperature of 600°C, and an oxygen pressure of 1.2×10^{-2} mbar. Therefore, for the first set of films we intended to use these conditions. However, the minimum pressure necessary to switch on the oxygen plasma in our system was 5×10^{-2} mbar and thus film growth was performed at this pressure.

Table 3.IV shows the values of the electrical resistivity, carrier density and mobility at RT for two ZnO films grown on Si substrates at 600°C, in 5×10^{-2} mbar oxygen pressure assisted by oxygen plasma. As it can be observed, at this pressure the films exhibited a difference

of one order magnitude of the carrier density. As seen below, this is probably due to film growth at the minimum pressure necessary to activate the oxygen plasma.

Table 3.IV. Values of the electrical resistivity, carrier density and mobility at RT for ZnO films grown on Si substrates at 600°C, in $5x10^{-2}$ mbar oxygen pressure assisted by oxygen plasma

Oxygen pressure (mbar)	Electrical resistivity (Ωcm)	Carrier density (cm^{-3})	Mobility ($cm^{2} V^{-1} s^{-1}$)	Thickness (nm)	Conductivity
$5x10^{-2}$	3	$2x10^{16}$	~15	100	*n*-type
$5x10^{-2}$	4	$3x10^{15}$	~3	80	*n*-type

In order to try to improve the reproducibility, the oxygen pressure of the chamber was increased. The values of the electrical resistivity, carrier density and mobility at RT for ZnO films grown on Si substrates at 600°C, in $1x10^{-1}$ mbar oxygen pressure assisted by oxygen plasma are shown in Table 3.V. As indicated by these values, the films obtained at these growth conditions are much more reproducible. Moreover, the electrical properties of these films are improved: they exhibited lower resistivity, higher carrier density and higher mobility than the films grown at $5x10^{-2}$ mbar oxygen.

Table 3.V. Values of the electrical resistivity, carrier density and mobility at RT for ZnO films grown on Si substrates at 600°C, and $1x10^{-1}$ mbar oxygen pressure assisted by oxygen plasma

Oxygen pressure (mbar)	Electrical resistivity (Ωcm)	Carrier density (cm^{-3})	Mobility ($cm^{2} V^{-1} s^{-1}$)	Thickness (nm)	Conductivity
$1x10^{-1}$	$2x10^{-2}$	$3x10^{19}$	~10	90	*n*-type
$1x10^{-1}$	$1.7x10^{-2}$	$2x10^{19}$	~24	90	*n*-type

Due to the improvement of the electrical properties of the films when the oxygen pressure in the chamber was increased, the oxygen pressure was increased further. The values of the electrical properties of ZnO films grown on Si substrates at 600°C, in $5x10^{-1}$ mbar oxygen pressure assisted by oxygen plasma are given in Table 3.VI. It is found that at this pressure the film transport properties are not reproducible at all. However, it is interesting to note that one of the films presented *p*-type conductivity. To test the reproducibility of this result, another four films were deposited at the same growth conditions. However, none of them exhibited *p*-type behavior. For that reason it was concluded that all the films grown by oxygen plasma assisted PLD presented *n*-type behavior. Maybe the *p*-type conductivity identified in the one film was caused by unintentional doping or contamination during the deposition, which was not reproduced in the next four films deposited. This irreproducible observation of *p*-type behavior is in agreement with the difficulty to stabilize a reliable *p*-type ZnO.

Table 3.VI. Values of the electrical properties for ZnO films grown on Si substrates at 600°C, in $5x10^{-1}$ mbar oxygen pressure assisted by oxygen plasma

Oxygen pressure (mbar)	Electrical resistivity (Ωcm)	Carrier density (cm^{-3})	Mobility ($cm^{2} V^{-1} s^{-1}$)	Thickness (nm)	Conductivity
$5x10^{-1}$	4	$7x10^{16}$	~10	150	*p*-type
$5x10^{-1}$	1.7	$3x10^{17}$	~10	120	*n*-type

According with these experiments the reactivity of oxygen does not affect the conductivity type at the different conditions used. However, when comparing the electrical properties of the films grown with and without oxygen plasma, we obtain that the films grown without oxygen plasma present slightly better properties (lower electrical resistivity). Therefore we concluded that PLD oxygen plasma assisted

technique did not present any advantages versus the conventional deposition technique.

Conclusions:

- ✓ Pellets of ZnO sintered at 1300°C exhibit the best quality for being used as target in a PLD chamber.
- ✓ Good ZnO polycrystalline films are obtained using Si as a substrate.
- ✓ The electrical resistivity increases when a) increasing the oxygen pressure during growth (optimal for 1.2×10^{-2} mbar), and b) decreasing growth temperature.
- ✓ All polycrystalline ZnO films present *n*-type conductivity.
- ✓ The crystal quality increases when the growth temperature increases and when the deposition pressure decreases.
- ✓ Oxygen plasma assisted PLD does not present any advantage vs. conventional PLD for ZnO: the films obtained by this method present lower quality (larger values for the electrical resistivity and a poorer crystal quality) and poorer reproducibility.

It seems that there is still much to be understood regarding electrical transport properties of ZnO and their relationship with structural defects. To develop future applications for electronic and optoelectronic devices, high-quality epitaxial thin films with minimal concentrations of native defects and controlled impurity incorporation are required. This study is followed up in the next section.

3.2. Epitaxial ZnO thin films on sapphire substrate

In order to achieve high quality ZnO epitaxial layers, sapphire substrate is a very good choice due to its hexagonal symmetry and commercial availability [23]. The crystal structure of ZnO and sapphire in different orientations are shown in Fig.3.12 and Fig.3.13 respectively. The lattice constants of these two materials are a=b=3.253Å, c=5.213Å for the wurtzite structure of the ZnO (JCPDS 76-0704) and a=b=4.7592Å, c=12.992Å for the corundum/ rhombohedral structure of the sapphire (JCPDS 43-1484). Even though between their basal hexagonal planes there is a large mismatch (18% or 32%, depending on crystallographic orientation relationships: $[10\underline{1}0]_{ZnO}||[11\underline{2}0]_{sapphire}$ and $[11\underline{2}0]_{ZnO}||[11\underline{2}0]_{sapphire}$ respectively[2]), good crystalline quality ZnO thin films can be obtained [5-6, 24-25].

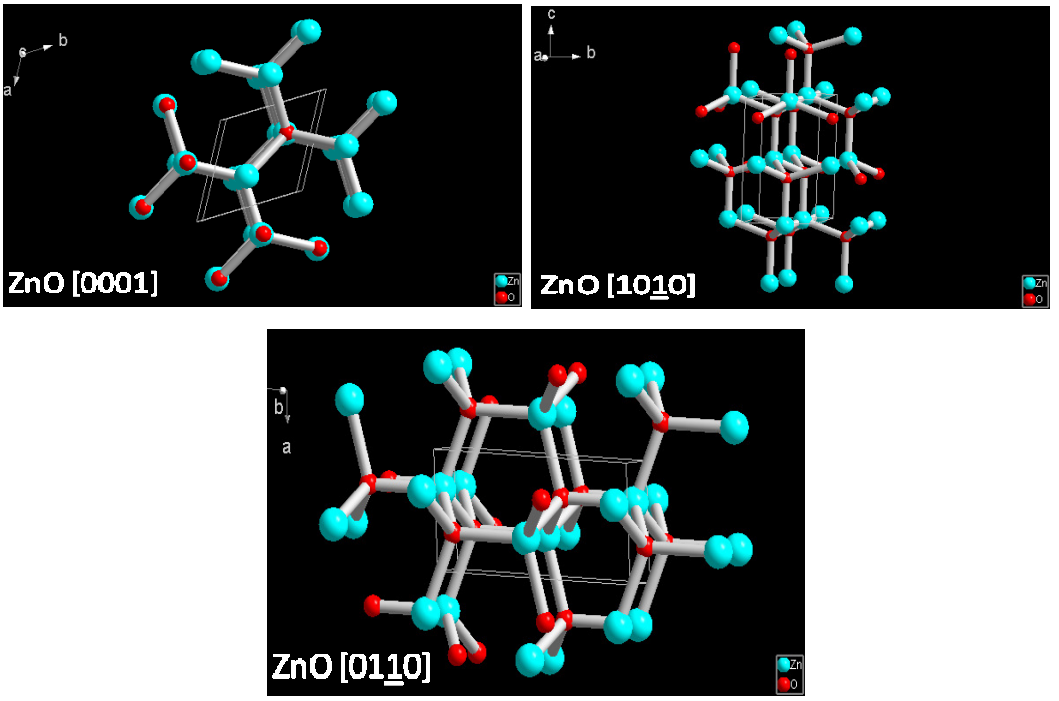

Fig.3.12. Different views of the crystal structure of ZnO

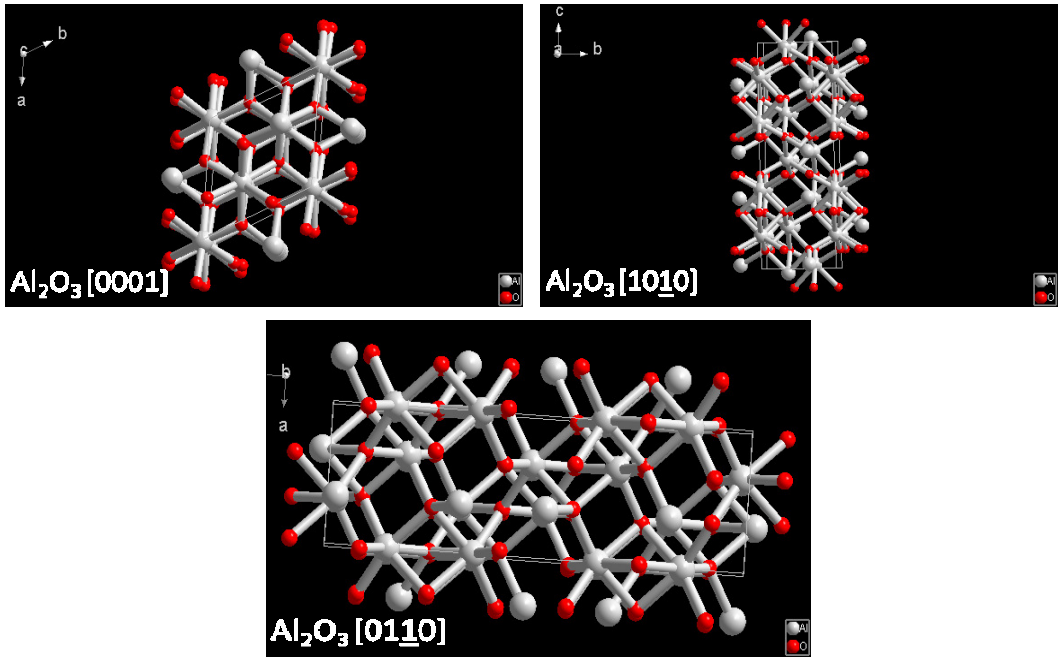

Fig.3.13. Different views of the crystal structure of sapphire (Al_2O_3).

Various sets of ZnO films have been grown by PLD at different temperatures. The ZnO targets were the same that the ones used for polycrystalline growth: ZnO target made from 99.9% purity ZnO powder sintered at 1300°C for 8 hours with >98% of the theoretical density. As substrate we use the *(0001) sapphire*. The deposition pressure in the chamber was *1.2 x10^{-2} mbar oxygen pressure*. The growth temperature was ranging from *200°C to 600°C*.

3.2.1. Structural characterization

3.2.1.1. Profilometer

The film thickness was measured by means of a Sentech FTP advanced profilometer, see experimental section. The film´s thickness varies from 300nm for the film grown at 200°C to 80nm for the film grown at 600°C.

3.2.1.2. X-ray diffraction

Fig.3.14 shows XRD 2Θ/ω scans for the ZnO films grown on (0001) sapphire substrates at the same oxygen pressure (Po_2=1.2 x10^{-2} mbar) and at temperatures from 200 to 600°C. All the diffraction maxima can be indexed either with the Al_2O_3 substrate or with the hexagonal wurtzite ZnO lattice (JCPDS 76-0704). The two ZnO diffraction maxima observed correspond to (0002) and (0004), which implies *c*-axis growth perpendicular to the substrate plane. In other words, all the ZnO films were oriented along the [0001] direction. The diffraction maxima positions and the calculated cell parameters are shown in Table 3.VII.

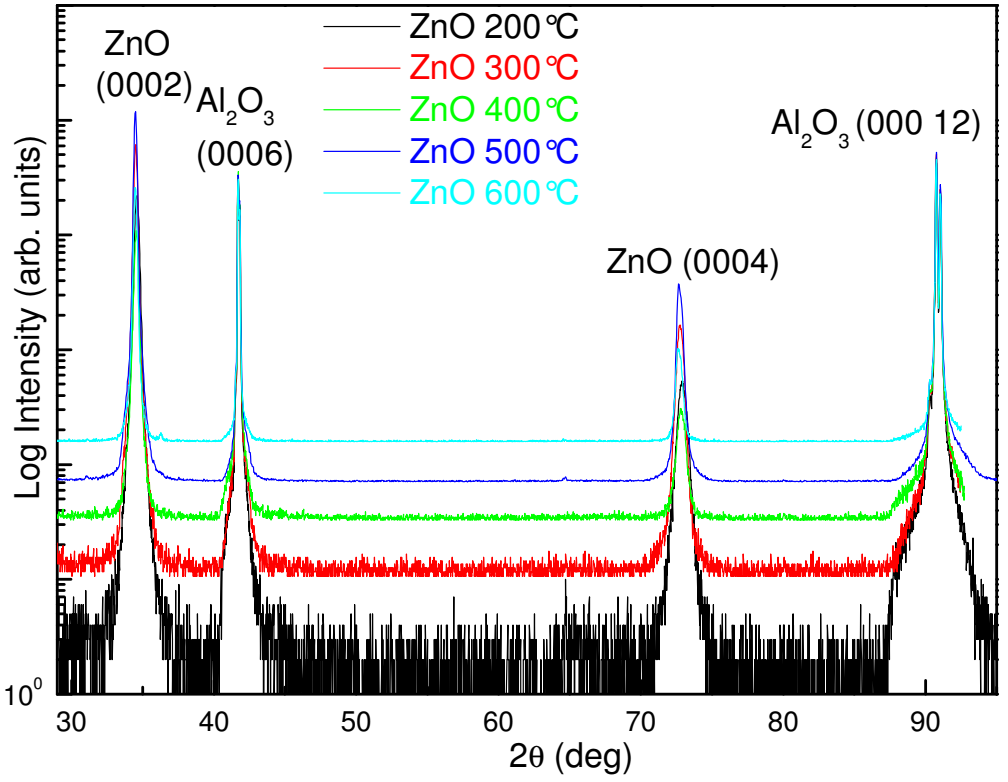

Fig.3.14. XRD 2Θ/ω scans for ZnO films grown on (0001) sapphire substrates under the same oxygen pressure (Po_2=1.2 x10^{-2} mbar), but at different growth temperatures: ranging from 200-600°C

Table 3.VII. Cell parameters, intensity relation between the (0004) and the (0002) peaks, FWHM values of the XRD rocking curves corresponding to the (0002)-ZnO reflection and the (10$\underline{1}$3)-in-plane Φ scan of the ZnO films, and percentage of domains aligned with the substrate

T_{growth} (°C)	2Θ	Lattice parameter c	0004/0002	FWHM ZnO(0002)	FWHM Phi	% domains aligned
200	34.56	5.190	$2.36\ 10^{-2}$	2.87	9.97	0
300	34.48	5.202	$2.55\ 10^{-2}$	1.65	7.83	60
400	34.52	5.195	$2.72\ 10^{-2}$	1.48	7.53	90
500	34.46	5.205	$3.12\ 10^{-2}$	1.46	3.43	100
600	34.45	5.206	$3.91\ 10^{-2}$	0.95	2.32	100

The crystal quality of the films was confirmed by ω-scans (rocking curves) of the diffraction peaks along the (0002) and (0004) directions. Fig.3.15 shows the rocking-curves corresponding to the (0002)-ZnO reflection. The FWHM value of the XRD rocking curve decreases from 2.87 to 0.95° when deposition temperature is raised from 200 to 600°C, revealing the crystallite size increases while increasing the growth temperature. The intensity ratio between the (0004) and the (0002) peaks are used as a measure of the degree of ordering along the (0001) direction. It can be observed that by increasing the growth temperature the intensity relationship increases from $2.36x10^{-2}$ at 200°C to $3.91x10^{-2}$ at 600°C. This last value is very close to the theoretical value of $3.85x10^{-2}$. So, the larger the temperature, the Zn and O atoms are more ordered along the 0001 direction (see Table 3.VII). These results are in agreement with Dutta *et al.* who demonstrated that the disorder parameter decreases when increasing ZnO grain size [26].

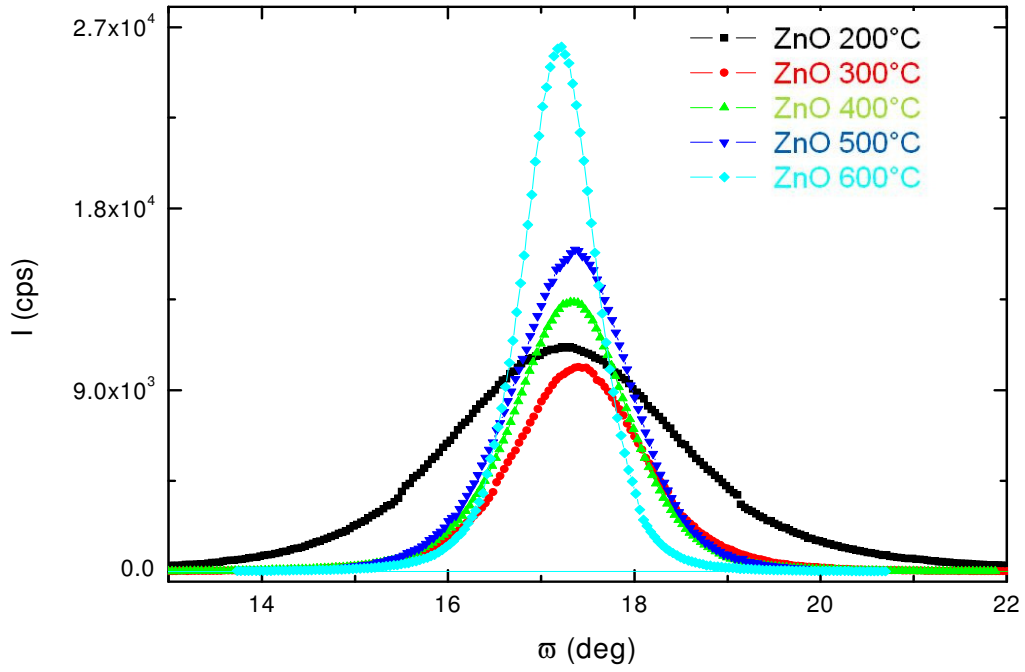

Fig.3.15. Rocking-curves corresponding to the (0002)-ZnO reflection for ZnO films grown on (0001) sapphire substrates under the same oxygen pressure (Po_2=1.2 x10^{-2} mbar), but different temperatures

Asymmetrical XRD measurements were performed in order to determine the epitaxial relationship between ZnO films and the sapphire substrates. Fig.3.16 displays the in-plane Φ scans for the (10$\underline{1}$3) plane of the ZnO films and for the (11$\underline{2}$3) plane of the sapphire substrate. All the films, including the one deposited at 200°C, exhibit an epitaxial relationship. As far as we know, this is the lowest temperature achieved for epitaxial growth of ZnO thin films compared to the 300°C reported in literature [6]. The diffraction maxima are separated 60°, which indicates six-fold symmetry.

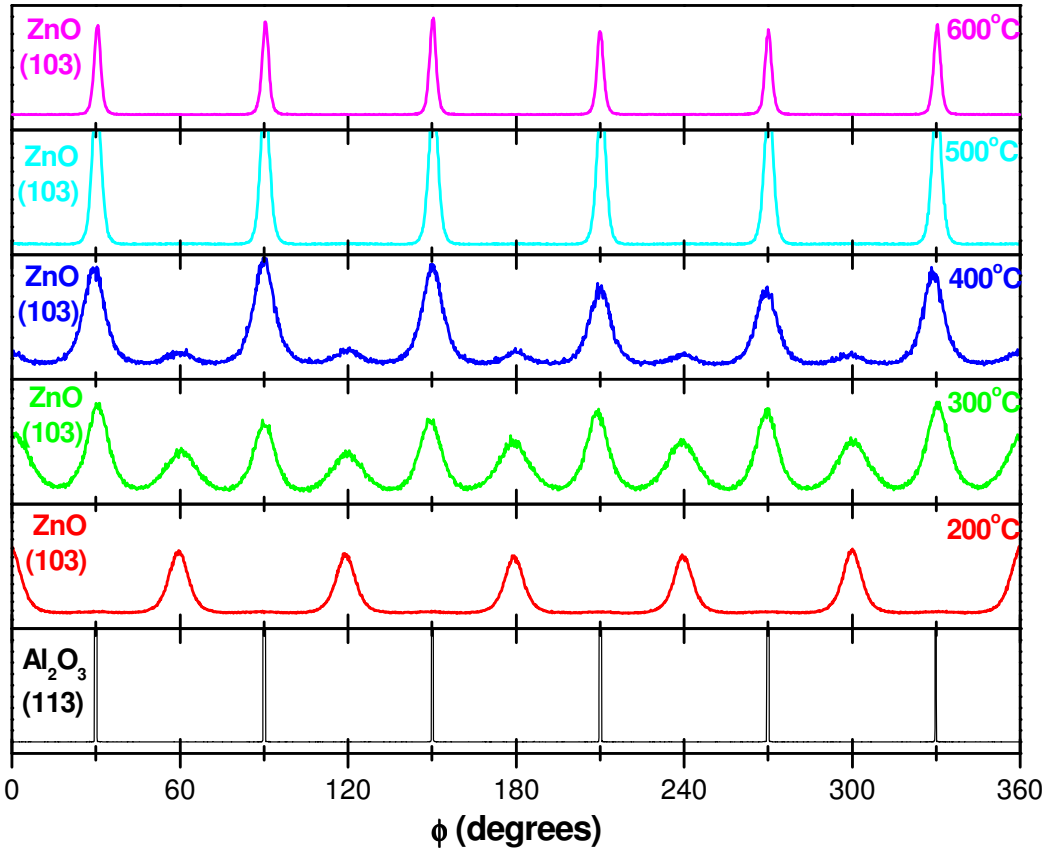

Fig.3.16. In-plane Φ scans for the (10$\underline{1}$3) plane of the ZnO films and for the (11$\underline{2}$3) plane of the sapphire substrate for ZnO films grown on (0001) sapphire substrates under the same oxygen pressure (Po_2=1.2 x10^{-2} mbar), but at different growth temperatures.

For the film grown at low temperature (200°C) the ZnO unit cell is rotated 30° with respect to the substrate, which establishes the epitaxial relationship $[11\underline{2}0]_{ZnO}||[11\underline{2}0]_{sapphire}$ for the in-plane orientation, as shown in Fig.3.17.

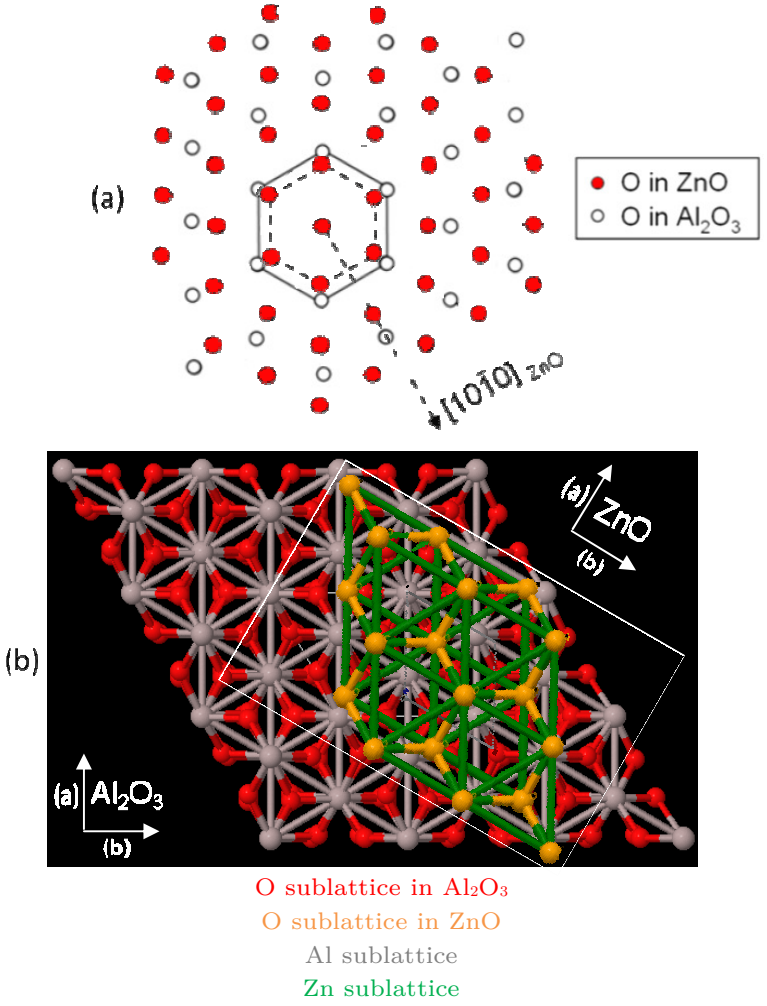

Fig.3.17. Schematic view of the ZnO unit cell rotation 30° with respect to the substrate according to the epitaxial relationship $[11\underline{2}0]_{ZnO}||[11\underline{2}0]_{sapphire}$ for the in-plane orientation. a) Scheme of the relative oxygen positions b) Top view of the epitaxial structure

For the films grown at temperatures of 300°C and 400°C 12 peaks are observed (see Fig.3.16), which indicate the coexistence of a combined structure composed of two in-plane domains: a main domain aligned with the sapphire substrate (as shown in Fig.3.18), and a "twin" domain [27, 28], which was rotated 30° with respect to the main one (as shown in Fig.3.17). The low intensity of the peaks of the twin domain suggests poor in-plane orientation.

As the growth temperature increases the twin peaks intensities decrease, and disappear for the films grown at temperature ≥500°C, which presents just a single domain aligned with the substrate according to the epitaxial relationship $[10\underline{1}0]_{ZnO}||[11\underline{2}0]_{sapphire}$ as shown in Fig.3.18. So it can be concluded that at lower temperature the more stable epitaxial relationship is $[11\underline{2}0]_{ZnO}||[11\underline{2}0]_{sapphire}$ (32% mismatch); while at higher temperatures the more stable one is $[10\underline{1}0]_{ZnO}||[11\underline{2}0]_{sapphire}$ (18% of mismatch).

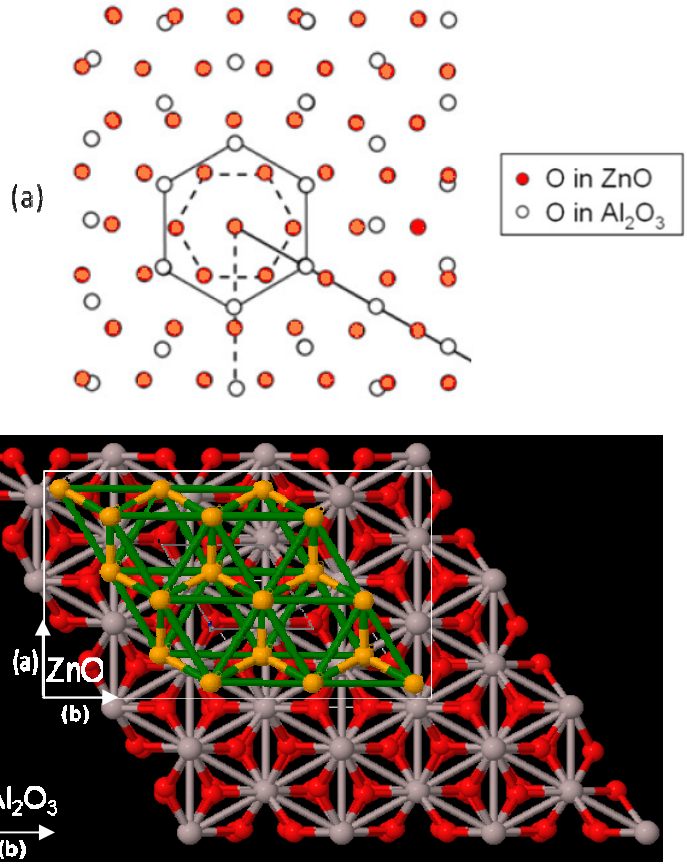

Fig.3.18. Schematic of the aligning of the ZnO unit cell with respect to the substrate according to the in-plane epitaxial relationship $[10\underline{1}0]_{ZnO}||[11\underline{2}0]_{sapphire}$. a) Scheme of the relative oxygen positions b) Top view of the epitaxial structure

From the analysis of the diffraction patterns the *c*-lattice parameters and the FWHM of the Φ scan were also obtained (see Table 3.VII). It can be deduced that when the growth temperature increased, the lattice presents less tensile stress. The FWHM of the Φ scan confirmed the improvement of the epitaxy as the deposition temperature increased (as the twinning decreased, the in-plane grain size increased).

3.2.1.3. Rutherford backscattering spectrometry

In order to accurately determine the elemental area density for the ZnO films deposited on Al_2O_3 substrates, Non-RBS measurements were performed in random configuration with a He^+ beam at the oxygen resonance energy (3.0 MeV) [29].

RBS angular scan curves were measured along <0001> crystal axis for a ZnO film grown at 300°C and a ZnO film grown at 600°C.

The elemental area density of the films was determined from Non-RBS data by comparing measured and simulated spectra. The simulations were made using the commercial computer program SIMNRA [30]. Non-RBS spectra measured in random configuration indicated that the layers consist of a ZnO thin film deposited on Al_2O_3 substrate. No impurity traces were observed.

Fig.3.19 and Fig.3.20 show the measured spectra for ZnO films grown at 300°C and 600°C respectively, and the corresponding simulated spectra.

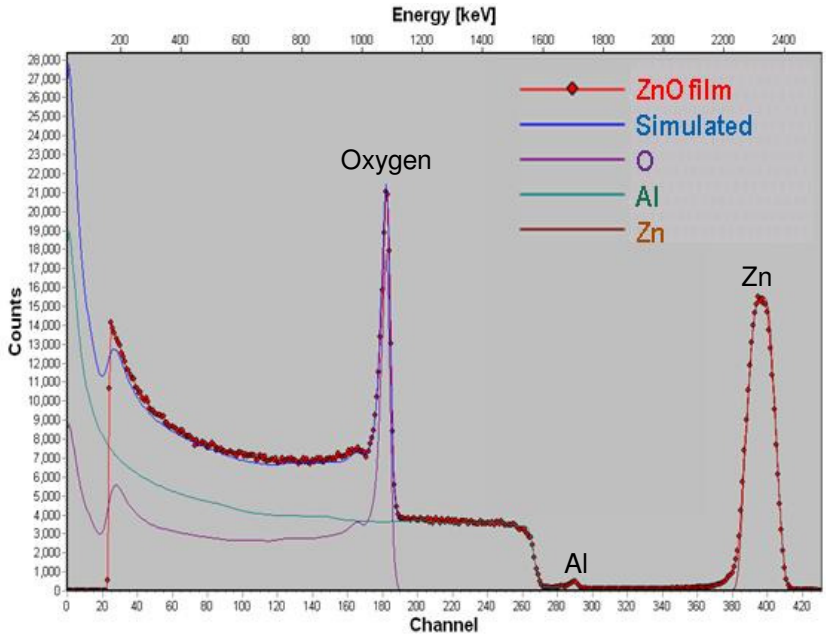

Fig.3.19. Non-RBS measured spectra in random configuration with a He^+ beam at 3.0 MeV, for ZnO films grown on Al_2O_3 substrate at 300°C, and the corresponding simulated spectra

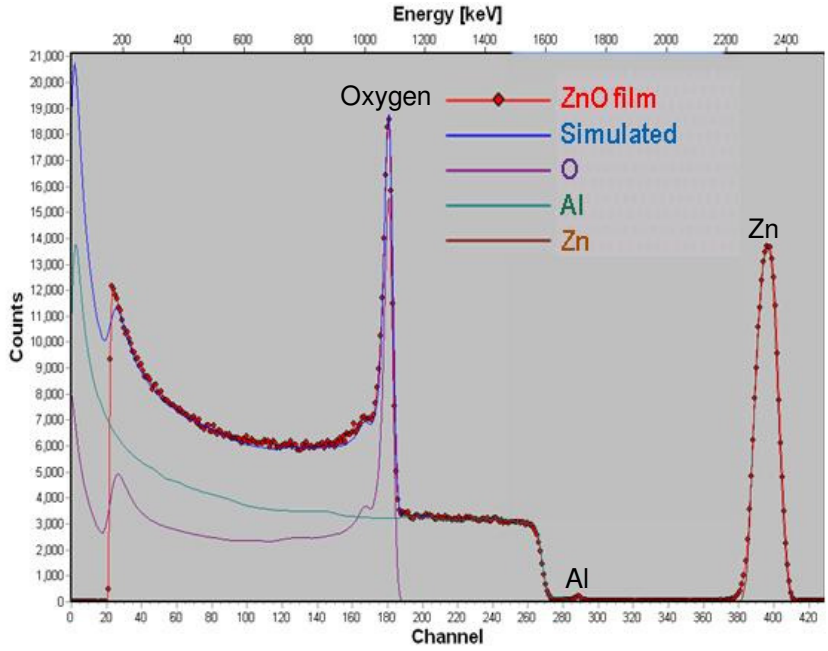

Fig.3.20. Non-RBS measured spectra in random configuration with a He^+ beam at 3.0 MeV, for ZnO films grown on Al_2O_3 substrate at 600°C, and the corresponding simulated spectra

The broad peak located in the channels 273-294 correspond to Al at the surface. If some of the Al would have been diffused into the ZnO films, Al should appear, in principle, distribute along the whole ZnO film, which is not the case. So we had interpreted the appearance of this peak as the fact that the films are not totally homogeneous and some pitting could exist, as shown in Fig.3.21. The atomic percentage of Al has been estimated to be around 3%, therefore those pits cannot be bigger than the 3% of the total ZnO film surface.

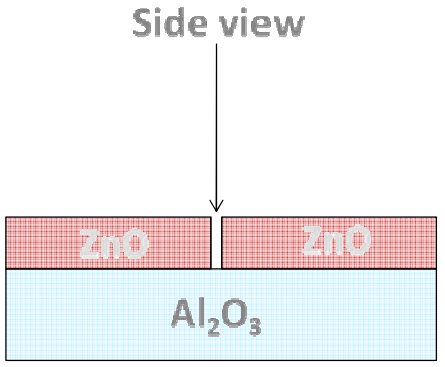

Fig.3.21. Schematic of a pore in the ZnO films surface, through which the Al_2O_3 substrate can be seen

The observed pitting might be related to the PLD technique. When the target material is ablated, different kind of particulates like powder particles, droplets or flakes are also generated. These particulates are carried on by the ablation plume, and their impact on the growing film causes holes on film´s surface [31]. Taking into account that in the conventional PLD set-up the substrate is exposed directly to the plasma, this became a major shortcoming of the PLD technique.

By comparing the measured and the simulated spectra for each film and making the calculations, we can conclude that: the films are stoichiometric; the atomic percentage ratio (Zn/O) is ≈1 for all the temperature range within the resolution limit (0.9%) of the experimental technique.

Additional non-RBS measurements in channeling configuration were performed in order to study separately the lattice order degree of both sublattices (oxygen and Zn), and also to compare them with the sublattices of Al and oxygen from the substrate. These measurements were made along the <0001> axis of ZnO and Al_2O_3 (see Fig.3.22), with a 3MeV He^+ beam.

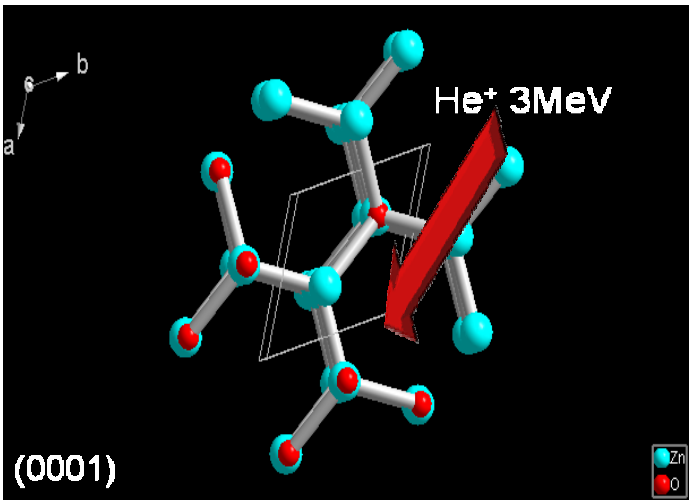

Fig.3.22. Schematic of the orientation of the beam in non-RBS channeling measurements along the <0001> axis

The minimum yield (χ_{min}) is a good indicator of the lattice disorder, being the ratio between the yield measured in channeling and random configuration. As expected from XRD measurements a different behavior is observed for films deposited at 300°C and at 600°C.

Firstly, the Non-RBS spectra measured in random (black line) and in channeling (red line) configuration are shown in Fig.3.23. The reduction observed in the aligned spectrum of the backscattered yield indicates a good crystal quality of the ZnO film.

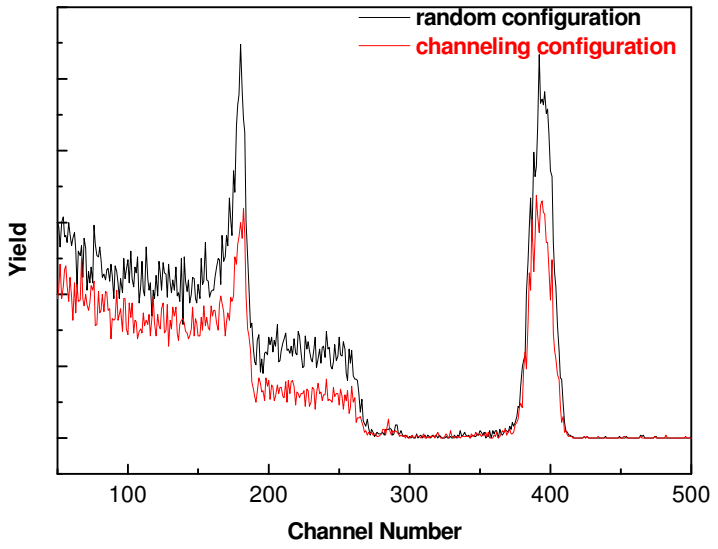

Fig.3.23. Non-RBS spectra measured in random and in channeling configuration for ZnO thin film grown on sapphire at 300°C

The angular scan curves for Al, O_{subs}, Zn and O_{film} sublattices of the ZnO film grown at 300°C are shown in Fig.3.24. The χ_{min} value obtained for the Zn sublattice and for the O sublattice in the ZnO film is the same and equal to 0.70. This indicates that both sublattices of Zn and of O present the same disorder degree. The 0.70 value is significantly higher than the one expected for a typical commercial monocrystal, which is χ_{min} = 0.02-0.03 [29]. However, the fact that channeling measurements could be performed indicates that the film has a good crystalline quality even for the films grown at relatively low temperatures (300°C), although they are not strictly single crystal. Comparing our data with data reported in the literature, we can see that χ_{min}=0.7 has been obtained for ZnO films grown at 600°C, when for ZnO films grown at lower temperatures like 400°C no channeling was detected [5].

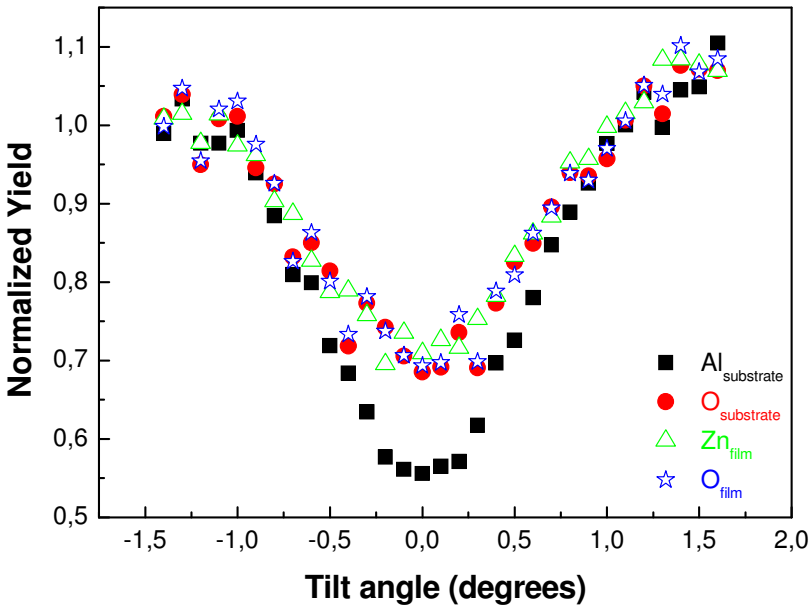

Fig.3.24. Angular scan curves for Al, O_{subs}, Zn and O_{film} sublattices measured by non-RBS in channeling configuration for ZnO film grown on sapphire at 300°C

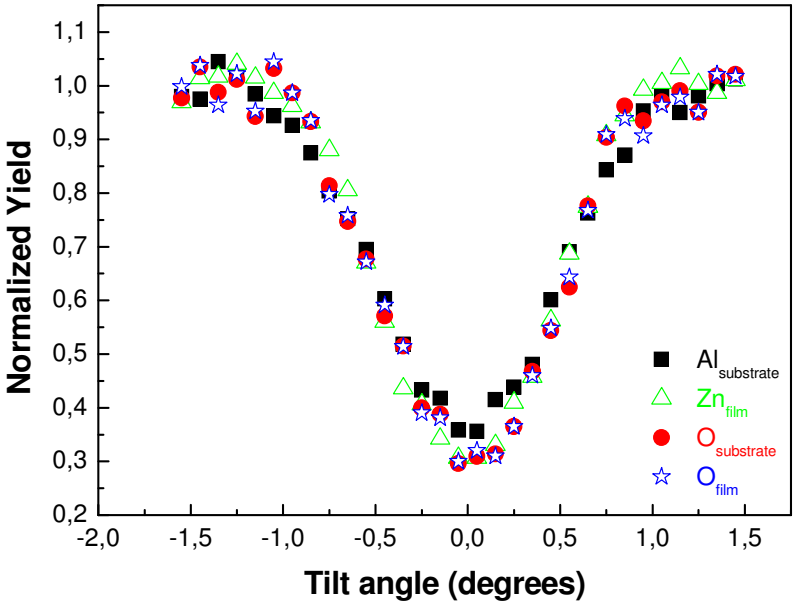

Fig.3.25. Angular scan curves for Al, O_{subs}, Zn and O_{film} sublattices measured by non-RBS in channeling configuration for ZnO film grown on sapphire at 600°C

In Fig.3.25, the angular scan curves for Al, O_{subs}, Zn and O_{film} sublattices of the ZnO film grown at 600°C are shown. The χ_{min} value obtained for the Zn sublattice and the O sublattice in the ZnO film is the same and equal to $\chi_{min} = 0.30$. This indicates a similar lattice order degree for the sublattice of O and for the sublattice of Zn. As expected the χ_{min} value is much lower than that for films deposited at 300°C. These results show that the χ_{min} value decreases when increasing growth temperature, which implies that the lattice order degree of both sublattices increases.

Comparing these results, we can conclude that the films presents a stoichiometry 1:1 (Zn:O). The Zn and the O_{film} sublattices presented the same sublattice order degree, for both films grown either at 300°C or at 600°C. Raising the deposition temperature results on an increase of the lattice order; getting closer to the behavior of a single crystal ZnO.

3.2.1.4. Particle induced x-ray emission

By RBS measurements only elements with a concentration >1% could be detected. PIXE is a very powerful tool for the microdetection of elements, having the ability to measure several ppm order of concentration. Therefore, it was interesting to perform PIXE measurements for our films, in order to detect with more precision the presence of any possible elements which could exist in a concentration <1%.

Additional PIXE measurements were carried out in channeling configuration along the <0001> crystal axis using a He^{++} beam at energy of 6 MeV. Fig.3.26 shows the corresponding spectra for ZnO film grown at 300°C and 600°C, respectively. No other element has been identified, confirming thus that the layers consisted only in ZnO on top of sapphire substrate without extrinsic contamination.

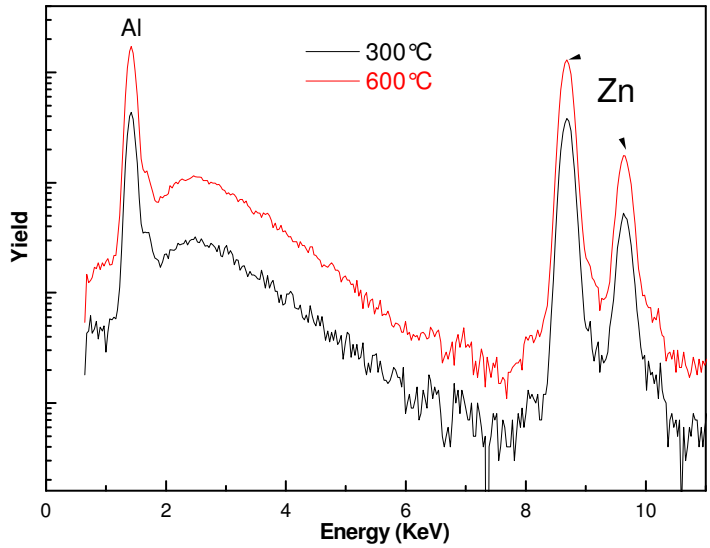

Fig.3.26. PIXE spectra corresponding to ZnO films grown at 300°C and 600°C

3.2.2. Morphology characterization: Atomic Force Microscopy

The film surface morphology was studied using Atomic Force Microscopy.

Fig.3.27 shows AFM images of ZnO films deposited by PLD, grown at different temperatures: (a) 300°C, (b) 500°C and (c) 600°C. Surface morphology varies greatly for the films grown at these temperatures. The film grown at 300°C shows an average roughness of 11.4nm and a typical grain size of about 50 nm. The thin film grown at 600°C possesses an average roughness of 4.1 nm and the biggest grain size of about 500 nm. From these images it can be concluded that the influence of growth temperature on film morphology was that crystal size increased and the films became smoother as the growth temperature increased. Nevertheless, all the films present the pores that had been detected by non-RBS measurements, no matter at what temperature the films had been deposited.

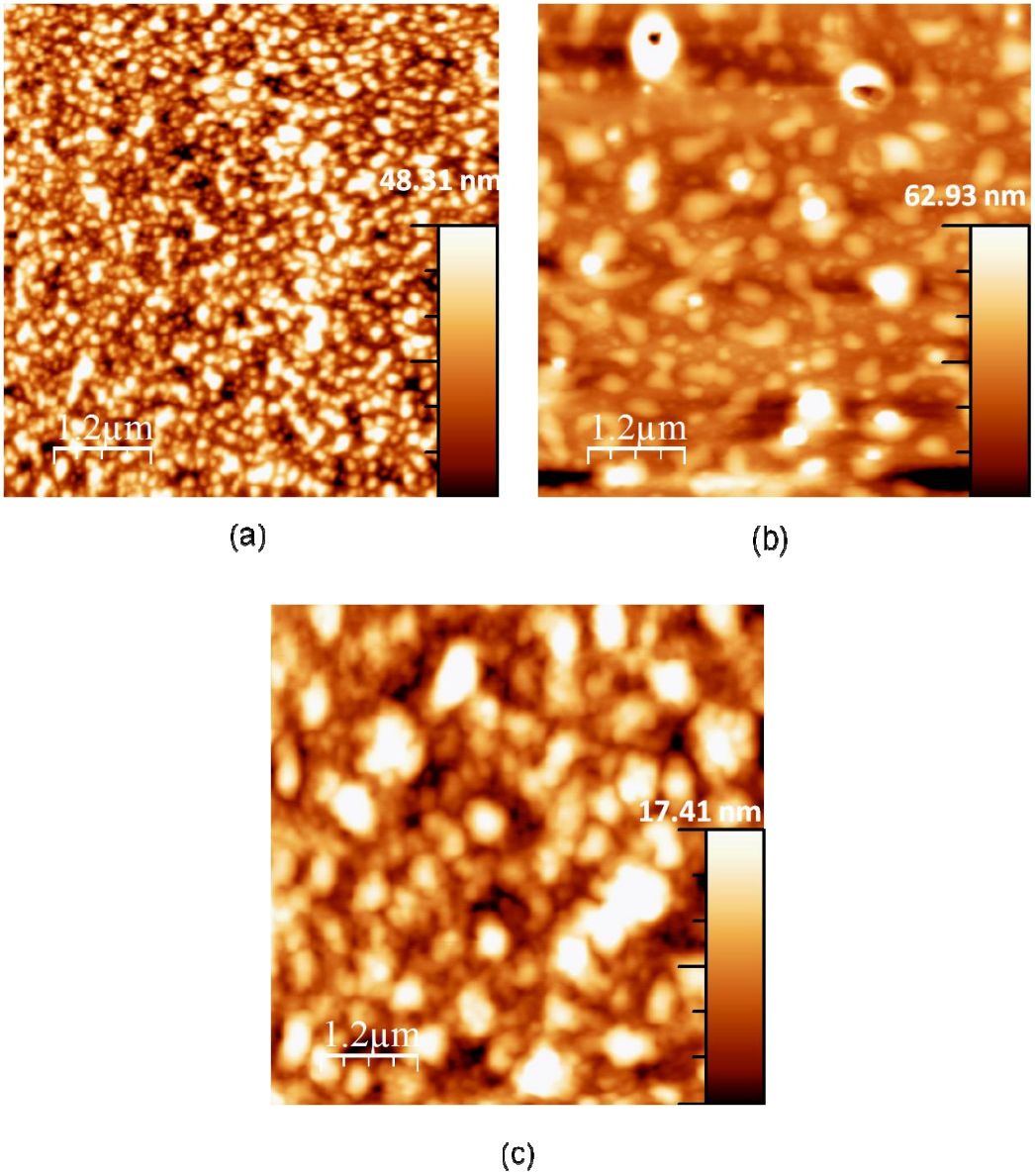

Fig.3.27. AFM images of ZnO films deposited by PLD on sapphire substrate, grown at different temperatures: (a) 300°C, (b) 500°C and (c) 600°C

3.2.3. Electrical properties: Hall effect measurements

The electrical properties (resistivity, carrier density and mobility) of the films were determined by Hall effect measurements using Van der Pauw configuration for ZnO films grown at temperature ranging from 200°C to 600°C. The fact that the sapphire substrate is an insulator guarantees that the obtained measurements came from the ZnO thin films.

Fig.3.28 (a-c) shows the behavior of the electrical properties versus temperature in the range 30-300 K for a film grown at 200°C. The ZnO film grown at 200°C shows low resistivity (5.8×10^{-3} Ωcm at RT and 7.6×10^{-3} Ωcm at 33 K). In the saturation region, between 80 and 180 K, the mobility starts to decrease towards a larger carrier density. After this point, the decreasing mobility with increasing carrier density can be understood by an increasing number of electrically active grain boundaries [32]. The carrier density at RT is found to be 6×10^{19} cm^{-3}. The mobility decreases from 42 cm^2 $V^{-1}s^{-1}$ at 33 K to 13 $cm^2V^{-1}s^{-1}$ at RT.

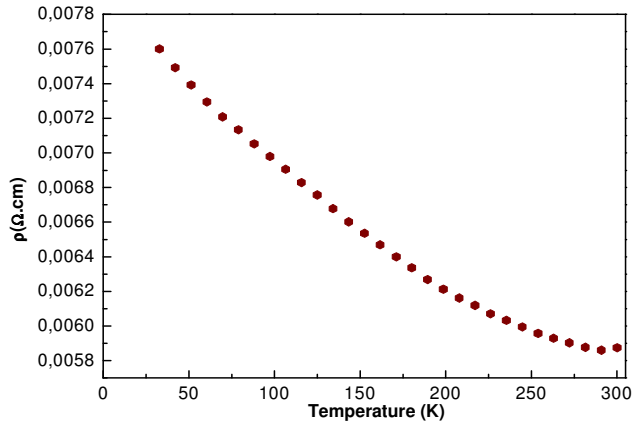

(a)

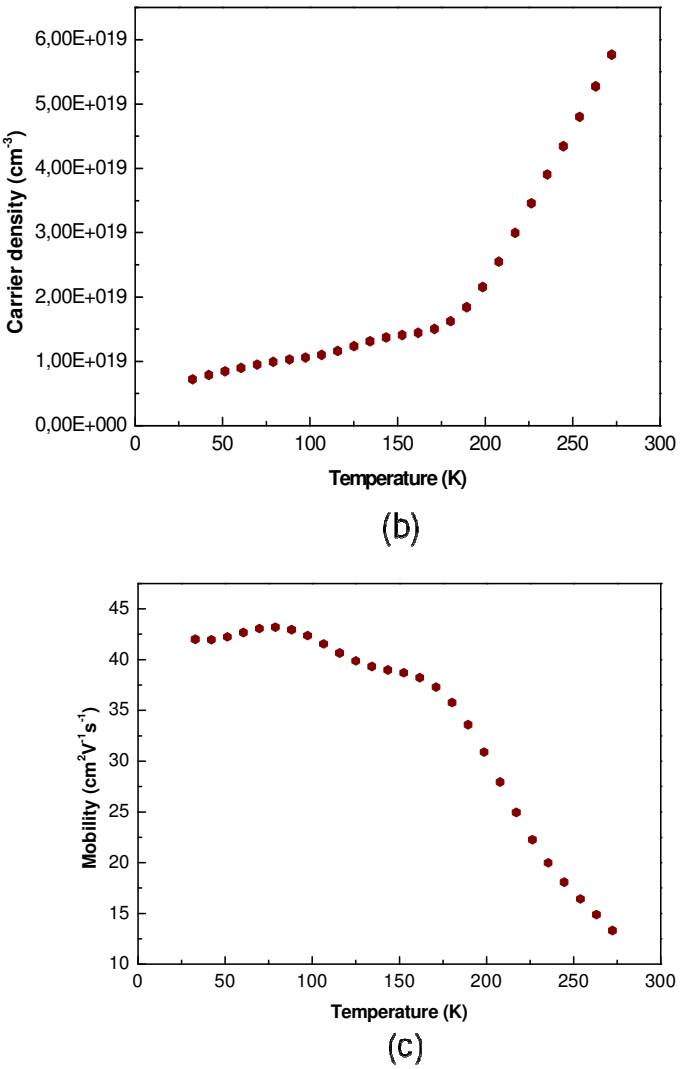

Fig.3.28. Electrical properties versus temperature in the range 30-300K for a ZnO film grown at 200°C: (a) electrical resistivity, (b) carrier density, (c) mobility

The ZnO films grown at 200 and 300°C exhibited *p*-type behavior. In order to confirm the reproducibility of this *p*-type behavior, four new series of films have been fabricated following the indicated procedure and their measurements obtained very similar results. Table 3.VIII shows the values of resistivity, carrier density and mobility at room temperature for all the series of ZnO films grown at different temperatures (average values).

Table 3.VIII. Values of the resistivity, carrier density and mobility at room temperature for all the series of epitaxial ZnO films (average values)

T_{growth} (°C)	Electrical resistivity (Ω cm)	Carrier density (cm^{-3})	Type	Mobility ($cm^{2} V^{-1} s^{-1}$)
200	$5.8x10^{-3}$	$6x10^{19}$	*p*-type	16
300	$3.7x10^{-3}$	$3x10^{19}$	*p*-type	40
400	$6x10^{-3}$	$1x10^{20}$	*n*-type	10
500	$1x10^{-2}$	$2x10^{19}$	*n*-type	20
600	$2x10^{-3}$	$1.5x10^{20}$	*n*-type	20

Fig.3.29 shows the resistivity of the epitaxial films as a function of the growth temperature. The resistivity of the ZnO thin films first decreases as the growth temperature changes from 200°C to 300°C, then increases from 300°C to 500°C, and finally decreases even more at a growth temperature of 600°C.

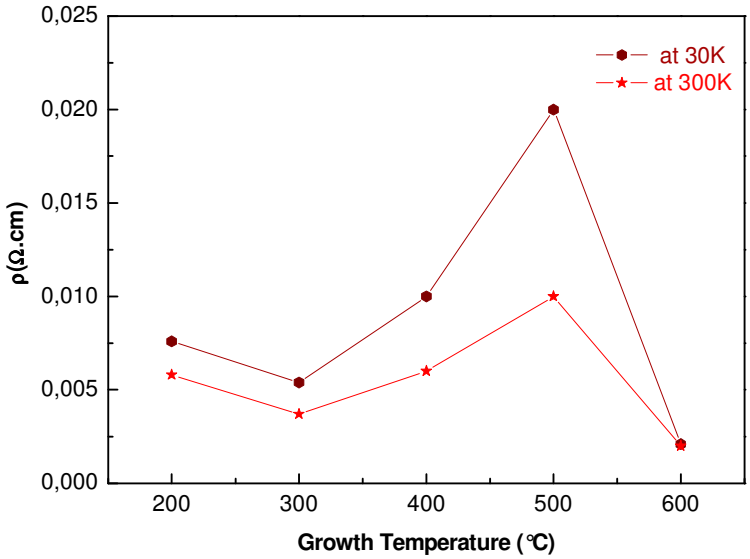

Fig.3.29. Electrical resistivity of epitaxial ZnO films as a function of the growth temperature

Fig.3.30 summarizes the carrier density versus growth temperature for all the series of epitaxial films. It can be seen that the films grown at 200°C and 300°C present *p*-type conductivity while the ones grown at 400°C, 500°C and 600°C exhibit *n*-type conductivity. It is worth to highlight the *p*-type conductivity of the ZnO films grown at 200 and 300°C, which have a large mobility of *16 and 40* $cm^2V^{-1}s^{-1}$, respectively. Also, a change from *p*- to *n*-type conductivity while increasing the growth temperature is observed in all the series.

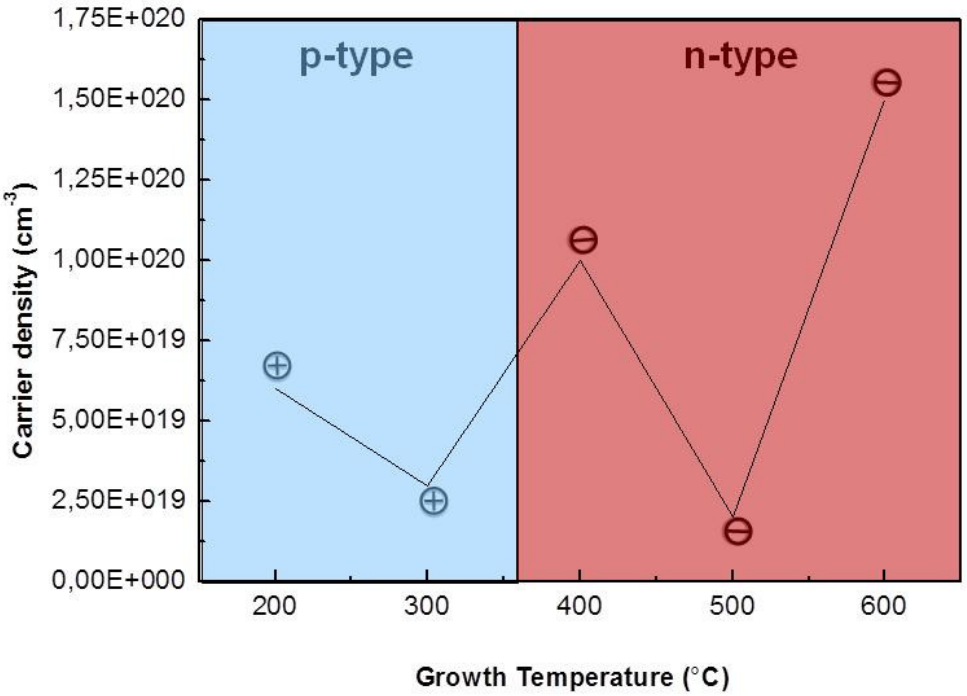

Fig.3.30. Carrier density versus growth temperature for all the series of epitaxial ZnO films

This is very interesting since one of the main issues to use this material in electronic devices is the difficulty to obtain reproducible and high mobility undoped *p*-type ZnO films. In Table 3.IX are summarized the values for the electrical properties of the nominally undoped *p*-type ZnO thin films reported in the literature and the values that we have obtained.

Table 3.IX. Values for the electrical properties of nominally undoped *p*-type ZnO thin films reported in the literature and the values obtained in this PhD work

Growth parameters	Electrical resistivity (Ωcm)	Carrier density (cm^{-3})	Mobility ($cm^2 V^{-1} s^{-1}$)	Ref.
On ZnS by heat-treating ZnO in O_2	10^3	10^{14}	23	[33]
@950°C on ZnSe by heat-treating ZnO in O_2	10^2	10^{15}	23	[34]
@350°C on Si by Reactive sputtering in O_2/Ar (O_2>55%)	3	$9x10^{17}$	2-130	[35]
@620°C on Al_2O_3 by MOVPE in DEZn/O_2 (O_2>55 Pa)	42.7	$1.59x10^{16}$	9.23	[36]
@500°C on Si by PLD in 3 $x10^{-4}$ Torr O_2		$5x10^{18}$		[37]
@250°C on Al_2O_3 by MOCVD+ O_2 plasma	15.8	$2.12x10^{17}$	1.86	[38]
@200°C on Al_2O_3 by PLD in 1.2 $x10^{-2}$ mbar O_2	$5.8x10^{-3}$	$6x10^{19}$	16	[our data]
@300°C on Al_2O_3 by PLD in 1.2 $x10^{-2}$ mbar O_2	$3.7x10^{-3}$	$3x10^{19}$	40	[our data]

When comparing these values, it is observed that the obtained ZnO films have better electrical properties: lower resistivity, higher carrier density and higher mobility. This could be due to our homemade PLD setup. There are a few important parameters that can be varied in PLD: the substrate temperature, the ambient pressure, the ambient gas flow rate, the target-substrate distance, and the laser fluency. In

order to improve the quality of the thin films some of these deposition parameters can be modified individually, but some of them are related. At a glance, an evident correlation is the one between the pressure in the chamber and the substrate temperature. For each substrate temperature the pressure in the chamber has to have an optimal value in order to deposit films with a good stoichiometry. This relationship is very important in processes where background oxygen is required (like ZnO deposition). Another correlation, which is not so obvious, is the one between the pressure in the chamber and the distance target-substrate. According to the Pressure-Distance (PD) scaling law, when the pressure in the chamber is higher, the distance between the target and the substrate should be shorter [39]. Indeed, in our homemade PLD setup, the target-substrate distance is just 2.5cm, which is much lower than any reported in the literature (usually 4-5cm or more).

Another important parameter in PLD is the position of the focusing lens. According to Liu *et al.*, the focus position has an important effect on the deposition rate, surface morphology, crystal quality and optical properties of the ZnO thin films [40]. At the focus position, the high laser energy density in the spot may exceed the saturation energy density [41]. As a result, the atoms already deposited may be re-sputtered, which is in detriment of the deposition rate. When the distance lens-target is smaller than the focusing lens the average energy density reduces, and at the same time the spot size increases. Consequently, the number of atoms that will reach the substrate is also increased. However, one has to find out the proper lens-target distance, because when this is too small the average energy density reduces too much, which means that very few atoms will arrive at the substrate. This detail has been also taken into account in our setup. Therefore, the difference in all these parameters may be responsible for our results. Our homemade PLD experimental setup, altogether: small distance between the target and the substrate, the gas pressure in the chamber, low substrate temperature, laser wavelength, laser fluency, and lens-target distance allowed us to find the narrow processing window for stabilizing *p*-type ZnO films. Due to the orientation of the substrate in the plume, an effective plasma/ion assisted PLD process occurs during deposition and forms point defects.

3.2.4. Magnetic properties of *p*- and *n*-type ZnO

Room-temperature ferromagnetism has been widely reported for undoped ZnO in all its forms (powder, nanoparticles, nanorods, and thin films), as well as in other undoped metal oxide systems (e.g., HfO_2, TiO_2, and SnO_2) [42-49].

There is a general consonance that FM in undoped ZnO originates from lattice defects, being independently asserted Zn and O vacancies as source of the observed magnetism [43-45, 50, 51]. N.H. Hong *et al.* claimed that laser-ablated undoped ZnO films can be ferromagnetic at RT and that this is a particular characteristic of the films only, not being present in bulk [52].

In order to assess this issue the magnetic properties of our undoped ZnO thin films have been investigated. Magnetic characterization of the films was performed by SQUID measurements. The temperature dependence of the magnetization at constant field and the field dependence at constant temperature were measured in the ZFC protocol. The field dependence of the magnetization was measured at 5 and 300K.

Fig.3.31 a) shows the temperature dependence of the magnetization at constant field for *p*-type ZnO film grown at 300°C; b) and c) show the magnetization versus field reversal loop (M-H) measured at 5 and 300K, respectively.

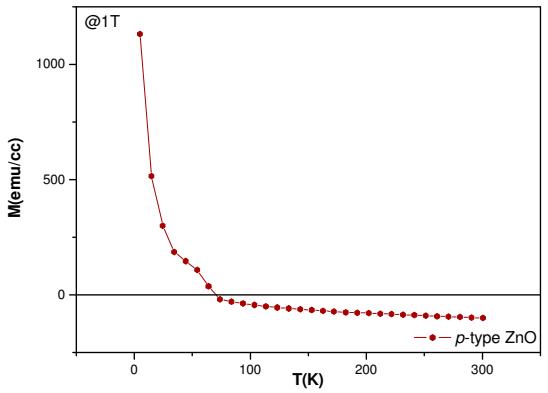

(a)

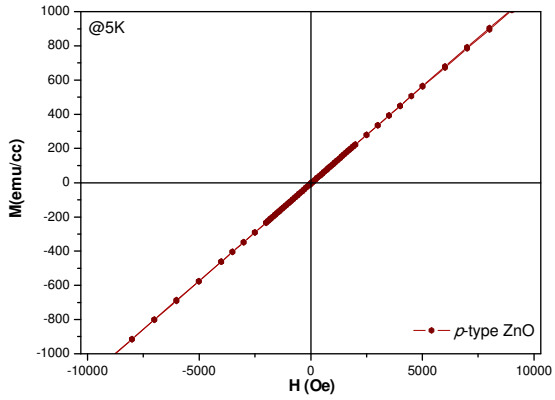

(b)

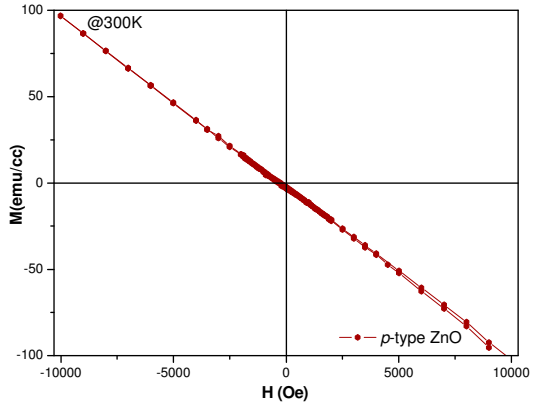

(c)

Fig.3.31. SQUID measurements for *p*-type ZnO film grown at 300°C a) The temperature dependence of the magnetization at constant field; b) and c) Magnetization versus field reversal (M-H) measured at 5 and 300K, respectively

The as-grown *p*-type ZnO thin film seems to be a mixture of diamagnetic and paramagnetic signals. The magnetic susceptibility is positive bellow 70K and negative above this temperature. This behavior must be due to the fact that both a paramagnetic (1/T dependence) and a diamagnetic signal (T independent) are present and superimposed. The loops are linear and reversible in all the temperature range. This paramagnetic component (due to isolated non-interacting spins - uncompensated bonds - free radicals) could be coming from the defects responsible of the electrical conducting behavior.

Fig.3.32 a) shows the temperature dependence of the magnetization at constant field for *n*-type ZnO film grown at 600°C; b) and c) show the magnetization versus field reversal loop (M-H) measured at 5 and 300K, respectively.

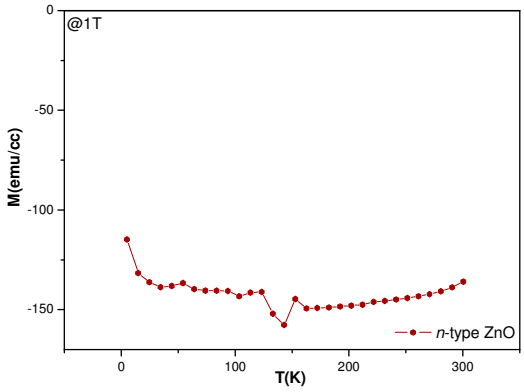

(a)

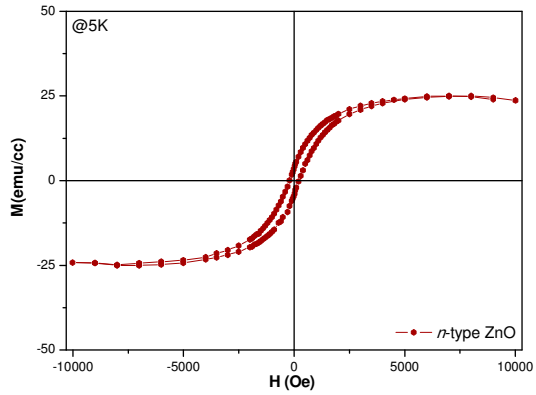

(b)

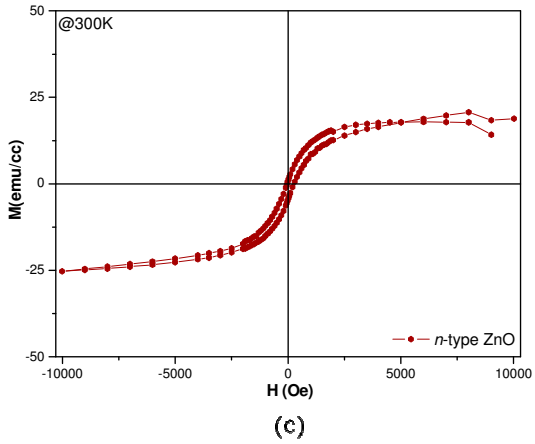

Fig.3.32. SQUID measurements for *n*-type ZnO film grown at 600°C a) The temperature dependence of the magnetization at constant field; b) and c) Magnetization versus field reversal (M-H) measured at 5 and 300K, respectively

The pristine *n*-type ZnO thin film presents a diamagnetic behavior in the whole studied temperature range (5-300K), with a small ferromagnetic component superimposed. The diamagnetic susceptibility is basically constant in all the temperature range as expected from a diamagnetic (chemical bonds satisfied – paired spins with S=0). The diamagnetic signal is justified in both *p*- and *n*-type ZnO films, since the ZnO targets used in this study are diamagnetic.

The small ferromagnetic component superimposed signal observed for the *n*-type ZnO films is something not easy to explain. Note that these films (*p*- and *n*-) are coming from the same series, using the same target and procedure. The only difference between both is the growth temperature. However, the *p*-type film does not show any small ferromagnetic component superimposed.

The sapphire substrate has a ferromagnetic component of about $1{,}5\text{x}10^{-5}$emu at RT. After subtracting the ferromagnetic signal corresponding to the substrate, a ferromagnetic component of $7\text{x}10^{5}$ emu is still obtained in the *n*-type film. This is less than one order of magnitude larger than the component coming from the substrate, and

must have a different origin. As the origin then is the ZnO film, this component should be ascribed to residual impurity levels coming from the target or from the oxygen gas (99.99%). In the case of the target Inductively Coupled Plasma Atomic Emission Spectroscopy (ICP-AES) for commercial ZnO powders from Aldrich was performed. This study shows a small amount of Fe atoms 28±3 ppm in the ZnO, which is in nanocluster form inhomogeniously distributed. Moreover, it is important to say at this point that, depending on the ZnO powder provider (Merck; Aldrich…) or even within the same provider by purchasing different particles sizes, different amount of Fe concentration were measured by ICP-AES. In our targets, giving the diamagnetic behavior measured these ppms of iron impurities are in a solid-solution inside the ZnO. The behavior of these possible impurities in the PLD grown films is not clear. A possible explanation for the weak ferromagnetic signal observed in the *n*-type film could be the incorporation of these defects in the film during PLD growth in a lower concentration than the one detected by PIXE. One could argue that they establish our impurity/uncertainty level magnetic base line. On the other side, according to D. Gao *et al.* a FM response in undoped ZnO could be originated from oxygen vacancies located at the grain surface [53]. According to their principle, the oxygen atoms at the surface escape from the ZnO because of the annealing temperature, and the unpaired electrons causes weak RT magnetism. We suggest that the unpaired electron spins on the ZnO grains could be responsible for the ferromagnetism in the un-doped ZnO films grown at 600°C. This theory needs to be confirmed by photoluminescence experiments, which will be carry on in the next chapter.

As a conclusion of these sets of measurements, it can be said that the "intentionally undoped" ZnO thin films are not ferromagnetic when films are grown at 300°C and do not present oxygen vacancies.

Conclusions:

- ✓ High quality epitaxial ZnO films have been grown on (0001) Al_2O_3 substrates by PLD technique. *All the films grow epitaxially.*
- ✓ *The epitaxial growth is demonstrated from 200°C. This is the lowest epitaxial growth temperature reported for PLD so far.*
- ✓ The film crystal quality increases as the growth temperature increases, as confirmed by AFM and XRD measurements.
- ✓ Electrical transport measurements revealed that *undoped p-type behavior occurred in thin films grown at 200 and 300°C.* Mobilities of 20-40 $cm^2V^{-1}s^{-1}$ have been measured at room temperature for the films grown at 200°C and 300°C, respectively. These values are the highest obtained for this "intentional undoped" *p*-type ZnO, to the best of our knowledge.
- ✓ Electrical transport characteristics of the films *changed from p- to n-type at larger growth temperatures (≥ 400°C).*
- ✓ The ZnO films present different magnetic behavior depending on the conductivity type. The different magnetic behavior (para –for *p*-type films, or diamagnetic –for *n*-type films) could be indicative of the defect responsible for the electronic transport. The "intentionally undoped" ZnO thin films grown at 300°C are not ferromagnetic, which might be related to the fact that these films do not present oxygen vacancies.

References

[1] J. Narayan, K. Dovidenko, A.K. Sharma, S. Oktyabrsky, J. Appl. Phys. 84 (1998) 2597

[2] I. Ohkubo, A. Ohtomo, T. Ohnishi, Y. Matsumoto, H. Koinuma, M. Kawasaki, Surf. Sci. 443 (1999) L1043

[3] S.H. Park, S.Y. Seo, S.H. Kim, S.W. Han, Appl. Phys. Lett. 88 (2006) 251903

[4] B. Zhang, L. Manh, K. Wakatsuki, K. Tamura, T. Ohnishi, M. Lippmaa, N. Usami, M. Kawasaki, H. Koinuma, Y. Segawa, Jpn. J. Appl. Phys. Part 2 42 (2003) L264

[5] R.D. Vispute, V. Talyansky, Z. Trajanovic, S. Choopun, M. Downes, R.P. Sharma, T. Venkatesan, M.C. Woods, R.T. Lareau, K.A. Jones, A.A. Iliadis, Appl. Phys. Lett. 70 (1997) 2735

[6] I.W. Kim, K.M. Lee, Thin Solid Films 516 (2008) 4921

[7] J. Schwartz, J. Perez, Y. Mo, "Growth and Characterization of Wide Band Gap Semiconductors (Zinc Oxide, Zinc Sulfide)", presented at the Fall 2007 Meeting of the Texas Section of the American Physical Society, October 18-20, (2007)

[8] R. Khanna, K. IP, K.K. Allums, K. Baik, C.R. Abernathy, S.J. Pearton, Y.W. Heo, D.P. Norton, F. Ren, S. Shojah-Ardalan, R. Wilkins, J. Electr. Mat. 34 (2005) 4

[9] B.T. Khuri-Yakub, G.S. Kino, P. Galle, J. Appl. Phys. 46 (8) (1975) 3266

[10] Y. Yoshino, K. Inoue, M. Takeuchi, T. Makino, Y. Katayama, T. Hata, Vacuum 59 (2000) 403

[11] A. Hachigo, H. Nakahata, K. Higaki, S. Fuji, S. Shkata, Appl. Phys. Lett. 65 (1994) 2556

[12] J. F. Chang, M. H. Hon, Thin Solid Films, 386 (2001) 79

[13] S.Y. Myong, S.J. Baik, C.H. Lee, W.Y. Cho, K.S. Lim, Jpn. J. Appl. Phys., Part 2, 36 (1997) L1078

[14] M.A.L. Johnson, S. Fujita, W.H. Rowland, Jr., W.C. Hughes, J.W.Cook, Jr., J.F. Schetzina, J. Electron. Mater. 25 (1996) 855

[15] M. Hiramatsu, K. Imaeda, N. Horio, M. Nawata, J. Vac. Sci. Technol. A 16 (1998) 669

[16] H. Kim, C. M. Gilmore, J. S. Horwitz, A. Pique, H. Murata, G. P. Kushto, R. Schlaf, Z. H. Kafafi, D. B. Chrisey, Appl. Phys. Lett. 76 (2000) 259

[17] W.S. Hu, Z.G. Liu, J. Sun, S.N. Zhu, Q.Q. Xu, D. Feng, Z.M. Ji, J. Phys. Chem. Solids. 58 (1997) 853

[18] F. Rubio-Marcos, A. Quesada, M.A. Garcia, M.A. Bañares, J.L.G. Fierro, M.S. Martin-Gonzalez, J.L. Costa-Krämer, J.F. Fernández, J. Sol. Sta. Chem. 182 1211 (2009)

[19] H. Schulz, K.H. Thiemann, Solid State Commun. 32 (1979) 783, 034477.

[20] N.A. Theodoropoulou , A.F. Hebard , D.P. Norton, J.D. Budai,

L.A. Boatner, J.S. Lee, Z.G. Khim, Y.D. Park, M.E. Overberg, S.J. Pearton, R.G. Wilson, Sol. St. Electr. 47 (2003) 2231

[21] S.B. Zhang, S.H. Wei, A. Zunger, Phys. Rev. B 63 (2001) 075205

[22] F.H. Leiter, H.R. Alves, A. Hofstaetter, D.M. Hofmann, B.K. Meyer, Phys. Status Solidi B 226 (2001) R4

[23] F. Vigué, P. Vennéguès, C. Deparis, S. Vézian, M. Laügt, J.P. Faurie, J. Appl. Phys. 90 (2001) 5115

[24] X. W. Sun, H. S. Kwok, J. Appl. Phys. 86, 1 (1999) 408

[25] Z.F. Liu, F.K. Shan, J.Y. Sohn, B.C. Shin, Y.S. Yu, S.C. Kim, Y.X. Li, J. Korean Phys. Soc. 44, 5 (2004) 1123

[26] S. Dutta, S. Chattopadhyay, A. Sarkar, M. Chakrabart, D. Sanyal, D. Jana, Progress in Mat. Sci. 54 (2009) 89

[27] P. Fons, K. Iwata, A. Yamada, K. Matsubara, S. Niki, K. Nakahara, T. Tanabe, H. Takasu, Appl. Phys. Lett. 77 (2000) 1801

[28] K. Iwata, P. Fons, A. Yamada, K. Matsubara, S. Niki, J. Cryst. Growth 209 (2000) 526

[29] J.R. Tesmer, M. Nastasi, Handbook of Modern Ion Beam Materials Analysis (1995) MRS Pittsburgh

[30] J.F. Ziegler, M.D. Ziegler, J.P. Biersack, SRIM-2006.02

[31] L.C. Chen, Particulates Generated by Pulsed Laser Ablation. In: Pulsed Laser Deposition of Thin Films, ed. by D.B. Chrisey, G.H. Hubler (Wiley, New York Chichester Brisbane Toronto Singapore 1994) 167

[32] N. Ohashi, I. Sakaguchi, S. Hishita, Y. Adachi, H. Hareda, T. Ogino, J. Appl. Phys. 92 (2002) 2378

[33] T.V. Butkhuzi, A.V. Bureyev, A.N.Georgobiani, N.P.Kekelidze, T.G.Khulordava, J. Cryst. Growth 117 (1992) 366

[34] A.N.Georgobiani, M.B.Kotlyarevskii, V.V.Kidalov, L.S.Lepnev, I.V.Rogozin, Inorganic Materials 37, 11 (2001) 1095

[35] G. Xiong, J.Wilkinson, B. Mischuck, S. Tuzemen, K.B.User, R.T.Williams, Appl. Phys. Lett. 80 (2002) 1195

[36] Y. Ma, G.T. Du, S.R. Yang, Z.T. Li, B.J. Zhao, X.T. Yang, T.P. Yang, Y.T. Zhang, D.L. Liu, J. Appl. Phys. 95,11 (2004) 6268

[37] M.S. Oh, S.H. Kim, T.Y. Seong, Appl. Phys. Lett. 87 (2005) 122103

[38] Y.J. Zeng, Z.Z. Ye, W.Z. Xu, J.G. Lu, H.P. He, L.P. Zhu, B.H. Zhao, Appl. Phys. Lett. 88 (2006) 262103

[39] H.S. Kwok, H.S. Kim, D.H. Kim, W.P. Shen, X.W. Sun, R.F. Xiao, Appl. Surf. Sci. 109-110 (1997) 595

[40] M. Liu, G. Sun, Z.G. Zhang, X.Q. Wei, C.S. Chen, C.S. Xue, B.Y. Man, Eur. Phys. J. Appl. Phys. 34 (2006) 73

[41] J. Brandenburg, V. Neu, H. Hendrock, B. Holzapfel, H.U. Krebs, S. Fähler, Appl. Phys. A 79 (2004) 1005

[42] N.H. Hong, J. Sakai, N. Poirot, V. Brizé, Phys. Rev. B 73 (2006) 132404

[43] S. Banerjee, M. Mandal, N. Gayathri, M. Sardar, Appl. Phys. Lett. 91 (2007) 182501

[44]A. Sundaresan, R. Bhargavi, N. Rangarajan, U. Siddesh, C.N.R. Rao, Phys. Rev. B 74 (2006) 161306

[45] Q. Xu, H. Schmidt, S. Zhou, K. Potzger, M. Helm, H. Hochmuth, M. Lorenz, A. Setzer, P. Esquinazi, C. Meinecke, M. Grundmann, Appl. Phys. Lett. 92 (2008) 082508

[46] M. Venkatesan, C.B. Fitzgerald, J.M.D. Coey, Nature(London) 430 (2004) 630

[47] J.M.D. Coey, M. Venkatesan, P. Stamenov, C.B. Fitzegerald, L.S. Dorneles, Phys. Rev. B 72 (2005) 024450

[48] Z. Yan, Y. Ma, D. Wang, J. Wang, Z. Gao, L. Wang, P. Yu, T. Song, Appl. Phys. Lett. 92 (2008) 081911

[49] S. Kumar, Y.J. Kim, B.H. Koo, S. Gautam, K.H. Chae, R. Kumar, C.G. Lee, Mater. Lett. 63 1(2009) 94

[50] W. Yan, Z. Sun, Q. Liu, Z. Li, Z. Pan, J. Wang, S. Wei, D. Wang, Y. Zhou, X. Zhang, Appl. Phys. Lett. 91 (2007) 062113

[51] Q. Xu, H. Schmidt, L. Hartman, H. Hochmuth, M. Lorenz, A. Setzer, P. Esquinazi, C. Meinecke, M. Grudmann, Appl. Phys. Lett. 91 (2007) 092503

[52] N.H. Hong, J. Sakai, V. Brizé, J. Phys. Condens. Matter 19 (2007) 036219

[53] D. Gao, Z. Zhang, J. Fu, Y. Xu, J. Qi, D. Xue, J. App. Phys. 105 (2009) 113928

4

SOME CLUES ABOUT THE p-TYPE BEHAVIOR IN UN-DOPED ZnO

Chapter 4

Some clues about the *p*-type behavior in "un-doped" ZnO

The experimental difficulties when trying to obtain *p*-type ZnO films are reviewed in this chapter, and a experimental approach trying to identify the responsible for the *p*-type transport is described.

To date most groups have tried to obtain *p*-type ZnO by extrinsic doping with Li, N, P, As, Sb, for example. One of the first attempts was doping with lithium. In ZnO lithium is amphoteric, and can act as an acceptor when is substitutional on zinc sites, and as a donor when interstitial [1]. Due to its thermal instability electron compensation takes place, and as a result semi-insulating layers of ZnO are obtained [2-4]. This is a main impediment for achieving *p*-type conductivity in homoepitaxial ZnO layers.

Other attempt was doping with nitrogen. In principle it should substitute in the oxygen sites because of its similar radius [5]. However a lot of issues have been encountered and the *p*-type conductivity was not stable [6]. Another option was doping with elements with larger ionic radius such as elements from group V [7-12]. P-type conductivity has been observed in ZnO when P, As and Sb where used as dopant. The theoretical community started to look into the electronic structures of the defects induced by these elements [13,14]. For doping with As or Sb, a stable acceptor should form between their antisite and two zinc vacancies in oxygen-rich conditions [13]. In the case of P doping, according to the calculations the acceptor should be

a zinc vacancy or the P_{Zn}-$2V_{Zn}$ complex depending if the dopant is P_2O_5, P_2O_3 or Zn_3P_2 [14]. Worthy of note is the fact that Zn_3As_2, Zn_3Sb_2 and Zn_3P_2 are *p*-type semiconductors. For that reason one might speculate if the existence of such impurity phases in ZnO could induce a *p*-type behavior. However this is another issue not answered yet. Another option is codoping, which can be made using two different acceptors (like N and As) or combining donors with a higher concentration of acceptors (like Ga and N).

Regarding nominally undoped *p*-type ZnO only a few reports can be found in the literature, where it is shown that the *p*-type conductivity depends on growth conditions. In 1992, Butkhuzi *et al.* reported for the first time intentionally undoped ZnO films grown onto ZnS substrates, by heat-treating ZnO in atomic oxygen, presenting weak *p*-type conductivity [15]. However, the ZnO films obtained by this method presented high resistivity of 10^3 Ω cm and low carrier density of 10^{14} cm^{-3}. It was not until almost 10 years later when Gergobiani *et al.* confirmed again the *p*-type conductivity in undoped ZnO thin films with a resistivity of 10^2 Ωcm and carrier density of 10^{15} cm^{-3}[16]. The deposition method in this case was also radical-beam getter epitaxy, a process involving heat-treatment of ZnO crystal in an activated oxygen atmosphere. Xiong *et al.* suggested that adjusting the Ar/oxygen gas ratio, the conductivity of ZnO films could be changed. Their ZnO films grown by reactive sputtering at low oxygen partial pressure presented *n*-type behaviour, while the films grown at higher oxygen pressure (>55%) exhibited *p*-type behaviour [17].

The theory that the conduction type in undoped ZnO thin films could be controlled by adjusting the oxygen partial pressure during growth was confirmed a few years later by two other groups. One of the groups reported the deposition of ZnO thin films on sapphire substrates by Metal-Organic Vapour Phase Epitaxy (MOVPE), where the films exhibited *n*-type conductivity under oxygen partial pressure lower than 45Pa, and at oxygen partial pressure higher than 55Pa intrinsic *p*-type ZnO was obtained. Remarkably, when increasing oxygen content the crystallinity of the ZnO films decreased and turned

polycrystalline [18]. This may also indicate that the grain boundaries play a role on the *p*-type conductivity. The other group reported nominally undoped *p*-type ZnO thin films grown on Si (111) substrates by PLD. Hall measurements showed that the undoped ZnO films changed from *n*-type to *p*-type conduction when the oxygen pressure changed from $6x10^{-5}$ to $3x10^{-4}$ Torr during growth [19].

The appearance of undoped *p*-type behavior has been ascribed by Zeng *et al.* to the formation of zinc vacancies and some complex acceptor center in ZnO films prepared by plasma-assisted low pressure Metal-Organic Chemical Vapor Deposition (MOCVD)[20]. In these films the optimal resistivity of the *p*-type film is 15.8 Ω cm, with a Hall mobility of 1.86 cm^2V^{-1} s^{-1}, and a hole concentration of 2.1 x 10^{17} cm^{-3} for films grown at 250°C. Also, Zn-vacancies seemed to be responsible for *p*-type behaviour in ZnO nanorods synthesized by hydrothermal method, according to Hsu *et al.* [21].

In this thesis work different possible effects that may influence the *p*-type behavior are studied: grain boundaries (by eliminating the twinning effect) and generating intrinsic defects in epitaxial *n*-type ZnO films.

4.1. Twinning effect in ZnO

The films that exhibit *p*-type behavior are the films grown at lower temperatures. At the same time, the thin films obtained at these temperatures present also a twinning effect. Since in previous studies a possible explanation for the *p*-type behavior is the trapping of electrons at the grain boundaries, one of the first efforts was to obtain ZnO films at low temperatures without that twining effect. For this reason our aim was first to find a way to control or prevent the appearance of twinning at lower temperatures. Once this objective was achieved, we could investigate the effect of twinning on the electrical properties of the films.

The twin formation in ZnO/Al_2O_3 (0001) films grown by MBE [22], MOCVD [23,24], PLD [25], and sputtering [26] has been studied. From this research it has been learned that: a) raising the growth temperature the twinning will disappear, b) the relative intensity of the twining domains vary for films grown in similar conditions, and c) the appearance and the intensity of the twinning maxima in the X-ray diffractograms depend on the film deposition rate.

In order to explain the twinning effect in ZnO films various theories have been formulated. Ohkubo *et al.* suggested that the appearance of the 30^0 rotated twin domains at low temperatures can be attributed to kinetic factors. The main domains are thermodynamically more stable than the 30^0 rotated domains when measured along the $(11\underline{2}3)$ direction for the Al_2O_3 and the $(10\underline{1}1)$ plane of ZnO [22]. According to Vispute *et al.* the improvement of the film alignment at large growth temperatures could be associated with the increase of surface mobility of the adatoms [25]. Kim *et al.* investigated the twin formation mechanism of sputter-grown epitaxial $ZnO/Al_2O_3(0001)$ films by means of real time synchrotron X-ray scattering measurements. In this case the twin formation was correlated with the strain evolution due to the existence of a transition thickness at which the twin domains nucleate followed by the gradual strain relaxation, indicating a mechanical twin [26].

In this section the twin formation origin of PLD grown epitaxial ZnO films deposited on (0001) Al_2O_3 substrates is studied.

4.1.1. Influence of film growth temperature

A new set of ZnO films have been grown, where the deposition conditions were the same as in the previous section: $1.2x10^{-2}$ mbar oxygen atmosphere and (0001) sapphire as substrates. The only difference was that this time the growth temperature was ranging from

RT to 600°C. Before the deposition the (0001) sapphire wafers were prepared using the standard chemical cleaning procedure described in the experimental section.

The out-of-plane orientation of the ZnO films was analyzed by performing XRD 2Θ/ω scans measurements (shown in Fig.4.1). All the diffraction maxima can be indexed either with the sapphire substrate or with the hexagonal wurtzite ZnO lattice. The fact that all diffraction maxima were {000*l*} indicates that the *c*-axis growths perpendicular to the substrate plane. However, the ZnO film grown at RT presents only the (0002) ZnO diffraction maxima, indicating poor crystal quality.

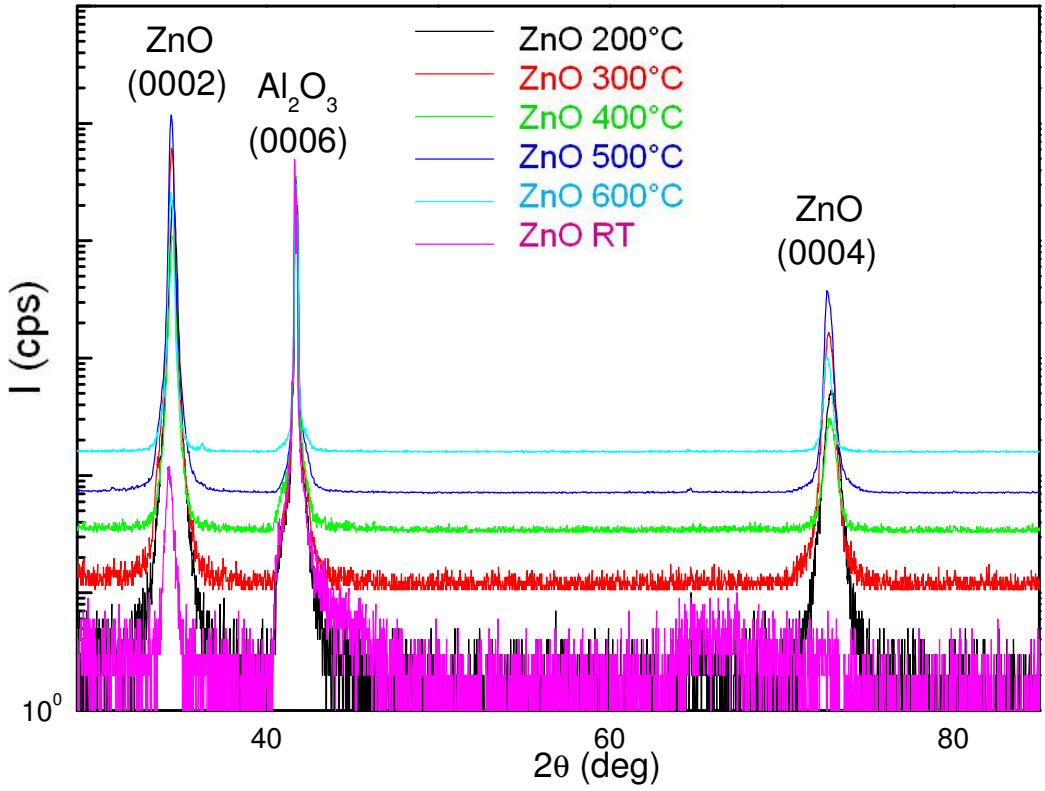

Fig.4.1. XRD 2Θ/ω scans for ZnO films grown on sapphire substrates cleaned by standard chemical procedure

The crystal coherence length of the films (calculated with Scherrer formula) plotted vs. substrate temperature is shown in Fig.4.2. For these calculations the FWHM of ZnO (0002) maxima of the 2θ/ω scan was used as input. It can be seen that for this set of films where the substrates were cleaned just by chemical procedure two regimes can be observed. This feature is attributed to the two-domain films. In this case it is ascribed to the activation of a new adatom surface diffusion process at T_s>200°C which becomes dominant at T_s>500°C.

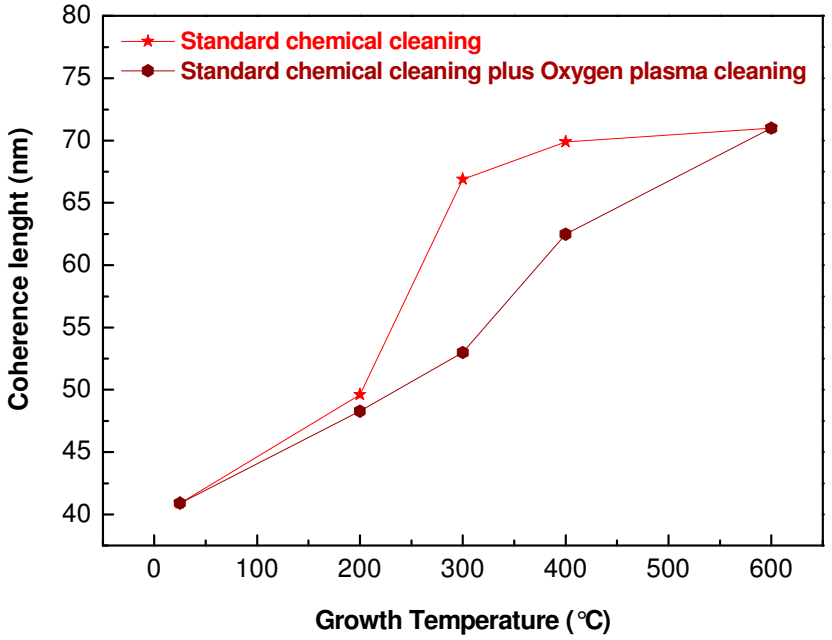

Fig.4.2. Crystalline coherence length for films grown at different temperature on substrates prepared by different cleaning procedures: standard chemical cleaning and standard chemical cleaning plus Oxygen plasma cleaning. (Reprinted from Thin Solid Films Ref. [27] © 2010, with permission from Elsevier)

The asymmetrical XRD measurements confirmed once again the epitaxial relationship $[11\underline{2}0]_{ZnO}||[11\underline{2}0]_{sapphire}$ for the film grown at 200°C and $[10\underline{1}0]_{ZnO}||[11\underline{2}0]_{sapphire}$ for the films grown at 500°C and 600°C; and the fact that the films grown at 300°C and 400°C exhibit twin domains (See Fig.3.16 from "Structural characterization of epitaxial ZnO thin

films on sapphire substrates"). The ZnO film grown at RT did not exhibit any epitaxial relationship.

4.1.2. Influence of substrate cleaning

In order to clarify the influence of the twinning on the electrical properties, a new set of films was prepared. This time the sapphire substrates were cleaned by a different procedure: with an extra oxygen plasma cleaning step before deposition to eliminate any possible carbon contamination coming from the conventional chemical cleaning. That is to say, after the usual chemical procedure the substrates were additionally immersed in oxygen plasma at 200 W for 5 minutes. Regarding the deposition parameters, the growth temperature was ranging just from RT to 400°C in $1.2x10^{-2}$ mbar oxygen pressure (since at 500°C and 600°C no twinning was observed).

The XRD 2Θ/ω scans measurements corresponding to ZnO films deposited on substrates cleaned by oxygen plasma are shown in Fig.4.3. All the diffraction maxima can be indexed either with the ZnO lattice or with the sapphire substrate. The two ZnO diffraction maxima observed correspond to (0002) and (0004), which implies *c*-axis growth perpendicular to the substrate plane. As expected, the intensity of the peaks increases and the width of the diffraction maxima decreases when increasing the growth temperature.

When comparing XRD 2Θ/ω scans measurements for the ZnO films grown on substrates cleaned with and without oxygen plasma the same diffraction pattern is observed. However, the ZnO films grown at RT vary considerably upon the cleaning procedure of the substrates. The presence of both the (0002) and (0004) ZnO diffraction maxima for ZnO film grown on substrate cleaned by oxygen plasma, indicates a

better crystal quality than the films grown on substrates cleaned just by the usual chemical procedure (where only the (0002) ZnO diffraction maxima have been identified).

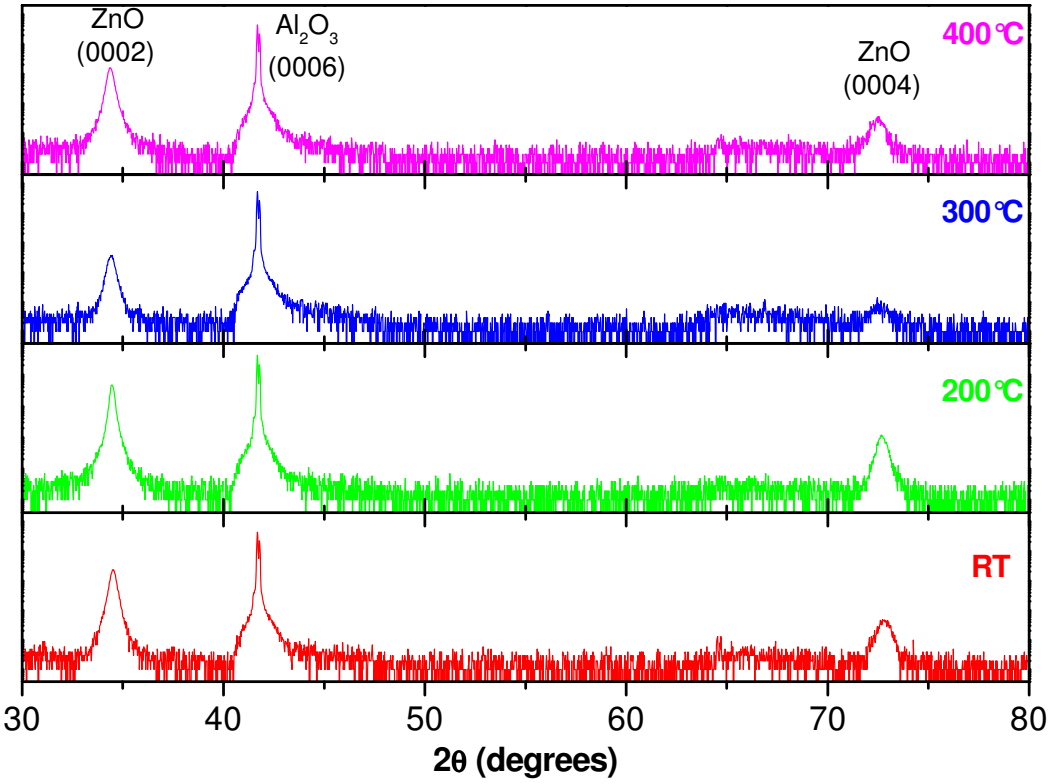

Fig.4.3. XRD 2Θ/ω scans measurements corresponding to ZnO films deposited at different temperature on substrates cleaned by oxygen plasma

The coherence length of the films cleaned with oxygen plasma display an almost linear relationship when plotted vs. growth temperature (see Fig.4.2). The increase in crystallite size when increasing growth temperature is also observed for both cases: with and without ulterior treatment with oxygen plasma.

The crystal quality of the films was analyzed by ω-scans of the diffraction peaks along the (0002) direction. Fig.4.4 shows the rocking-curves corresponding to the (0002)-ZnO reflection. The FWHM value of the XRD rocking curve decreases from 4.81° for the film grown at RT, 3.35° for the film grown at 200°C, 2.95° for the one grown at 300°C, to 1.93° for the film grown at 400°C.

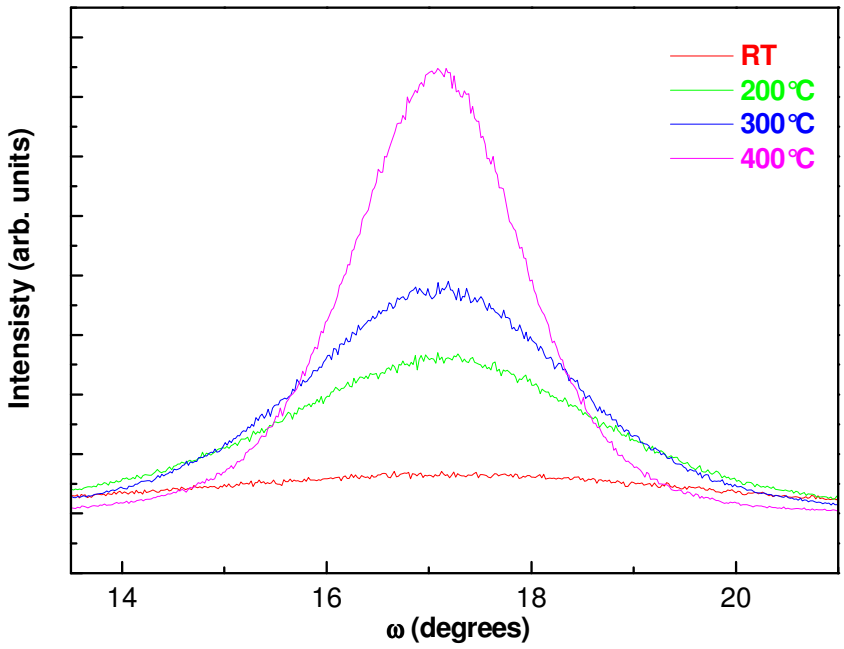

Fig.4.4. Rocking-curves corresponding to the (0002)-ZnO reflection for ZnO films deposited at different temperature on substrates cleaned by oxygen plasma

Fig.4.5 displays the in-plane Φ scans for the (11$\underline{2}$3) plane of the sapphire substrate and for the (10$\underline{1}$3) plane of the ZnO films grown at different temperatures on substrates cleaned with oxygen plasma. All the films are free of twin domains. The peaks are separated 60° confirming the six-fold symmetry. The main domains are aligned with the substrate according to the epitaxial relationship $[10\underline{1}0]_{ZnO}||[11\underline{2}0]_{sapphire}$. The Φ-scans of the films deposited on oxygen plasma pretreated substrates always show only six strong peaks

separated by 60°. This characteristic reveals a single-domain in-plane orientation around the *c*-axis, with the *a*-axis aligned with respect to the substrate. As it can be seen, *for the films grown on substrates cleaned by oxygen plasma the epitaxial relationship starts as low as RT*, which is even lower compared to the temperature of 200°C obtained for the films grown on substrates cleaned just by the routine chemical procedure. To the best of our knowledge, *up to date it has not been reported yet the starting of epitaxial growth of ZnO films at RT*.

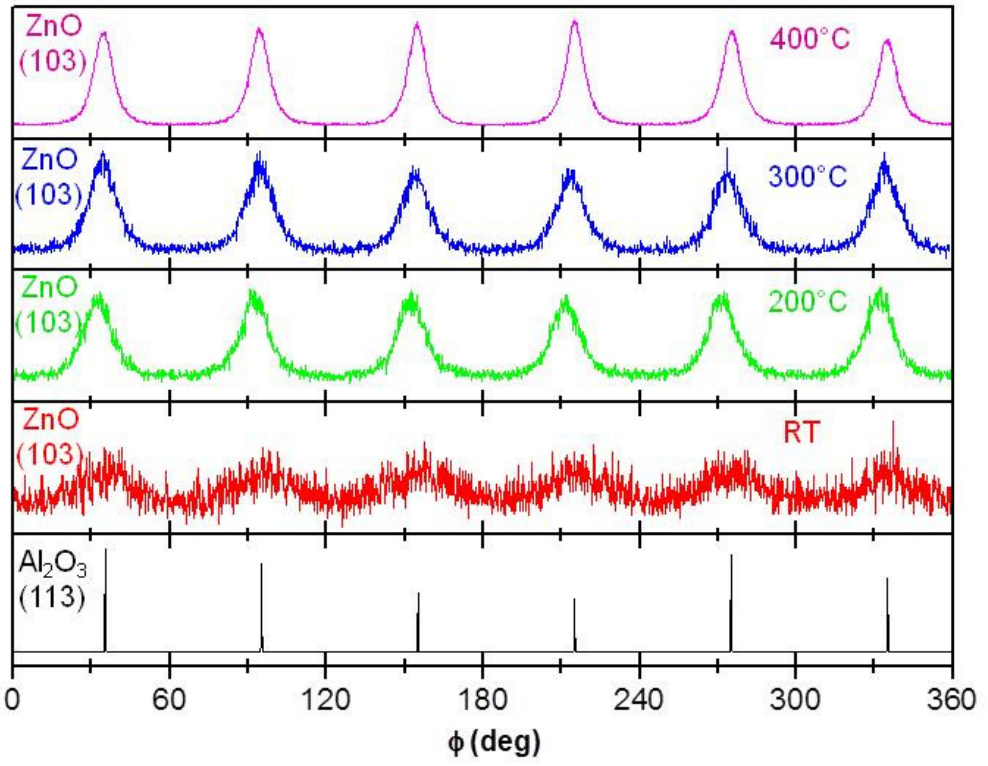

Fig.4.5. In-plane Φ scans for the (11$\underline{2}$3) plane of the sapphire substrate and for the (10$\underline{1}$3) plane of the ZnO films grown at different temperatures on substrates cleaned with oxygen plasma

The origin of the 30° twining rotation could be ascribed to residual hydrocarbons (C-H-O) on the sapphire surface because of the chemical cleaning procedure. By eliminating these residues during the plasma cleaning (atomic oxygen generated during exposure to oxygen plasma

is known to remove amorphous carboneus components [28]) the formation of the 30° rotated domain was avoided. The temperature at which a new adatom surface diffusion process is activated (200°C, see Fig.4.2) could indicate that at this point the hydrocarbons layer started to desorbs from the sapphire surface in vacuum. When the substrates were heated in vacuum conditions at temperature >500°C this hydrocarbon residues were completely removed. If between 200 and 500°C the desorption of the hydrocarbon residues *was not homogeneous, the aligned peaks appeared where the hydrocarbon residues were eliminated, while the 30° set of diffraction maxima were originated where the hydrocarbon residues were still* present when ZnO film started to grow. This fact could explain the variation of the diffraction peak domain intensities for different series of films.

Another possible explanation for the appearance of the twinning could be associated to the Al-terminated layer of the sapphire substrate. When the substrate is not exposed to any pre-treatment, a single Al-terminated layer would be the most stable for the *c*-plane of the (0001) sapphire substrate, as it has been confirmed by low energy diffraction and x-ray scattering studies [29]. When the deposition of ZnO films begins on these substrates, two different domains are obtained. The main domain, which follows the Al sublattice, is formed by the oxygen atoms of the first ZnO layer and the Al atoms of sapphire. At the same time the twin domain, which follows the oxygen sublattice of the sapphire substrate, is formed by the Zn atoms of the ZnO layer and the oxygen atoms of the substrate. Between the main and the twin domains there is a 30° rotation. Thus, when the ZnO lattice forms onto the Al sublattice, the epitaxial relationship between the ZnO film and the sapphire substrate would be $[11\underline{2}0]_{ZnO}||[11\underline{2}0]_{sapphire}$ with a lattice mismatch of 32%. After the substrate has been exposed to the oxygen plasma is expected to be O-terminated. Therefore, in this case, when the deposition starts the ZnO lattice will form onto the O sublattice, and the epitaxial relationship would be $[10\underline{1}0]_{ZnO}||[11\underline{2}0]_{sapphire}$, with a lattice mismatch of 18%.

Measurements of the electrical properties have been also performed on these films. Fig.4.6 (a-c) shows the behavior of the electrical resistivity, carrier density and Hall mobility versus temperature, in the range 33-300K, for films grown at 300°C. Table 4.I shows the values of the electrical properties at RT for ZnO films prepared by both cleaning procedures. It can be seen that the electrical transport characteristics of the films are not influenced much by the twinning. Both films present *p*-type conductivity and have almost the same resistivity; the only significant difference is the higher mobility values of the film un-exposed to the oxygen plasma cleaning.

Table 4.I. Electrical properties (resistivity, carrier density and mobility) measured at RT for ZnO films grown at the same temperature of 300°C, but prepared by different cleaning procedure: with and without oxygen plasma.

T_{growth} (°C)	Cleaning procedure	Resistivity (Ω cm)	Carrier density (cm^{-3})	Mobility ($cm^2 V^{-1} s^{-1}$)
300	With oxygen plasma	$1.1x10^{-3}$	$9x10^{19}$ *p*-type	15
300	Without oxygen plasma	$2.3x10^{-3}$	$5x10^{19}$ *p*-type	36

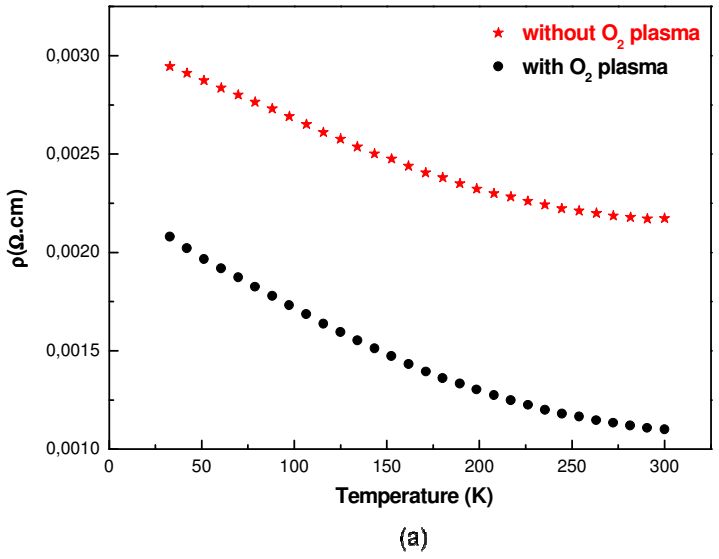

(a)

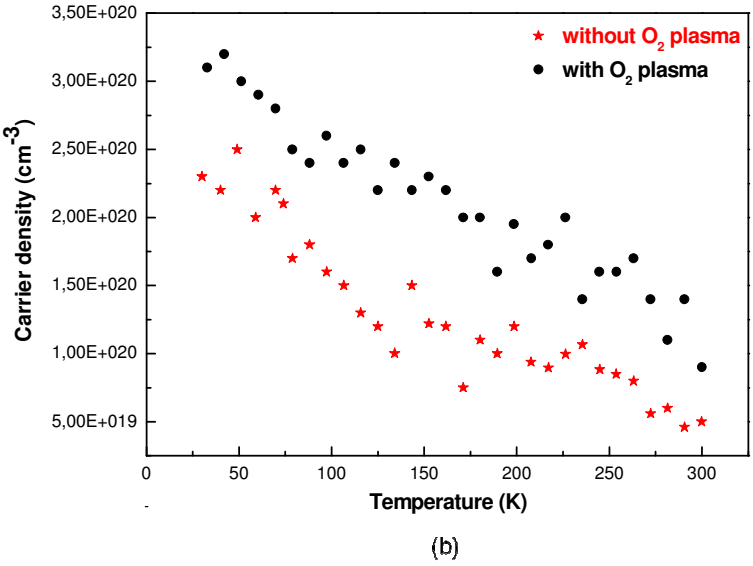

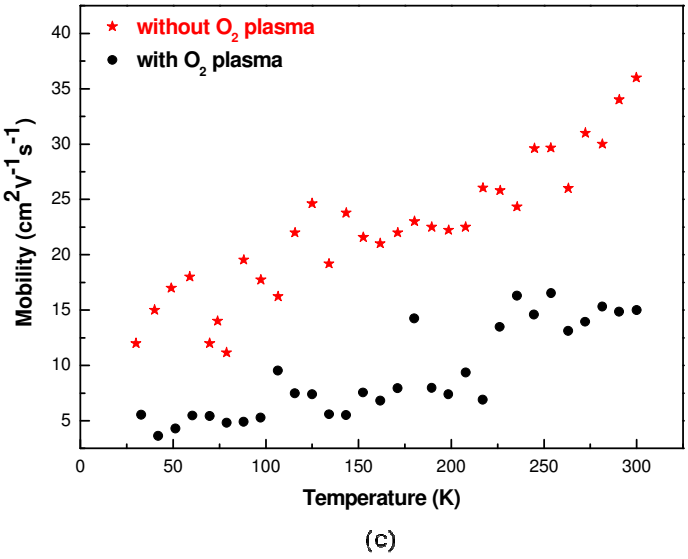

Fig.4.6. Measurements of electrical properties for ZnO films grown at 300°C on sapphire substrates cleaned by 2 different procedures: (a) resistivity versus temperature, (b) carrier density versus temperature, (c) mobility versus temperature

Conclusions:

- ✓ The structural and electrical transport properties of epitaxial ZnO thin films grown on (0001) sapphire substrates by PLD were investigated as a function of film growth temperature and substrate cleaning procedure.
- ✓ This study demonstrates that the cleaning procedure influences extremely the twin formation. *When the substrates are exposed to oxygen plasma* after a standard chemical cleaning procedure, *the appearance of the twin domains is avoided.*
- ✓ The origin of the appearance of the twin domains has been correlated with the residual hydrocarbons present on the substrate or with the Al-terminated layer of the sapphire substrate.
- ✓ The electrical transport characteristics of the films are not affected significantly by the existence of the twinning.

4.2. Generating defects in ZnO by irradiation

What it has been observed so far is that the *p*-type behavior of ZnO films grown at low temperature is not related to the twining effect. The objective now is to investigate if the observed *p*-type behavior is due to intrinsic defects. For that purpose, three *n*-type ZnO films with high crystallinity (grown at 600°C), with a Zn:O 1:1 ratio as measured by PIXE, were irradiated with protons. The objective here is double fold. On one hand to determine if by reducing the lattice order degree and creating intrinsic defects we can make a *n*-type ZnO to become *p*-type. And on the other hand to study the radiation hardness of these PLD grown films.

ZnO is hard radiation-resistance material, characteristic which makes it a potential candidate for space devices. It is well known that space radiation (electromagnetic and cosmic) interacts with the materials inducing various structural transformations and point lattice defects, which affect the working parameters of devices, and ultimately lead to devices failure. Therefore, in order to avoid undesirable fails, hard radiation-resistant materials such as ZnO are required. Previous studies illustrate that the reason for the hard radiation-resistant in ZnO films is mainly due to a significant radiation-induced defect annihilations which take place even at low temperatures [30,31].

This section is dedicated to the investigation of the changes promoted by irradiation with protons in the structural and electrical properties of our ZnO thin films.

4.2.1. Irradiation process

Three epitaxial *n*-type ZnO films were grown by PLD in 1.2 $x10^{-2}$ mbar oxygen atmosphere, at a substrate temperature of 600°C, and on (0001) Al_2O_3 substrates. Then they were irradiated with different proton fluencies at energy of 2 MeV: $1x10^{15}$, $1x10^{16}$, and $1x10^{17}$ at/cm^2. Fig.4.7 shows the stopping power of H^+ in ZnO calculated for hydrogen beam as a function of the energy using the SRIM code, indicating that at 2 MeV energy irradiation takes place in an energy range dominated by electronic processes [32].

The chosen doses of 10^{15}-10^{17} at/$cm^2$are very high since, according to [33] a year in a low-earth satellite orbit corresponds to a dose of around $3x10^5$ at/cm^2. The ZnO films have been irradiated mainly in the centre, as shown in Fig.4.8. The irradiation was performed in non-channeling incidence at RT. After the experiment, the safety of the ionizing films was confirmed with a Geiger counter.

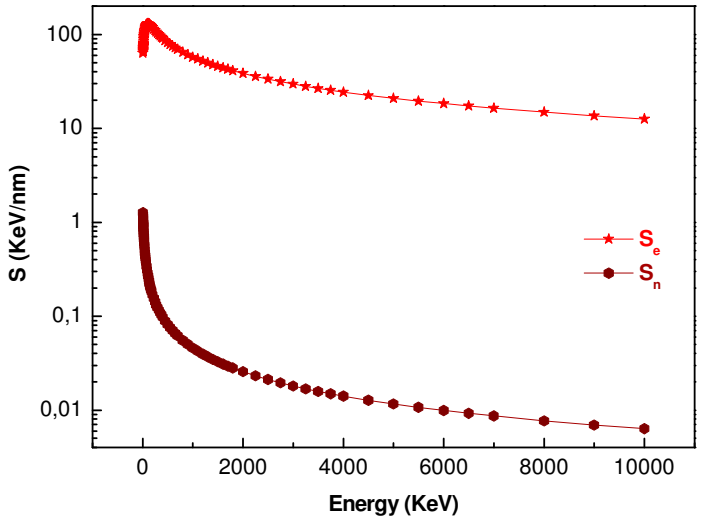

Fig.4.7. Stopping power of H^+ in ZnO calculated for hydrogen beam as a function of the energy using the SRIM code

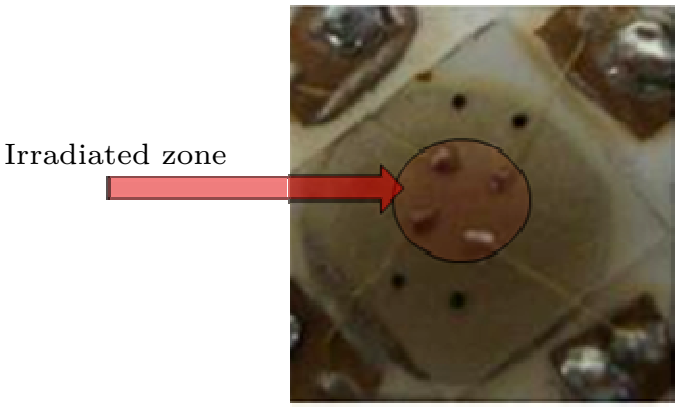

Fig.4.8. Image of a ZnO sample: the red circle indicates the area which has been irradiated

4.2.2. Structural characterization

Microbeam X-Ray diffraction

In order to study the effect of the irradiation on the crystal quality of the ZnO films, structural characterisation of the films was done ex-situ by μ-XRD in Debye-Scherrer geometry using a diffractometer

equipped with a GADDS from Bruker-AXS (model D8 Advanced). The μ-beam in XRD measurements is very useful, due to the fact that it allows focusing the spot in and out of the irradiated area for the same sample. Fig.4.9 shows Charge-Coupled Device (CCD) images taken during the measurements and shows where the beam spot was focused on the sample surface: (a) on the irradiated zone and (b) outside the irradiated zone.

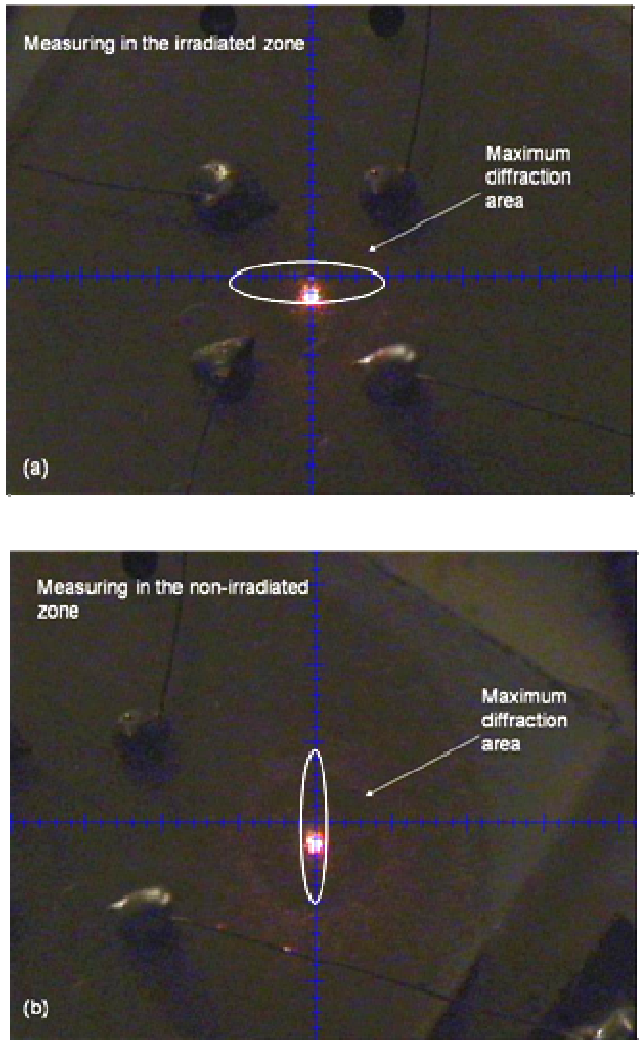

Fig.4.9. CCD images taken during the μ-XRD measurements illustrating where the beam spot was focused on the sample surface: (a) on the irradiated zone and (b) outside the irradiated zone.

Fig.4.10 shows the µ-XRD 2Θ/ω scans measurements for ZnO film before and after irradiation at a H^+ fluency of 10^{16} at/cm^2. It can be seen that both scans exhibit the same diffraction maxima: the (0002) and (0004) planes of the ZnO lattice, together with the (0006) and (00012) diffraction maxima from the sapphire substrate lattice. Hence, it can be concluded that the ZnO films presents the same diffraction pattern before and after irradiation at this fluency.

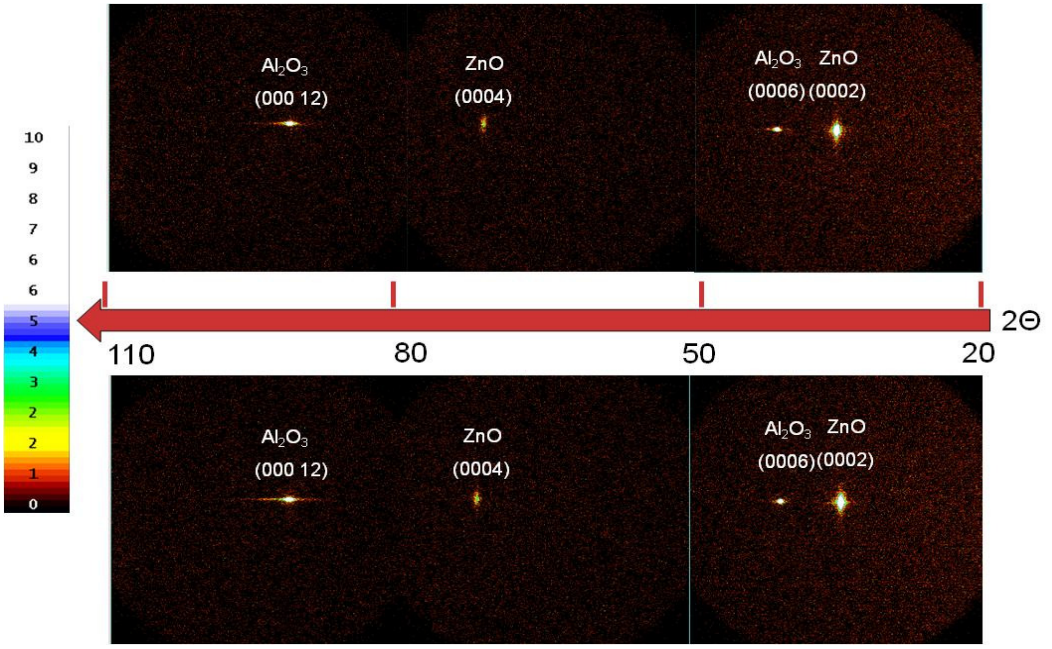

Fig.4.10. µ-XRD 2Θ/ω scans measurements corresponding to ZnO film before (upper) and after (lower) it has been irradiated at a H^+ fluency of 10^{16} at/cm^2

Fig.4.11 shows the µ-XRD 2Θ/ω scan measurements before and after irradiation for the films irradiated at different fluencies. For simplicity the measurements shown here are ranging from 20 to 80 2Θ degrees. For films irradiated at a fluency of $1x10^{15}$ cm^{-2} no significant changes were observed, neither in the 2Θ position nor in the FWHM value. This fact indicates that this irradiation fluency does not significantly modify the structural properties of the ZnO film. However, very small changes in FWHM of the (0002) ZnO peak for the ZnO films irradiated at higher fluencies ($\leq 1x10^{16}$ cm^{-2}) were observed

when compared to the non-irradiated area. These changes must be related to radiation-induced damage. As seen in Fig.4.11, the (0002) ZnO peak for these films became a little broader than for the as-deposited sample, indicating a higher lattice disorder for the irradiated films. The calculated FWHM before and after irradiation presents a variation of 0% for the film irradiated with H^+ at a fluency of $1x10^{15}$ at/cm^2, 4% for the film irradiated at a fluency of $1x10^{16}$ at/cm^2, and 7% for the film irradiated at $1x10^{17}$ at/cm^2. These measurements indicate that the crystal quality of the films is not affected at fluencies of $1x10^{15}$ at/cm^2; it is very little affected at fluencies of $1x10^{16}$ at/cm^2 and it starts to degrade at fluencies of $1x10^{17}$ at/cm^2.

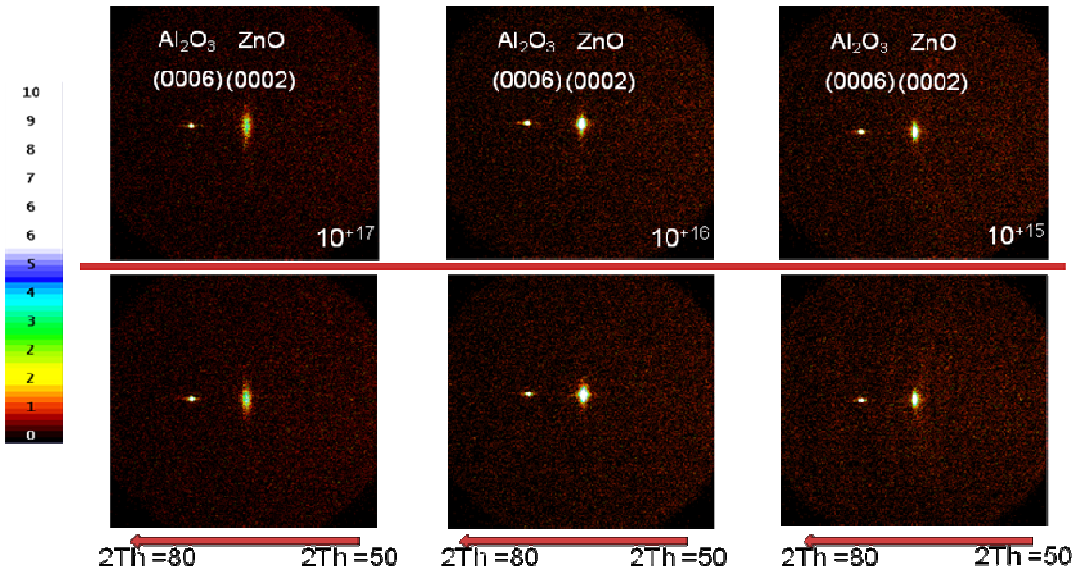

Fig.4.11. μ-XRD 2Θ/ω scans measurements before (upper) and after (lower) irradiation for ZnO films irradiated by different fluencies

RBS

The atomic composition of the ZnO films was determined before and after irradiation by comparing experimental and simulated non-RBS spectra measured in random configuration. The simulations were made using the SIMNRA code [34]. The results show that both

unirradiated and irradiated films are stoichiometric (Zn:O~1:1) within the resolution limit (0.9%). Thus, irradiation does not induce any significant change in the atomic composition of the films.

The radiation-induced damage in the Zn and in the O sublattices was studied separately from Non-RBS data taken in channelling configuration. The lattice order degree was obtained from the measured minimum yield in the angular scans. Non-RBS angular scan curves measured prior to and after irradiation are depicted in Fig.4.12. Before irradiation, it is observed that the χ_{min} for the Zn sublattice ($\chi^{zn}{}_{min}$) is significantly lower than that for the oxygen sublattice ($\chi^{o}{}_{min}$), which points out that in these films the order degree is better for the Zn than for the oxygen. The values for $\chi^{zn}{}_{min}$ are similar to the values obtained previously, while the values for the oxygen sublatices change from film to film. Since the films were not simultaneously deposited, the small differences observed in the χ_{min} for unirradiated films might be related to small changes in the oxygen sublattice order inherent to the deposition process at 600°C. The $\chi^{zn}{}_{min}$ and $\chi^{o}{}_{min}$ values measured prior to and after irradiation are graphed in Table 4.II.

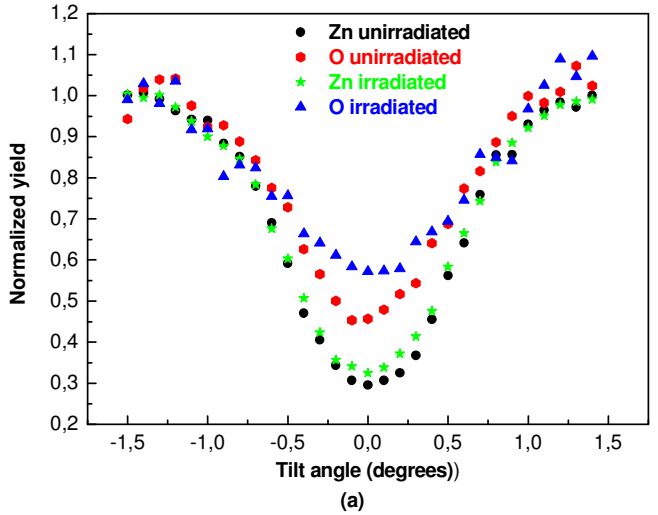

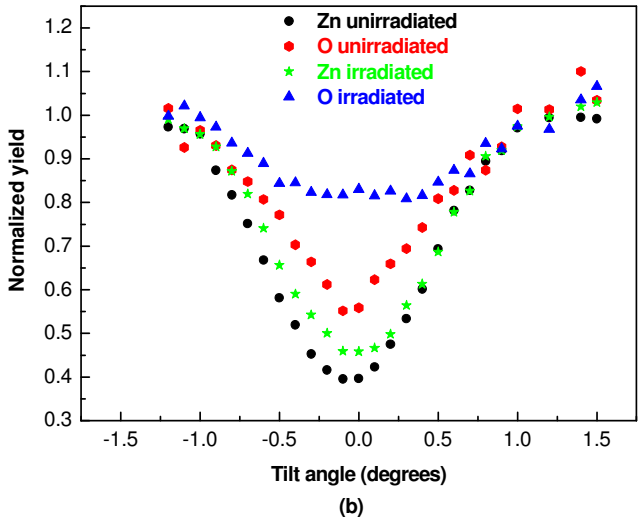

Fig.4.12. Non-RBS angular scan curves measured prior to and after irradiation with different fluencies: (a) $1x10^{15}$ cm^{-2} (b) $1x10^{17}cm^{-2}$

Table 4.II. χ^{zn}_{min} and χ^{o}_{min} values measured prior to and after irradiation with different fluencies

	Irradiation fluency (ion/cm^{-2})	Normalized χ^{zn}_{min}	Normalized χ^{o}_{min}
Unirradiated	-	0.30	0.46
Irradiated	1×10^{15}	0.32	0.57
Unirradiated	-	0.39	0.56
Irradiated	1×10^{17}	0.45	0.81

As illustrated in Table 4.II proton irradiation in the selected fluency range slightly enhances the χ^{zn}_{min} value, but substantially increases the χ^{o}_{min} one. These results show that irradiation with protons, in the energy regime mainly dominated by electronic processes, does not significantly modify the lattice order degree for the Zn sublattice at a fluence of 10^{15} at/cm^2 and a small reduction of the Zn sublattice order degree is observed for 10^{17} at/cm^2 irradiated film. The changes detected for the oxygen sublattice are larger, which

means that this sublattice degrades more than the Zn sublattice. So, in conclusion, by this procedure Zn and oxygen intrinsic defects are generated, being oxygen defects in higher concentration than Zn defects and both increasing with the irradiation fluencies.

Nevertheless, it is important to notice here that even when the ZnO epitaxial films are exposed at such very high irradiation fluencies 10^{17} at/cm^2 the number of generated defects is high, but still preserve crystalline features. These results confirm once again that ZnO films can be considered an appropriate option for application in irradiation environments.

4.2.3. Electrical properties-HALL measurements

Measurements of the electrical resistivity, carrier density and Hall mobility were performed on the films before and after irradiation.

Fig.4.13 shows the behavior of the electrical properties versus temperature in the range 30-300K for the ZnO film irradiated at a fluency of $1x10^{15}$ at/cm^2. When comparing the values obtained at RT, we see that there are slight variations. The electrical resistivity of the film increased a little after the irradiation from $1.4x10^{-3}$ to $1.9x10^{-3}$ Ωcm, but the values of carrier density and mobility did not change. The film presented *n*-type conductivity before the irradiation with a value of $2.5x10^{20}$ cm^{-3} of the carrier density. After the irradiation process the carrier density decreases to $2x10^{20}$ cm^{-3}, and still exhibits *n*-type conductivity. This is in agreement with a small increment of the mobility after irradiation from 12 to 15cm^{2}V^{-1}s^{-1}.

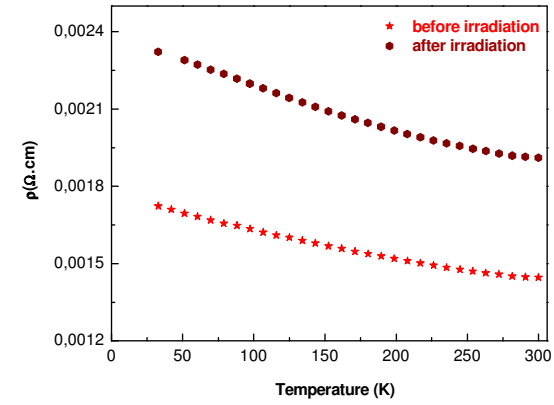

(a)

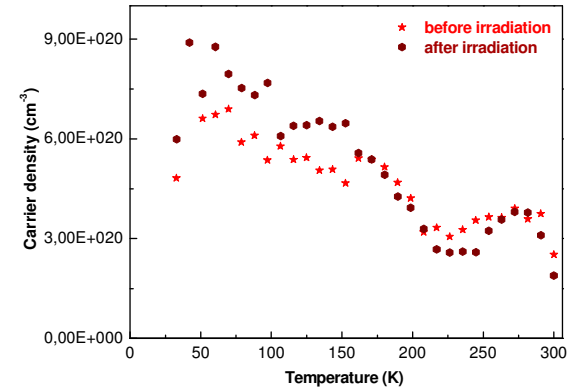

(b)

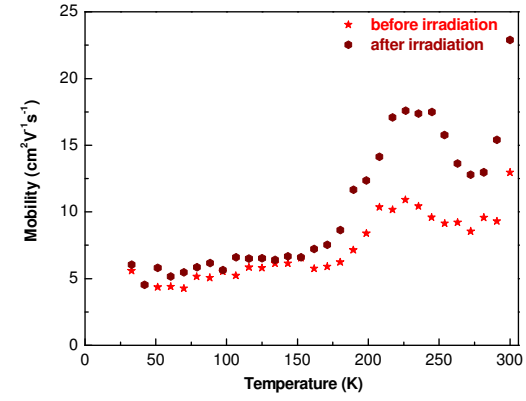

(c)

Fig.4.13. Electrical properties versus temperature in the range 30-300K, before and after irradiation, for ZnO film irradiated at a fluency of $1x10^{15}$ at/cm^2: (a) electrical resistivity, (b) carrier density, (c) mobility

The electrical properties versus temperature, before and after irradiation, in the range 30-300K for the ZnO film irradiated at a fluency of $1x10^{16}$ at/cm^2 are shown in Fig.4.14. As observed, at this fluency the electrical properties of the film change considerably. The carrier density presents a difference of one order magnitude before and after the irradiation, decreasing from $2x10^{21}$ to $4.8x10^{20}$ cm^{-3}. The film exhibited *n*-type conductivity before and after irradiation. Again, the decrease of the carrier density is in agreement with an increment of the mobility after irradiation from 1.5 to 6 cm^{2}V^{-1}s^{-1}. The electrical resistivity of the film increased after irradiation from $1.5x10^{-3}$ to $2.2x10^{-3}$ Ωcm.

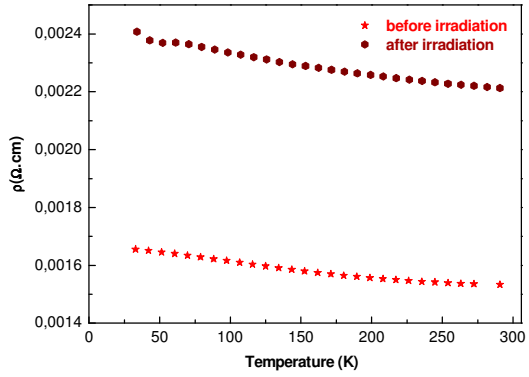

(a)

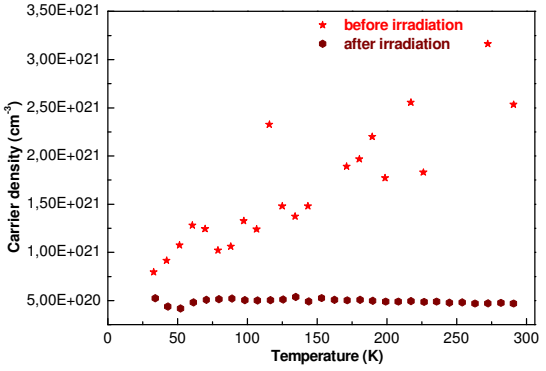

(b)

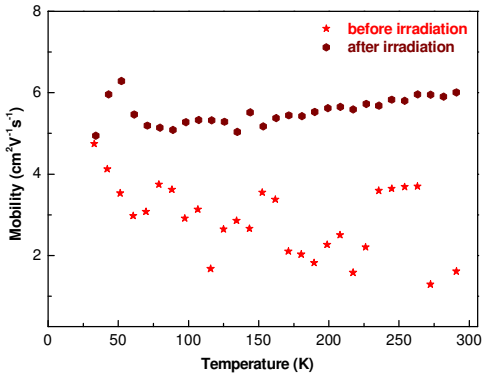

(c)

Fig.4.14. Electrical properties versus temperature in the range 30-300K for a ZnO film irradiated at a fluency of $1x10^{16}$ at/cm^2 before and after the irradiation process: (a) electrical resistivity, (b) carrier density, (c) mobility

Fig.4.15 shows the behavior of the electrical properties versus temperature in the range 30-300K for the ZnO film irradiated at a fluency of $1x10^{17}$ at/cm^2, before and after irradiation. In this case the difference between the electrical properties before and after the irradiation is significant. The electrical resistivity of the film increases after irradiation from $8x10^{-3}$ to $47x10^{-3}$ Ωcm. The mobility also changes considerably, by a factor of almost 10, increasing from 2.5 to 20 cm^{2}V^{-1} s^{-1} after the film has been exposed to the irradiation. The most significant change is observed for the carrier density, where a variation of 2 orders magnitude is obtained. The carrier density decreases from $3x10^{20}$ to $6x10^{18}$ cm^{-3} after the irradiation. Noteworthy is the fact that at this fluency, the type of the charge carriers of the film changes. Before the irradiation the film exhibited *n*-type conductivity. After the film it has been exposed to the irradiation, it presents *p*-type conductivity. The *p*-type behavior seems to be related with the crystal quality of the film and its intrinsic defects.

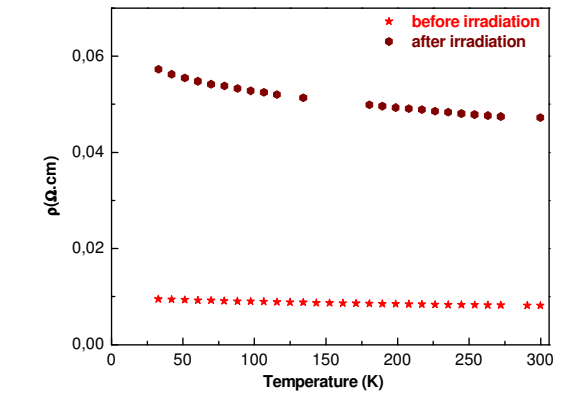

(a)

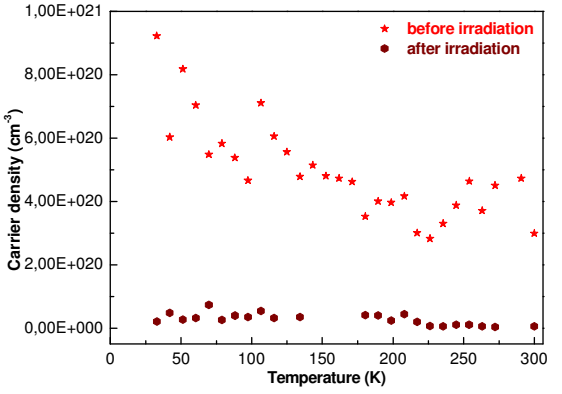

(b)

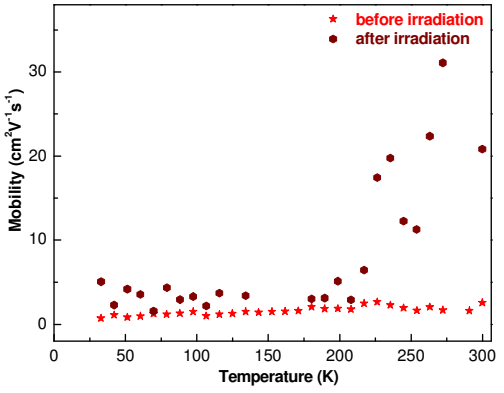

(c)

Fig.4.15. Electrical properties versus temperature in the range 30-300K for ZnO film irradiated at a fluency of $1x10^{17}$ at/cm^2, before and after the irradiation: (a) electrical resistivity, (b) carrier density, (c) mobility

These results are consistent with the previous ones, where it is shown that ZnO films grown at lower substrate temperature present poorer crystal quality (which means that it has more intrinsic defects) and exhibit *p*-type behavior.

Conclusions:

- ✓ ZnO films are proved to be hard radiation resistant materials up to a fluency of $1x10^{15}$ at/cm^2, suggesting that ZnO films are suitable for applications requiring high radiation tolerance.
- ✓ At a fluency of $1x10^{16}$ at/cm^2 the properties of ZnO films start to deteriorate.
- ✓ *At very high fluency of $1x10^{17}$ at/cm^2 major alterations are produced in ZnO films*; the crystal quality of the films irradiated at this fluency decreased, defects were generated in the crystal lattice *and as a consequence a change from n-type to p-type conductivity has been identified.*

4.3. Study of the *p*-type behavior by photoluminescence

It has been observed that as the growth temperature increases ZnO films change from *p*-type to *n*-type conductivity. Also, when increasing the number of intrinsic defects by irradiation the samples also change from *n*-type to *p*-type conductivity. Since the electrical transport properties of the films are not affected by the existence of twinning, a study of the intrinsic defects by photoluminescence has been performed on ZnO thin films.

The PL spectra of the ZnO films show several emission bands (see Fig.4.16). The Near-Band-Edge (NBE) UV luminescence dominates the spectrum with a maximum at 382 nm (3.24 eV) for the films grown at 300 and 500°C, and at 380 nm (3.26 eV) for the film grown at 600°C. It is interesting to note that the *p*-type film (grown at 300°C) shows a relatively stronger UV emission compared to the *n*-type film.

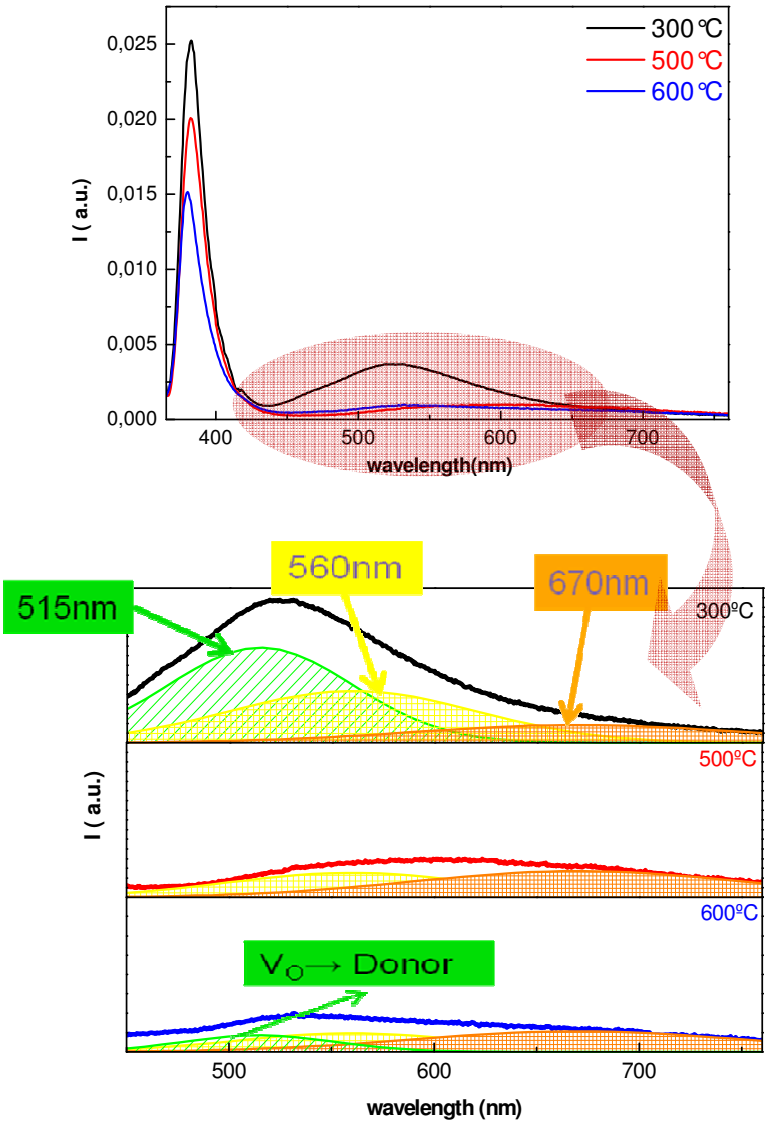

Fig.4.16. PL spectra of ZnO films grown at 300, 500 and 600°C. The measurements are performed at RT. The inset is a detail of the main figure together with the peak deconvolution.

In the visible range, weaker emission bands are observed. The strong UV emission and the weak visible bands reveal a high optical quality of the ZnO films. The bands in the visible region appear centered between 450-650 nm. These bands have to be correlated to defects or to impurities. Since our films are basically free of impurities, as confirmed by RBS and PIXE measurements, these bands should be associated to intrinsic defects. The emission at 500-650nm is too wide to be associated only to one defect, so it has been deconvoluted into three peaks: a green component centered at 515nm (2.41eV); a yellow at 560nm (2.21eV); and an orange-red centered at 670nm (1.85eV) (see inset of Fig.4.16). The integrated intensity for each peak has been normalized to the total visible intensity together with the thickness of each sample for comparison purpose. It can be observed that while the emission at 560nm and 670nm suffered minor changes, the peak at 515nm practically disappears for the film grown at 500°C. This band appears again for the film grown at 600°C, but with a different peak width, which could indicate a different defect origin. Taking all these into account, the defect that originated the emission at 515 nm could be associated with the origin of undoped *p*-type behavior. In the present thin films no unintentionally dopants have been introduced because the ZnO target was previously treated at 1300°C from high purity ZnO powders and as it was confirmed by PIXE measurement of the films.

The exact nature of the defects and/or impurities, which cause the visible emission in ZnO is still a subject of great controversy [35]. Theoretical calculations had suggested that there are some intrinsic defects, such as Zn vacancy, oxygen antisite, and oxygen interstitials, behaving as acceptors in ZnO. Among them, the Zn vacancy has the lowest formation energy in all the range of the Fermi energy and could be the main acceptor in intrinsic ZnO [36-38].

In order to clarify the origin of our emission the recent complete theoretical study of Janotti *et al.* [39] has been used. According to their calculations the following assignation was made*:* for the film grown at 300°C a small amount of Zn vacancies may be responsible for

the observed green luminescence. The calculated binding energy of V_{Zn} is 0.87 eV, which would yield the luminescence around 2.5 eV (515 nm) (see Fig.4.17). Zinc vacancies originate occupied states in the band gap and they act as deep acceptor. Moreover, Zinc vacancies have an annealing temperature around 300°C [39]. Therefore for higher temperatures they should disappear. This is in agreement with the study of Zhang *et al.*, where at temperatures >400°C zinc vacancies have disappeared and a loss of oxygen (that promotes the formation of oxygen vacancies V_O) has been observed [36,40]. The films grown at 200°C presents a more pronounced *p*-type behavior (see Fig.3.30), since the deposition temperature is lower that the Zn vacancies annealing. The green emission does not appear for the films grown at 500°C which exhibit *n*-type behavior. The green emission observed for the film grown at 600°C must be due to another kind of defects, different from zinc vacancies, which act as donors and disappear around 300K. One possibility is oxygen vacancies that present a binding energy at 2.51 eV [36, 40]. Z.Q. Chen *et al.* have also interpreted the inversion to *n*-type conductivity as the compensation effect by the ionized oxygen vacancy donor, which appears at a high growth temperature [41].

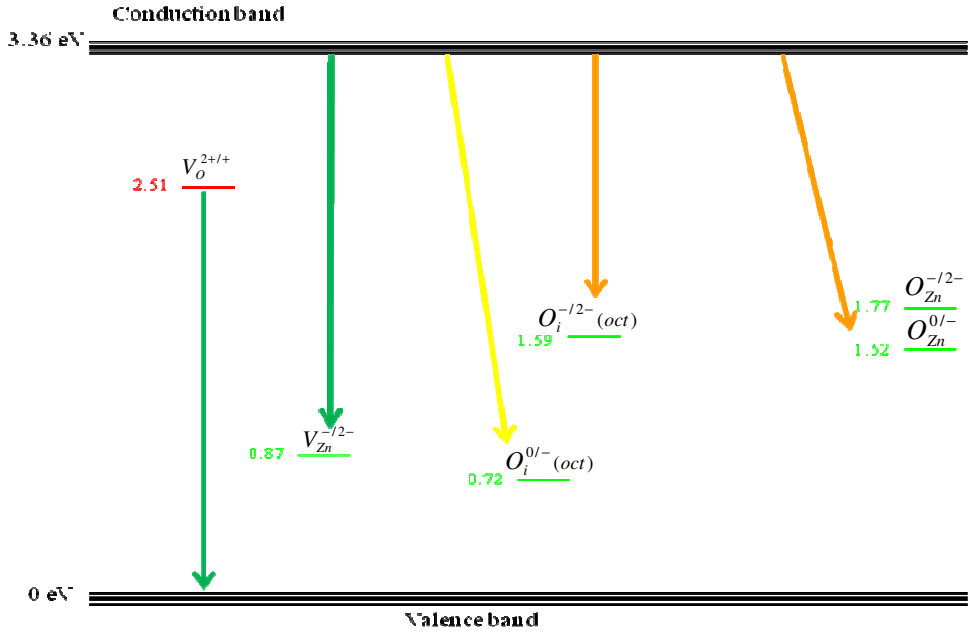

Fig.4.17. Possible emissions of ZnO (Adapted from Ref. [39,42,43]). The colors of the lines indicate the color of the different emissions

The appearance of *p*-type behavior is interesting since the ZnO target that has been used to produce the films was sintered at 1300°C and presented *n*-type behavior with Hall mobility of 20 $cm^2V^{-1}s^{-1}$ [44]. A possible explanation can be that the PLD process must keep only partially the pellet native defects while the growth of films at low temperatures ≤300°C produce a larger amount of zinc vacancies, which act as acceptors. In the structural characterization section of epitaxial ZnO thin films it has been shown that at lower growth temperatures the films have smaller grain sizes and higher disorder along the *c*-direction compared to the films grown at larger temperatures. An important effect of disorder in a system is that the electrons may get trapped in a particular lattice site or at the grain boundaries. Dutta *et al.* [45] found that annealing ZnO nanoparticles below 350°C produced a band tailing due to zinc vacancies, meanwhile annealing above 350°C oxygen vacancies were created in large number. Oxygen vacancies act as donors, so they are related to the *n*-type behavior. All these results are in agreement with our data. At lower growth temperature we have identified the presence of zinc vacancies (green emission in PL) and the ZnO films were less perfect, which played the role of trapping the electrons from the donor defects. Both things contribute to the *p*-type behavior as confirmed by Hall measurements. While more perfect ZnO epitaxial films (T_{growth} >400°C) were not as good trapping electrons and the higher treatment temperature made that zinc vacancies disappear and the oxygen vacancies appear, which act as donors and promotes the observed *n*-type behavior.

Conclusions:

- ✓ Photoluminescence emission in the visible range of the spectra is much weaker than the near-gap luminescence, indicating that the ZnO films are of high optical quality and with a relatively low number of defects.
- ✓ Based on PL measurements it can be concluded that PLD ZnO films grown at 200 and 300°C present *Zn vacancies that*

act as acceptors and could be the origin of p-type transport.

- ✓ The fact that the ZnO films grown at lower temperature are less perfect and with more grain boundaries play the role of trapping the electrons from the possible donor defects, enhancing the *p*-type behavior.
- ✓ The *n*-type conductivity of the ZnO films grown at temperature ≥400°C can be understood by considering that at higher temperatures the concentration of oxygen vacancies starts to increase and zinc vacancies disappear. These *oxygen vacancies act as deep donors, promoting the n-type behavior of ZnO.*
- ✓ As the growth temperature increases (≥400°C), the crystal lattice becomes more perfect, so it has less possibilities of trapping electrons. Therefore, the *n*-type behavior is enhanced.

4.4. Study of the aging mechanism

Another encountered issue when dealing with ZnO thin films is the fact that the *p*-type conductivity seems to have a "lifetime". In other words, generally a ZnO thin film which presents *p*-type conductivity tends to turn to *n*-type over time [46-48]. Xiang *et al.* reported that the *p*-type conductance of annealed ZnO:P NWs stored in air was found to persist for 2 months before showing *n*-type behavior [49]. On the other hand, Cao *et al.* have found that the *p*-type conductivity of their ZnO:P microwires was stable for about 6 months [50].

In order to check if the *p*-type behavior is maintained over time, the electrical properties of our *p*-type ZnO thin films have been measured over time. Fig.4.18 shows the electrical resistivity, carrier

density and Hall mobility measurements performed 0, 4, 7, and 12 months later, for a film grown at 200°C. During all this time the films have been stored in air at RT.

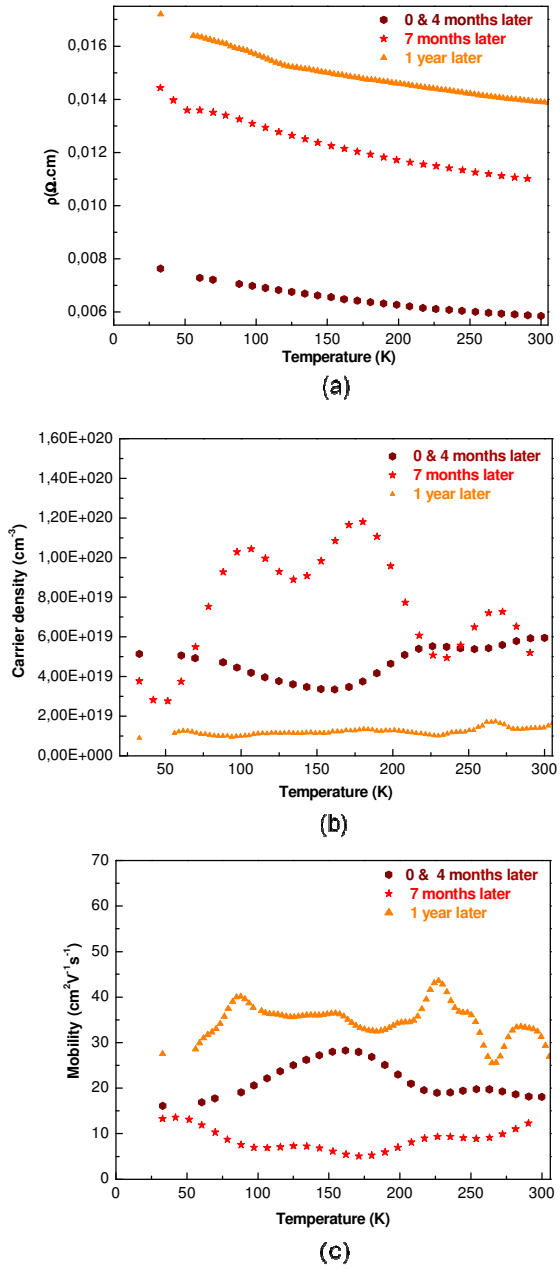

Fig.4.18. Electrical resistivity, carrier density and Hall mobility measurements performed early on, 4, 7 and 12 months later for a ZnO thin film grown at 200°C: (a) electrical resistivity, (b) carrier density, (c) mobility

The electrical properties just after the deposition were very similar to the ones performed after 4 months. Fig.4.19 shows the carrier density versus the time that passed since the film has been grown. As observed, 0, 4 and 7 months later the conductivity type was the same (*p*), with no significant change in their values. However, after 1 year the film became *n*-type. In order to estimate the time when the change from *p*-type to *n*-type conductivity had occurred, these data were adjusted to an exponential decay. According to this fitting, we can conclude that the film lost its *p*-type conductivity somewhere around the 10th month after the film was grown, see Fig.4.19.

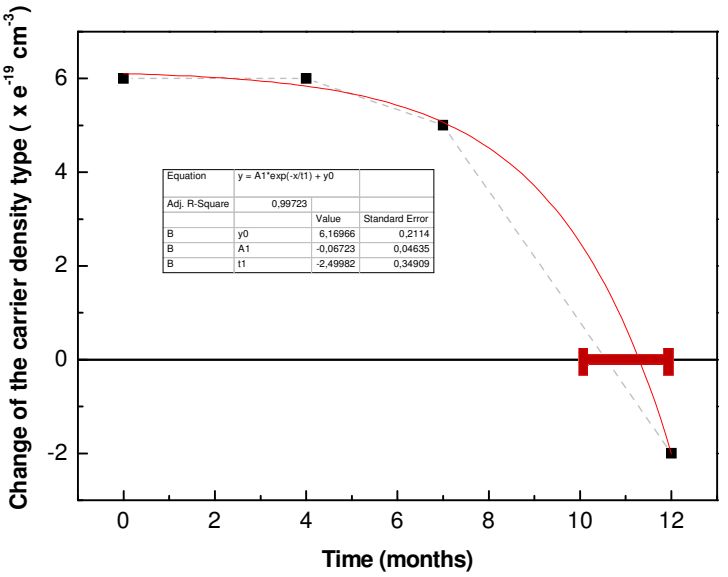

Fig.4.19. Carrier density versus the time that passed since the film has been grown

The fact that, as time passes, the conductivity changes from *p*-type to *n*-type, could be due to either a decrease of the *p*-type carrier, an increment of the *n*-type carrier, or both.

Few mechanisms have been suggested for the aging effect in ZnO, such as electron trapping, dipole orientation, ion migration, and oxygen desorption. However, among these mechanisms it seems that the migration of two type ions (both oxygen and zinc interstitials) is

the dominant one [51-53]. According to Janotti *et al.*, these types of defects have a migration temperature of 335 K and 219 K, respectively [39]. Therefore, they are mobile at room temperature. Moreover, it has also been observed by PL measurements over time that all the intrinsic defects tend to disappear slowly with time [54-56]. Their PL measurements revealed that the structure of the ZnO present less defects over time, as confirmed by a more intense NBE emission and lower green emission (see Fig.4.20) [54].

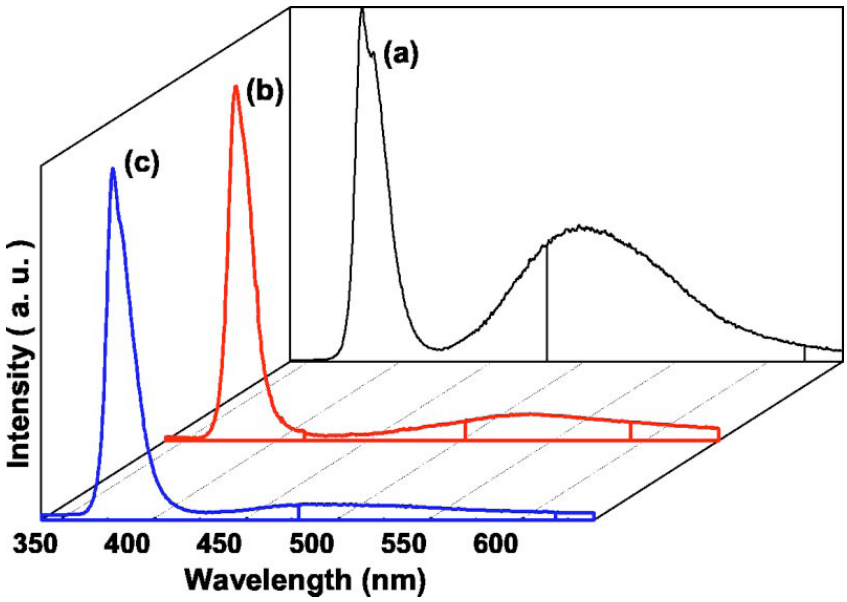

Fig.4.20. Aging effect of ZnO thin film deposited at 400°C on sapphire substrate. (Reprinted with permission from Ref. [54]. © 2005, American Institute of Physics)

Taking into account this information and knowing that $Zn^{2-}_{vacancies}$ could be the source of *p*-type behavior in our films as explained in the previous section, it could be assumed that the $Zn^{2+}_{interstitial}$ during the migration found $Zn^{2-}_{vacancies}$ producing a Zn in their lattice position, according to:

$$Zn^{2+}_{interstitial} + Zn^{2-}_{vacancies} = Zn_{lattice\ position} \qquad (1)$$

Although the following reaction could not be ruled out:

$$Zn^{2+}_{interstitial} + Zn^{2-}_{vacancies} = Zn^{0}_{interstitial} + Zn^{0}_{vacancies} \qquad (2)$$

Therefore both reactions will produce the reduction of Zn vacancies producing species which are not radiative.

Moreover, it has also been proposed by Chiang *et al.* [57] that when ZnO is acted by an electric field the previous reactions take place at the grain boundaries. So every time Hall measurements are performed ZnO is reducing its number of $Zn^{2-}_{vacancies}$ and consequently its *p*-type behavior. Hence these reactions (1 and 2) would explain why *p*-type ZnO becomes *n*-type over time.

Therefore it can be concluded that the decrease of the *p*-type carrier concentration over time is due to a reduction in the number of acceptors (according with reactions (1) and/or (2)), more than by an increment of the number of donors. Also, environmental factors like light, humidity, etc. may also contribute to the total aging effect.

Conclusions:

- ✓ The *p*-type behavior of our ZnO thin films was enduring for approximately 10 months.
- ✓ The decrease of the *p*-type carrier concentration over time might be related to the reduction of the acceptors more than an increment of the donors.

References

[1] C. H. Park, S. B. Zhang and S. H. Wei, Phys. Rev. B 66 (2002) 073202

[2] D. C. Look, D. C. Reynolds, C. W. Litton, R. L. Jones, D. B. Eason, G. Cantwell, Appl. Phys. Lett. 81 (2002) 1830

[3] A. Y. Polyakov, N. B. Smirnov, A. V. Govorkov, E. A. Kozhukhova, S. J. Pearton, D. P. Norton, A. Osinsky, A. Dabiran, J. Electron. Mater. 35 (2006) 663

[4] S. Graubner, C. Neumann, N. Volbers, B. K. Meyer, J. Bläsing, A. Krost, Appl. Phys. Lett. 90 (2007) 042103

[5] A. Kobayashi, O. F. Sankey, J. D. Dow, Phys. Rev. B 28 (1983) 946

[6] B. Claflin, D.C. Look, S.J. Park, G. Cantwell, J. Cryst. Growth 287 (2006)16

[7] Y.W. Heo, Y.W. Kwon, Y.Li, S.J. Pearton, D.P. Norton, Appl. Phys. Lett. 84 (2004) 3474

[8] K.K. Kim, H.S. Kim, D.K. Hwang, J.H. Lim, S.J. Park, Appl. Phys. Lett. 83 (2003) 63

[9] F.X. Xiu, Z. Yang, L.J. Mandalapu, J.L. Liu, W.P. Beyermann, Appl. Phys. Lett. 88 (2006) 052106

[10] Y.R. Ryu, T.S. Lee, H.W. White, Appl. Phys. Lett. 83 (2003) 87

[11] D.C. Look, G.M. Renlund, R.H. Burgener II, J.R. Sizelove, Appl. Phys. Lett. 85 (2004) 5269

[12] F.X. Xiu. Z. Yang, L.J. Mandalapu, D.T. Zhao, J.L. Liu, Appl. Phys. Lett. 87 (2005) 152101

[13] S. Limpijumnong, S.B. Zhang, S.H. Wei, C.H. Park, Phys. Rev. Lett. 92 (2004) 155504

[14] W.J. Lee, J. Kang, K.J. Chang, Phys. Rev. B 73 (2006) 024117

[15] T.V. Butkhuzi, A.V. Bureyev, A.N. Georgobiani, N.P. Kekelidze, T.G. Khulordava, J. Cryst. Growth 117 (1992) 366

[16] A.N. Georgobiani, M.B. Kotlyarevskii, V.V. Kidalov, L.S. Lepnev, I.V. Rogozin, Inorganic Materials 37, 11 (2001) 1095

[17] G. Xiong, J. Wilkinson, B. Mischuck, S. Tuzemen, K.B. User, R.T. Williams, Appl. Phys. Lett. 80 (2002) 1195

[18] Y.Ma, G.T. Du, S.R. Yang, Z.T. Li, B.J. Zhao, X.T. Yang, T.P. Yang, Y.T. Zhang, D.L. Liu, J. Appl. Phys. 95,11 (2004) 6268

[19] M.S. Oh, S.H. Kim, T.Y. Seong, Appl. Phys. Lett. 87 (2005) 122103

[20] Y.J. Zeng, Z.Z. Ye, W.Z. Xu, J.G. Lu, H.P. He, L.P. Zhu, B.H. Zhao, Appl. Phys. Lett. 88 (2006) 262103

[21] Y.F. Hsu, Y.Y. Xi, K.H. Tam, A.B. Djurisic, J. Luo, C.C. Ling, C.K. Cheung, A.M.C. Ng, W.K. Chan, X. Deng, C.D. Beling, S. Fung, K.W. Cheah, P.W.K. Fong, C.C. Surya, Adv. Funct. Mater. 18 (2008) 1020

[22] I. Ohkubo, A. Ohtomo, T. Ohnishi, Y. Matsumoto, H. Koinuma, M. Kawasaki, Surf. Sci. 443 (1999) L1043

[23] S.H. Park, S.Y. Seo, S.H. Kim, S.W. Han, Appl. Phys. Lett. 88 (2006) 251903

[24] B. Zhang, L. Manh, K. Wakatsuki, K. Tamura, T. Ohnishi, M. Lippmaa, N. Usami, M. Kawasaki, H. Koinuma, Y. Segawa, Jpn. J. Appl. Phys. Part 2 42 (2003) L264

[25] R.D. Vispute, V. Talyansky, Z. Trajanovic, S. Choopun, M. Downes, R.P. Sharma, T. Venkatesan, M.C. Woods, R.T. Lareau, K.A. Jones, A.A. Iliadis, Appl. Phys. Lett. 70 (1997) 2735

[26] I.W. Kim, K.M. Lee, Thin Solid Films 516 (2008) 4921

[27] C.S. Steplecaru, M.S. Martin-Gonzalez, J.F. Fernandez, J.L. Costa-Krämer, Thin Solid Films 518 (2010) 4630

[28] T. Ono, Y. Suda, M. Akazawa, Y. Sakai, K. Suzuki, Jpn. J. Appl. Phys. Vol. 41 (2002) 4651

[29] J. Toofan, P.R. Watson, Surf. Sci. 401 (1998) 162

[30] B.S. Kang, H.T. Wang, L.C. Tien, F. Ren, B.P. Gila, D.P. Norton, C.R. Abernathy, J. Lin, S.J. Pearton, Sensors 6 (2006) 643

[31] D.C. Look, Materials Science and Engineering B80 (2001) 383

[32] J. F. Ziegler, M. D. Ziegler, J. P. Biersack SRIM-2006.02

[33] http ://conferences.esa.int/96a09/Abstracts/abstract45/paper/

[34] M. Mayer, SIMNRA, Version 5.02, Max Plank Institut für Plasmaphysik

[35] A.B. Djurisic, Y.H. Leung, Small 2 (2006) 944

[36] S.B. Zhang, S.H. Wei, A. Zunger, Phys. Rev. B 63 (2001) 075205

[37] A.F. Kohan, G. Ceder, D.Morgan, Phys. Rev. B 61 (2000) 15019

[38] F. Tuomisto, V. Ranki, K. Saarinen, D.C. Look, Phys. Rev. Lett. 91 (2003) 205502

[39] A. Janotti, C.G. Van de Walle, Phys. Rev. B 76 (2007) 165202

[40] F.H. Leiter, H.R. Alves, A. Hofstaetter, D. Hofmann, B. K. Meyer, Phys. Status Solidi B 226 (2001) R4

[41] Z.Q. Chen, S. Yamamoto, M. Maekawa, A. Kawasuso, X.L. Yuan, T. Sekiguchi, J. Appl. Phys. 94 (2003) 4807

[42] D. Alegre, DEA "Fotoluminiscencia de películas de ZnO obtenidas mediante electrodeposición" presented in 2008

[43] C.V. Manzano, D. Alegre, M.S. Martin-Gonzalez, in preparation

[44] F. Rubio-Marcos, A. Quesada, M.A. García, M.A. Bañares, J.L.G. Fierro, M.S. Martin-González, J.L. Costa-Krämer, J.F. Fernández, J. Sol. Sta. Chem. 182 (2009) 1211

[45] S. Dutta, S. Chattopadhyay, A. Sarkar, M. Chakrabart, D. Sanyal, D. Jana, Progress in Mat. Sci. 54 (2009) 89

[46] K. Minegishi, Y. Koiwai, Y. Kikuchi, K. Yano, M. Kasuga, A. Shimizu, Jpn. Appl. Phys. 36 (1997) L1453

[47] X.L. Guo, H. Tabata, T. Kawai, J. Cryst. Growth 223 (2001) 135

[48] L.G. Wang, A. Zunger, Phys. Rev. Lett. 90 (2003) 256401

[49] B. Xiang, P. Wang, X. Zhang, S.A. Dayeh, D.P.R. Aplin, C. Soci, D. Yu, D. Wang, Nano Letters 7, 2, (2007) 323

[50] B.Q. Cao, M. Lorentz, H. von Wenckstern, J. Lenzner, G. Biehne, M. Grundmann, Phys. Stat. Sol. (RRL) 2, 1 (2008) 37

[51] T.K. Gupta, J. Am. Ceram. Soc. 73 (1990) 1817

[52] T.K. Gupta, W.G. Carlson, P.L. Hower, J. Appl. Phys. 52 (1981) 4104

[53] M. Hayashi, M. Haba, S. Hirano, M. Okamoto, M. Watanabe, J. Appl. Phys. 53 (1982) 5754

[54] F.K. Shan, G.X. Liu, W.J. Lee, G.H. Lee, I.S. Kim, B.C. Shinb, Appl. Phys. Lett. 86 (2005) 221910

[55] L. Xu, L. Shi, X. Li, Appl. Surf. Sci. 255 (2009) 5957

[56] F.K. Shan, Z.F. Liu, G.X. Liu, W.J. Lee, G.H. Lee, I.S. Kim, B.C. Shin, Y.S. Yu, J. Electr. 13 (2004) 195

[57] Y.M. Chiang, W.D. Kingery, L.M. Levinson, J. Appl. Phys. 53 (1982) 1765

5

ZnO WITH TRANSITION METAL. Zn-O-Co SYSTEM: DIFFERENT APPROACHES

Chapter 5

ZnO with cobalt oxides (Zn-O-Co): Different approaches

As we have seen in the introduction chapter, the results obtained by different research groups are questionable, but it can be concluded that FM depends on the sample preparation method, and it might be related to interfaces. Moreover, a study comparing the experimental results obtained for *p*-type and *n*-type ZnO system has not been reported to date. Therefore, motivated by the need to understand the origin of the magnetic properties in the Zn-O-Co system, this chapter is dedicated to a complete study of the Zn-O-Co system made by different approaches, and comparing the results obtained for *p*- and *n*-type ZnO when mixed with cobalt by different techniques.

5.1. ZnO/Co_3O_4 co-growth

A first possible approach to study the Zn-O-Co system was by ZnO/Co_3O_4 co-growth. In other words, the Zn-O-Co thin films would be deposited by PLD using a ZnO/Co_3O_4 target. For that purpose, ZnO/Co_3O_4 pellets have been prepared by conventional ceramic routes, as explained in the experimental technique section. In order to eliminate any possible contamination, during all this procedure, no metallic tools, containers or sieves were used [1]. Afterwards the obtained ceramic disks were thermally treated between 500 and 1000°C

for 12 hours. The pellet composition was determined with an error of ±0.5%. The structural characterization was also performed on the obtained ceramic pellets.

Fig.5.1 shows the 2Θ/ω X-Ray diffraction patterns of the pellets sintered at different temperatures. The pellets are polycrystalline and all the diffraction maxima can be indexed with the Co_3O_4 lattice (marked with asterisks) and hexagonal wurtzite ZnO lattice (non-indexed maxima). According to the phase diagram for T > 450°C only the spinel exists. However, from the X-Ray diffraction patterns we cannot identify the $ZnCo_2O_4$ spinel, due to the fact that the $ZnCo_2O_4$ spinel and Co_3O_4 are isostructural. At 800°C the Co_3O_4 diffraction maxima started to disappear, and disappeared completely at temperatures >800°C. Thus after annealing above 800°C there is no more Co_3O_4 present. No new peaks were identified up to the resolution limit of our XRD system. A possible explanation for these XRD patterns is that between ZnO and Co_3O_4 a reaction took place, and as a result a solid solution $Zn_{1-x}Co_xO$ was formed. This solid solution would have a wurtzite-type structure with the same lattice parameter as ZnO, and this could justify why only ZnO diffraction maxima are identified in the XRD patterns above the 800°C. This was consistent with the theoretical predictions for the phase diagram of the Zn-O:Co-O mixture made by J. Robin, as seen in Fig.5.2 [2].

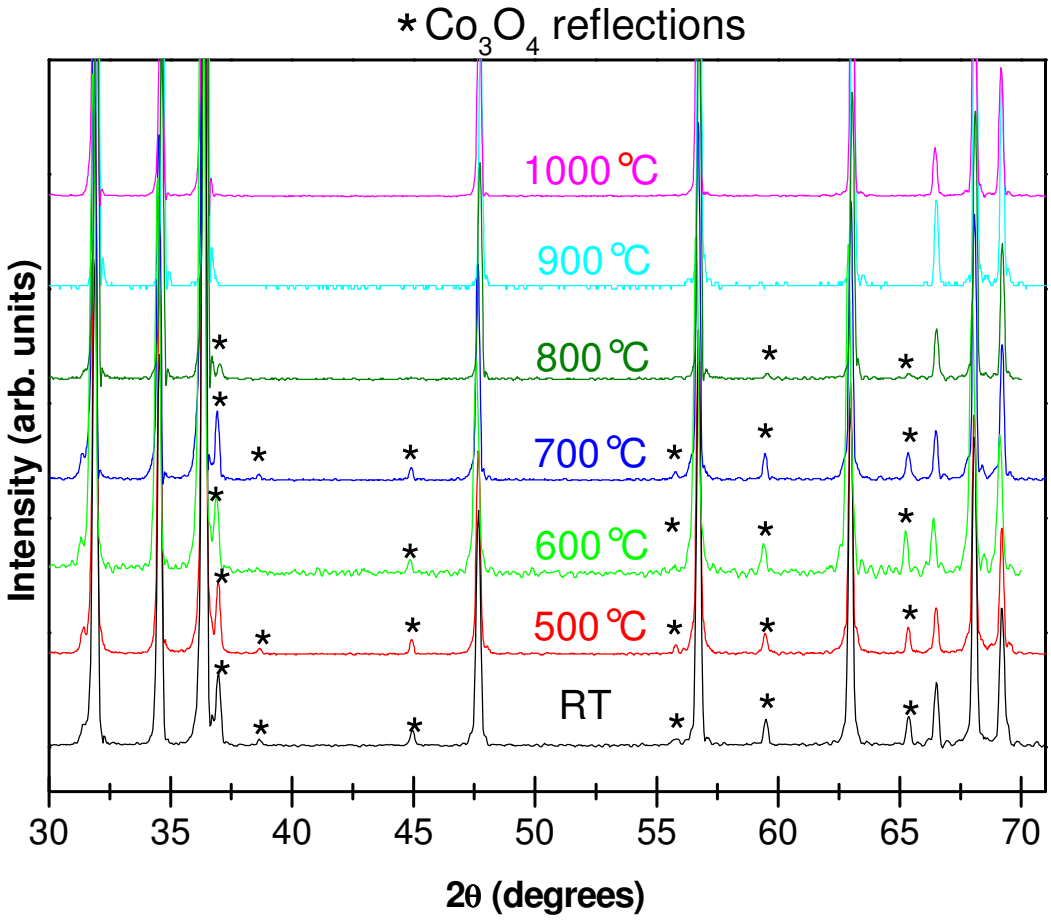

Fig.5.1. 2Θ/ω X-Ray diffraction pattern of (ZnO)/(Co_3O_4) pellets sintered at different temperatures. The Co_3O_4 diffraction maxima are indicated by asterisks; the other maxima correspond to ZnO

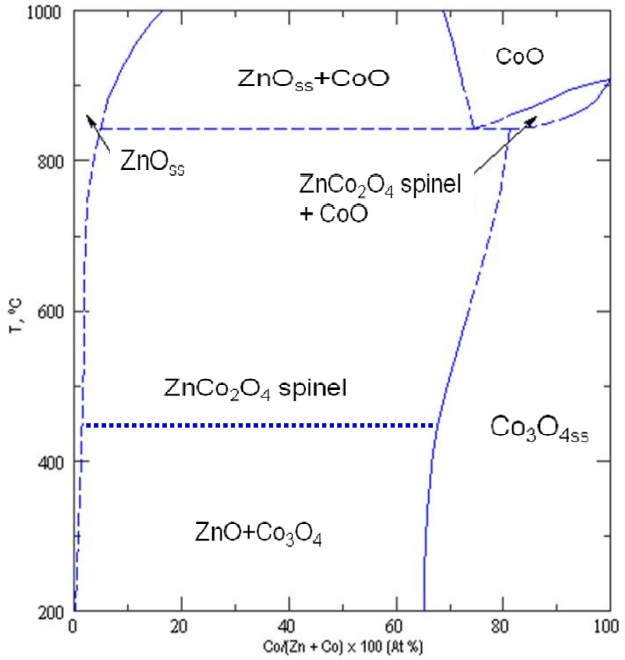

Fig.5.2. Phase Diagram Zn-O:Co-O mixture (Adapted from Ref. [2])

In Quesada *et al.* work the highest magnetization is obtained for the pellets which were not exposed to heat treatment [3]. When representing the Saturation Magnetization (M_S) versus the sintering temperature (Fig.5.3) it can be concluded that annealing the pellets produces a decrease of their FM. The M_S decreased when the sintering temperature increased, and disappeared totally for temperatures above 800°C.

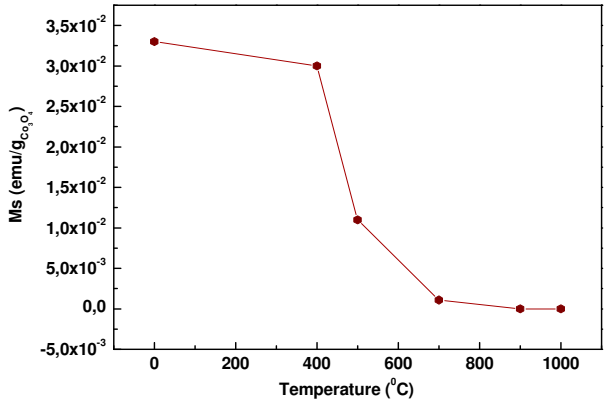

Fig.5.3. Saturation magnetization versus the sintering temperature for ZnO/Co_3O_4 pellets (Adapted from Ref. [3])

However, we did not use these pellets to deposit Zn-O-Co thin films by PLD. The low temperature pellets where the mixture of ZnO/Co_3O_4 is present are not dense enough to avoid pitting problems during PLD film growth. On the other hand, the targets sintered at high temperature are dense enough, but instead of a mixture of Co_3O_4 with ZnO the $ZnCo_2O_4$ spinel phase is present (which is non-ferromagnetic and it is very stable). So this route was discarded.

Conclusions:

- ✓ In the ZnO/Co_3O_4 pellets the following reactions path take place upon increasing the annealing temperature:

$$ZnO/Co_3O_4 \xrightarrow{T>450^0C} ZnO/\ ZnCo_2O_4 \xrightarrow{T>800^0C} Zn_{1-x}Co_xO_{\ ss}$$

- ✓ The saturation moment of ZnO/Co_3O_4 pellets decreases when the sintering temperature increases, disappearing eventually for temperatures above 800°C when the solid solution is formed.
- ✓ The ZnO/Co_3O_4 pellets were not suitable for our study.

5.2. ZnO/Co_3O_4 multilayers

So the next possibility explored was the preparation of ZnO/Co_3O_4 multilayers using two different targets optimized for each compound. Also, the appearance of ferromagnetic behavior in ZnO/Co_3O_4 pellets is believed to be mediated by a solid-state electrochemical reaction involving superficial OH (created by exposition of the oxides surface to ambient conditions) [4]. These conditions are obviously not the same as in our PLD vacuum chamber. According to theoretical studies an important property of compounds with strong ionic character is the

effect of surface charge on the stability of polar surfaces and interfaces [5-7]. The charge compensation is responsible for important modifications of the surface atomic and electronic structure [5-10]. Recently it has been shown that Co_3O_4 thin films grown by MBE exhibit (1x1) surfaces according to LEED. The (1 x 1) pattern was attributed to a surface structure consisting of a Co-terminated layer, with large relaxations of the top four atomic layers, which could lead to charge compensation and to surface stability [6]. This has been attributed to the conversion of tetrahedral Co^{2+} cations to a trivalent state, which corresponds to an inversion in the spinel structure at the surface [11,12]. If a ferrimagnetic signal appears due to a change in the valence band of the Co^{3+} in octahedral coordination of just mixed Co_3O_4 and ZnO nanoparticles, maybe a similar magnetic signal could also arise at ZnO/Co_3O_4 interphases according with the theory just outlined. This motivation leads towards a study of ZnO/Co_3O_4 multilayers, to test if the effect could be controlled and maximized.

Before studying the properties of the ZnO/Co_3O_4 multilayers, it is appropriate understanding the properties of each material separately. At this stage, we already control the technique of growing epitaxial *n*- and *p*-type ZnO thin films. We are familiar with the properties of this wide bandgap semiconductor material and comprehend its behavior. Therefore, the next step towards the preparation of the ZnO/Co_3O_4 multilayers is understanding Co_3O_4 thin films grown on ZnO, and only afterwards the ZnO/Co_3O_4 multilayers will be investigated.

5.2.1. Co_3O_4 thin films

5.2.1.1. Co_3O_4 targets

The Co_3O_4 targets were prepared by conventional ceramic routes, using high purity (>99.99% Aldrich) Co_3O_4 raw powder. The densities of the different targets were calculated by the immersion Archimedes method using mercury as a liquid and are shown in Table 5.I.

Table 5.I. Densities of the Co_3O_4 targets sintered at different temperatures

Sintering Temperature (°C)	Time (h)	Density (g/cm^3)
600	12	2.71
700	12	6.67
800	12	3.70
1000	12	4.12

Fig.5.4 shows the 2Θ/ω X-Ray diffraction pattern of high density Co_3O_4 pellets sintered at different temperatures. The pellets are polycrystalline in all the cases. For the pellets sintered at 600 and 700°C all the diffraction maxima can be indexed with the cubic Co_3O_4 lattice (JCPDS 42-1467, a = 8.0837 Å, and spatial group Fd3m) [13]. As the sintering temperature increases above 800°C, the CoO cubic structure is identified (JCPDS 48-1719, a = 4.2612 Å, and spatial group Fm3m) [14], and became dominant at a temperature of 1000°C as expected. This behavior explains the variation in density observed in Table 5.I.

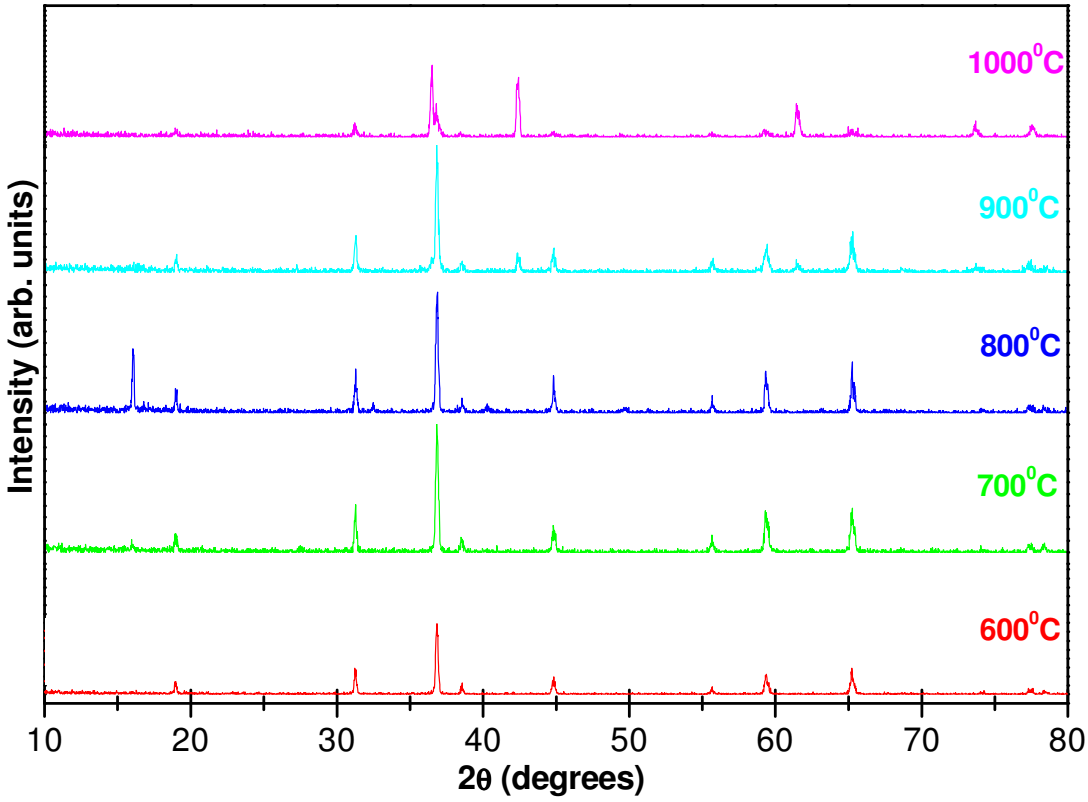

Fig.5.4. 2Θ/ω X-Ray diffraction pattern of high density Co_3O_4 pellets sintered at different temperatures

Therefore, taking into account that the theoretical density of Co_3O_4 is 6.11 g/cm^3 and the X-ray diffraction data, it can be concluded that: the pellets made from high-purity Co_3O_4 powder sintered at 700°C for 12 hours are the ones most suitable to be used as PLD target.

The characterization of the electrical properties performed by Hall effect measurements reveled that all pellets exhibit a *p*-type semiconductor behavior. The electrical resistivity of high density Co_3O_4 pellets is depicted in Fig.5.5. The Co_3O_4 pellets sintered at 700°C present a very high resistivity of 3.9×10^3 Ωcm and low carrier density of 1×10^{13} cm^{-3} at RT.

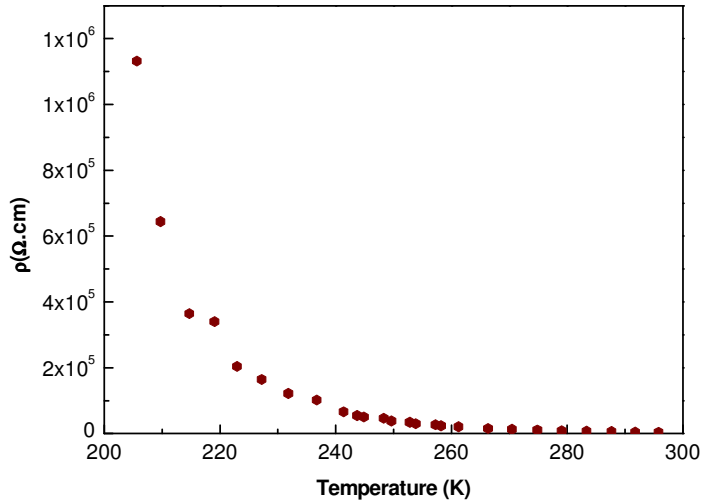

Fig.5.5. Electrical resistivity of high density Co_3O_4 pellets sintered at 700°C

5.2.1.2. Polycrystalline Co_3O_4 thin films

The Co_3O_4 ceramic pellets sintered at 700°C, with typical radius of 2cm and thickness of 2mm, were used as target for PLD. In order to remove dust and surface contamination, the substrates were prepared by the routine chemical cleaning.

The first attempts to deposit Co_3O_4 thin films were on silicon substrates at the temperature of 400°C in $1.2x10^{-2}$ mbar oxygen pressure.

Fig.5.6 shows the XRD 2Θ/ω scans for the Co_3O_4 films grown directly on silicon, and using a buffer ZnO layer on top of the silicon substrate. It can be seen that in the former case the Co_3O_4 thin films obtained are amorphous, since no diffraction maxima different than the silicon substrates are detected. In the latter case, all the diffraction maxima are indexed with the substrate (JCPDS 27-1402, a = 5.4308 Å, and spatial group Fd3m [15]), with the hexagonal wurtzite ZnO

lattice (JCPDS 76-0704, a = 3.250 Å, c = 5.207 Å and spatial group P63mc [16]), and with the Co_3O_4 lattice (JCPDS 42-1467, a = 8.0837 Å, and spatial group Fd3m [13]). The Co_3O_4 diffraction maxima correspond to (111), (311), (222) and (511) plane, which implies that the films are polycrystalline. However, not all diffraction maxima of a polycrystalline Co_3O_4 powder appear, since (220), (400), (422) and (440) are not identified. This means that although the film is polycrystalline it shows a preferential orientation along the cube diagonal direction.

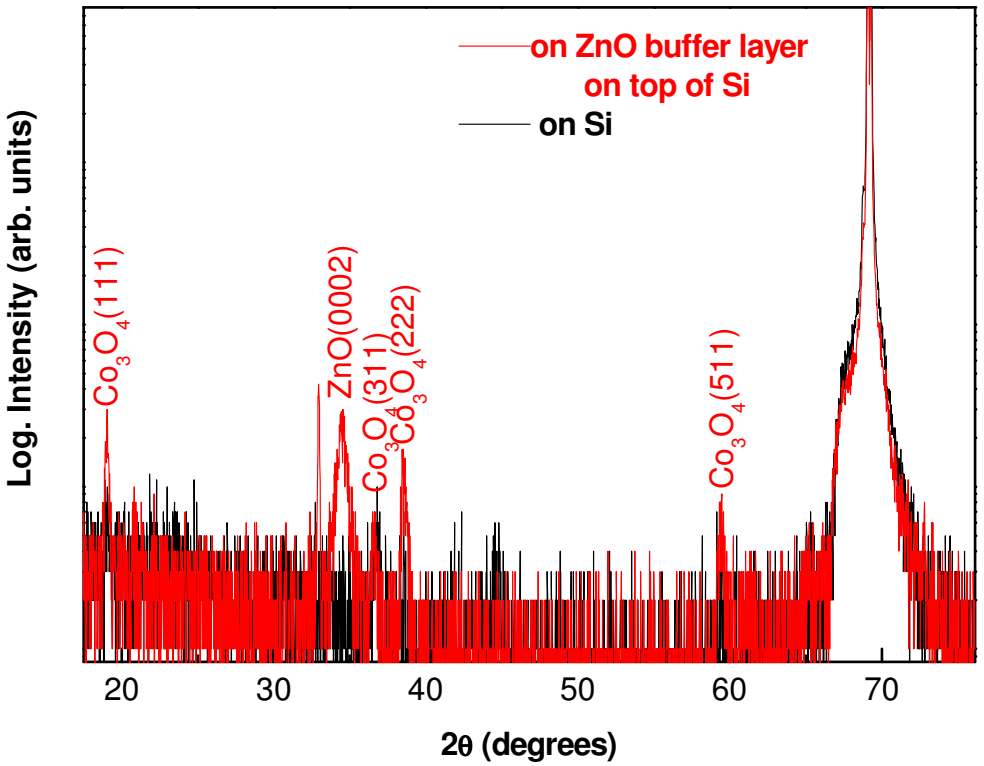

Fig.5.6. 2Θ/ω XRD scans for the Co_3O_4 films grown at 400°C, in $1.2x10^{-2}$ mbar oxygen pressure, but on different substrates: directly on silicon and on a buffer ZnO layer on top of the silicon substrate

Measurements of the electrical properties were also performed on these Co_3O_4 films, revealing their *p*-type conductivity. Fig.5.7 shows the electrical resistivity (a) and carrier density (b) versus temperature for Co_3O_4 thin films grown on ZnO buffer layers. The values of the

electrical resistivity and carrier density at RT are $6x10^{-1}$ Ωcm and $4x10^{17}$ cm^{-3}, respectively. Comparing these values with the ones obtained for the Co_3O_4 pellets ($3.9x10^3$ Ωcm and carrier density of $1x10^{13}$ cm^{-3} at RT), it is observed that the films exhibit better electrical properties: much lower resistivity and larger carrier density.

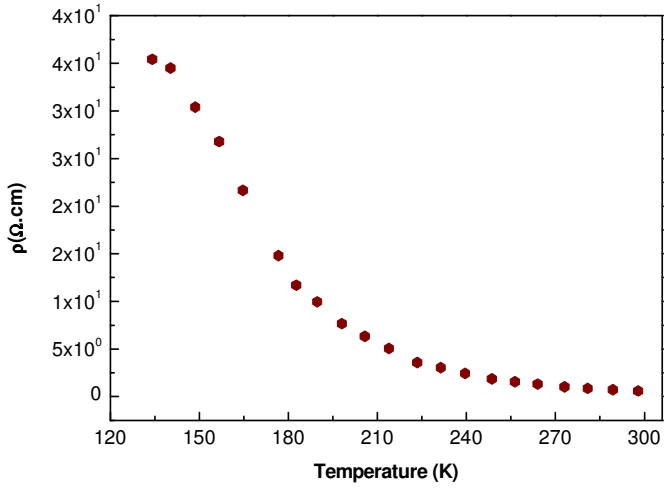

(a)

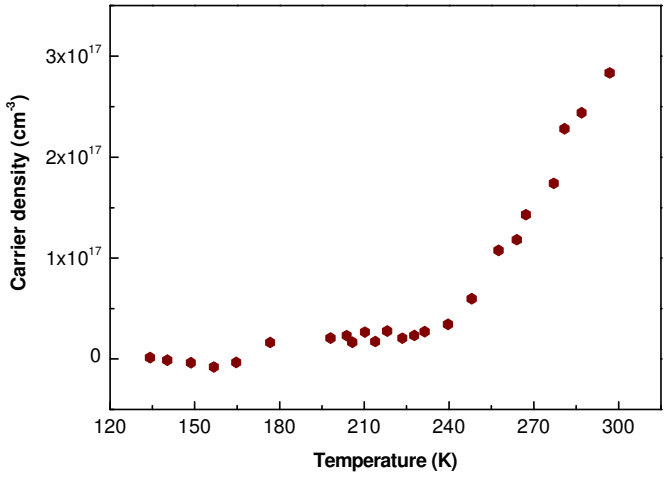

(b)

Fig.5.7. Electrical resistivity (a) and carrier density (b) versus temperature for Co_3O_4 thin films grown on ZnO buffer layer deposited on top of Si substrate, at 400°C in $1.2x10^{-2}$ mbar oxygen pressure

There are few experimental reports on the electrical properties of polycrystalline Co_3O_4 thin films in the literature. Patil *et al.* [17] have studied the electrical properties of Co_3O_4 thin films deposited by spray pyrolysis technique on amorphous glass substrate. Their films exhibited semiconductor behavior with electrical resistivity of $2x10^2$ Ωcm and carrier density of $2.4x10^{19}$ cm^{-3} at RT. Ten years later, Shinde *et al.* [18] reproduced that experiment obtaining an electrical resistivity at RT of the order $1.5x10^3$ Ωcm. It is important to highlight here that the electrical properties of our polycrystalline Co_3O_4 thin films deposited by PLD were better than the ones reported in the literature (presenting lower electrical resistivity, see Table.5.II). Nevertheless, our aim is the optimization of the growth conditions in order to obtain epitaxial Co_3O_4 thin films.

Table.5.II. Electrical properties of polycrystalline *p*-type Co_3O_4 thin films reported so far

Growth method	Electrical resistivity(Ωcm)	Carrier density (cm^{-3})	Ref.
Spray pyrolisis	200	$2.4x10^{19}$	[17]
Spray pyrolisis	1500	-	[18]
PLD	60	$4x10^{17}$	Our data

5.2.1.3. Epitaxial Co_3O_4 thin films

Thin films of cobalt oxide have been previously obtained by several methods, as mentioned above, but epitaxial film growth has been reported only a very few times. Highly oriented epitaxial films have been reported by MOCVD on $SrTiO_3$ and on MgO (100) at T≥400°C [19,20], Atomic Layer Deposition (ALD) on SiO_2/Si(100), MgO(001) and sapphire [21,22], MBE [23], and PLD on $SrTiO_3$ (100) at 540°C [24]. In our case, since the final purpose is to grow ZnO/Co_3O_4

multilayers, epitaxial ZnO on sapphire was used as the substrate. Various sets of Co_3O_4 thin films have been grown by PLD at different growth temperatures. The targets were the same than the ones used for polycrystalline growth. The growth temperature was ranging from *300°C to 600°C*.

a) Structural characterization

Thicknesses

The films thicknesses vary from 70nm for the film grown at 300°C to 36nm for the one grown at 600°C. Comparing these values with the ones corresponding to the ZnO thin films grown at the same temperature (275nm and 80nm, respectively), it can be seen that the deposition rate of ZnO is 4 times higher than the one for Co_3O_4.

X-ray diffraction

Fig.5.8 shows XRD 2Θ/ω scans for the Co_3O_4 thin films grown on (0001) sapphire substrates under the same oxygen pressure (Po_2=1.2 x10^{-2} mbar), but at different temperatures (from 300-600°C). For the film grown at 300°C, the diffraction maxima can be indexed with the corundum/ rhombohedral structure of the sapphire substrate (JCPDS 43-1484), the hexagonal wurtzite ZnO lattice (JCPDS 76-0704), and the Co_3O_4 lattice (JCPDS 42-1467). The Co_3O_4 diffraction maxima observed correspond to (222) plane, indicating that the Co_3O_4 films are crystalline and highly oriented along the [111] direction. For the film grown at 500°C, the diffraction maxima can be indexed with the sapphire substrate (JCPDS 43-1484), and with the Co_3O_4 lattice (JCPDS 42-1467). The Co_3O_4 diffraction maxima observed correspond to (400) plane, which implies that the Co_3O_4 film grown at this temperature was oriented along the [100] direction. For the (222) plane

of the Co_3O_4 lattice just a very weak reflection can be notice. It seems that at this temperature a reaction took place between the ZnO and Co_3O_4, and the spinel $ZnCo_2O_4$ started to form, as deduced from the weak (311) reflection of the spinel $ZnCo_2O_4$ (JCPDS 81-2299, a = 8.1019 Å, and spatial group Fd3m).

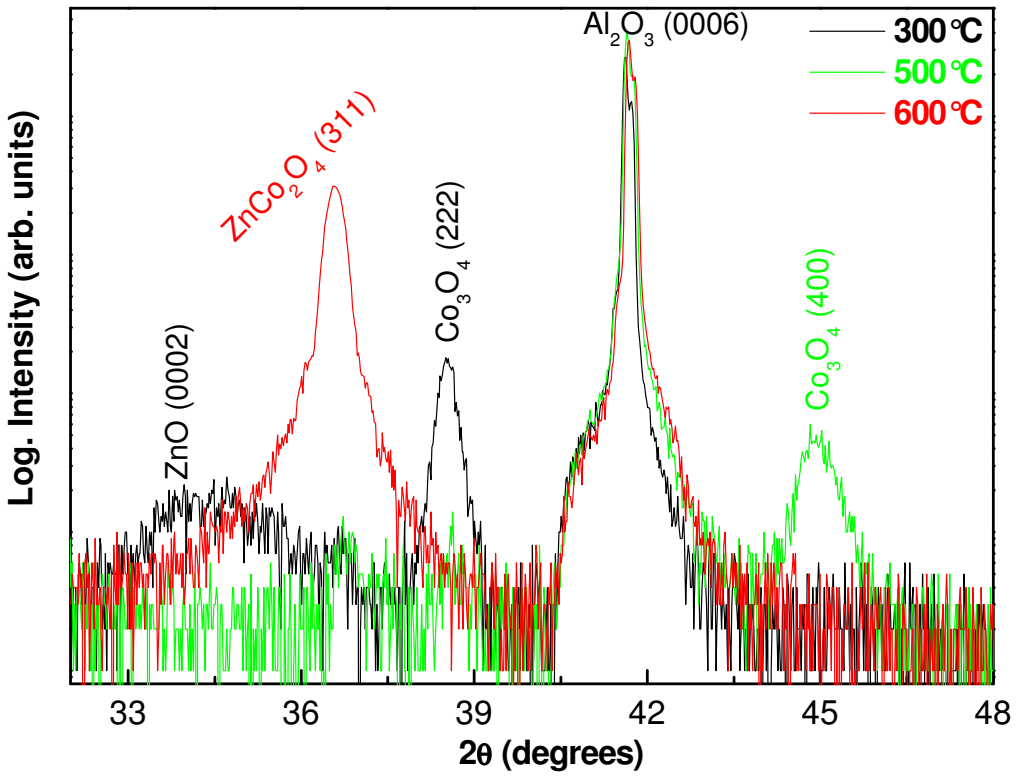

Fig.5.8. 2Θ/ω XRD scans for the Co_3O_4 thin films grown on (0001) sapphire substrates in 1.2 x10^{-2} mbar oxygen pressure, at temperatures ranging from 300 to 600°C

These results are in agreement with the observations of Krezhov *et al.* [25] where they detected that in the 350°C to 450°C range the $ZnCo_2O_4$ spinel is formed. In our case this new phase must be formed at the interface between the ZnO and Co_3O_4, probably by indiffusion between layers. This "new" layer could be the reason why the Co_3O_4 layer changes from a [111] to [100] orientation. In Fig.5.9 (a) and (b) a scheme of the layers formed at different temperatures can be observed. For the film grown at 500°C, between the ZnO buffer layer and the

Co_3O_4 thin film, the $ZnCo_2O_4$ spinel layer is indicated (see Fig.5.9 (a)). For the film grown at 600°C, the diffraction maxima can be indexed either with the sapphire substrate (JCPDS 43-1484), or with the spinel $ZnCo_2O_4$ structure (JCPDS 81-2299) (Fig.5.8). The spinel $ZnCo_2O_4$ diffraction maxima observed correspond to the (311) plane. Since no other diffraction maxima are present, it can be concluded that ZnO and Co_3O_4 have reacted completely within the resolution limit of XRD (see Fig.5.9 (b)).

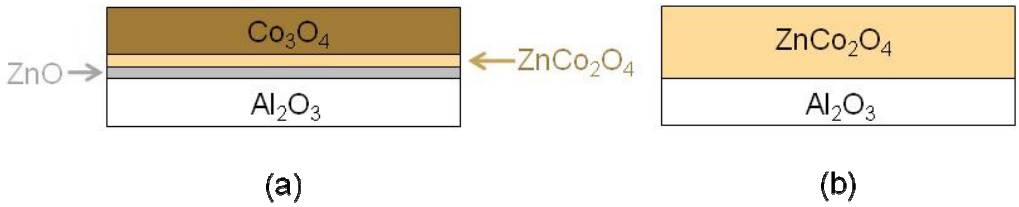

Fig.5.9. Schematic of the layers composition for Co_3O_4 thin films deposited at (a) 500°C and (b) 600°C

Fig.5.10 displays the in-plane Φ scans for the (113) plane of the sapphire substrate, and for the (311) plane of the Co_3O_4 films grown at 300 and 500°C. The in-plane Φ scans of the Co_3O_4 films grown at 600°C were not investigated, since at this temperature just the $ZnCo_2O_4$ spinel structure is obtained. All the films exhibit an epitaxial relationship, including the one grown at 300°C, which is a relatively low temperature for obtaining epitaxial films, as compared with previous works [19-21,24]. Notice that in all the performed measurements six peaks separated 60° and rotated 30° with respect to the sapphire substrate can be identified. This indicates a six-fold symmetry due to the 3-fold rotation symmetry along the [111] direction of the Co_3O_4 cubic structure. For the Co_3O_4 thin films grown at 500°C 12 peaks are observed, which indicate the coexistence of 2 domains: a main domain aligned with the sapphire substrate, and a twin domain rotated 30° with respect to the substrate. Thus, epitaxial growth has been established with the following relationship: at 300°C $[111]_{Co3O4}||[100]_{sapphire}$ out of plane and $[011]_{Co3O4}||[110]_{sapphire}$ in plane; and at 500°C $[100]_{Co3O4}||[100]_{sapphire}$ out of plane and $[011]_{Co3O4}||[110]_{sapphire}$ in plane.

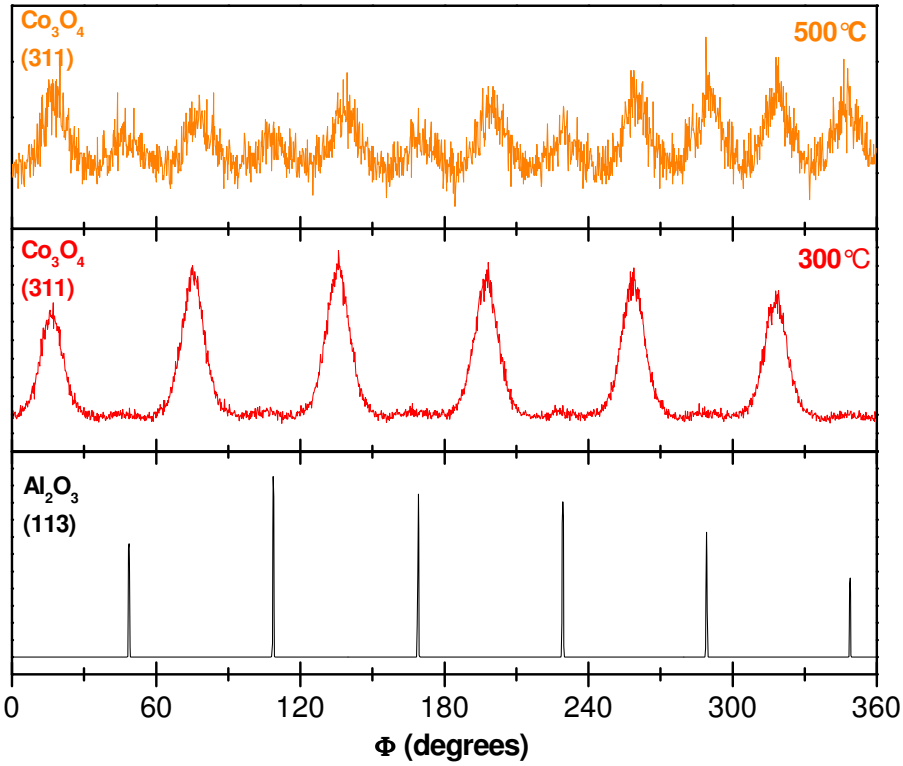

Fig.5.10. In-plane Φ scans for the (113) plane of the sapphire substrate, and for the (311) plane of the Co_3O_4 films grown at 300 and 500°C

b) Surface Morphology

Fig.5.11 shows AFM images of Co_3O_4 thin films deposited by PLD at different temperatures: (a) 300°C, (b) 500°C and (c) 600°C. As expected, the surface morphology varies greatly for the films grown at different temperatures. The roughness of the films was 34Å, 6Å and 10Å, respectively. These values are smoother than for ZnO films grown at equivalent conditions. The Co_3O_4 films become smoother as the growth temperature increases from 300 to 500°C. Nevertheless, at a growth temperature of 600°C the spinel structure was formed, and therefore a different thin film with different characteristics is obtained. This change is also evident in the measured topography.

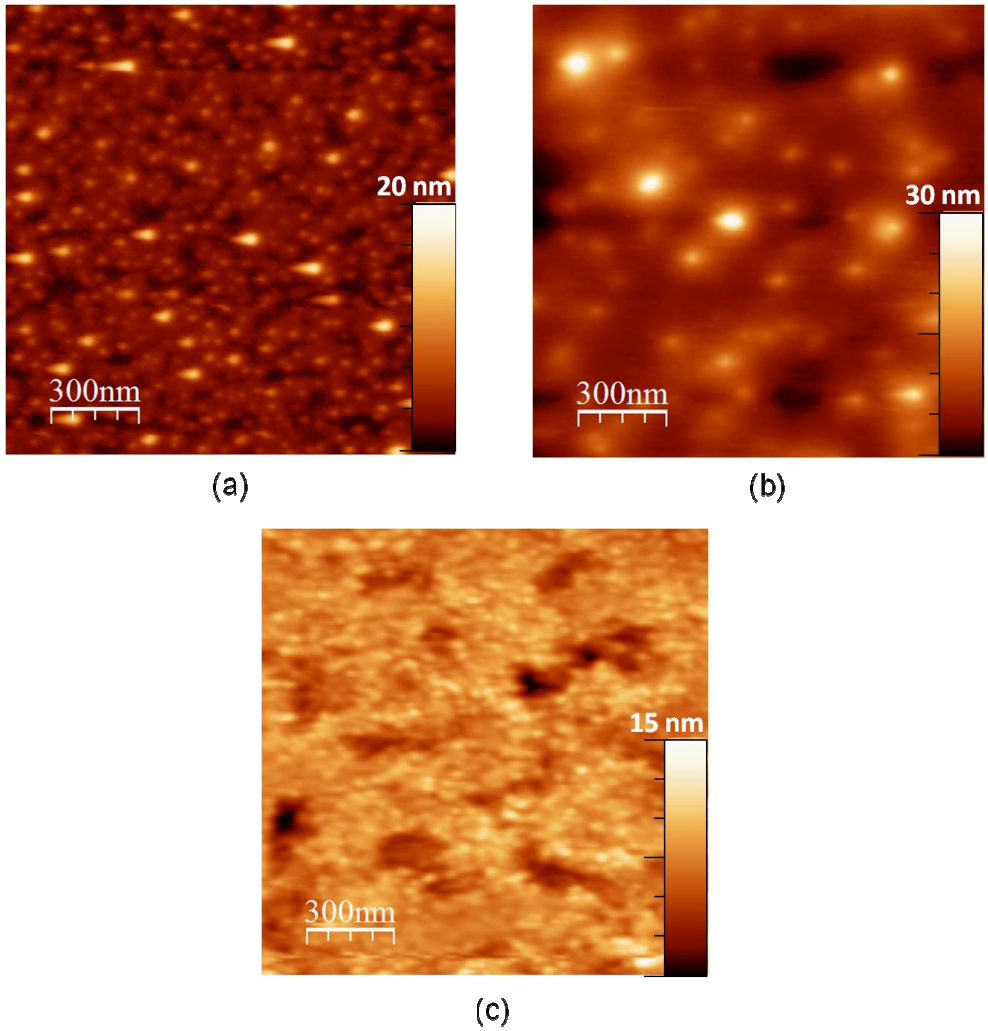

Fig.5.11. AFM images of Co_3O_4 thin films deposited by PLD, grown at different temperatures: (a) 300°C, (b) 500°C and (c) 600°C.

c) Electrical properties

To the best of our knowledge there is no report about electrical properties of epitaxial Co_3O_4 thin films on the literature, and this PhD work provides a first electrical characterization of epitaxial Co_3O_4 thin films.

For the Van der Pauw four-probe geometry the same procedure like for ZnO thin films was used. The Ti/Al/Pt/Au metallic contacts exhibited ohmic behavior. Unlike the ZnO films which were transparent and cannot be distinguished within the sapphire substrate, the Co_3O_4 films are brown colored. Moreover, their color changes slightly with the growth temperature. The Co_3O_4 thin films grown at 300 and 500°C are dark brown and opaque, while the one grown at 600°C (where the $ZnCo_2O_4$ spinel had formed) become light brown and semitransparent, another clear sign of a completed reaction (see Fig.5.12).

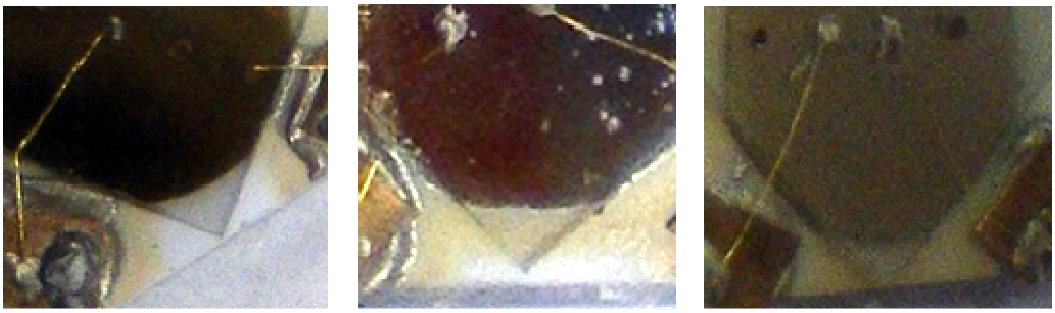

Fig.5.12. Co_3O_4 epitaxial thin films on sapphire prepared for Hall measurements: (a) T_{growth}=300°C, (b) 500°C and (c) 600°C

Fig.5.13 (a-c) shows the behavior of the electrical properties versus temperature for Co_3O_4 thin film grown at 300°C. Unlike the electrical properties measurements of ZnO films which were performed in the range 30-300K, in the case of Co_3O_4 thin films the measurements could be performed just from 100-300K for films grown at 300°C, and from 200-300K for films grown at 500°C. That was due to the fact that at those temperatures the resistivity of the Co_3O_4 thin films increased very much and reached the detection limit of our Hall measurements system. As seen in Fig.5.13 the Co_3O_4 thin film grown at 300°C exhibits *p*-type semiconductor behavior and presents a resistivity of 1.4 Ωcm at RT, which is very high (almost 4 orders magnitude) when compared to the resistivity exhibited by the ZnO thin films. High mobility of 300 $cm^2V^1s^{-1}$ and carrier density of $1x10^{16}$ cm^{-3} at RT correspond to this high resistivity.

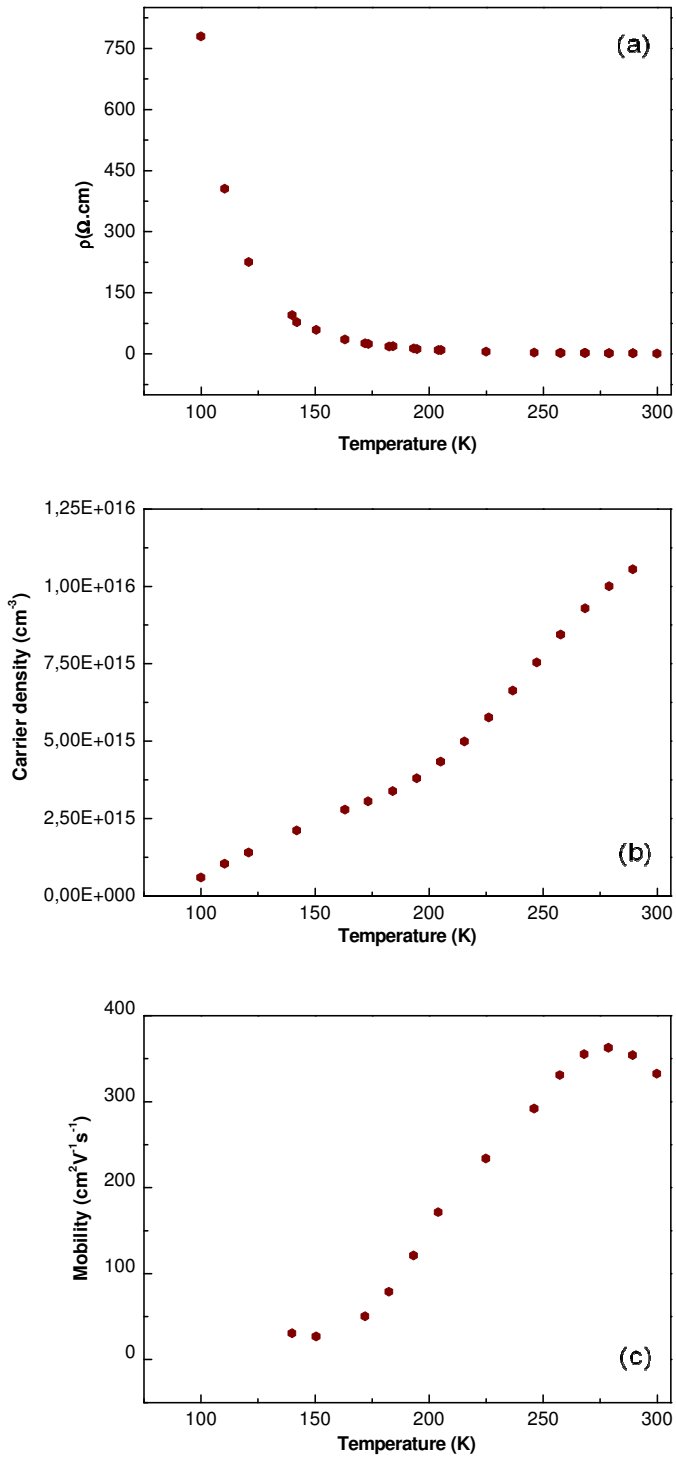

Fig.5.13. Electrical properties versus temperature for Co_3O_4 thin film grown at 300°C: a) electrical resistivity, b) carrier density, c) mobility

Table.5.III depicts the values of the electrical properties measurements (electrical resistivity, carrier density, and mobility) for Co_3O_4 thin films grown at 300°C and 500°C. With the increasing of the growth temperature from 300 to 500°C, the resistivity increases to 54 Ωcm at RT, and consequently even higher mobility of 700 $cm^2\ V^{-1}s^{-1}$ and lower carrier density of $3x10^{14}\ cm^{-3}$ at RT are obtained. The films deposited at 600°C exhibit very high resistivity (>200MΩ), which did not allow us to perform electrical measurements on it. Therefore, the increase in the insulating character as the growth temperature increases could be related to the fact that an insulating Zn-Co-O spinel phase is formed.

Table.5.III. Values of the electrical properties (electrical resistivity, carrier density, and mobility) for *p*-type Co_3O_4 thin films grown at 300°C and 500°C

T_{growth} (°C)	Electrical resistivity (Ωcm)	Carrier density (cm^{-3})	Mobility ($cm^2 V^{-1} s^{-1}$)
300	1.4	$1x10^{16}$	300
500	54	$3x10^{14}$	700
600	>200MΩ	--	--

Conclusions:

- ✓ Epitaxial *p*-type Co_3O_4 thin films have been grown on (0001) sapphire substrates including at 300°C, which is a relatively low temperature for obtaining epitaxial Co_3O_4 thin films.
- ✓ Depending on the growth temperature different orientations of the Co_3O_4 films are obtained. This change might be related to the spinel $ZnCo_2O_4$ which is formed at the interface between ZnO and Co_3O_4 for films grown at 500°C.
- ✓ At 600°C ZnO and Co_3O_4 have reacted completely and only the $ZnCo_2O_4$ spinel structure could be identified.

- ✓ The increase in the insulating character as the growth temperature increases could be related to the fact that a Zn-Co-O spinel phase is formed.

5.2.2. Multilayers

After determining the reactivity and the properties of the Co_3O_4 thin films, we can now address the study of the Zn-O-Co system as ZnO/Co_3O_4 epitaxial multilayers. Various sets of ZnO/Co_3O_4 multilayers have been grown by PLD at different growth temperatures. The targets were the same like the ones used for ZnO and Co_3O_4 thin film growth. The deposition pressure in the chamber was *1.2 x10^{-2} mbar oxygen pressure*, and as *substrate* the *(0001) sapphire* was used. The growth temperature was ranging from *RT to 600°C*.

5.2.2.1. Structural characterization

The film´s thickness varies from 100nm for the multilayer grown at RT to 60nm for the multilayer grown at 600°C.

X-ray diffraction

Fig.5.14 shows XRD 2Θ/ω scans for the ZnO/Co_3O_4 multilayers grown on (0001) sapphire substrates in 1.2x10^{-2}mbar oxygen pressure, at temperatures ranging from RT to 600°C. For the multilayer grown at RT, the diffraction maxima can be indexed only with the corundum/ rhombohedral structure of the sapphire substrate (JCPDS 43-1484), indicating that the multilayer is amorphous to XRD. For the multilayer grown at 200°C, the diffraction maxima can be indexed with the sapphire substrate, the hexagonal wurtzite ZnO lattice (JCPDS 76-0704), the Co_3O_4 lattice (JCPDS 42-1467), and with the $ZnCo_2O_4$ spinel (JCPDS 81-2299). The ZnO diffraction maxima

observed correspond to (0002) and (0004) planes. The Co_3O_4 and $ZnCo_2O_4$ spinel diffraction maxima correspond to (400) plane, and (311) and (440) planes respectively. For the multilayers grown at temperatures above 300°C only diffraction maxima corresponding to the sapphire substrate and the ZnO lattice can be identified. Also a very weak reflection corresponding to the (311) plane of the $ZnCo_2O_4$ spinel can be noticed, indicating that Co_3O_4 has reacted completely.

It seems that in the case of the multilayers the Zn-Co-O spinel started to be formed at temperatures as low as 200°C. Therefore, it can be stated that interdiffusion takes place at lower temperatures in the case of multilayers, as compared with solid-state methods. These results indicate that the control of the interdiffusion is a decisive parameter in multilayers [26].

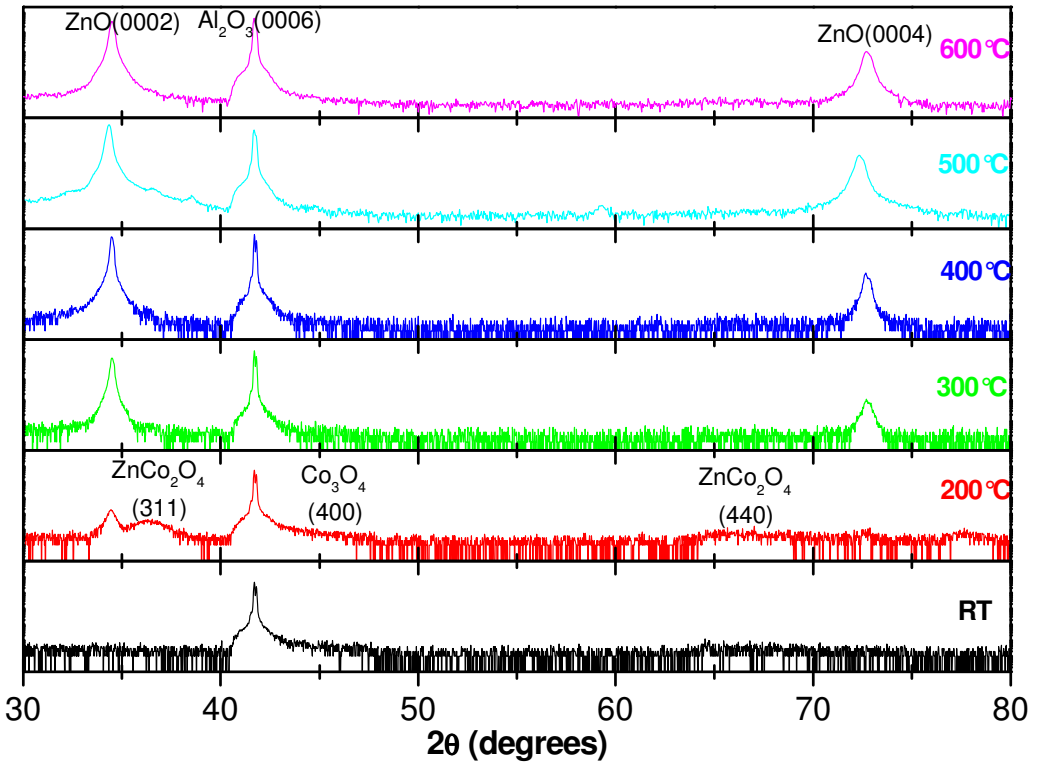

Fig.5.14. 2Θ/ω XRD scans for ZnO/Co_3O_4 multilayers grown on (0001) sapphire substrates in $1.2x10^{-2}$mbar oxygen pressure, at temperatures ranging from RT to 600°C

Fig.5.15 displays the in-plane Φ scans for the (113) plane of the sapphire substrate, and for the (103) plane of the ZnO films. The multilayers grown at RT and 200°C did not exhibit epitaxial relationship. For the epitaxial ZnO/$ZnCo_2O_4$multilayers, the diffraction pattern exhibits diffraction maxima separated 60°, which indicates the six-fold symmetry. Thus, epitaxial growth has been established with the following relationships: $(0001)_{ZnO}||(0001)_{sapphire}$ and $[11\underline{2}0]_{ZnO}||[11\underline{2}0]_{sapphire}$.

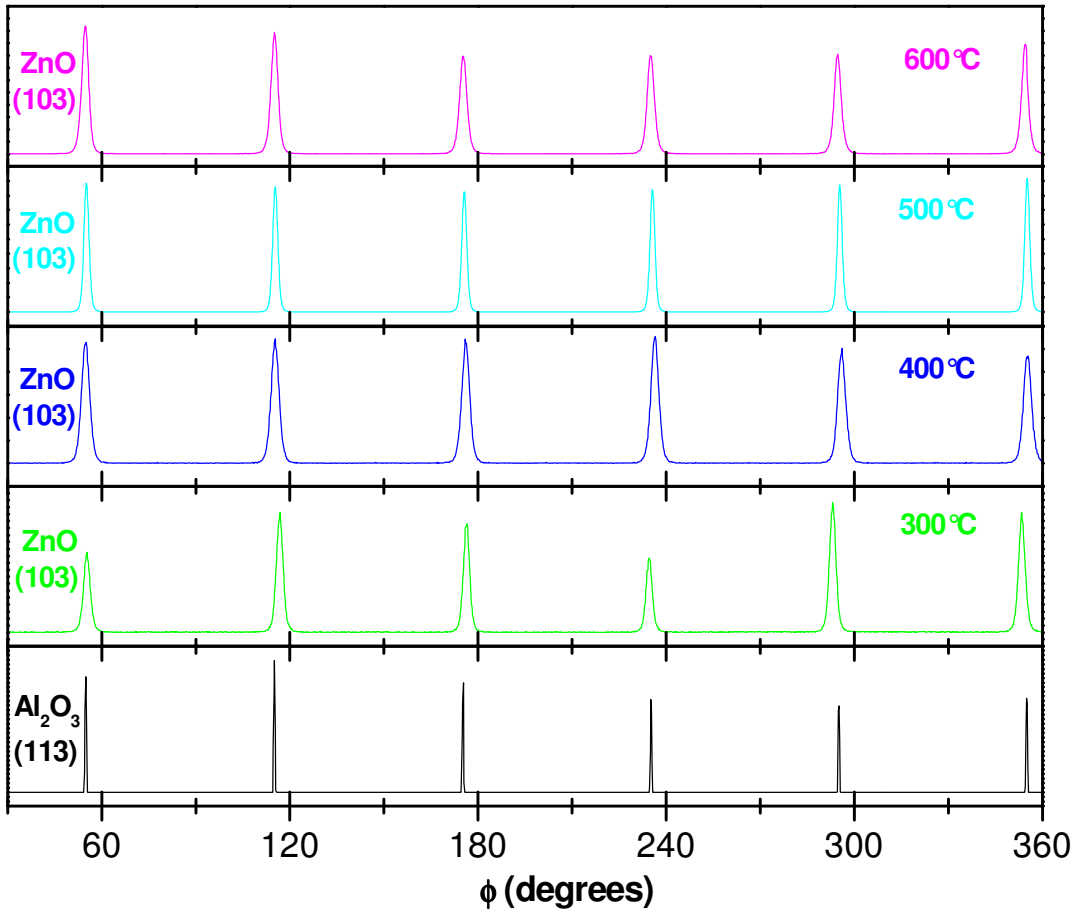

Fig.5.15. In-plane Φ scans for the (113) plane of the sapphire substrate, and for the (103) plane of the ZnO films for multilayers grown on (0001) sapphire substrates in $1.2x10^{-2}$mbar oxygen pressure, at temperatures ranging from 300°C to 600°C

5.2.2.2. Electrical properties

For the Van der Pauw four-probe geometry the previous procedure with metallic contacts of Ti/Al/Pt/Au was used. Fig.5.16 shows a ZnO/Co_3O_4 multilayer sample prepared for Hall measurements. Unlike the Co_3O_4 films which were opaque, the multilayers are light-green, almost transparent. The film edge has been underlined in the photograph.

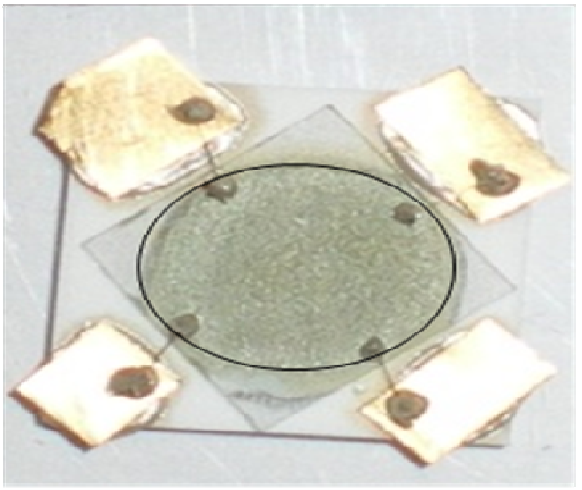

Fig.5.16. Multilayer sample with metallic contacts and the corresponding pads prepared for Hall measurements. The film edge has been underlined

Fig.5.17 (a-c) shows the behavior of the electrical properties versus temperature for ZnO/Co_3O_4 multilayers grown at 400°C. The multilayer exhibits *n*-type semiconductor behavior with a resistivity of 0.077 Ωcm at RT. This value of the resistivity should be related to the values of the resistivities of the individual layers. The simplest relation would be the comparison assuming that the deposited layers behave as resistors in parallel. Taking into account that the ZnO layer is 4 times thicker than the Co oxide layer, and that its resistivity is two orders of magnitude lower, the multilayer should have a resistivity value close to ZnO. However, this is not the case, and this is proof that the resistive behavior of the multilayers cannot be understood as additive of the individual layers. This rules out also (and this was also a motivation of this work) the presence of an oxide interphase with high conductivity properties.

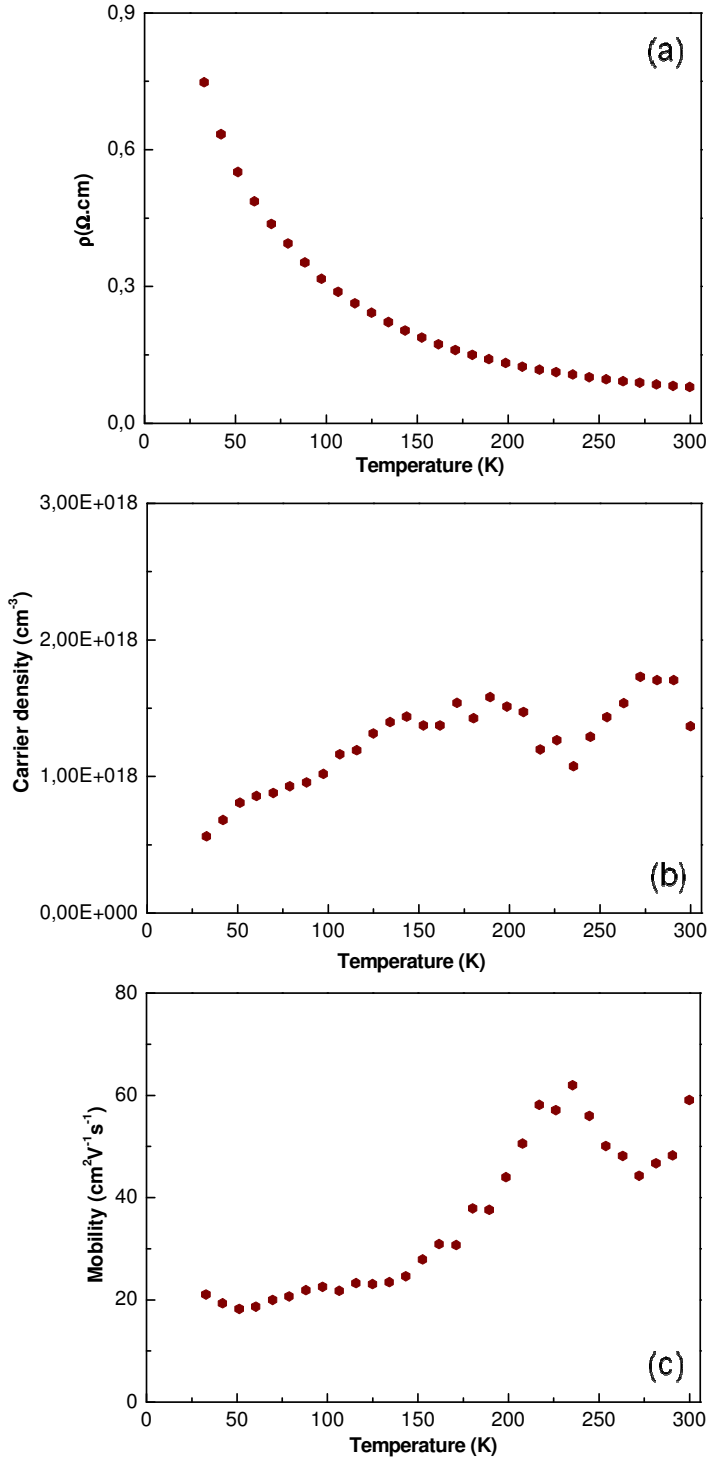

Fig.5.17. Electrical properties versus temperature in the range 30-300K for ZnO/Co_3O_4 multilayers grown at 400°C: (a) electrical resistivity, (b) carrier density, (c) mobility

Table.5.IV. Values of the electrical properties for *n*-type ZnO/Co_3O_4 multilayers grown at different temperatures

T_{growth} (°C)	Electrical resistivity (Ωcm)	Carrier density (cm^{-3})	Mobility ($cm^2 V^{-1} s^{-1}$)
300	0,32	$4,4x10^{16}$	300
400	0,077	$1,3x10^{18}$	60
600	0,6	$1x10^{18}$	10

Table 5.IV depicts the values of the electrical properties for ZnO/Co_3O_4 multilayers grown at different temperatures. The multilayers deposited at RT and 200°C are not depicted in this table, because they could not be measured due to their very high resistance (order of MΩ). When the growth temperature increased from 300 to 400°C, the resistivity decreased. The carrier density increased ~2 orders of magnitude and a lower mobility was obtained. As the growth temperature increased further the resistivity increased again, but the fluctuation of its value was smaller (~1 order of magnitude).

5.2.2.3. Magnetic properties (SQUID)

The magnetic properties of the ZnO/Co_3O_4 multilayers were investigated by SQUID measurements.

Fig.5.18 shows a) the temperature dependence of the magnetization at constant field for ZnO/Co_3O_4 multilayers grown at different temperatures; and b) the magnetization versus field reversal loop (M-H) measured at 5K.

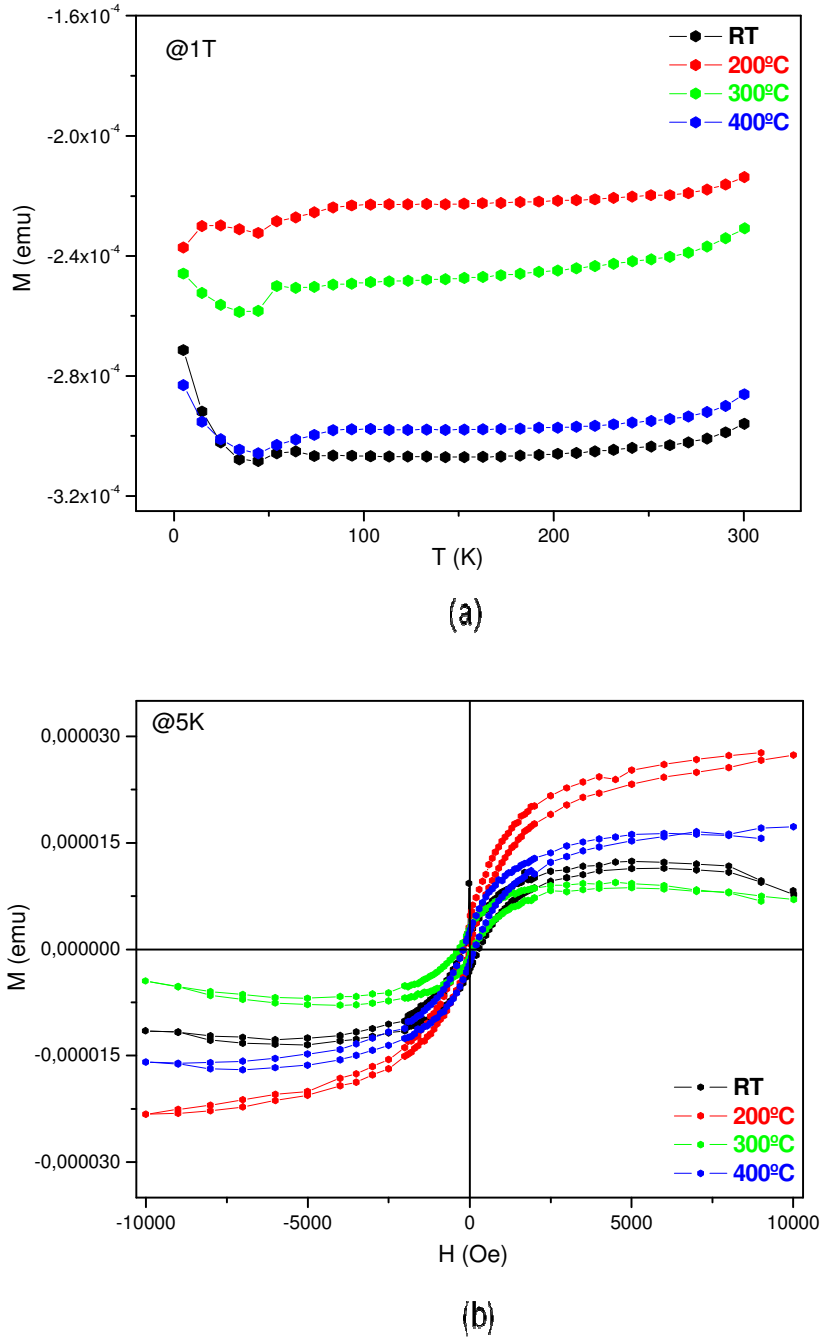

Fig.5.18. SQUID measurements for ZnO/Co_3O_4 multilayers grown at different temperatures: a) Temperature dependence of the magnetization at constant field; and b) Magnetization versus field reversal loop (M-H) measured at 5K.

The ZnO/Co_3O_4 multilayers are diamagnetic in the whole studied temperature range (5-300K). The multilayers grown at RT exhibit the lowest diamagnetic susceptibility, and the multilayers grown at 200°C exhibit the highest one. Then it starts to decrease as the growth temperature increases. This is in agreement with what is observed by XRD, where the mutilayers grown at 200°C are the ones that present ZnO and Co_3O_4 layers. However, the Zn-Co-O spinel started to form at this temperature, and as the growth temperature increases the ZnO and Co_3O_4 layers reacted more resulting in a decrease of the diamagnetic susceptibility.

After subtracting the diamagnetic signal a small ferromagnetic component is obtained. This ferromagnetic component is very small for the multilayers grown at RT, 300 and 400°C. Accordingly, the multilayers grown at 200°C present a notably ferromagnetic signal. The fact that the signal is somehow weak might be related to the thickness ratio between the layers (4:1).

Therefore, it can be concluded that the control of the interdiffusion is essential and can help to explain the variety of results of magnetic measurements in multilayers. It seems that in the case of the ZnO/Co_3O_4 multilayers the Zn-Co-O spinel started to form at very low temperatures (200°C). The ferromagnetic component decreases considerably when the spinel is formed.

Conclusions:

- ✓ *n*-type ZnO/Co_3O_4 multilayers have been grown by PLD on *(0001) sapphire substrate.*
- ✓ Multilayers interdiffusion is found at very low temperatures (the Zn-Co-O spinel starting to form at 200°C), and therefore epitaxial ZnO/Co_3O_4 interface was not stabilized.
- ✓ The multilayers grown at 200°C exhibit the highest FM compared to the other mulilayers, although this FM signal is somehow weak.

5.3. ZnO implanted with Co

The best approach used to produce ferromagnetic semiconductors is by introducing magnetic ions (Co, Mn, Fe, or Ni) into a non-magnetic semiconductor obtaining thus a DMS.

Therefore, the next study was the implantation of ZnO films (*p* and *n*) with transition metal ions. The ion implantation technique is very useful due to its ability to control the dopant profile with high precision. In this section epitaxial ZnO films were implanted with Co. Their structural, electrical, optical and magnetic properties are studied in order to determine the influence of the implantation on the magnetic properties of the film. The influence of rapid thermal annealing process after implantation is also studied.

ZnO layers grown at *300°C for p-type* (thickness of 150 nm) and at *600°C for n-type* films (130 nm) have been prepared for this study. It is important to remember at this point that no comparative study on the implantation of Co in *p*- and *n*-type ZnO has been performed to date.

Once the ZnO films have been obtained, each one has been divided into 4 pieces. One piece has been used as reference. The other 3 pieces corresponding to each ZnO film were implanted with Co ions at fluences of $1x10^{16}$ ions/cm^2 and energies of 120 KeV (for the film grown at 600°C, 130nm thickness) and 140 KeV (for the film grown at 300°C, 150nm). The projected ranges of the implanted Co ions are calculated with the TRIM code [27] to be 64 nm for the film implanted at 120 KeV and 70 nm for the one implanted at 140 KeV. As shown in Fig.5.19 and Fig.5.20 the elemental depth distribution inside the ZnO film presents a Gaussian-like shape, which is centered at the center of the film. The calculations indicate that the maximum number of target atom displacements per ion is 2.8 and 2.4 for layers implanted at 140

and 120 KeV, respectively. All the implantations were carried out at room temperature and out of channeling incidence.

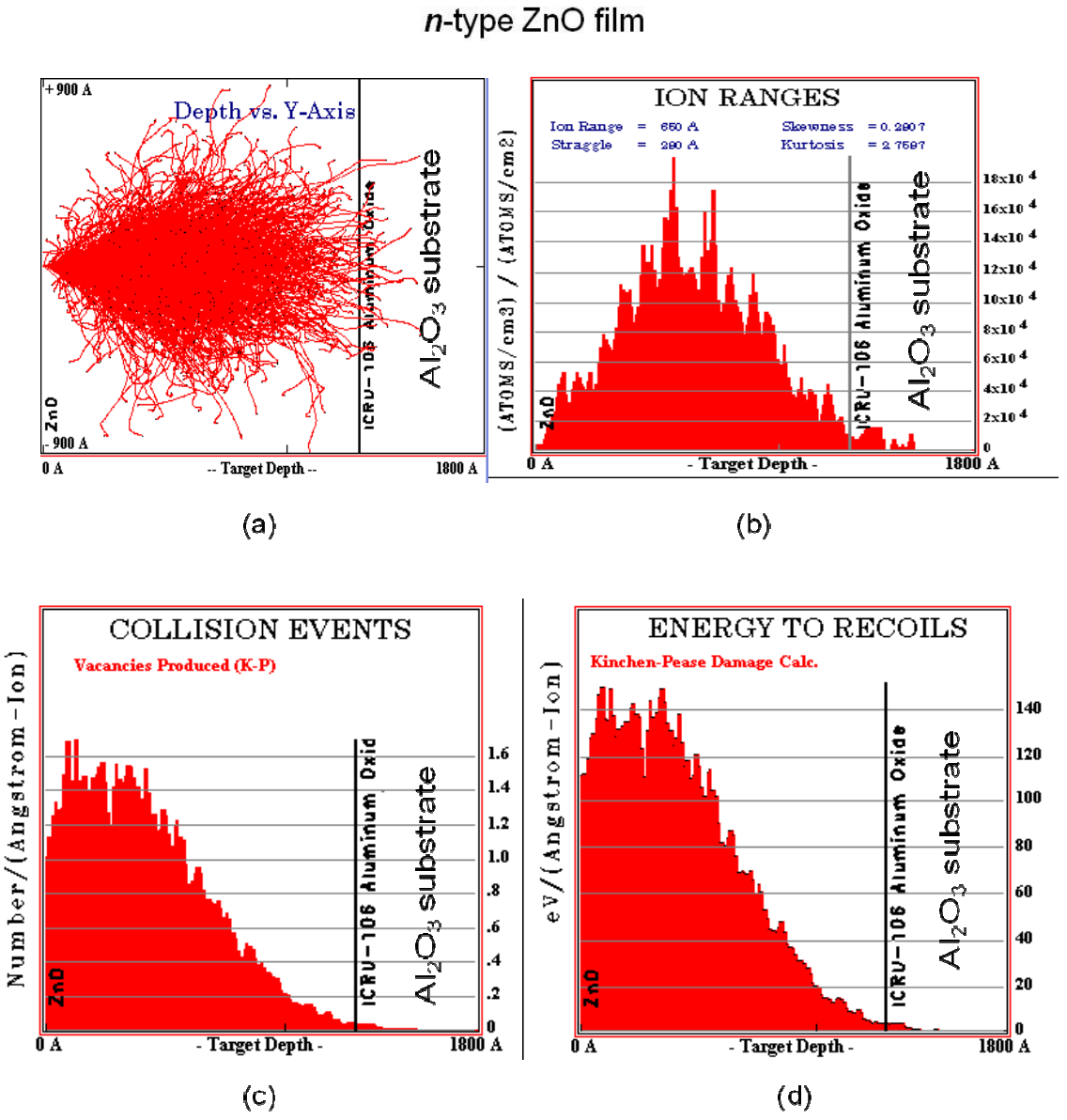

Fig.5.19. Simulation calculated with the TRIM code [27] for 130nm ZnO film implanted with Co ions at fluences of $1x10^{16}$ ions/cm^2 and energies of 120 KeV): (a) trajectories of ions into ZnO film (b) distribution of the ions in the ZnO film (c) plot of target vacancies (d) plot of the energy transferred from the ion to recoil atoms

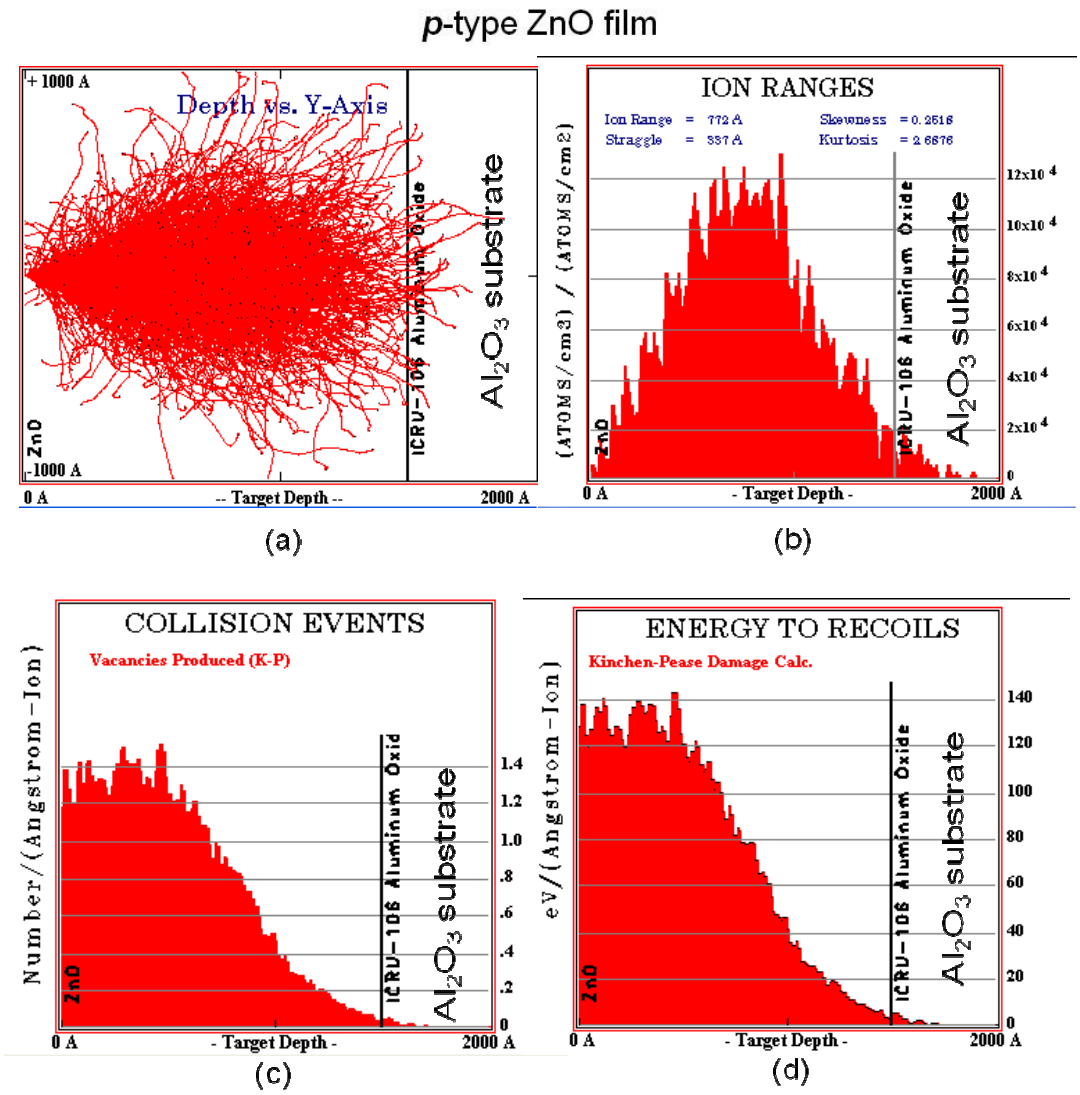

Fig.5.20. Simulations calculated with the TRIM code [27] for 150nm ZnO film implanted with Co ions at fluences of $1x10^{16}$ ions/cm^2 and energies of 140 KeV): (a) trajectories of ions into ZnO film (b) distribution of the ions in the ZnO film (c) plot of target vacancies (d) plot of the energy transferred from the ion to recoil atoms

Afterwards two pieces of each ZnO implanted films were also rapidly annealed in a commercial RTA system in Ar atmosphere for 30 seconds at temperatures of 400 and 750°C, respectively. During annealing, the sample surface was covered with a ZnO/Al_2O_3 layer to avoid any possible evaporation or contamination.

5.3.1. Structural characterization

XRD

Fig.5.21 shows 2Θ/ω XRD scans for different ZnO films. All the diffraction maxima can be indexed either with the Al_2O_3 substrate or with the hexagonal wurtzite ZnO lattice (JCPDS 76-0704). The two diffraction maxima observed for the ZnO correspond to the (0002) and (0004) planes, which implies that ZnO grows along the (0001) direction. After implantation or RTA treatments no other diffraction maxima were observed. The maxima position and the cell parameter obtained values are shown in Table 5.V.

Table 5.V. The maxima position, the FWHM obtained values of each maximum, and the cell parameter for epitaxial ZnO films grown at 300°C (*p*-type) and 600°C (*n*-type), and after Co implantation and RTA annealing

	2θ (0002) ZnO	FWHM (0002)	2θ (0004) ZnO	FWHM (0004)	I(0004)/ I(0002)	Cell parameter c	H_c (RT)	Ms (RT)
p-ZnO	34.40	1.65	72.52	1.71	0.0290	5.213	-	-
p-ZnO+ Co Impl	34.39	2.16	72.48	2.08	0.0267	5.215	82	160
p-ZnO+ Co+RTA 400°C	34.35	2.31	72.41	2.30	0.0257	5.220	-	-
p-ZnO+ Co+RTA 750°C	34.42	1.92	72.56	1.92	0.0296	5.211	-	-
n-ZnO	34.48	0.93	72.69	0.99	0.0278	5.202	-	-
n-ZnO+ Co Impl	34.48	1.80	72.71	1.78	0.0231	5.201	50	180

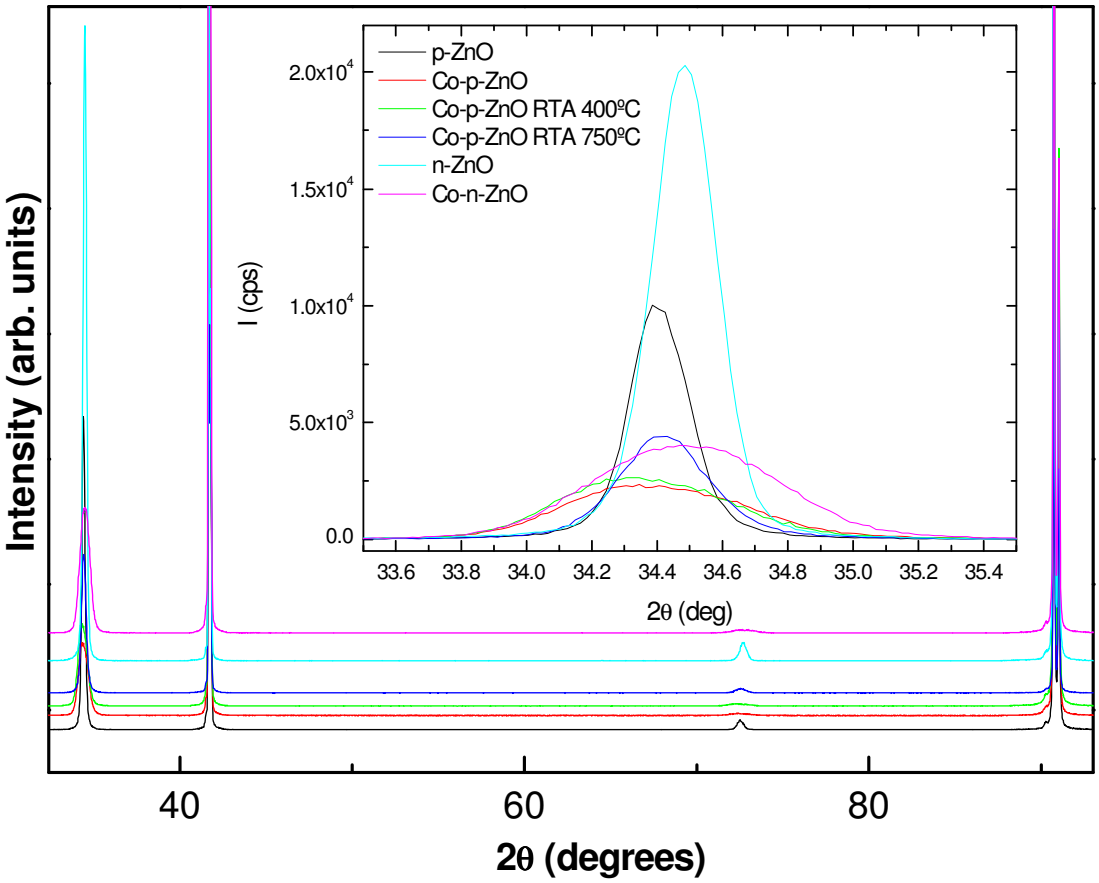

Fig.5.21. 2θ/ω scan X-ray diffraction for epitaxial ZnO films grown at 300°C (*p*-type) and 600°C (*n*-type), and after Co implantation and RTA. Inset: detail of the (0002) ZnO peak.

Fig.5.22 shows the *ω*-rocking curve of the (0002) ZnO reflection for epitaxial ZnO films grown at 300°C (*p*-type) and 600°C (*n*-type), and after Co implantation and RTA. The FWHM value of the XRD rocking curve increases from 1.66 to 2.16° upon Co-implantation in the *p*-type sample, which is a symptom of a decrease in the crystalline quality of the film (see Table 5.V for FWHM of each maximum). This crystalline quality does not recover after RTA at 400°C, but starts to increase after annealing at 750°C according to the data shown in Table 5.V. When the growth temperature increases, the lattice presents less tensile stress in the out of plane direction (perpendicular to the substrate). In the case of the *n*-type film, the rocking curve indicates

that the crystal quality is higher than of the *p*-type films, as it was expected due to a higher growth temperature. Also, a reduction of crystal quality upon implantation is observed in this case.

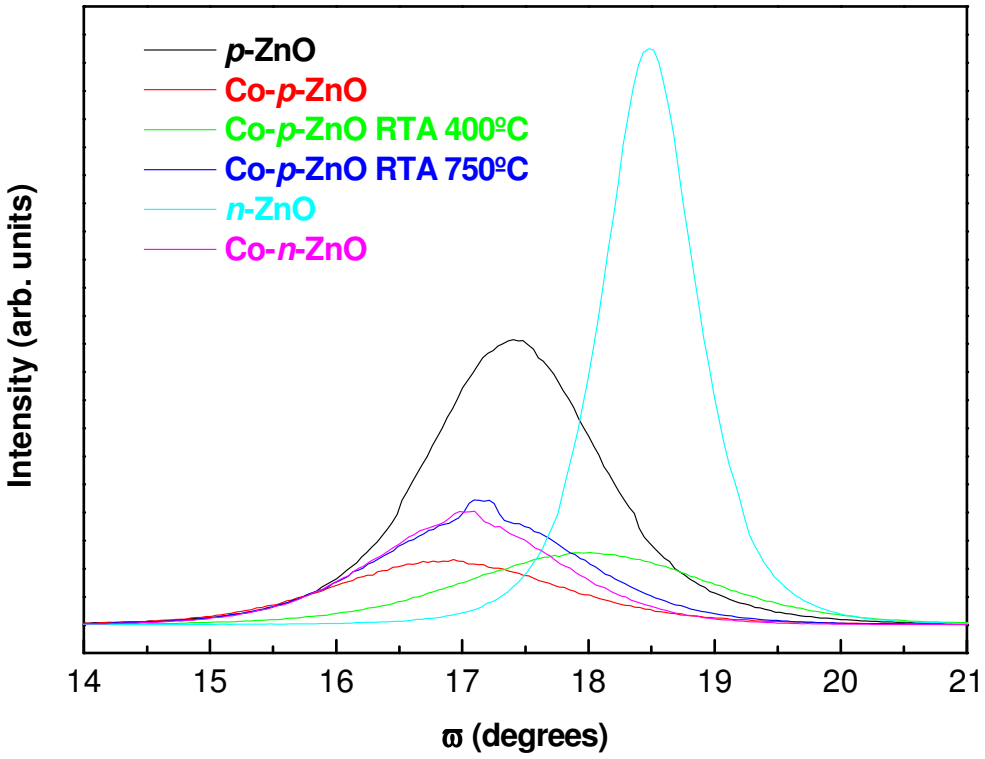

Fig.5.22. ω-rocking curves corresponding to the ZnO (0002) reflection for epitaxial ZnO films grown at 300°C (*p*-type) and 600°C (*n*-type), and after Co implantation and RTA

Fig.5.23 displays the in-plane Φ scans for the (10$\underline{1}$3) ZnO planes and for the (11$\underline{2}$3) plane of the sapphire substrate. The six-fold symmetry is confirmed by the peaks which are separated 60°. Besides the main domains aligned with the sapphire substrate, twin domains are also observed for the *p*-type films. The *n*-type films showed no twinning due to the higher growth temperature used (600°C) [28]. All the films grow according to the epitaxial relationship $(0001)_{ZnO}$ || $(0001)_{sapphire}$ and $[11\underline{2}0]_{ZnO}$||$[11\underline{2}0]_{sapphire}$.

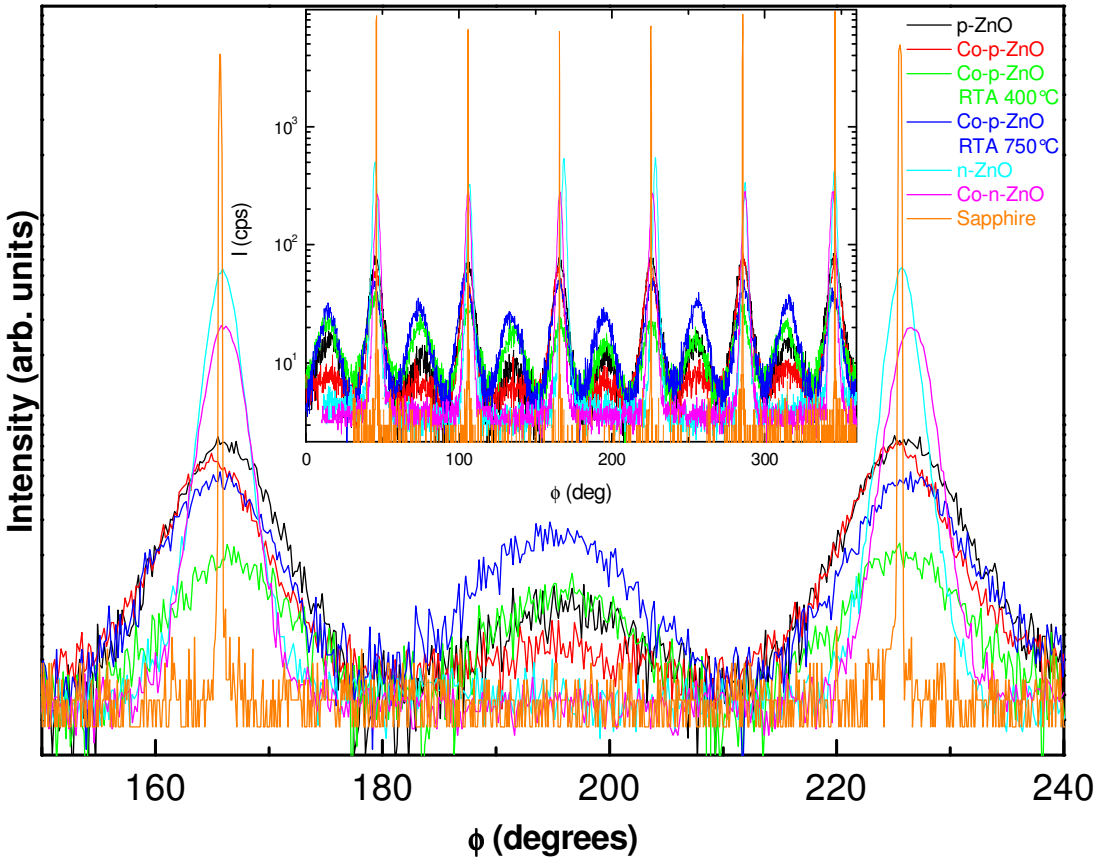

Fig.5.23. Detail of in-plane Φ scan of the (10$\underline{1}$3) ZnO planes and (11$\underline{2}$3) sapphire plane. The insert shows the complete 360° Φ scan.

RBS

For the ZnO films deposited on Al_2O_3 substrates non-RBS measurements were performed in random configuration with a He^+ beam at the oxygen resonance energy (3.045 MeV) [29]. These data show that both the *n*- and *p*-type layers are stoichiometric (Zn/O~1) within the resolution limit of the technique (0.9%) (See section 3.2.1.3).

Non-RBS spectra were also measured at the same energy in channeling configuration along the <0001> axis to independently

determine the lattice order degree of the sublattices. Because of similarity in atomic numbers of Zn and Co, non-RBS data do not allow to resolve the Zn and Co signals.

PIXE

PIXE measurements in channeling configuration were performed on the implanted and annealed films, in order to determine the Co lattice location within the ZnO host matrix. The position of the Co atoms inside the ZnO host matrix is obtained comparing the shape of the Co angular scan curve with the one for Zn.

PIXE angular scan curves along <0001> crystal axes taken from the Zn-K_α+K_β, Co-K_α and Al-K_α for Co-implanted and postannealed (750°C) ZnO films are depicted in Fig.5.24 and Fig.5.25 respectively. For comparison purpose PIXE angular scan curves corresponding to the as-grown pristine films are also presented for reference.

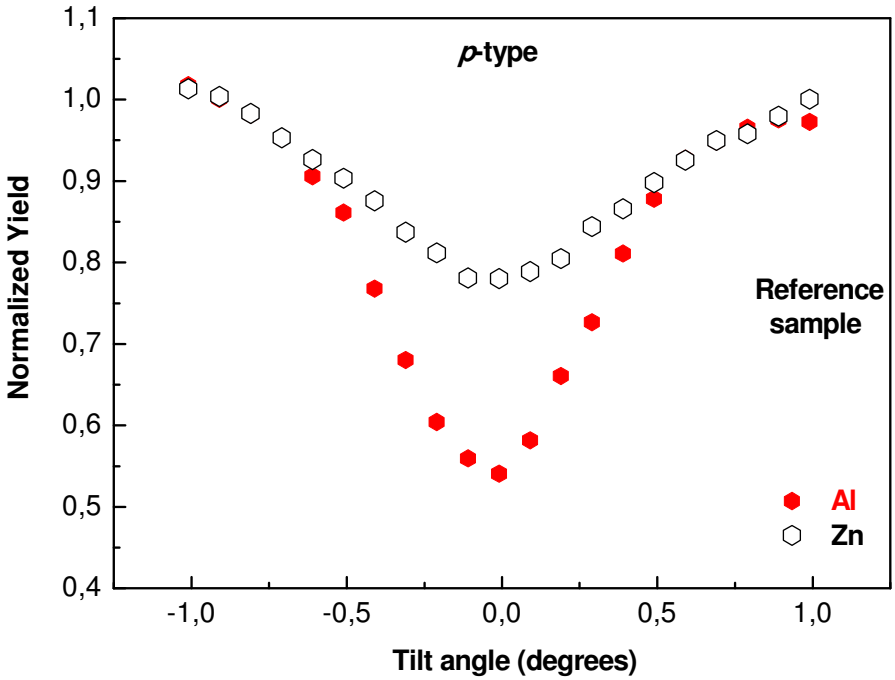

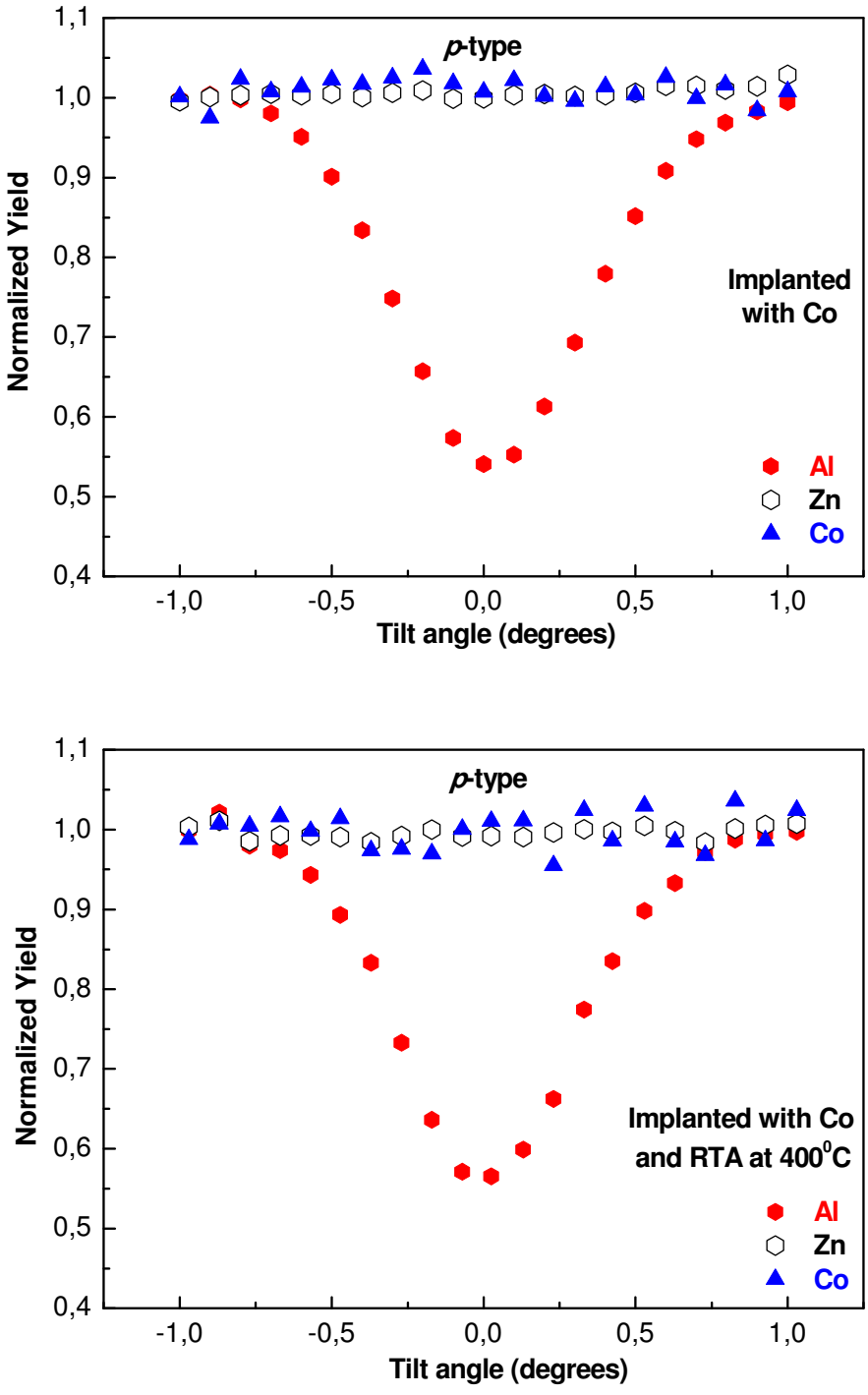

Fig.5.24. PIXE angular scan curves along the <0001> axes of the Zn-K_α+K_β (empty black) and Co-K_α (filled blue) for *p*-type films. For comparison the Al-K_α signal from the substrate (filled red) is also shown

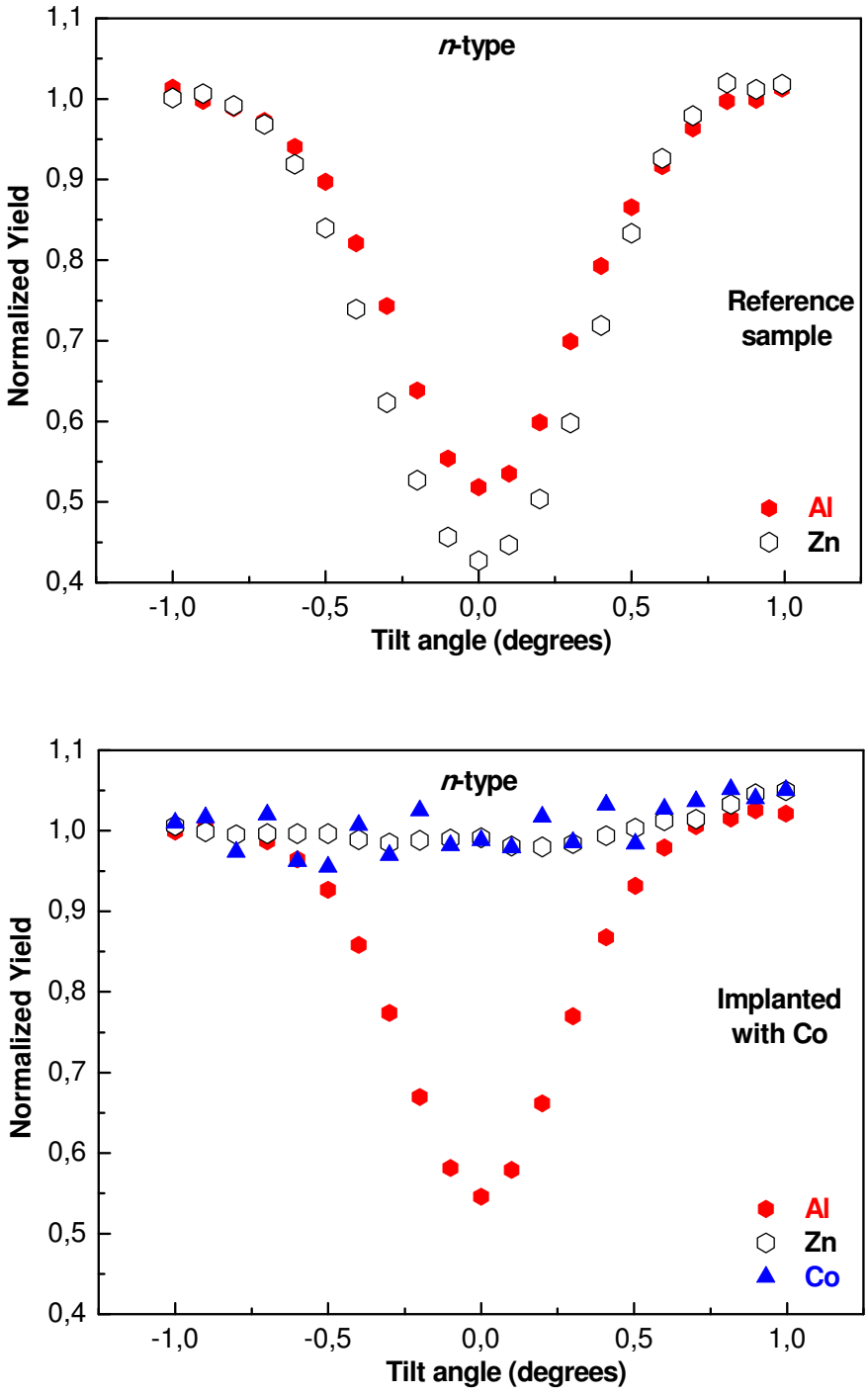

Fig.5.25. PIXE angular scan curves along the <0001> axes of the Zn-K_α+K_β (empty black) and Co-K_α (filled blue) for *n*-type films. For comparison the Al-K_α signal from the substrate (filled red) is also shown

In agreement with XRD data, PIXE scan curves for both types of films confirm once again that RT Co-implantation induces a high lattice damage moving almost all Zn atoms out from their positions. This is indicated by the non-angular dependent flat curve. The same behavior is observed for Co-implanted atoms, which indicate that they do not substitutionally incorporate into the host matrix, unlike its behavior when it is implanted in InAs [30]. As shown in Fig.5.24 no significant changes were observed in the scan curves after RTA, neither for Zn nor for Co in any of the studied films, indicating that annealing does not significantly help damage recovery.

The implantation-induced damage can be understood on the basis of the nuclear collision regime, where the nuclear stopping power (Sn) dominates. The total stopping power (nuclear plus electronics, Se) is calculated with the TRIM code to be 1359 eV/nm for the sample implanted at 120 KeV and 1358 eV/nm for the one implanted at 140 KeV. TRIM calculations also show that in this energy range the maximum number of Zn-displaced atoms is two times higher than the Oxygen atoms, which could explain the high disorder in the Zn sublattice after implantation.

5.3.2. Electrical properties

Measurements of the electrical resistivity, carrier density and Hall mobility were also performed on the implanted films. For the four-probe geometry the same procedure as for the ZnO films was followed.

Fig.5.26 (a-c) shows the electrical properties versus temperature in the range 30-300K for the pristine ZnO films grown at 300°C and 600°C. The ZnO films exhibit semiconductor behavior. The film grown at 300°C shows a low resistivity of 5.8×10^{-3} Ωcm at RT and 7.6×10^{-3} Ωcm at 33 K, while the film grown at 600°C does not vary much from RT(2×10^{-3} Ωcm) to 33K (2.1×10^{-3} Ωcm) (see Fig.5.26 (a)). The film

grown at 300°C presents *p*-type conductivity, whereas the film grown at 600°C exhibits *n*-type conductivity as seen before. Corresponding to a lower carrier density of 5,5x10^{19}cm^{-3} at RT for the *p*-type film compared to 1,5x10^{20}cm^{-3} for the *n*-type film, the mobility is higher for the *p*-type film (~20 times larger) (Fig.5.26 (b) and (c)).

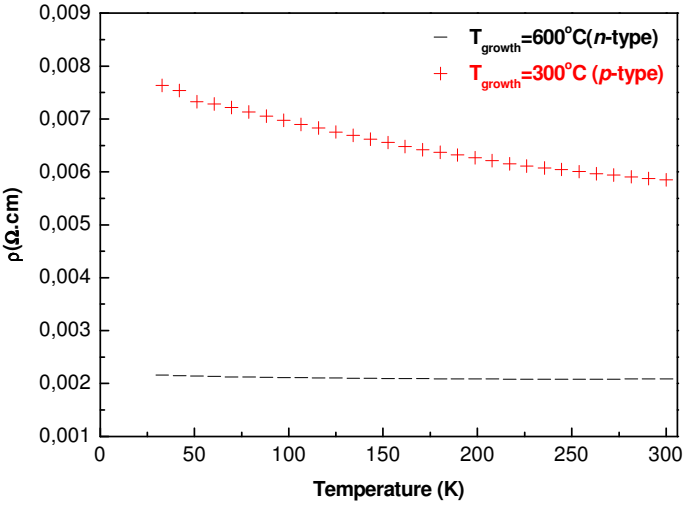

(a)

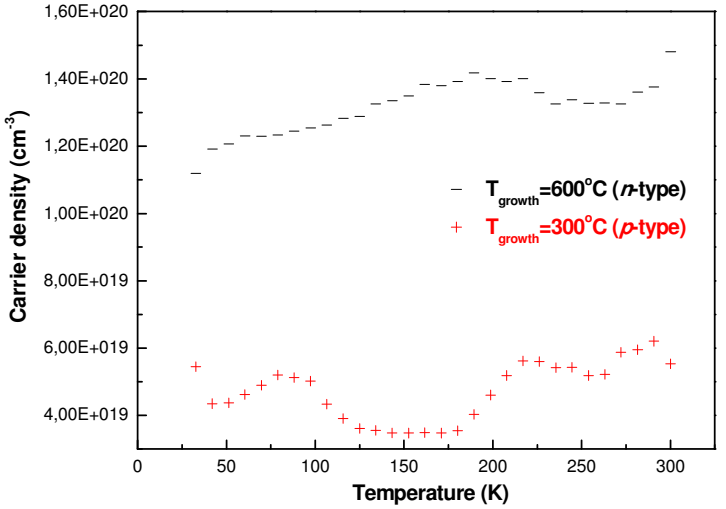

(b)

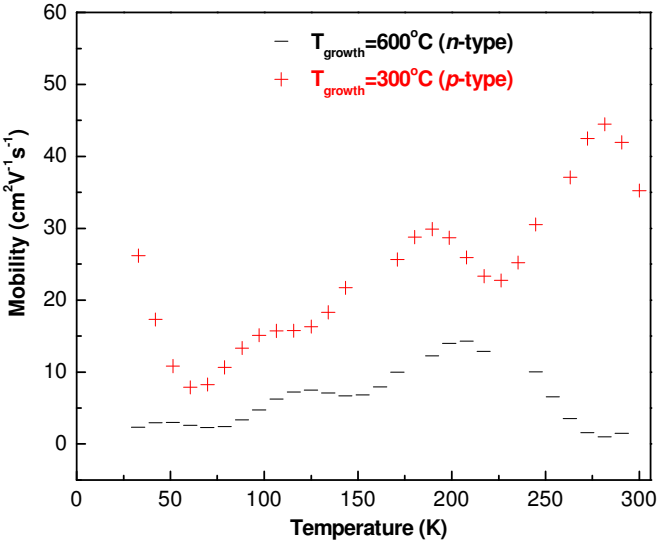

(c)

Fig.5.26. Electrical properties measurements for different types of pristine ZnO films grown by PLD at different temperatures: (a) resistivity versus temperature; (b) carrier density versus temperature; (c) mobility versus temperature

Fig.5.27 (a-c) shows the electrical properties versus temperature for different types of ZnO films after they have been implanted with Co. After the films have been implanted, they have lost their semiconductor behavior. The *p*-type film became much more resistive, with a mobility ~200 times larger and lower carrier density. On the other hand, the *n*-type film presents lower resistivity and a higher carrier density (4 orders of magnitude). Therefore, it can be concluded that implantation of Co ions into the ZnO host matrix affects drastically the electrical properties of the ZnO films, either *p*-type or *n*-type.

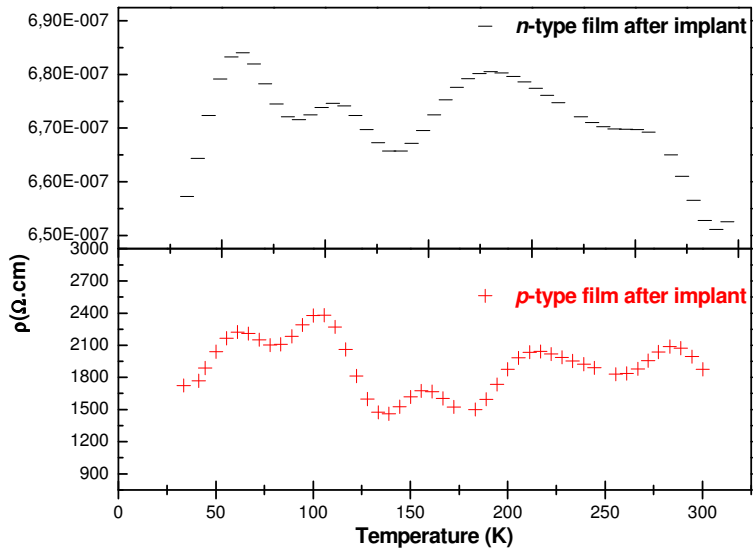
n-type film after implant
p-type film after implant
ρ(Ω.cm)
Temperature (K)

(a)

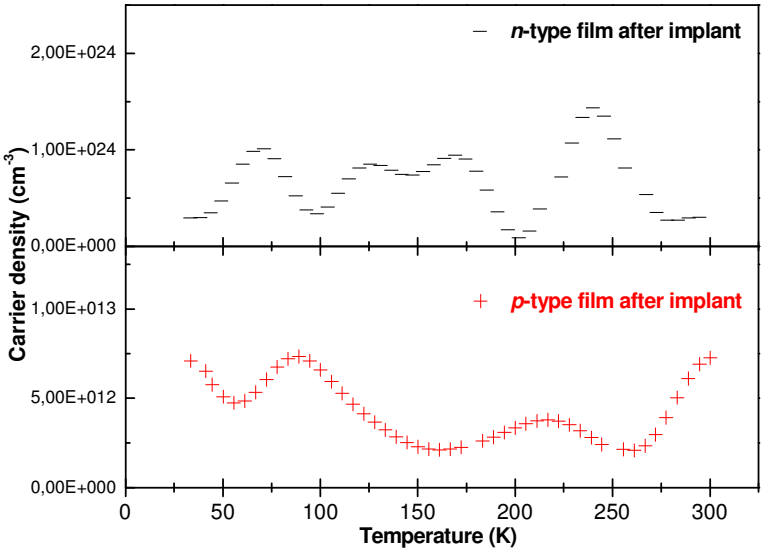
n-type film after implant
p-type film after implant
Carrier density (cm-3)
Temperature (K)

(b)

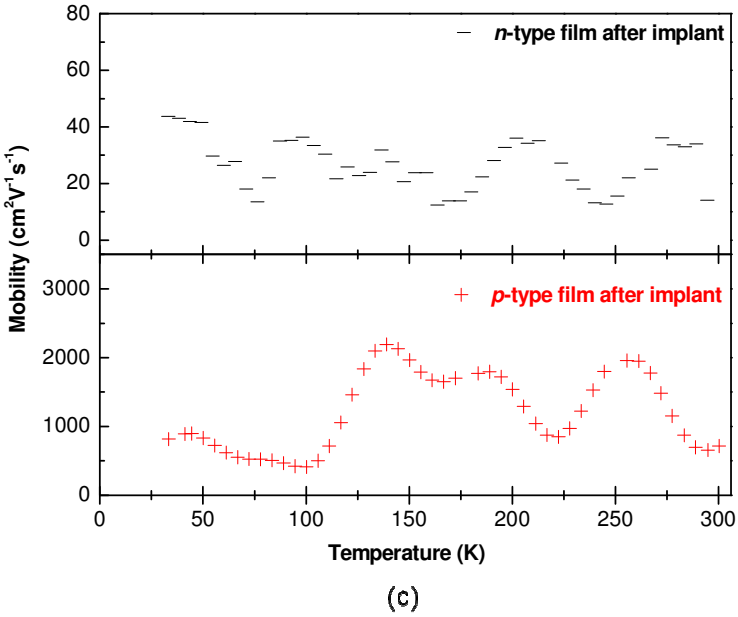

Fig.5.27. Electrical properties of different types of ZnO films after they have been implanted with Co: (a) resistivity versus temperature; (b) carrier density versus temperature; (c) mobility versus temperature

5.3.3. Optical properties

The optical properties of the films were characterized by photoluminescence spectroscopy. The PL spectra of the ZnO films show several emission bands, as seen in Fig.5.28. The NBE UV luminescence dominates the spectrum with a maximum at 382 nm (3.24 eV) for the films grown at 300°C and at 380 nm (3.26 eV) for the film grown at 600°C. In the case of the *p*-type ZnO film the NBE emission disappears after implantation and it is not recovered after RTA at 400°C. This is in agreement with what has been observed by XRD and non-RBS, where a destruction of the cell lattice is observed after implantation. In the case of the *n*-type film, the NBE emission is displaced toward lower wavelength after implantation and become narrower.

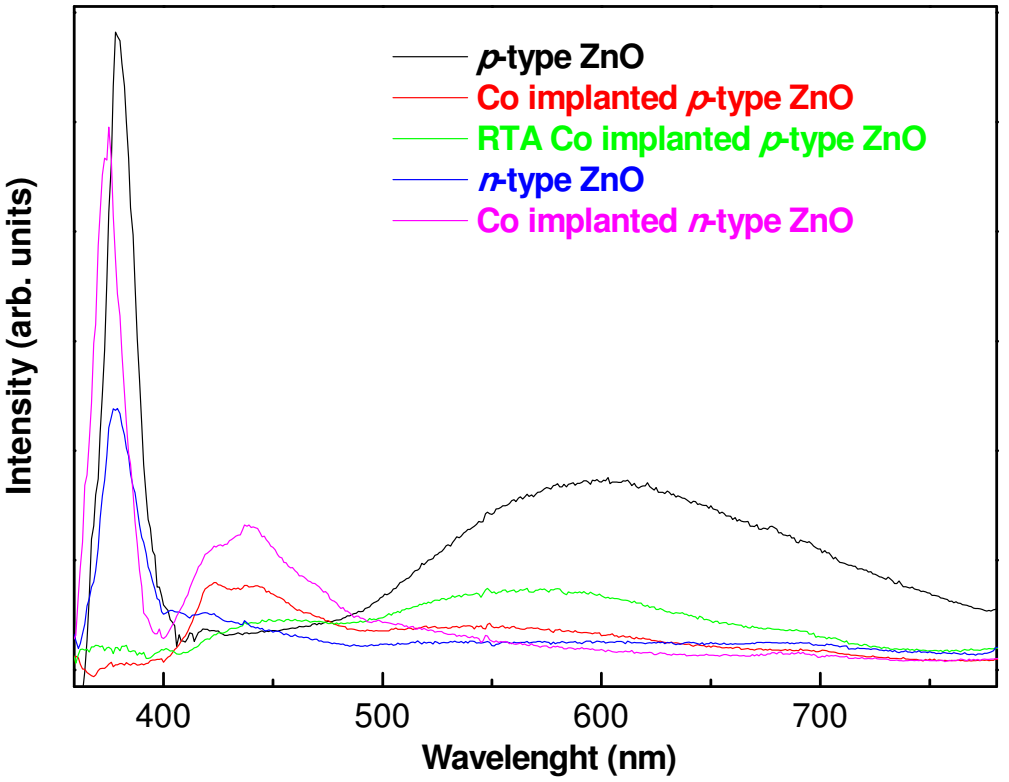

Fig.5.28. Room-temperature PL spectra of pristine ZnO films grown at 300 and 600°C, Co implanted and RTA treatment for the film grown at 300°C.

In the visible region of the spectra differences between the emission band for the *p*-type and the *n*-type pristine films can be found, as it was explained in section 4.3. "Study of the *p*-type behavior by PL". These emissions are strongly reduced in the implanted samples. This could be explained by a possible annealing/migration of those defects due to the ion implantation. It has been observed by RBS and PIXE that, upon implantation, the atoms of the cell had moved out from their positions, which explains the strong reduction of the NBE emission. Another possible explanation could be the formation of non-radiative defects by their association with Co ions, as Co^{2+} ions act as deep traps in II-VI materials and new non-radiative relaxation pathways become available [31]. Although, the most exciting feature upon implantation is the appearance of broad peak around 423nm (2.93 eV) and 439nm (2.82 eV) in the cobalt implanted films (either *p*-

or *n*-type), which corresponds to a blue-violet emission [32]. This emission is strongly reduced upon RTA. These peaks could be related to the presence of Co clusters in the films.

5.3.4. Magnetic properties

SQUID measurements were employed in order to analyze the magnetic properties of the Co implanted ZnO films.

Fig.5.29 and Fig.5.30 show: a) the temperature dependence of the magnetization at constant field; b) and c) show the magnetization versus field reversal loop (M-H) measured at 5 and 300K, before and after Co implantation for *p*-type and *n*-type ZnO film, respectively.

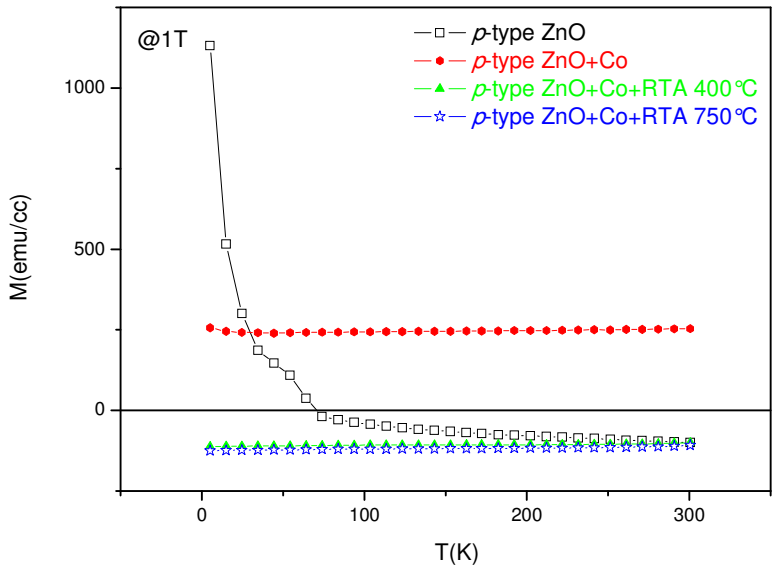

(a)

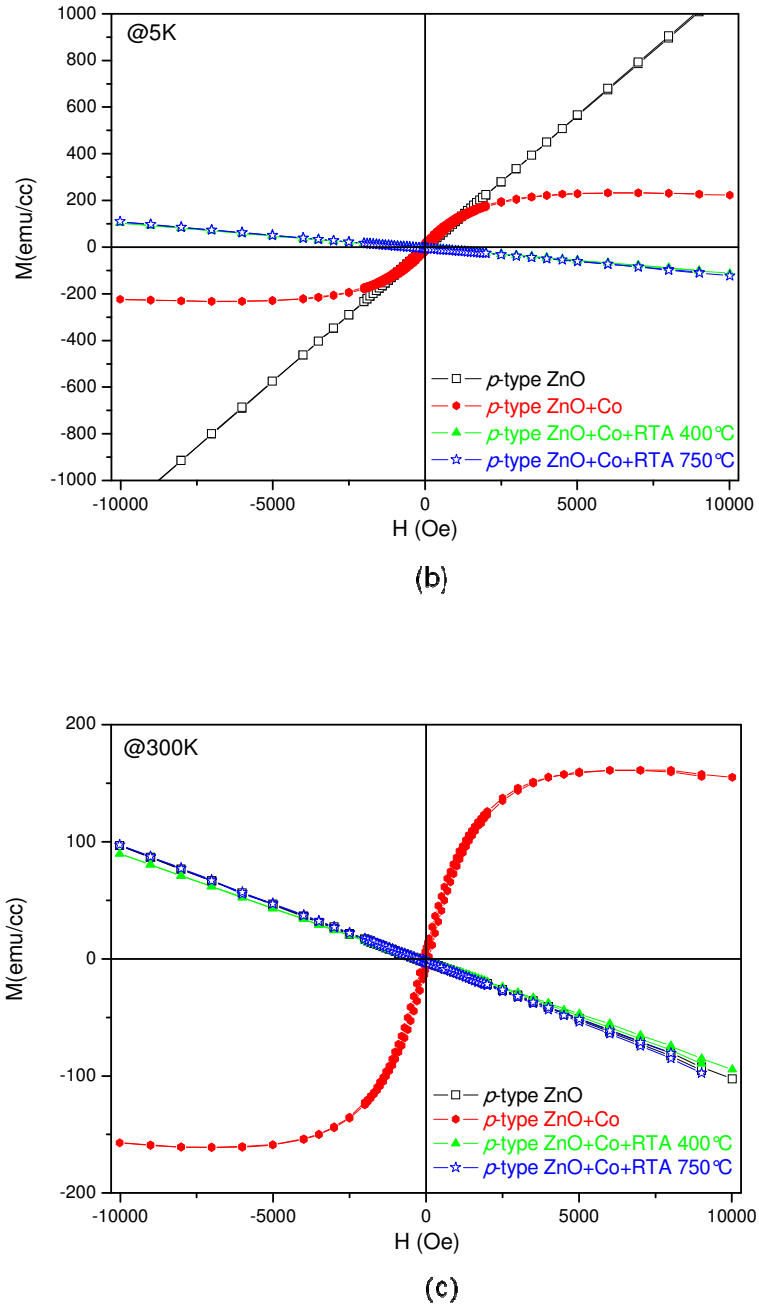

Fig.5.29. SQUID measurements for *p*-type ZnO film grown at 300°C before and after Co implantation, and RTA treatment a) The temperature dependence of the magnetization at constant field; b) and c) Magnetization versus field reversal (M-H) measured at 5 and 300K, respectively

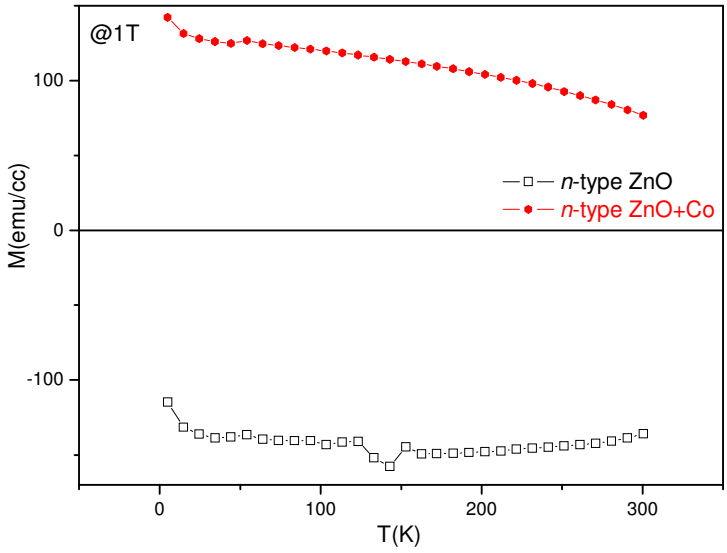
@1T
100
0
-100
M(emu/cc)
0
100
200
300
T(K)
n-type ZnO
n-type ZnO+Co

(a)

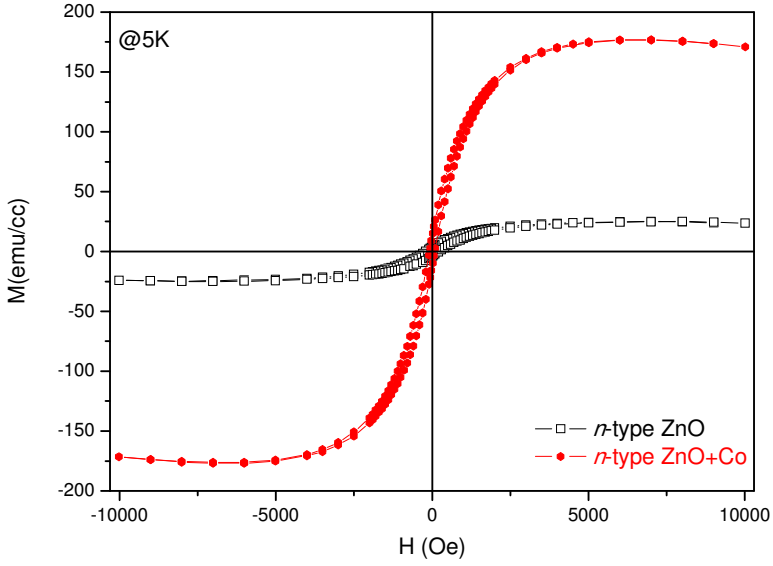
@5K
200
150
100
50
0
-50
-100
-150
-200
M(emu/cc)
-10000
-5000
0
5000
10000
H (Oe)
n-type ZnO
n-type ZnO+Co

(b)

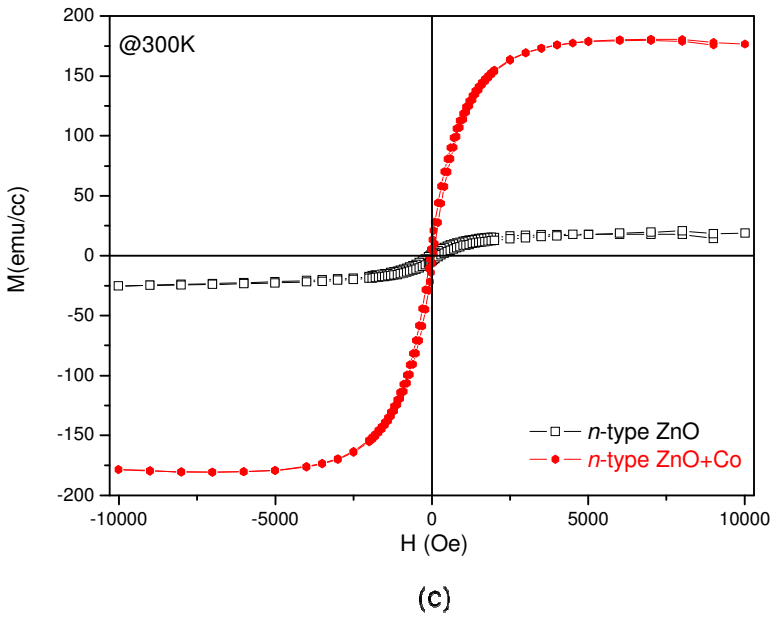

Fig.5.30. SQUID measurements for *n*-type ZnO film grown at 600°C before and after Co implantation a) The temperature dependence of the magnetization at constant field; b) and c) Magnetization versus field reversal (M-H) measured at 5 and 300K, respectively

The as obtained *n*- and *p*- type films (grown at 600 and 300°C) show pure diamagnetic, and a mixture of diamagnetic and paramagnetic behavior respectively. After implantation both films exhibit a ferromagnetic component of about 150-200 emu/cc, far beyond our uncertainty/impurity levels. The shape of the loops is very similar, but the temperature dependence of the magnetic signal is quite different. While for ZnO *p*-type film Co implanted the magnetization is flat, for *n*-type Co implanted the magnetization decays faster, pointing to a lower Curie temperature of the magnetic entities responsible of the signal. This could be an indicative of Co clusters behavior. Small Co clusters are superparamagnetic at RT when they are smaller than about 7.5 nm diameter [33]. It is possible that there is a distribution of sizes such the *p*-type film has a larger size distribution of Co cluster. This is in agreement with structural and electrical properties of the films. It has been seen that the *n*-type film grown at 600°C presents a

very good crystal quality. Therefore as the Co ions encounter very few defects on their trajectory will form very small clusters. At the same time the conductivity of this film improves. On the other hand, the *p*-type film grown at lower temperature (300°C) present lower crystal quality. As the Co ions penetrate into the film encounter bigger defects, and as a result will form larger Co clusters. Consequently the conductivity of the film decreases. These Co bigger clusters must annihilate the NBE PL emission. This hypothesis is confirmed further after the film has been annealed. As it can be seen in Fig.5.29 the FM disappears after the film has been exposed to RTA at 400 and 750°C. This behavior could indicate that annealing promotes the oxidation of metallic Co clusters existing in the films, validating thus the theory that the FM signal in these films might come from the segregated clusters.

Conclusions:

- ✓ Epitaxial *p*- and *n*- type ZnO films were implanted with Co ions at fluences of $1x10^{16}$ ions/cm^2 and energies of 120 KeV and 140 KeV, respectively.
- ✓ Channeling particle induced X-ray emission experiments show that after Co implantation the ZnO crystalline lattice is destroyed and that Co-implanted atoms do not substitutionally incorporate into the host matrix.
- ✓ The implantation of Co ions into the ZnO host matrix affect drastically the electrical properties of the ZnO films, either *p*-type or *n*-type.
- ✓ The Co implanted films exhibit ferromagnetic like behavior and become diamagnetic after RTA. The FM in this case has been associated to the formation of Co clusters.

References

[1] M.A. Garcia, E. Fernandez Pinel, J. de la Venta, A. Quesada, V. Bouzas, J.F. Fernández, J.J. Romero, M.S. Martín González, J.L. Costa-Krämer, J. Appl. Phys. 105 (2009) 013925

[2] J. Robin, Ann. Chim. (Paris) 10 (1955) 389

[3] A. Quesada, M.A. Garcia, M. Andrés, A. Hernando, J.F. Fernández, A.C. Caballero, M.S. Martín González, F. Briones, J. Appl. Phys. 100 (2006) 113909

[4] M.S. Martin-Gonzalez, M.A. Garcia, I. Lorite, J.L. Costa Kramer, F. Rubio-Marcos, N. Carmona, J.F. Fernandez, J.Electrochem. Soc. 157 (2010) E31

[5] P.W. Tasker, J. Phys. C: Solid State Phys. 12 (1979) 4977

[6] C. Noguera, J. Phys.: Condens. Matter 12 (2000) R367

[7] J. Goniakowski, F. Finocchi, C. Noguera, Rep. Prog. Phys. 71 (2008) 016501

[8] W.A. Harrison, E.A. Kraut, J.R. Waldrop, R.W. Grant, Phys. Rev. B 18 (1978) 4402

[9] M. Gajdardziska-Josifovska, R. Plass, M.A. Schoeld, D.R. Giese, R. Sharma, J. Electron Microsc. 51 (2002) S13

[10] V.K. Lazarov, R. Plass, H.C. Poon, D.K. Saldin, M. Weinert, S.A. Chambers, M. Gajdardziska-Josifovska, Phys. Rev. B 71 (2005) 115434

[11] C.A.F. Vaz, H. Wang, C.H. Ahn, V.E. Henrich, M.Z. Baykara, T. Schwendemann, N. Pilet, B.J. Albers, U. Schwarz, L.H. Zhang, Y. Zhu, J. Wang, E.I. Altman, Surf. Sci. 603 (2009) 291

[12] W. Meyer, K. Biedermann, M. Gubo, L. Hammer, K. Heinz, J. Phys.: Condens. Matter 20 (2008) 265011

[13] K. Martin, G. McCarthy, North Dakota State University, Fargo, North Dakota, USA ICDD Grant-in-Aid (1990)

[14] J. Visser, J. Appl. Crystallogr.2 (1969) 89

[15] Natl. Bur. Stand. (U.S.) Monogr. 25, 13 (1976) 35

[16] H. Schulz, K.H. Thiemann, Solid State Commun. 32, 783 (1979) 034477

[17] P.S. Patil, L.D. Kadam, C.D. Lokhande, Thin Solid Films 272 (1996) 29

[18] V.R. Shinde, S.B. Mahadik, T.P. Gujar, C.D. Lokhande, Appl. Surf. Science 252 (2006) 7487

[19] K. Shalini, A.U. Mane, S.A. Shivashankar, M. Rajeswari, S. Choopun, J. Crystal Growth 231 (2001) 242

[20] A.U. Mane, K. Shalini, A. Wohlfart, A. Devi, S.A. Shivashankar, J. Crystal Growth 240 (2002) 157

[21] M. Rooth, E. Lindahl, A. Harsta, Chem. Vap. Dep. 12 (2006) 209

[22] K.B. Klepper, O. Nilsen, H. Fjellvag, J. Crystal Growth 307 (2007) 457

[23] C.A.F. Vaz, D. Prabhakaran, E.I. Altman, V.E. Henrich, Phys. Rev. B 80 (2009) 155457

[24] R.J. Kennedy, IEEE Trans Magn. 31 (1995) 3829

[25] K. Krezhov, P. Konstantinov, J. Phys.: Condens. Matter 5 (1993) 9287

[26] M.S. Martín-González, C.S. Steplecaru, F. Briones, E. López-Ponce, J.F. Fernández, M.A. García, A. Quesada, C. Ballesteros, J.L. Costa-Krämer, Thin solid films 518 (2010) 4607

[27] J.F. Ziegler, M.D. Ziegler, J.P.Biersack SRIM-2006.02

[28] C.S. Steplecaru, M.S. Martin-González, J.F. fernández, J.L. Costa-Krämer, Thin Solid Films 518 (2010) 4630

[29] J.R. Tesmer, M. Nastasi, Handbook of Modern Ion Beam Materials Analysis, MRS (1995)

[30] R. González-Arrabal, Y. González, L. González, M. García-Hernández, F. Munnik, M.S. Martín-González, J. Appl. Phys. 105 (2009) 073911

[31] C. Liu, F. Yun, H. Morkoc¸ J. Mat. Sci.: Mat. Electr. 16 (2005) 555

[32] R. Kumar, F. Singh, B. Angadi, J.W. Choi, W.K. Choi, K. Jeong, J.H. Song, M. Wasi Khan, J.P. Srivastava, A. Kumar, R.P. Tandon, J. Appl. Phys. 100 (2006) 113708

[33] M. Opel, K.W. Nielsen, S. Bauer, S.T.B. Goennenwein, J.C. Cezar, D. Schmeisser, J. Simon, W. Mader, R. Gross, Eur. Phys. J. B 63 (2008) 437

CONCLUSIONS

This thesis work has focused on some of the critical issues of ZnO based DMS materials for spintronic applications. The main objectives have been accomplished, namely: i) fabricate epitaxial *p*-type and *n*-type ZnO based films, ii) understand the effect of crystal defects on their electrical conductivity; and iii) grow high quality Co_3O_4 films and to explore the potential of the ZnO:Co system, starting from ZnO/ Co_3O_4 multilayers, as a possible ZnO based DMS.

The general conclusions of this PhD work are:

- ✓ E*pitaxial growth of ZnO films* on (0001) Al_2O_3 substrates *is demonstrated from 200°C. This is the lowest epitaxial growth temperature reported for PLD so far.*

- ✓ *p-type behavior is demonstrated in ZnO thin films grown at 200 and 300°C* with mobilities of 20-40 $cm^2V^{-1}s^{-1}$, the largest in the literature to the best of our knowledge. This *p*-type behavior persists for approximately 10 months.

- ✓ *n*-type ZnO films were irradiated with protons at different fluencies. The films are hard radiation resistant materials up to *a fluency of* $1x10^{17}$ *at/cm*^{2}. *Upon radiation t*he crystal quality decreased. The generated defects are the responsible of *a change from n-type to p-type* conductivity.

- ✓ Correlation between PL and transport measurements conclude that PLD ZnO films grown at 200 and 300°C present *Zn vacancies that act as acceptors, and could be responsible of the p-type behavior*. The *oxygen vacancies act as deep donors, promoting the n-type behavior for the ZnO* films grown at temperatures ≥400°C.

- ✓ The ZnO/Co_3O_4 multilayers grown above 200°C are not FM.

- ✓ The *implantation of Co ions into the ZnO* host matrix affects drastically the properties of the ZnO films, both *p*- or *n*-type: the ZnO crystalline lattice is destroyed and the Co-implanted atoms do not substitutionally incorporate into the host matrix. These *films exhibit ferromagnetic like behavior, associated to the formation of Co nanoclusters*. This behavior is destroyed upon film heating.

CONCLUSIONES

Este trabajo de tesis se ha centrado en algunos de los problemas más importantes en el desarrollo de materiales DMS basados en ZnO para aplicaciones en espintrónica. Los objetivos principales han sido conseguidos, siendo principalmente: i) fabricar películas epitaxiales de ZnO tipo *p* y tipo *n*, ii) entender cómo afectan los defectos del cristal a su conductividad eléctrica; y iii) crecer películas de alta calidad de Co_3O_4 y explorar el potencial del sistema ZnO:Co como un posible DMS basado en ZnO.

Las conclusiones generales de este trabajo de doctorado son:

- ✓ *Se ha obtenido crecimiento epitaxial de películas ZnO* sobre sustratos de Al_2O_3 (0001) *a partir de 200°C. Ésta es la temperatura más baja* de crecimiento epitaxial de ZnO por PLD descrita en la literatura hasta ahora.

- ✓ *Se ha demostrado comportamiento tipo p en películas delgadas epitaxiales de ZnO crecidas a 200 y 300°C* con movilidades de 20-40 $cm^2V^{-1}s^{-1}$, siendo hasta donde sabemos los valores más altos descritos en la literatura. Este comportamiento tipo *p* se mantiene durante aproximadamente unos 10 meses.

- ✓ Se han irradiado películas delgadas de ZnO tipo *n* con diferentes dosis de protones. Estas películas son resistentes a la radiación hasta una *dosis de* $1x10^{17}$ at/cm^2. A partir de ésta dosis la calidad cristalina de las películas irradiadas disminuye. Los defectos generados son responsables *del cambio de comportamiento de tipo n a tipo p.*

- ✓ Las medidas de PL revelan que las películas de ZnO crecidas a 200 y 300°C tienen *vacantes de Zn, que actúan como aceptores y parecen ser responsables del comportamiento de tipo p. Las vacantes de oxígeno actúan como donores,*

promoviendo el comportamiento de tipo n para las películas de ZnO crecidas a temperaturas ≥400°C.

- ✓ Las multicapas ZnO/Co_3O_4 crecidas a temperaturas>200°C no son FM.

- ✓ La implantación de iones de Co en la matriz de ZnO afecta drásticamente las propiedades de las películas de ZnO, ya sea tipo *p* o tipo *n*: la red cristalina de ZnO se destruye y los átomos de Co implantados no se incorporan en posición substitucional en la matriz de ZnO. Estas películas exhiben comportamiento ferromagnético, asociado a la formación de "nanoclusters" de Co. Este ferromagnetismo desaparece al calentar la película.

LIST OF ACRONYMS

AFM	Atomic Force Microscopy
ALD	Atomic Layer Deposition
ALE	Atomic Layer Epitaxy
CAI	Centro de Asistencia a la Investigación
CCD	Charge-Coupled Device
CVD	Chemical Vapor Deposition
DMS	Diluted Magnetic Semiconductor
DRAM	Dynamic Random Access Memory
e-beam	Electron beam
EC	Electro-Chromic
FM	Ferromagnetism
FWHM	Full-Width Half Maximum
GADDS	General Area Detector Diffraction System
GMR	Giant Magneto Resistance
HVEC	High Voltage Engineering Corp.
IBA	Ion Beam Analysis
ICMAB	Instituto de Ciencia de Materiales Barcelona
ICP-AES	Inductively Coupled Plasma Atomic Emission Spectroscopy
IMM	Instituto Microelectronica Madrid
ITO	Indium Tin Oxide

JCPDS	Joint Committee on Powder Diffraction Standards
LED	Light Emitting Diode
MBE	Molecular Beam Epitaxy
MOCVD	Metal-Organic Chemical Vapor Deposition
MOVPE	Metal-Organic Vapour Phase Epitaxy
MRAM	Magnetoresistive Random Access Memory
MTJ	Magnetic Tunnel Junctions
NBE	Near-Band-Edge
PD	Pressure-Distance
PIXE	Particle Induced X-ray Emission
PL	Photoluminescence
PLD	Pulsed Laser Deposition
PVD	Physical Vapor Deposition
RBS	Rutherford Backscattering Spectrometry
RT	Room Temperature
RTA	Rapid Thermal Annealing
SQUID	Superconducting Quantum Interference Device
STT	Spin Torque Transfer
TAS	Thermal Assisted Switching

TCO	Transparent Conducting Oxide
TM	Transition Metal
TMR	Tunnel Magneto Resistance
UV	Ultraviolet
WBS	Wide Bandgap Semiconductor
XRD	X-Rays Diffraction
ZFC	Zero Field Cooled
µ-XRD	Micro X-Rays Diffraction

LIST OF SYMBOLS

A	Beam area 48
Al	Aluminum 67
Al_2O_3	Aluminum oxide (Sapphire) 8
Ar	Argon 127
As	Arsenic 139
Au	Gold 78
B	Magnetic field 72
Be	Beryllium 58
C	Carbon 62
Co	Cobalt 7
CoO	Cobalt monoxide 7
Co_3O_4	Cobalt oxide 8
d	Thickness 73
D_m	Supersaturation 36
E	Energy 47
E_H	Hall field 73
F	Magnetic force 72
Fe	Iron 133
Ga	Gallium 78
GaAs	Gallium arsenide 87
GaN	Gallium nitride 6
H	Hydrogen 58
H^+	Proton 45
H	Magnetic field strength 129

H_C	Coercive field	210
He	Helium	58
HfO_2	Hafnium oxide	129
(hkl)	Miller Index	54
I	Current	48
In	Indium	78
k	Kinematic factor	58
k	Boltzmann constant	36
Li	Lithium	58
m	Ion mass	59
M	Atom mass	59
M	Magnetization	129
MgO	Magnesium Oxide	193
Mn	Manganese	6
MnO_2	Manganese dioxide	6
M_S	Saturation magnetization	210
n	Carrier concentration	31
N	Nitrogen	139
Ni	Nickel	207
O	Oxygen	61
O_{film}	Oxygen in the film	61
O_{subs}	Oxygen in the substrate	61
OH	Hydroxyl	183
P	Phosphorus	139

Pt	Platinum	78
q	Charge	72
q_i	Charge per ion	48
R	Actual deposition rate	36
R	Range	47
R	Resistance	74
R_e	Equilibrium value of the deposition rate	36
R_H	Hall coefficient	73
R_p	Projected range	47
S	Total stopping power	48
Sb	Antimony	139
S_e	Electronic stopping power	46
S_n	Nuclear stopping power	46
Si	Silicon	62
SiO_2	Silicon dioxide	8
SnO_2	Tin dioxide	129
$SrTiO_3$	Strontium titanate	190
t	Time	48
T	Substrate temperature	36
T_C	Curie temperature	5
T_{growth}	Growth temperature	101
Ti	Titanium	78
TiO_2	Titanium dioxide	7
U	Uranium	58

v	Velocity	72
V_O	Oxygen vacancy	166
V_{Zn}	Zinc vacancy	168
V_E	Ettingshausen voltage	74
V_H	Hall voltage	73
V_N	Nernst voltage	74
V_R	Righi-Leduc voltage	74
V_S	Seebeck voltage	74
Zn	Zinc	61
ZnO	Zinc oxide	6
Φ	Implantation dose	47
ρ	Electrical resistivity	31
Θ	Scattering angle	59
σ	Conductivity	75
μ	Hall mobility	31
χ_{min}	Minimum yield	65